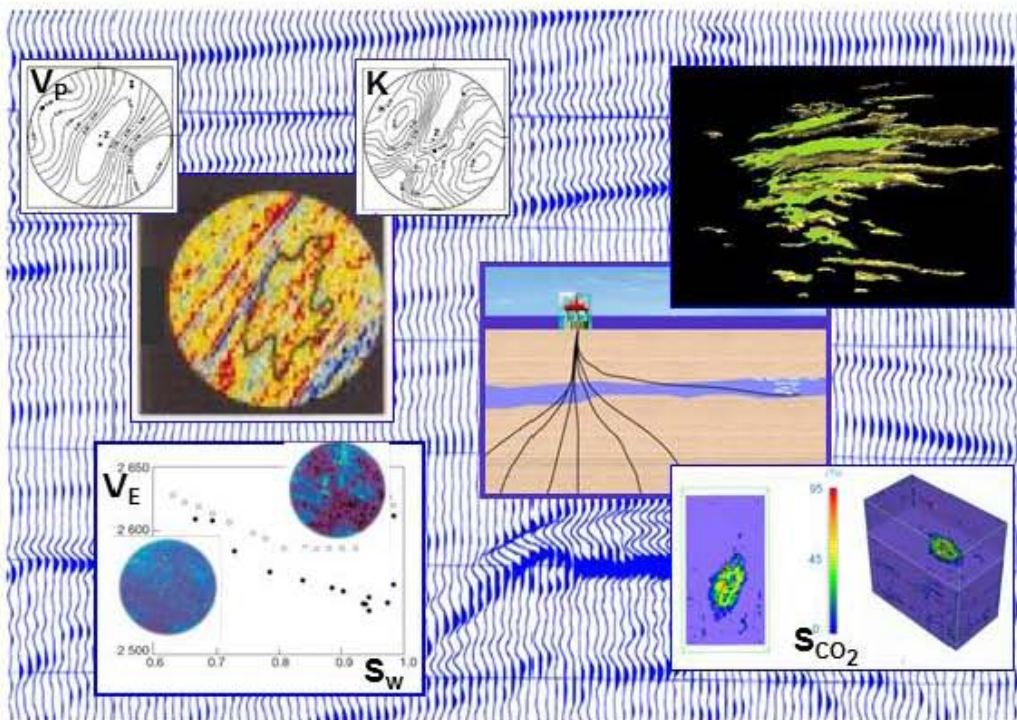


PETROACOUSTICS

- A TOOL FOR APPLIED SEISMICS -

Patrick Rasolofosaon and Bernard Zinszner



ISBN: 2-901638-14-7
EAN: 9782901638148

Book DOI : 10.2516/ifpen/2014002
Chapter 4 DOI : 10.2516/ifpen/2014002.c004

PETROACOUSTICS

- A TOOL FOR APPLIED SEISMICS –

Patrick Rasolofosaon and Bernard Zinszner

DOI: [10.2516/ifpen/2014002](https://doi.org/10.2516/ifpen/2014002)

PETROACOUSTICS

The book "PETROACOUSTICS" consists of 8 chapters intended to be published independently on the Internet:

- Chapter 1 - Some more or less basic notions (and General Introduction)
- Chapter 2 - Petroacoustics laboratory measurements
- Chapter 3 - Elastic waves in isotropic, homogeneous rocks
- Chapter 4 - Elastic anisotropy
- Chapter 5 - Frequency/wavelength dependence (impact of fluids and heterogeneities)
- Chapter 6 - Poroelasticity applied to petroacoustics
- Chapter 7 - Nonlinear elasticity
- Chapter 8 - Applications to seismic interpretation

A detailed Table of Content, Nomenclature, Reference List, Subject Index and Author Index is annexed to each Chapter

Each chapter is published independently as a pdf file. To comply with the rules of copyright no modification is allowed after the publication on the web, this is the reason why no information regarding the other chapters, which are subject to changes (e.g. the precise table of content or expected date of publication), are given in a published Chapter. These updated data are shown on a dedicated web site: <http://books.ifpenergiesnouvelles.fr>

This work is dedicated to the memory of Olivier Coussy (1953-2010), who, in the beginning of his career, enormously contributed to popularizing Poromechanics among petroleum geoscientists, through numerous fruitful collaborations with IFP Energies nouvelles. At that time we were incredibly lucky to be witnesses and sometimes actors, with Olivier's help, in this revolution.

ACKNOWLEDGMENTS

We are highly indebted to many of our colleagues for their contribution to this work.

Firstly a word of thanks to those who, at IFP Energies nouvelles (IFPEN) contributed directly (review, assistance in computing): Jean Francois Nauroy, Laurence Nicoletis, Noalwenn Dubos-Sallée and Olivier Vincké.

At IFPEN Rock Physics Laboratory, a lot of work was done by PhD students and Interns. Many quotes in this book are testimony to the contribution of Rob Arts, Louanas Azoune, Ana Bayon, Thierry Cadoret, Nathalie Lucet, Didier Martin, Bruno Pouet, Hocine Tabti, Pierre Tarif. For many years, Michel Masson was of great help for the experiments.

The Rock Acoustics courses taught at IFP School and at the Universities Pierre et Marie Curie and Denis Diderot of Paris, and the numerous questions of the students have greatly stimulated the writing of this book.

We are indebted to many of our colleagues (or professors!) for the indirect but invaluable contributions made over the years during discussions or collaborative works. We are grouping them according to their institutions:

- IFPEN: Olga Vizika, Gérard Grau, Christian Jacquin
- Beicip-Franlab: Bernard Colletta
- IGP and French Universities: Maria Zamora, Mathias Fink, Daniel Royer, Jean-Paul Poirier, Daniel Broseta, André Zarembowitch, Michel Dietrich, Pascal Challande
- IRSN: Justo Cabrera, Philippe Volant
- Stanford University: Amos Nur, Gary Mavko
- Colorado School of Mines: Mike Batzle, Manika Prasad
- Oil and Service companies (CGG, GdFSuez, Petrobras, Schlumberger, Statoil, Shell, Total): Ivar Brevik, Lucia Dillon, Dominique Marion, Eric De Bazelaire, Christian Hubans, Jean Arnaud, Colin Sayers, Thierry Coléou, Arnoult Colpaert, Ronny Hofmann, Mark Kittridge, Salvador Rodriguez.

We wish to express our deepest gratitude to Klaus Helbig for longtime collaboration on Seismic Anisotropy, and even far beyond. Also, within the global community of volunteering Anisotropists, special mention goes to the late Mike Schoenberg, Ivan Psencik, Evgeny Chesnokov, Leon Thomsen, Erling Fjaer, Joe Dellinger, Véronique Farra, Boris Gurevich, Michael Slawinski, and Ilya Tsvankin.

Paul Johnson, of Los Alamos National Laboratory, introduced us to the frightening field of Nonlinear Elasticity. We gratefully acknowledge him and the active community of Nonlinear Elasticity in Geomaterials, including Tom Shankland, Jim TenCate, Koen Van den Abelee, Katherine McCall, Robert Guyer, for long time and fruitful collaboration.

Thanks to Lionel Jannaud, inspired by the great pioneering seismologist Keiti Aki in his work on wave propagation in random media, for allowing us to use some of his results for the writing of chapter 5 on Frequency/wavelength dependence.

Finally we would like to give special thanks to Thierry Bourbié. This book is an offshoot of our first textbook "Acoustics of Porous Media", and we gained great experience from him.

GENERAL INTRODUCTION

Petroacoustics, or more commonly Rock Acoustics, is the study of mechanical wave propagation in rocks. It is one of the most prolific branches of 'Rock Physics', aiming itself to make the link between the rock response to remote physical solicitations (often by wave methods or by potential methods) and the physical properties of rocks (such as mineralogy, porosity, permeability, fluid content...). Rock physics is a very active field, which has early evolved from a sophisticated curiosity for specialists to a mainstream research topic leading to practical tools now routinely integrated in oil exploration and exploitation. On the leading edge of this wave, volunteering groups of specialists of Rock Physics constituting a global community meet during the International Workshop on Rock Physics (IWRP), involving both industry and academia, and not associated with any formal organisation or institution, as documented on their website <http://www.rockphysicists.org/Home>.

After this website, many references on petroacoustics are already available for decades. For the 1990s numerous experimental and theoretical works have accumulated and new books have been published, for instance 'The Rock Physics Handbook' of Gary Mavko, Tapan Mukerji and Jack Dvorkin, among the most recommended. So one could fairly ask why a new book in the field?

This book can be considered as a natural continuation of the book entitled 'Acoustics of Porous Media', co-authored by Thierry Bourbié, Olivier Coussy and Bernard Zinszner, and issued by our laboratory in 1986 for the French version, and in 1987 for the English version.

However, here the clear guideline is experimentation. In contrast to previous books, all the techniques, from the most conventional (using piezoelectric transducers) to the most recent space-age methods (as laser ultrasonics) are detailed. Furthermore the book is mainly based on experimental data allowing to select the most appropriate theories for describing elastic wave propagation in rocks. Emphasis on Nonlinear elasticity and Seismic anisotropy are also originality of the book. A part of the book also focuses on the history of the different sub-fields dealt with, having in mind that the knowledge of the history of a field contributes to understanding the field itself. For instance, in spite of the clear anteriority of their work the names of the Persian mathematician, physicist and optics engineer Ibn Sahl, and of the English astronomer and mathematician Thomas Harriot are unfairly not, or rarely, associated with the law of refraction, compared to the names of the Dutch astronomer and mathematician Willebrord Snell van Royen, known as Snellius, and of the French philosopher and writer René Descartes, as detailed in the first chapter.

The book is divided into eight chapters.

The **first chapter** deals with what we call some more or less basic notions that will be used in the following chapters. Some notions described in this chapter are well known and/or straightforward and can be found in any classical textbook on Continuum Mechanics or on Acoustics. Some other notions are unfortunately not commonly appreciated and need to be introduced for studying physics in geological media. The chapter is divided into three sections. First we introduce Petroacoustics, or more commonly Rock acoustics, and Geoacoustics, that is to say acoustics of geological media, as particular branches of Acoustics (section 1.1). Then we give the basics of classical Mechanics in Continuous Media, including the description of stress, strain and elastic wave propagation, together with the main deviations from the ideal homogeneous isotropic linearly elastic behaviour, that is to say heterogeneity, dispersion, attenuation, anisotropy, and nonlinearity possibly with the presence of hysteresis (section 1.2). Last, because natural media are all but continuous media at many scales, we describe in section 1.3 the way to adapt the previous descriptions to the case of discontinuous media with hierarchical structure, such as geological media, with the introduction of fundamental notions such as Representative Elementary Volume and Continuum Representation in such media. These are precisely the less obvious notions that are referred to in the title of this chapter.

In **Chapter 2**, we describe the most common techniques for performing acoustic experiments on rocks in the laboratory. The chapter is divided into three sections. First we discuss the reliability of petroacoustic measurements, we introduce the main petrophysical parameters (porosity, permeability), and we emphasize various experimental cautions (damage, saturation process...) (section 2.1). Then we introduce the two main types of experiments performed in petroacoustic laboratories, characterized by contrasted aims. The first type experiment, described in section 2.2, aims to measure the acoustic properties of geological materials. In this case it is important that the measured sample is representative of the studied geological formation. Another important aspect is the physical state of the rock sample. Obviously altered and/or damaged samples must be avoided. Finally the pressure and temperature state have to be as close as possible to the in-situ condition. Section 2.3 deals with the second type of experiments in rocks, aiming to better understand physical phenomena involved in elastic wave propagation, or to study wave propagation on scaled-down physical models in the laboratory. In this case, temperature and pressure condition, have less importance, unless these parameters are precisely in the central parameters of the study. The chosen materials, possibly artificial materials (such as sintered glass beads), can be chosen according to the purpose of the physical study.

Chapter 3 addresses the dependence of the acoustic parameters (mainly velocity and attenuation) of geomaterials on their lithologic nature (mineralogy, porosity) and on physical parameters (fluid saturation, pressure, and temperature). All these relationships are obviously at the height of applications of petroacoustics to the interpretation of seismic data in a broad sense (i.e., seismological data, applied seismic data, acoustic logs data...). As a matter of fact, it is from the quantitative knowledge of these relationships that we can hope to extract information such as porosity or saturation state of underground formations.

In **chapter 4** we discuss elastic anisotropy under different points of view but, as in the other chapters, always more or less in relation with experimental aspects. The chapter is divided into seven sections. In the first section (4.1), we summarize the history of seismic anisotropy. Section 4.2 introduces the symmetry principles in physical phenomena, due to the great scientist Pierre Curie, and the way they can simplify the description of elastic anisotropy. In the next section 4.3 we introduce the classical theory of static and dynamic elasticity in anisotropic media, and we describe and illustrate the main manifestations of elastic anisotropy in rock (i.e. directional dependence of the elastic wave velocities, shear-wave splitting of shear-wave birefringence, and the fact that the seismic rays are generally not normal to the wavefronts). Because rocks generally exhibit moderate to weak anisotropy strength it is possible to use perturbation theories to simplify the exact theoretical derivation as described in the next section (4.4). This is followed by a description of the main causes of elastic anisotropy and the corresponding rock physics models (section 4.5). In addition to elastic anisotropy, experimental studies have unambiguously other robust results, namely porous nature (poroelasticity), frequency dependence (viscoelasticity), or the dependence on stress-strain level (nonlinearity) which lead to use more sophisticated models as pointed out in the next part (section 4.6). The last section (4.7) explains how elastic anisotropy alters the seismic response and necessitates the adaptation of existing seismic processing tools to take into account the anisotropic case. Conversely it also explains how seismic response can be analyzed in order to characterize the studied rocks.

The dependence of the mechanical properties of geological media with respect to frequency, or equivalently with wavelength, is illustrated by countless examples at various scales and is discussed in **Chapter 5**. This chapter also describes and details the main causes of this dependence. The chapter is divided into five sections. We start (section 5.1) by distinguishing the geometry-induced, or extrinsic, frequency/wavelength dependence from the intrinsic one, due to the property of the rock itself. The rest of the chapter is focused on intrinsic frequency/wavelength dependence. Next we describe the main causes of intrinsic frequency/wavelength dependence in rocks, which can be summarized in two words, namely fluids and heterogeneities. In the third section we describe the frequency/wavelength dependence due to the presence of fluid. It is essentially an anelastic mechanism (see Chapter 1 section 1.2.3.5), where the energy dissipation (conversion of wave energy to heat) is due to the viscosity of the saturating fluid. In contrast, the frequency/wavelength dependence due to the presence of heterogeneities described in section 4 is not due to energy dissipation but, rather, to energy redistribution from the first arriving coherent waves to the later chaotic arrivals, or codas, the total wave-field energy being conserved. Finally, instead of specifying the physical mechanisms involved in the frequency/wavelength dependence, an alternative way is to phenomenologically describe the mechanical behaviour of rock as done in the last section, by studying the empirical relation between the applied stress and the resulting strain. We shall see that, among the large class of phenomenological models, the sub-class of linear viscoelastic models can closely mimic the behaviour of a broad class of dissipative processes, resulting from rapid and small-amplitude variations in strain due to waves that propagate in rocks.

Chapter 6 deals with the poroelastic description of rock behaviour. In other words the chapter describes the elasticity of rocks considered as porous media. The chapter is divided into four sections. First we introduce the general field of Poromechanics, that is to say Mechanics in porous media, including the sub-fields of Poroelasticity and Poroacoustics, that is to say, respectively, Elasticity and Acoustics of porous media (section 6.1). Then we give the basics of the classical theory of poroelasticity, including the description of the stresses and the strains in porous media, of the static couplings (i.e., change of fluid pressure or mass due to applied stress, or change of porous frame volume due to fluid pressure or mass change]) and of the dynamic couplings (i.e., viscous and inertial couplings). The section ends with wave propagation (section 6.2), emphasizing the influence of the

presence of macroscopic mechanical discontinuities, that is to say interfaces, and of fluid transfer through these interfaces on the observed wavefields. The next section (section 6.3) describes the various sophistications of the initial model imposed by experimental reality, mainly the necessity of integrating viscoelasticity [mainly due to the presence of compliant features (e.g., cracks, micro fractures)] and/or anisotropy into the poroelastic model. This leads to a new classification of wave propagation regimes in fluid-saturated porous media distinguishing four regimes represented in a ξ (crack density)- k_G (interface permeability) diagram [k_G characterizing the fluid exchange through the macroscopic mechanical discontinuities (or interfaces)]. The last section explains how poroelastic signature of rocks can be used to characterize fluid substitution in different context of underground exploitation (section 6.4).

The perfect linear relation between stress and strain is often a convenient simplification in most real media, but does not reflect experimental reality. In fact, nonlinear elasticity is a pervasive characteristic of rocks, mainly due to the presence of compliant porosity (e.g., cracks, microfractures), but not only, and is addressed in **Chapter 7**. The chapter is divided into six parts. First we introduce the multiple aspects of nonlinear science and briefly introduce the history of nonlinear elasticity (section 7.1). Then we give the basics of nonlinear elasticity. This include the description of stresses in the presence of finite deformations, that is to say Cauchy stress relative to the present configuration and Piola-Kirchhoff stress relative to the reference configuration.

The classical third order nonlinear elasticity (implying expansion of the elastic deformation energy to the third power of the strain components) is detailed in the static case and in the dynamic case, especially wave propagation (section 7.2). Section 3 describes the main experimental manifestations of nonlinear elasticity, namely the stress-dependence of the velocities/moduli, the generation of harmonic frequency not present in the source frequency spectrum, and wave-to-wave interaction (section 7.3). Then we detail the two main fields of nonlinear elasticity in rocks (section 7.4), namely nonlinear acoustics (i.e., the study of wave of finite amplitude) and acoustoelasticity (i.e., the study perturbative waves in statically pre-stressed media). In the next section we introduce the most used sophistications of the nonlinear elastic model, namely the higher order nonlinear models and nonlinear hysteretic models of Preisach type. Associated to Kelvin's description in eigenstresses and eigenstrains, the last approach demonstrates that there seems to be no limit in the sophistication of the models with media exhibiting simultaneously dispersion/attenuation, anisotropy, and nonlinearity possibly with the presence of hysteresis (section 7.5). In the last section (section 7.6) we illustrate how the multiple ramifications of nonlinear response of rocks may affect various areas of research in Geosciences. These include Rock mechanics, and more generally speaking material science, where the nonlinear response of material may be used for characterization purposes, and Seismology, where the spectral distortion of seismic waves has to be considered. The characterization of material property change by monitoring the nonlinear response may be valuable (e.g., changes due to fluid saturation, to stress variations or to damage induced by fatigue...).

Finally, in **Chapter 8**, we describe some case histories showing practical applications of each of the theories introduced in the previous chapters. The chapter is divided into four sections. In the first part (section 8.1) we deal with fracture characterization from the analysis of seismic anisotropy. Section 8.2 illustrates the application of Poroelasticity theory to seismic monitoring of subsurface exploitation with Hydrocarbon Reservoir monitoring and CO2 geological storage. This will be followed in the section 8.3 by the exploitation of the scattered seismic wavefields for the characterization of heterogeneity in the subsurface. The last section (8.4) illustrates by field examples how the principle of nonlinear elasticity can be exploited for inverting the stress state in the subsurface.

Lastly, we wrote the book as if it were the book we wished we had available on our shelf at the time we were newcomers in the field. That is why we make it freely downloadable on the internet in order to facilitate sharing our experimental and theoretical expertise of these last decades with the community, and above all to encourage young newcomers to the fascinating field of Petroacoustics. We hope that some readers will actually experience as much pleasure as we experienced when writing this book.

Rueil-Malmaison, April 2014

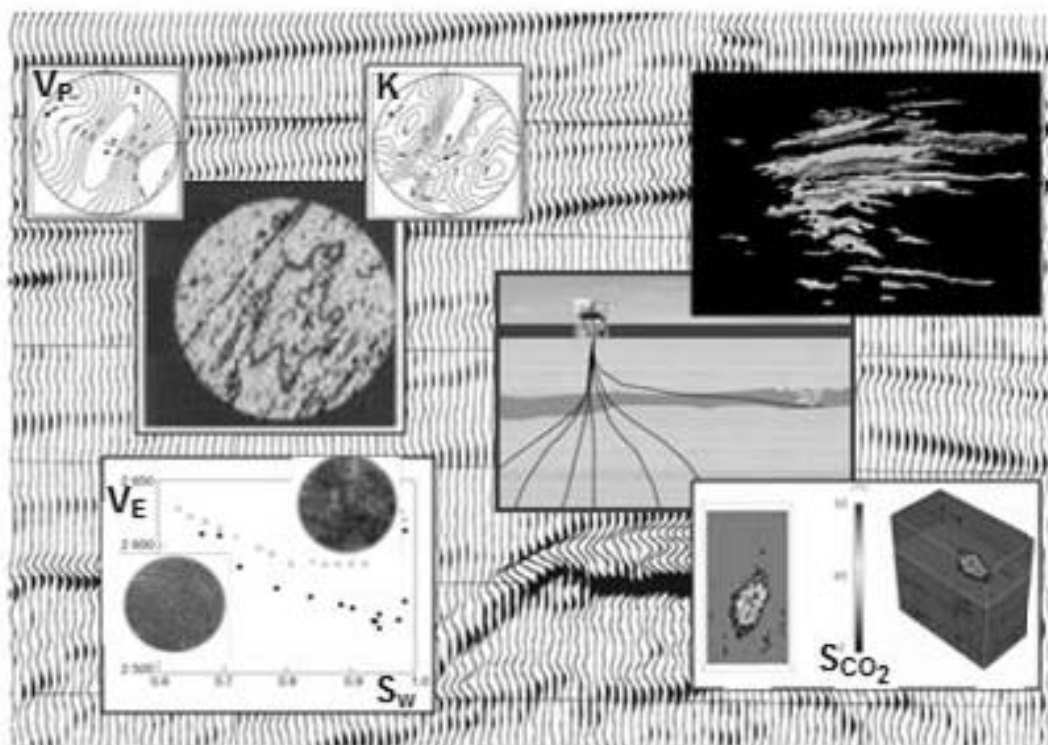
Patrick Rasolofosaon and Bernard Zinszner

PETROACOUSTICS

- A TOOL FOR APPLIED SEISMICS -

CHAPTER 4 ELASTIC ANISOTROPY

Patrick Rasolofosaon and Bernard Zinszner



PETROACOUSTICS – CHAPTER 4

NOMENCLATURE.....	a
4 - ELASTIC ANISOTROPY	4.1-1
4.1 A brief history of seismic anisotropy	4.1-2
4.2 Anisotropy and Curie's symmetry principle	4.2-5
4.2.1 Curie's symmetry principle and some consequences for elastic anisotropy...	4.2-7
4.2.2 Curie's limit group and symmetry of geological media	4.2-11
4.2.2.1 Curie's symmetry group or limit group of symmetry.....	4.2-11
4.2.2.2 Hierarchical link between Curie's symmetry groups and the crystallographic groups. Symmetry groups in Geological media	4.2-14
4.3 Seismic anisotropy, the classical theory	4.3-20
4.3.1 Stress, strain and Voigt's notation	4.3-20
4.3.2 Anisotropic version of the generalized Hooke's law	4.3-23
4.3.2.1 Strain-stress and stress-strain relations, and elasticity matrix.	4.3-23
4.3.2.2 Rotation of the elasticity tensor	4.3-31
4.3.2.3 Hierarchical relation between the elastic symmetry systems	4.3-34
4.3.3 Anisotropic elastodynamics and Kelvin-Christoffel equations.....	4.3-41
4.4 The main symptoms of seismic anisotropy	4.4-47
4.4.1 The directional dependence of the elastic velocities	4.4-47
4.4.2 The shear wave birefringence or shear-wave splitting.....	4.4-48
4.4.3 The ray velocity is not perpendicular to the wavefront.....	4.4-51
4.5 Simplification of the formalism.....	4.5-52
4.5.1 Weak anisotropy approximation and Thomsen type parametrization in TI media	4.5-52
4.5.2 General parametrization for other symmetry types.....	4.5-61
4.6 The main rock models incorporating elastic anisotropy.....	4.6-68
4.6.1 Anisotropy due to mineral and/or structure alignment.....	4.6-68
4.6.1.1 Anisotropy due to mineral alignment or to the presence of shale.....	4.6-68
4.6.1.2 Thinly layered media	4.6-80

PETROACOUSTICS – CHAPTER 4

4.6.2	Anisotropy due to aligned compliant pores (cracks, fractures, grain contacts...)	
	4.6-89	
4.6.2.1	Fractures media with non-welded (linear slip) interfaces.....	4.6-89
4.6.2.2	Aligned ellipsoidal cracks.....	4.6-101
4.6.3	Stress-induced anisotropy and anisotropic nonlinear elasticity	4.6-105
4.7	Anisotropic viscoelasticity	4.7-105
4.8	Seismic anisotropy for earth subsurface exploration and exploitation ... what is it for?	4.8-112
4.8.1	Anisotropy as noise to be eliminated or corrected ... for Seismic processing.	4.8-112
4.8.2	Anisotropy as an information to be used ... for Reservoir characterization.....	4.8-115
4.9	References	1
4.10	Subject index.....	11
4.11	Authors index.....	2

NOMENCLATURE

The notations *div* , **grad** , **curl** and ∇^2 designate the divergence, gradient, curl and Laplacian operators, namely in Cartesian coordinates:

$$\mathit{div} \Psi = \frac{\partial \Psi_x}{\partial x} + \frac{\partial \Psi_y}{\partial y} + \frac{\partial \Psi_z}{\partial z}$$

$$\mathbf{grad} \varphi = \left(\frac{\partial \varphi}{\partial x}, \frac{\partial \varphi}{\partial y}, \frac{\partial \varphi}{\partial z} \right)$$

$$\mathbf{curl} \Psi = \left(\frac{\partial \Psi_z}{\partial y} - \frac{\partial \Psi_y}{\partial z}, \frac{\partial \Psi_x}{\partial z} - \frac{\partial \Psi_z}{\partial x}, \frac{\partial \Psi_y}{\partial x} - \frac{\partial \Psi_x}{\partial y} \right)$$

$$\nabla^2 \varphi = \frac{\partial^2 \varphi}{\partial x^2} + \frac{\partial^2 \varphi}{\partial y^2} + \frac{\partial^2 \varphi}{\partial z^2}$$

The real and imaginary parts of a complex quantity are indicated by:

$$\text{Real part} = ()_R \text{ or } \text{Re}()$$

$$\text{Imaginary part} = ()_I \text{ or } \text{Im}()$$

A dot above a quantity denotes a derivative with respect to time

The brackets $\langle . \rangle$ denotes averaging over the texture distribution and over a Representative Elementary Volume of the rock sample

The norm $\| . \|$ of an arbitrary tensor *A* of rank 4 is the euclidian norm defined by $\|A\|^2 = A_{ijkl} A_{ijkl}$ (with implicit summation on the repeated indices)

Symbols

The nomenclature below does not include the multiple constants used in the text. These are generally represented by the Characters A, B, C... a, b, c...etc.

a	radius of cracks idealized as oblate ellipsoides of revolution
c	half-thickness of cracks idealized as oblate ellipsoides of revolution
C	stiffness tensor
\mathbf{C}	stiffness matrix
\mathbf{C}^*	complex stiffness matrix
\mathbf{C}'	real part of the complex stiffness matrix
\mathbf{C}''	imaginary part of the complex stiffness matrix
\bar{C}	effective stiffness tensor
C_{ijkl}	components of the elastic stiffness tensor C
C_{IJ}	components of the stiffness tensor C in two-index (or Voigt) notation
$C^{(m)}$	stiffness tensor of the intact rock matrix (m)
C_α	short notation for $\cos \alpha$, that is to say the cosine of an angle α
$C^{(background)}$	stiffness tensor of the background medium
\bar{C}_{IJ}	components of the effective stiffness tensor \bar{C} in two-index (or Voigt) notation
$\bar{C}^{(ISO)}$	isotropic effective stiffness tensor
$\bar{C}^{(Voigt)}$	effectitive stiffness tensor of Voigt
E_J	Young's modulus in direction J
I_{ijkl}	components of the identity tensor I of rank 4
\mathbf{K}	wave vector
$\bar{K}^{(ISO)}$	effective bulk modulus of an isotropic medium
$K^{(m)}$	bulk modulus of the intact rock matrix (m)
$M_P^{(c)}$	P-wave modulus of the material contained in the cracks (c)
$M_P^{(m)}$	P-wave modulus of the intact rock matrix (m)
$M_S^{(c)}$	S-wave modulus of the material contained in the cracks (c)
$M_S^{(m)}$	S-wave modulus of the intact rock matrix (m)

PETROACOUSTICS – CHAPTER 4

M_P^{REF}	P-wave reference modulus
M_{qP}	quasi-P wave modulus
M_{qSV}	quasi-SV wave modulus
$M_{P,S1,S2}^*$	complex moduli of P, S1 or S2 wave
n	number of fractures per unit length in the direction normal to the fracture planes
\mathbf{n}	unit vector in the direction of propagation
n_i	components of the unit vector \mathbf{n} in the direction of propagation
N	number of cracks per unit volume
$Q_{P,S1,S2}$	phase quality factor of P, S1 or S2-wave
\mathbf{r}	position vector
$\mathbf{R}_\alpha^{(x')}$	rotation of angle α about an axis x'
$\mathbf{R}_{xyz \rightarrow XYZ}$	rotation bringing the initial frame xyz to the position of the final frame XYZ
$(\mathbf{R}_{xyz \rightarrow XYZ})_{ij}$	$= r_{ij}$ ij components of the rotation matrix corresponding to the rotation $\mathbf{R}_{xyz \rightarrow XYZ}$
S	compliance tensor
\mathbf{S}	compliance matrix
\bar{S}	effective compliance tensor
S_{ijkl}	components of the elastic compliance tensor
S_{IJ}	components of the compliance tensor S in two-index (or Voigt) notation
S_N	individual normal compliance of a single fracture
S_T	individual tangential compliance of a single fracture
S_β	short notation for $\sin \beta$, that is to say the sine of an angle β
$S^{(background)}$	compliance tensor of the background medium
$S^{(frac)}$	additional compliance tensor due to fractures
$S_{ijkl}^{(frac)}$	components of the additional compliance tensor due to fractures
$S_{ijkl}^{(m)}$	components of the compliance tensor of the intact rock matrix (m)
$S_{IJ}^{(frac)}$	components of the additional compliance tensor due to fractures in two-index (or Voigt) notation

PETROACOUSTICS – CHAPTER 4

$\bar{S}^{(\text{Reuss})}$	effectictive compliance tensor of Reuss
$S_{P,S1,S2}^*$	complex phase slowness of P, S1 or S2-wave
t	time
\vec{u}	displacement vector
u_i	components of the displacement vector \vec{u}
\mathbf{U}	particle displacement vector
V_P	P-wave or longitudinal wave velocity in an isotropic medium
$V_P^{(c)}$	P-wave velocity in the material contained in the cracks (c)
V_S	S-wave or shear wave velocity in an isotropic medium
$V_{P,S1,S2}$	phase velocity of P, S1 or S2-wave
$V_S^{(m)}$	S-wave velocity in the intact rock matrix (m)
V_{vertical}^P	P-wave phase velocity in the vertical direction
V_{vertical}^S	shear-wave phase velocity in the vertical direction
$V_{P_0}^{(i)}$	P-wave phase velocity in the vertical direction in the VTI constituent number i of a compound medium
$V_{S_0}^{(i)}$	S-wave phase velocity in the vertical direction in the VTI constituent number i of a compound medium
$V_{P,S1,S2}^*$	complex phase velocity of P, S1 or S2-wave
$W(\xi, \psi, \varphi)$	Orientation Distribution Function (ODF) of the crystallographic texture
W_{lmn}	coefficients of the expansion of the Orientation Distribution Function (ODF) $W(\xi, \psi, \varphi)$ of the crystallographic texture in generalized Legendre functions $Z_{lmn}(\xi)$
x_1, x_2, x_3	components of the position vector \mathbf{r}
Z_N	overall normal compliance of fractures
Z_T	overall tangential compliance of fractures
Z_{ij}	components of the fracture compliance tensor
$Z_{lmn}(\xi)$	generalized Legendre functions
α	crack aspect ratio,
δ	second anisotropy parameter of Thomsen for P-wave in VTI media

$\delta(\lambda)$	function depending on the azimuth λ and generalizing the second anisotropy parameter δ of Thomsen in the case of media of arbitrary anisotropy type
$\bar{\delta}$	effective second anisotropy parameter of Thomsen for P-wave
$\delta^{(i)}$	second anisotropy parameter of Thomsen for P-wave in the VTI constituent number i of a compound medium
δ_{ik}	components of Kroneker identity tensor of rank 2
$\delta_x, \delta_y, \delta_z$	generalization of Thomsen's anisotropy parameter δ in the case of arbitrary anisotropy type
$\Delta C^{(frac)}$	perturbation stiffness tensor induced by fractures
$\Delta C_{IJ}^{(frac)}$	components of the perturbation stiffness tensor induced by fractures in two-index (or Voigt) notation
ε	first anisotropy parameter of Thomsen for P-wave in VTI media
$\varepsilon(\lambda)$	function depending on the azimuth λ and generalizing the first anisotropy parameter ε of Thomsen in the case of media of arbitrary anisotropy type
$\bar{\varepsilon}$	effective first anisotropy parameter of Thomsen for P-wave
$\boldsymbol{\varepsilon}$	strain tensor
$\varepsilon^{(i)}$	first anisotropy parameter of Thomsen for P-wave in the VTI constituent number i of a compound medium
ε_{ij}	two-index components of the strain tensor $\boldsymbol{\varepsilon}$
ε_J	components of the strain tensor $\boldsymbol{\varepsilon}$ in one-index (or Voigt) contracted notation
ε_N	dimensionless overall normal compliance of fractures
ε_T	dimensionless overall tangential compliance of fractures
$\varepsilon_x, \varepsilon_y, \varepsilon_z$	generalization of Thomsen's anisotropy parameter ε in the case of arbitrary anisotropy type
$\varepsilon_{ij}^{(m)}$	components of macroscopic strain associated with the intact rock matrix (m)
$\varepsilon_{ij}^{(frac)}$	components of additional macroscopic strain due to the presence of fractures
φ	third rotation angle, or intrinsic rotation angle, of Euler
$\eta^{(i)}$	volumetric proportion of constituent number i of a compound medium
γ	shear-wave anisotropy parameter of Thomsen, or SH-wave moveout parameter in VTI media
$\bar{\gamma}$	effective shear-wave anisotropy parameter of Thomsen
$\gamma^{(i)}$	shear-wave anisotropy parameter of Thomsen in the VTI constituent number i of a compound medium

$\gamma_{IJ}^{(CD)}$	compression/distorsion (CD) coupling coefficient corresponding to a distorsion in the plane normal to the direction J when unit uniaxial stress is applied in the direction I
$\gamma_{IJ}^{(SD)}$	shear/dilatation (SD) coupling coefficient corresponding to uniaxial strain in direction J when unit shear stress is applied in plane normal to the direction I
Γ	Kelvin-Christoffel tensor
Γ_{ij}	components of Kelvin-Christoffel tensor Γ
χ_x, χ_y, χ_z	additional anisotropy parameters in the case of arbitrary anisotropy type
$\bar{\mu}^{(ISO)}$	effective shear modulus of an isotropic medium
$\mu^{(m)}$	shear modulus of the intact rock matrix (m)
μ_J	shear modulus in the plane normal to direction J
ν_{ij}	Poisson's ratio corresponding to an elongation in direction j when uniaxial stress is applied in direction i
$\nu_{ij}^{(S)}$	Poisson shear (S) ratio corresponding to distorsion in the plane normal to direction j when shear stress is applied in the plane normal to direction i
ω	angular frequency
ρ	density
σ	SV-wave moveout parameter in VTI media
$\boldsymbol{\sigma}$	stress tensor
σ_{ij}	two-index components of the stress tensor $\boldsymbol{\sigma}$
σ_J	components of the stress tensor $\boldsymbol{\sigma}$ in one-index (or Voigt) contracted notation
$\sigma_I, \sigma_{II}, \sigma_{III}$	principal stresses
$\zeta = \frac{M_S^{(m)}}{M_P^{(m)}}$	ratio of S-wave and P-wave moduli of the intact rock matrix (m)
θ	second rotation angle, or nutation angle, of Euler
ψ	first rotation angle, or precession angle, of Euler
ζ	dimensionless crack density parameter

Acronyms

HTI	transverse isotropy or transversely isotropic with a horizontal symmetry axis
ISO	isotropic
MON	monoclinic
NMO	normal move-out
ODF	Orientation Distribution Function
ORT	orthotropic or orthorhombic
SH	shear wave polarized in horizontal direction
SV	shear wave polarized in a vertical plane
TI	transverse isotropy or transversely isotropic
TRI	triclinic
VTI	transverse isotropy or transversely isotropic with a vertical symmetry axis

4 - ELASTIC ANISOTROPY

*" Ut tensio sic vis
tamen dissimiliter prout dissimilis iter" §*

Robertus J. Arts

The genesis (sedimentation, tectonics, etc...) of geological media (Paterson and Weiss [1961]; Allen [1984]) often favours directions of the space (gravity, stress or flow directions for instance), which often renders such media anisotropic with respect to various physical properties [Anderson, 1989]. In other words, the physical properties of these media depend on the direction of investigation. Such directional dependence is called anisotropy with respect to the considered physical property, as introduced in Chapter 1. This is particularly true for elastic properties (e.g., Babuska and Cara [1991]; Helbig [1994]).

This chapter deals with elastic anisotropy from different points of view but, as in the other chapters, always more or less in relation with experimental aspects. First, we summarize the history of seismic anisotropy. Then we introduce the symmetry principles in physical phenomena, due to the great scientist Pierre Curie, and the way they can simplify the description of elastic anisotropy. In the next section we introduce the classical theory of static and dynamic elasticity in anisotropic media, describe and illustrate the main manifestations of elastic anisotropy in rock (i.e. directional dependence of the elastic wave velocities, shear-wave splitting of shear-wave birefringence, and the fact that the seismic rays are generally not normal to the wavefronts). Because rocks generally exhibit moderate to weak anisotropy strength it is possible to use perturbation theories to simplify the exact theoretical derivation as will be described in the next part. This will be followed by a description of the main causes of elastic anisotropy and the corresponding rock physics models. In addition to elastic anisotropy, experimental studies give unambiguously other robust results, namely porous nature (poroelasticity), frequency dependence (viscoelasticity), or the dependence on stress-strain level (nonlinearity) which lead to use more sophisticated models as pointed out in the next part. The last part explains how elastic anisotropy alter the seismic response and

§ Anisotropic Hooke's law, a rough translation would give *"As the Tension ("Extension" or more generally "Strain"), so the Force (or more generally "Stress"), however in a different way according to the direction"*. Quoted by Mensch and Rasolofosaon [1997] and published in the epigraph of Arts [1993] in the form of the two anagrams

*"ceiinossttuv,
addeeiioiiiiillmmnopr rrrrrsssstttu"*

freely modified from Robert Hooke's "De potentia restitutiva"[1678], quoted by A.E.H. Love [1944].

necessitates the adaptation of existing seismic processing tools to take into account the anisotropic case. Conversely it also explains how seismic response can be analyzed in order to characterize the studied rocks.

4.1 A brief history of seismic anisotropy

The development of a theoretical understanding of anisotropic elasticity and all the related implications, especially in wave propagation has its origins in the first decades of the 19th century. Important figures in the history of Physics and Mathematics, such as G.R. Hamilton, G. Green, and W. Thomson (Lord Kelvin) to name a few, realized that in principle the velocity of propagation of elastic wave could depend on the direction of propagation. In his history of the first 100 years of elastic anisotropy Helbig [2003] distinguished four periods., as illustrated by Figure 4.1.1-1 containing milestone references, and the corresponding authors and date of publication .

The first period, is called the “prehistoric” period in the last reference and mainly distinguished by the pioneering works of Hamilton [1837] and McCullagh [1837] on ray theory. According to Helbig [1994] both of these authors were the first to introduce the usefull concept of slowness surface that is so conveniently linked with various wave characteristics, such as the direction of wave normal and ray, and the trace slowness along an interface, itself closely linked with the reflection law and the Ibn Sahl–Harriot-Snell–Descartes (IHSD) refraction law (see Box 1.2.2-3 in Chapter 1). More generally, William R. Hamilton (1805-1865) is well-known for his remarkable contributions in classical mechanics, in optics and in algebra. For instance, during his first years he created and developed the theory of geometrical optics, based on the use of a characteristic function, bearing his name and completely developed in his *Third Supplement to an Essay on the Theory of Systems of Rays* [Hamilton, 1837].

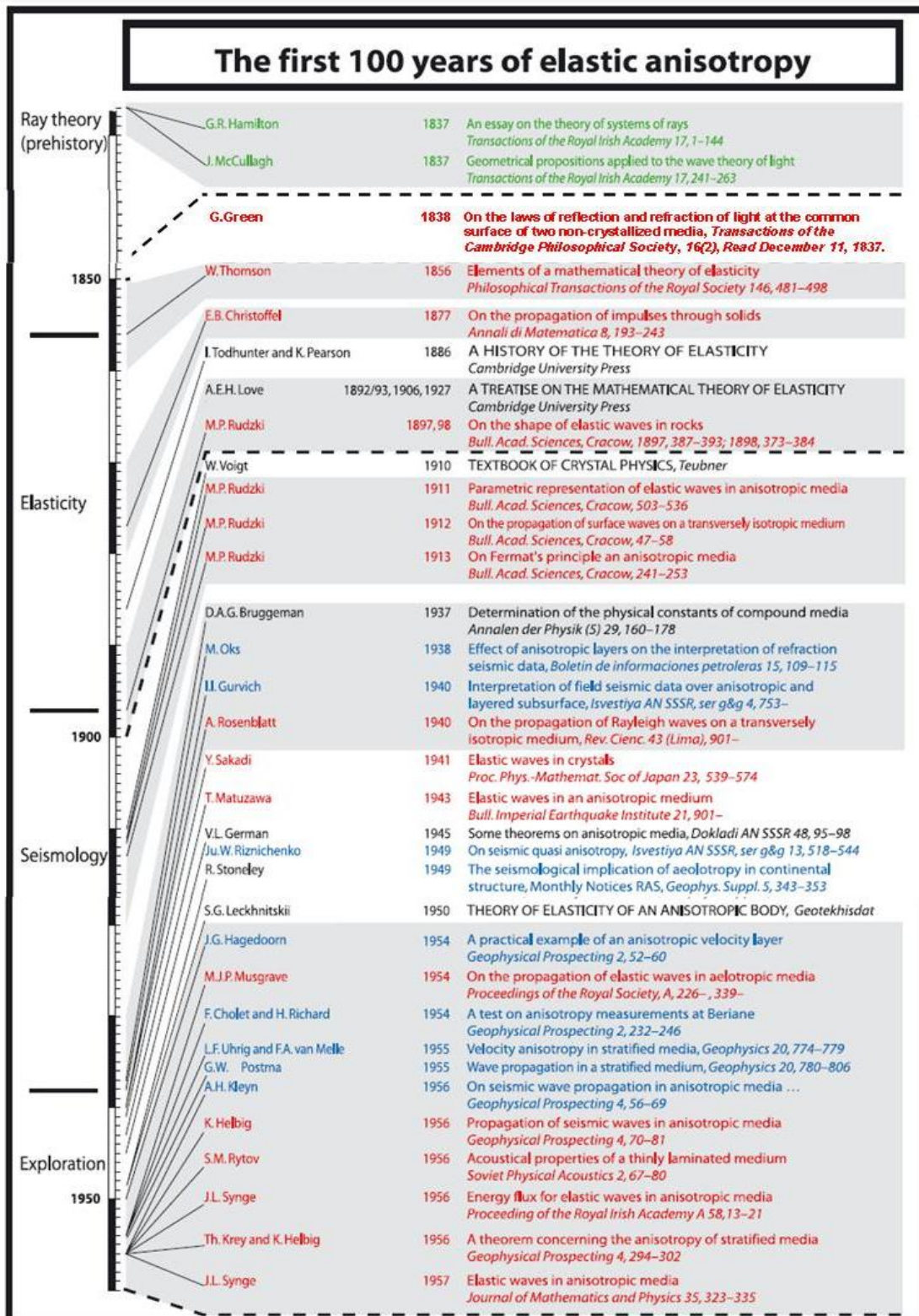


Figure 4.1.1-1: The first 100 years of elastic anisotropy after Helbig [2003], slightly modified by Helbig and Rasolofosaon [2004].

The second period is the “elasticity” period with the remarkable contributions of Green [1838], Thomson [1856] and Christoffel [1877], among others, on the theory of anisotropic elasticity. George Green (1793-1841), initially a humble miller of Nottingham UK, is a famous British mathematical physicist. He is the Green of Green's functions and Green's theorem and many more. He is often considered as the founder of "Cambridge School" of natural philosophers, of which Kelvin (to whom we owe the rediscovery of much of Green's work), Rayleigh, Maxwell, Lamb are some of the best known - but by no means the only - examples. Green [1838] also happens to be the first who gave the analytical expression of the elastic strain energy characterized by 21 elastic constants in arbitrarily anisotropic media... enunciating in passing for the first time the principle of conservation of work (e.g., Helbig and Rasolofosaon [2004]). William Thomson (knighted as Lord Kelvin) (1824-1907) was a famous British mathematical physicist and engineer, mostly known for his work on thermodynamics, electricity and magnetism. His theoretical paper of 1856 on the *mathematical theory of elasticity*, was much ahead of his time and was unfortunately not understood by his contemporaries. It was unearthed and reviewed over hundred years later (e.g., Mehrabadi and Cowin [1990]; Helbig [1994] and Helbig [1996]). Kelvin introduced representations of the stress the strain and the elastic tensor in a coordinate-free form. As pointed out by some authors (e.g., Helbig [1996]; Helbig and Rasolofosaon [2000]), Kelvin's ideas allows to efficiently handle many problems of the theory of elasticity and far beyond, as illustrated by recent contributions. For instance Carcione [2007] uses Kelvin's representation to describe the behaviour of media exhibiting attenuation/dispersion and anisotropy. There even seems to be no limit in the sophistication of the models using Kelvin's representation in porous elastic media [Helbig and Rasolofosaon, 2009] or in media exhibiting simultaneously dispersion/attenuation, anisotropy, and nonlinearity possibly with the presence of hysteresis (e.g., either in non-porous media: Rasolofosaon [2009]; or in porous media: Rasolofosaon [2011]). Christoffel [1877] and Kelvin [1878] independently derived the elastic-wave equation for anisotropic media, known as the Kelvin-Christoffel equation, from which the directional dependence of the velocities are obtained (see section 4.3.3). In fact, as pointed out by Helbig and Thomsen [2005], Kelvin was the first to formulate these equations, unfortunately in his overlooked paper of 1856. Thus the solution of the anisotropic wave equation is often attributed to Christoffel [1877].

The third period is marked by the application of anisotropy to “seismology”. After Helbig and Szaraniek [2000] the beginning of research on the application of elastic anisotropy to seismology, commonly called seismic anisotropy, can be precisely fixed in early 1896 with the first official appointment of a professor of geophysics, namely Maurice Rudzki. Maurycy Pius Rudzki (1862-1916) assumed this professor position in 1895 at the Jagiellonian University of Cracow. Early he stated that his research would be directed at seismology, and primarily at the propagation of seismic waves in anisotropic media, on which topic he published regularly during the next 20 years until his untimely passing in 1916. After a bit more than half a century later the study of seismic anisotropy has brought important contribution to global seismology (e.g., Anderson [1989]). The presence of anisotropy in nearly all the main “radial layers” composing the Earth from the upper crust to the inner core, except the lower mantle and the outer core, is now clearly established (e.g., Savage [2006]) and led for instance to the first isotropic and anisotropic global earth model, called the Preliminary Reference Earth Model (PREM) [Dziewonski and Anderson, 1981] (see Box 1.3.3-1 in Chapter 1).

Seismic anisotropy in global seismology is still a key issue, but since the 1950s, and more markedly after the 1970s, an overwhelming number of contributions in the field of hydrocarbon exploration, open the last and still on-going “exploration” period. As pointed out by Helbig and Thomsen [2005], since that time there is hardly an issue of a geophysical journal without at least one article on anisotropy, and exploration meetings often have several sessions on seismic anisotropy. Clearly seismic anisotropy has evolved from a sophisticated curiosity for specialists to a mainstream research topic leading to practical tools now routinely used in oil exploration and exploitation (e.g., Thomsen [2002]; Grechka [2009]). Since 1982, on the leading edge of this wave, volunteering groups of specialists of seismic anisotropy constituting a global community meet during the International Workshop on Seismic Anisotropy (IWSA). According to Crampin and Gao [2009], the idea was initiated by Evgeny Chesnokov and Stuart Crampin who organized, with the authoritative help of the Russian academician Magnitsky, the two first workshops in Russia (i.e., 1WSA held in 1982 in Suzdal, and 2IWSA in 1986 in Moscow). The IWSA involves both industry and academia, and is not associated with any formal organisation or institution. Since the 3IWSA in 1988 it is organized every two years alternatively in Europe [i.e., 4IWSA in Edinburgh (UK), 6IWSA in Trondheim (Norway), 8IWSA in Bousens (France), 10IWSA in Tützing (Germany)] and in North America [i.e., 3IWSA held in Berkeley (US), 5IWSA in Banff (Canada), 7IWSA in Miami (US), 9IWSA in Camp Allen (US), 11IWSA in Saint John’s (Canada), 13IWSA in Winter Park (US)] with some notable exceptions [i.e., 12IWSA held in Beijing (China), 14IWSA in Perth (Australia), 15IWSA in Bahrain in the Persian-Arabian Gulf, and 16IWSA in Natal (Brazil)]. These workshops usually cover all aspects of seismic anisotropy in a broad sense and its implication and applications from global seismology to seismics oriented toward earth exploration and exploitation.

4.2 Anisotropy and Curie's symmetry principle

In the first lines of his famous paper of 1894 on the symmetry principle in physics, written in french [P. Curie, 1894], Pierre Curie (see Box 4.2.1-1) writes “I believe that it would be of interest to study physical phenomena with allowance for symmetry consideration so common for crystallographers” and further adds “Physicists often use conditions following from symmetry but, as a rule, neglect the rigorous definition of the symmetry of the phenomenon under consideration since such conditions are often simple and a priori almost obvious”.

As pointed out by Shubnikov [1956], these remarks have not lost their validity more than a century later. For instance when geophysicists talk about “axial symmetry”, they usually refer, without being aware of it, to only one of the five types of symmetry groups preserving rotational invariance, as will be detailed in sub-section 4.2.2-1 and illustrated by Figure 4.2.2-1.

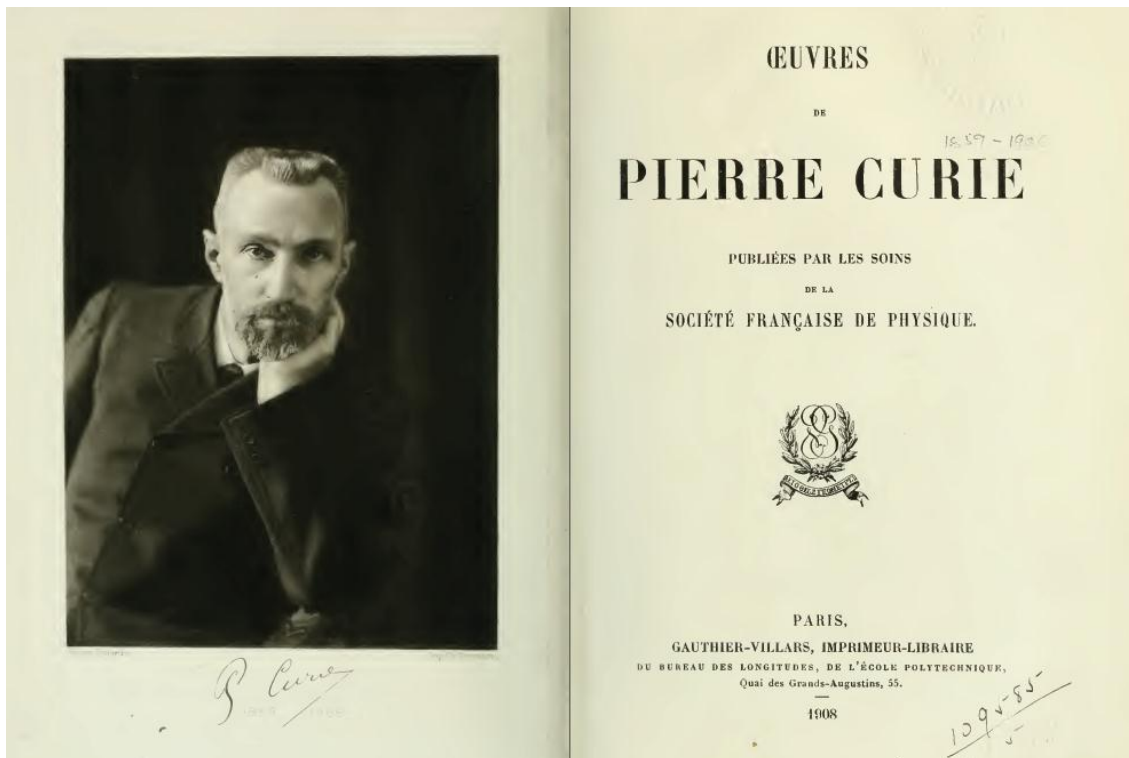
In this section we focus on two central - but by no means only – results of this paper, namely Curie's symmetry principle and Curie's limit groups of symmetry and their practical implications in the study of elastic anisotropy.

BOX 4.2.1-1-1

Pierre Curie (1859-1906) and his work outside the field of radioactivity

The name of the French physicist Pierre Curie (1859-1906) is often systematically associated with the name of his wife the Polish physicist and chemist Marie Skłodowska-Curie (1867-1934), and joined together in a common glory for their work on radioactivity (e.g., see Website of the Institut Curie on Pierre and Marie Curie: http://www.curie.fr/fondation/musee/marie-pierre-curie.cfm/lang_gb.htm).

In contrast much less is known about the remarkable pioneering-work of Pierre Curie before this period (e.g., Hurwic 1995), including the discovery of piezoelectricity with his brother Jacques, the demonstration of the change of magnetic properties with temperature (in particular, the temperature above which a material ceases to be ferromagnetic is now known as Curie point), the construction of delicate, and now commonly used instruments, to assist his experiments (balances, electrometers, piezoelectric crystals ...), and an advanced theory on symmetry. In the whole work of Pierre Curie the brevity of the descriptions strongly contrasts with the depth of the reflections. As pointed out by Shubnikov (1956) the complete collection of his papers (P. Curie, 1908) is contained in 610 pages including 61 articles, which represents an average of only 10 pages per article, each article containing major contributions as will be illustrated with Curie's paper of 1894 written in french (P. Curie, 1894).



Facsimile of the two first pages of the book on the complete collection of Pierre Curie' papers (P. Curie, 1908)

4.2.1 Curie's symmetry principle and some consequences for elastic anisotropy

Ahead of his contemporaries, Curie was the first to realize the difference between the symmetry of a medium and the symmetry of its physical properties. The present section is focused on the work of Pierre Curie on the symmetry of physical phenomena. Curie's symmetry principle, illustrated by the Fig.4.2.1-1, generalizes to any physical phenomena Neumann's principle initially restricted to crystal physics [Voigt, 1910].

CURIE'S SYMMETRY PRINCIPLE

Concise formulation:

The effects are more symmetric than the causes

DIRECT FORMULATION

Original formulation:

Lorsque certaines causes produisent certains effets, les éléments de symétrie des causes doivent se retrouver dans les effets produits.

Translation:

If certain causes yield known effects, the symmetry elements of the causes must be contained in the generated effects.

COROLLARY

Original formulation:

Lorsque certains effets révèlent une certaine dissymétrie, cette dissymétrie doit se retrouver dans les causes qui lui ont donné

Translation:

If the known effects manifest certain dissymmetry (lack of symmetry elements), this latter must be contained in the causes which generated these effects

MODERN FORMULATION

The symmetry group of the causes of any physical phenomenon is a sub-group of the symmetry group of the observed effects relative to this phenomenon.

(after Curie 1894, Sirotine and Chaskolskaya 1979)

Figure 4.2.1-1: Original and modern formulations of Curie's principle of symmetry on physical phenomena.

The original direct formulation of the principle can be translated in english in the following way: "...if certain causes yield known effects, the symmetry causes must be contained in the generated effects...". In modern language this means that, if we designate by $G_{\text{cause}\#i}$ the symmetry group of the cause number i ($i=1$ to n), the intersection of the n symmetry groups of all the causes is a sub-group of the symmetry group G_{effect} of the observed effects, or mathematically:

$$(4.2.1-1) \quad G_{\text{cause}\#1} \cap G_{\text{cause}\#2} \cap G_{\text{cause}\#3} \cap \dots \cap G_{\text{cause}\#n} \subset G_{\text{effect}}$$

In other words, and more concisely, the effects are more symmetric than the causes, which leads to a minimalistic direct formulation fixing a lower bound for the effects.

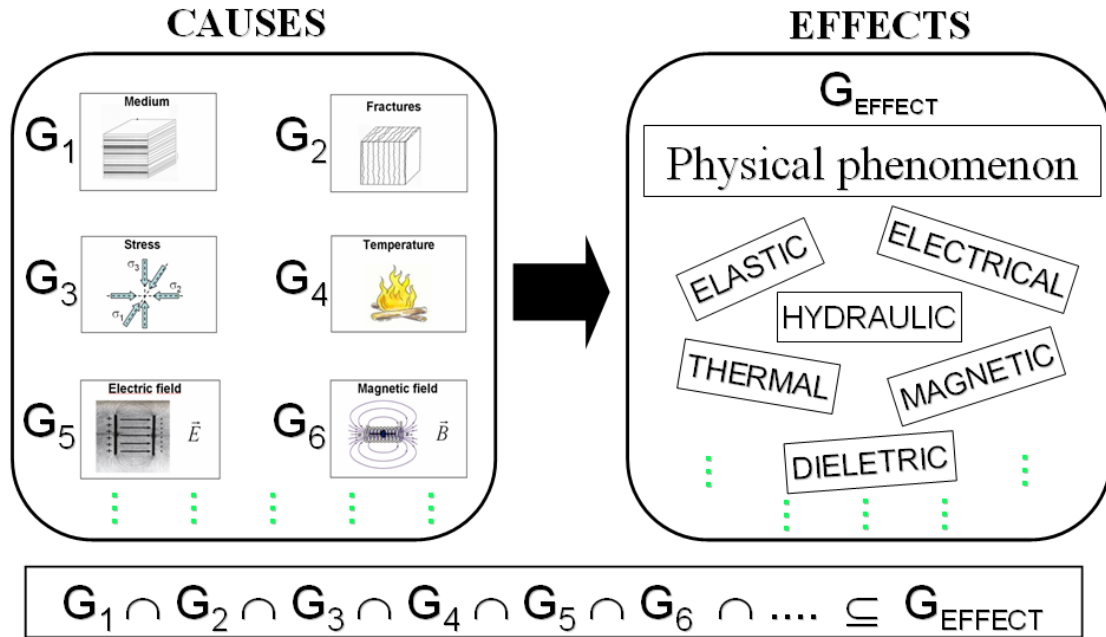


Figure 4.2.1-2: Curie's principle of symmetry on physical phenomena.

Fig. 4.2.1-2 illustrates more explicitly Curie's symmetry principle with all the causes on the left part of the figure and various physical phenomena on the right part of the figure. The first cause is obviously the considered medium itself. The other causes can be as various as the presence of additional fracture systems, applied fields (stress, electric or magnetic fields), or temperature variations. All the causes must be identified in order for the principle to be applicable. The observed effects can be any physical phenomenon (elastic, electrical, hydraulic, thermal etc...) which illustrate the generality of the principle.

The corollary of the principle is formulated in the following way: "...if the known effects manifest certain dissymmetry (lack of symmetry elements), this latter must be contained in the causes which generated these effects ...". In modern language this means that if one of the observed effects lack a symmetry element (e.g, a symmetry axis or a plane), necessarily one of the causes lack this symmetry element. In other words, and more concisely, the causes cannot be more symmetric than the effects, which leads to a maximalistic formulation fixing an upper bound for the symmetry of the causes.

In order to figure out more clearly Curie's principle in action we shall give one practical example of its direct principle and one of its corollary.

Figure 4.2.1-3 considers an isotropic medium of symmetry G_1 corresponding to Curie's limit group $\infty\infty m$, for which any plane is a symmetry plane and any axis is a symmetry axis (see next sub-section). This was the first cause. The second cause is the applied stress field which is assumed triaxial. Such a stress field can be put in a one-to-one correspondence with an ellipsoid, namely Lamé's stress ellipsoid (e.g., Fung [1994]), characterized by three symmetry planes orthogonal to each other and leading to an orthorhombic symmetry group G_2 designated by mmm in the international notation (e.g., Hahn [1983]). Obviously both G_1 and G_2 share the three symmetry planes orthogonal to each other. In other words the

symmetry groups $G_1 \cap G_2$ of all the causes is also orthorhombic. As a consequence an initially isotropic medium, when tri-axially stressed, cannot be less symmetric than orthorhombic. This result was derived by Nur [1971] in less direct alternative way and was re-established by Johnson and Rasolofosaon [1996] using Curie's principle.

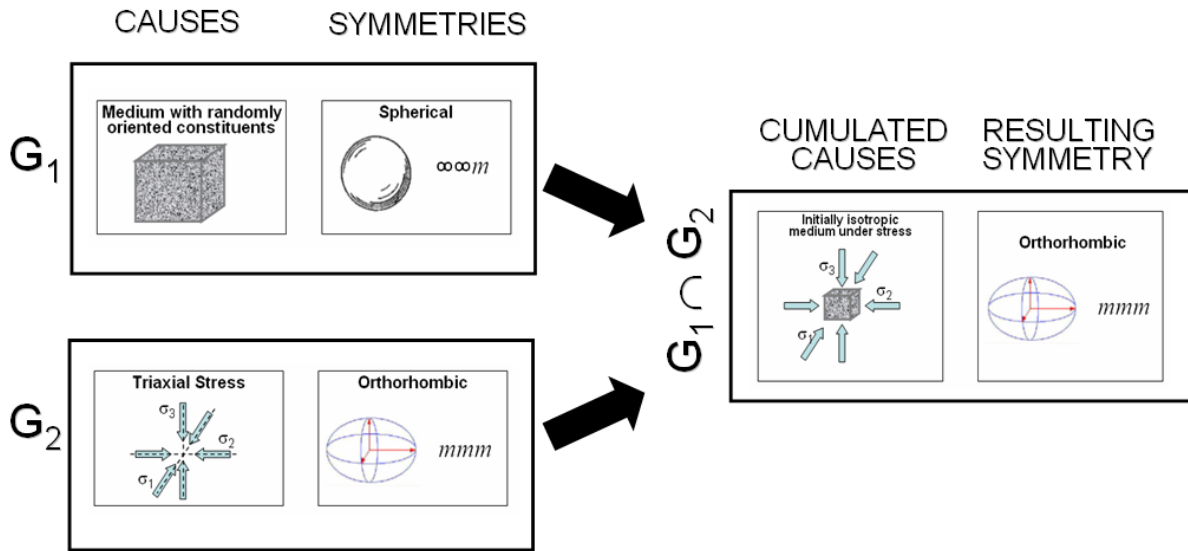


Figure 4.2.1-3: Curie's symmetry principle in action. A initially isotropic medium when tri-axially stressed cannot be less symmetric than orthorhombic.

Here, once again we emphasize the generality of Curie's principle. The results hold for any physical property and are completely independent of the rock model and of the strength of the stress field, as pointed out in the last reference.

Figure 4.2.1-4 gives an example the corollary of Curie's principle. The considered example concerns the piezoelectric effect, experimentally demonstrated by Pierre Curie and his brother Jacques [P. Curie and J. Curie, 1880]. Piezoelectricity is the property of a material to become electrically polarized when mechanically stressed (e.g., Cady [1946]; Dieulesaint and Royer [1974]; Nye [1985]; Ikeda [1996]). Examples of natural piezoelectric materials are quartz, tourmaline, topaz, or Rochelle salt (sodium potassium tartrate tetrahydrate). Under stress, the observed effect is an electric polarization, represented by a polar vector. A polar vector has the symmetry of a right circular cone at rest (see detail in the next section 4.2.2), characterized by an axis of rotational invariance (i.e. the axis of the cone) and an infinite number of symmetry planes (i.e. any plane containing the cone axis), but no center of symmetry. As illustrated by Figure 4.1.1-1 and the corresponding comments, the corollary of Curie's symmetry principle is that if one of observed effects lack a symmetry element (here a center of symmetry), necessarily one of the causes lack this symmetry element. The two causes of the observed phenomenon are the applied stress and the considered medium itself. Because the stress, as any symmetric tensor of rank 2, can be put in a one-to-one correspondence with an ellipsoid, namely Lamé's stress ellipsoid (e.g., Fung [1994]), as a consequence the stress

exhibits a center of symmetry. As a consequence the remaining cause, namely the medium, must lack a center of symmetry. The result that piezoelectric media must lack a center of symmetry is well-known in crystal physics (e.g., Dieulesaint and Royer [1974]; Sirotine and Chaskolskaya [1975]; Nye [1985]).

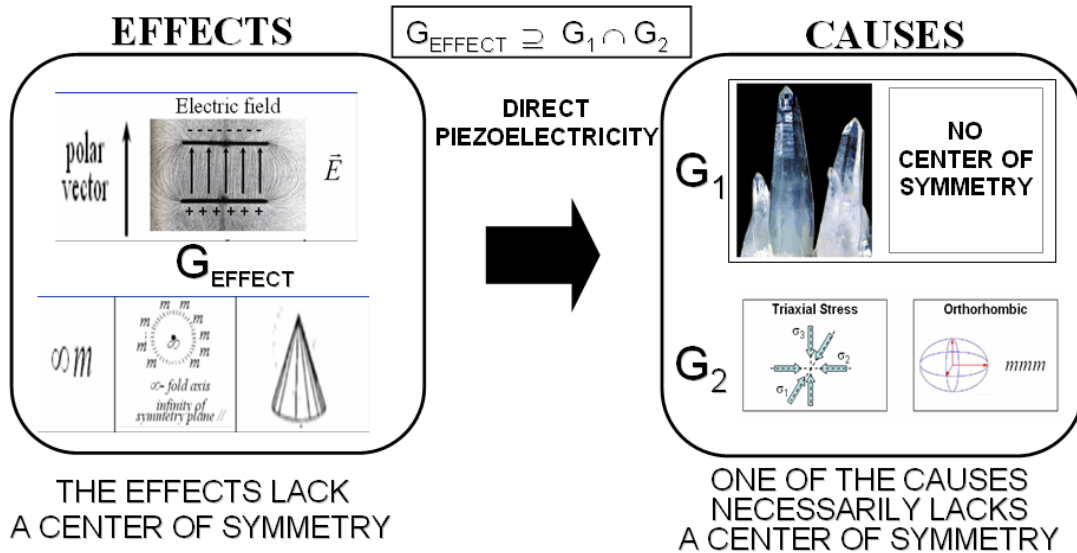


Figure 4.2.1-4: The corollary of Curie's symmetry principle in action. A piezoelectric medium necessarily lacks a center of symmetry.

In practice, given the symmetry of the causes, Curie's principle allows to qualitatively predict the minimum symmetry of the effects and to simplify the formulation of the problem for further quantitative analyses. For instance, in seismic anisotropy the most complex symmetry exhibited by an arbitrarily but uniformly stressed medium (initially isotropic) is orthorhombic. And an unstressed Vertical TI medium cannot be more complex than orthorhombic when triaxially stressed if one of the eigenstress directions is vertical, and then monoclinic when uniaxially stressed. All these results are completely independent of the stress level and of the rock model.

Lastly, a fertile concept initiated by Curie is that of symmetry breaking (modern terminology not used by him). In one of his last paragraphs Curie explains that the dissymmetry, or more clearly the lowering of the symmetry group (symmetry breaking in modern language) of the medium is what "creates the phenomenon". Symmetry breaking now plays a central role in many branches of modern physics (e.g., see Website of Stanford Encyclopedia of Philosophy: <http://plato.stanford.edu/>).

4.2.2 Curie's limit group and symmetry of geological media

4.2.2.1 Curie's symmetry group or limit group of symmetry

Another major result of Curie's paper of 1894 is the introduction of non-crystallographic limit groups of symmetry, now called Curie's groups of symmetry and including infinite-fold axes of symmetry [Curie, 1894]. The seven Curie's symmetry group are illustrated by Fig. 4.2.2-1 in the form of a table. The designations of each symmetry class are listed in the two first columns, with the international notation of Hermann-Mauguin in the first column and Schoenflies notation in the second column (e.g., Sirovine and Chaskolskaya [1975]; Nowick [1995]). In order to facilitate the identification of each class some simple examples of each class are given in the two next columns, with classical geometrical illustrations (i.e., cones, cylinders and spheres) in the third column and laymen examples in the fourth column. The different symmetry elements are detailed in the fifth column, and the last column gives some geophysical examples illustrating each class.

The seven classes are grouped into two systems. The “cylindrical” system gathers the five classes exhibiting a single axis of rotational invariance and the “spherical” system the two classes characterized by an infinite number of axes of rotational invariance.

Regarding the “cylindrical” system, Curie realized, ahead of his contemporaries, the essential difference between the electric field symmetry ∞m (of a cone at rest) and the magnetic field symmetry ∞ / m (of a rotating cylinder). The electric field vector is a polar vector which exhibits an axis of rotational invariance, parallel to the electric field vector, and an infinite number of symmetry plane (i.e. any plane containing the infinite-fold axis). For instance the force vector and the velocity vector share the same symmetry as the electric field vector. The magnetic field is an axial vector or a pseudo-vector, and also exhibits an axis of rotational invariance parallel to the magnetic field vector. However it exhibits a single symmetry plane perpendicular to the symmetry axis. For instance the moment vector of a force, or the torque vector, and the rotation vector share the same symmetry as the magnetic field vector.

Systems	Classes		Classical illustration	Laymen example	Symmetry elements (out-of-plane ∞ -fold axis)	Geophysical examples	
	Intl notation	Schoenflies notation					
Cylindrical	∞	C_{∞}		rotating cone		 Structure of the vicinity of an hurricane eye	
	∞m	$C_{\infty v}$		cone at rest		Force vector \vec{F} Electric field vector \vec{E} Velocity vector \vec{V}	
	∞/m	$C_{\infty h}$		rotating cylinder		Rotation vector $\vec{\omega}$ Magnetic field vector \vec{B} Torque vector $\vec{\Gamma}$	
	$\infty 2$	D_{∞}		twisted cylinder		Toroidal or twisting mode T_0 of free oscillations of a radially stratified earth	
	∞ / mm	$D_{\infty h}$		cylinder at rest		Thinly layered Elastic Medium with randomly distributed constituents	
	$\infty \infty$	R		sphere with all radii rotating	infinity of ∞ -fold axes no symmetry plane	Isotropic Gyrotropic Medium (elastic and optic)	
	$\infty \infty m$	R_i		sphere at rest	infinity of ∞ -fold axes infinity of symmetry planes	Elastic Medium with randomly oriented and distributed constituents	

Figure 4.2.2-1: The seven non-crystallographic limit group of symmetry or Curie's symmetry groups characterized by at least an infinite-fold symmetry axis, including five classes in the cylindrical system and two classes in the spherical system. Each class is referenced by its international notation (2nd column) and Schoenflies notation (3rd column), sketched in the 4th column, and illustrated by a simple example in the 5th column and by geophysical examples in the last column (modified after Hahn [1983]).

The lowest symmetry class of the “cylindrical” system, is noted ∞ and is characterized by just an axis of rotational invariance. It is the symmetry of a rotating cone and a simple geophysical example is the flow velocity field in the vicinity of a hurricane eye. The fourth symmetry class is noted $\infty 2$, corresponding to the symmetry of a twisted cylinder, exhibits an axis of rotational invariance (i.e. the axis of the cylinder) and an infinite number of symmetry axes of order 2 perpendicular to the infinite-fold axis.

The chosen geophysical example is particle displacement field corresponding to the lowest toroidal or twisting mode ${}_0T_2$ of free oscillation of the earth, which are mainly excited by large earthquakes (e.g., Lay and Wallace [1995]; Shearer [1999]). The last symmetry class, noted ∞/mm , corresponding to the highest symmetry, is the symmetry of a cylinder at rest. It is characterized by an axis of rotational invariance, parallel to the axis of the cylinder, an infinite number of symmetry planes (i.e. any plane containing the infinite-fold axis), and a symmetry plane normal to the cylinder axis. Let us note in passing that there are five classes of symmetry exhibiting an axis of rotational invariance, and not a single one. The Transverse Isotropy (TI) symmetry commonly considered in the geophysical literature (e.g., Thomsen [1986]; Tsvankin [1996]), illustrated by thinly layered media with randomly distributed constituents, belongs to the class ∞/mm . Note that the term “transversely isotropic” was first coined by Love [1892], according to Helbig and Thomsen [2005].

The “spherical” system is composed of two symmetry classes. The lowest symmetry class is noted $\infty\infty$, and is characterized by a double infinity of axes of rotational invariance but no symmetry plane. In other words, any axis is an infinite-fold symmetry axis. This is the symmetry exhibited by an isotropic gyrotropic or active material (elastic or optical). The polarization of an elastic or optical wave propagating in a gyrotropic material rotates during the propagation (e.g., Sirovina and Chaskolskaya [1975]; Haussühl [1983]). Optical gyrotropy was discovered in quartz by the French mathematician, physicist, astronomer and politician François Arago (1786-1853) in 1811 (e.g., Arago [1811]; Rossmorduc [1988]).

Acoustical gyrotropy, the analog of optical gyrotropy, has been investigated later, since the 1960s (e.g., Andronov [1960]; Portigal D.L. and Burstein E. [1968]), and much later in the seismic frequency band by Obolentseva [1992] (more details on seismic gyrotropy can be found in Chichinina [1998]).

For the highest symmetry class, noted $\infty\infty m$, any axis is an axis of rotational invariance and any plane is a symmetry plane. Here again let us note that there are two isotropic symmetry classes, and not a single one. The Isotropic (ISO) symmetry commonly considered in the geophysical literature, illustrated by an elastic medium with randomly oriented and distributed constituents, belongs to the class $\infty\infty m$.

4.2.2.2 Hierarchical link between Curie's symmetry groups and the crystallographic groups. Symmetry groups in Geological media

4.2.2.2.1 Hierarchical link between Curie's symmetry groups and the crystallographic groups.

Figure 4.2.2-2 illustrates the hierarchical link between the seven Curie's symmetry groups, described in the previous sub-section, and the 32 crystallographic groups (e.g., Haussühl [1983]; Tilley [2006]), with the least symmetric triclinic group 1 (lacking any symmetry element) in the bottom of the figure to the most symmetric isotropic $\infty\infty m$ (exhibiting any symmetry element: any axis is an axis of rotational invariance, and any plane is a symmetry plane) in the top of the figure. The name of each symmetry group is written inside a disk. The multiplicity of each sub-group, as defined in group theory (e.g., Wooster [1973]; Joshi [1982]; Hamermesh [1989]), is indicated on the left part and on the right part of the figure.

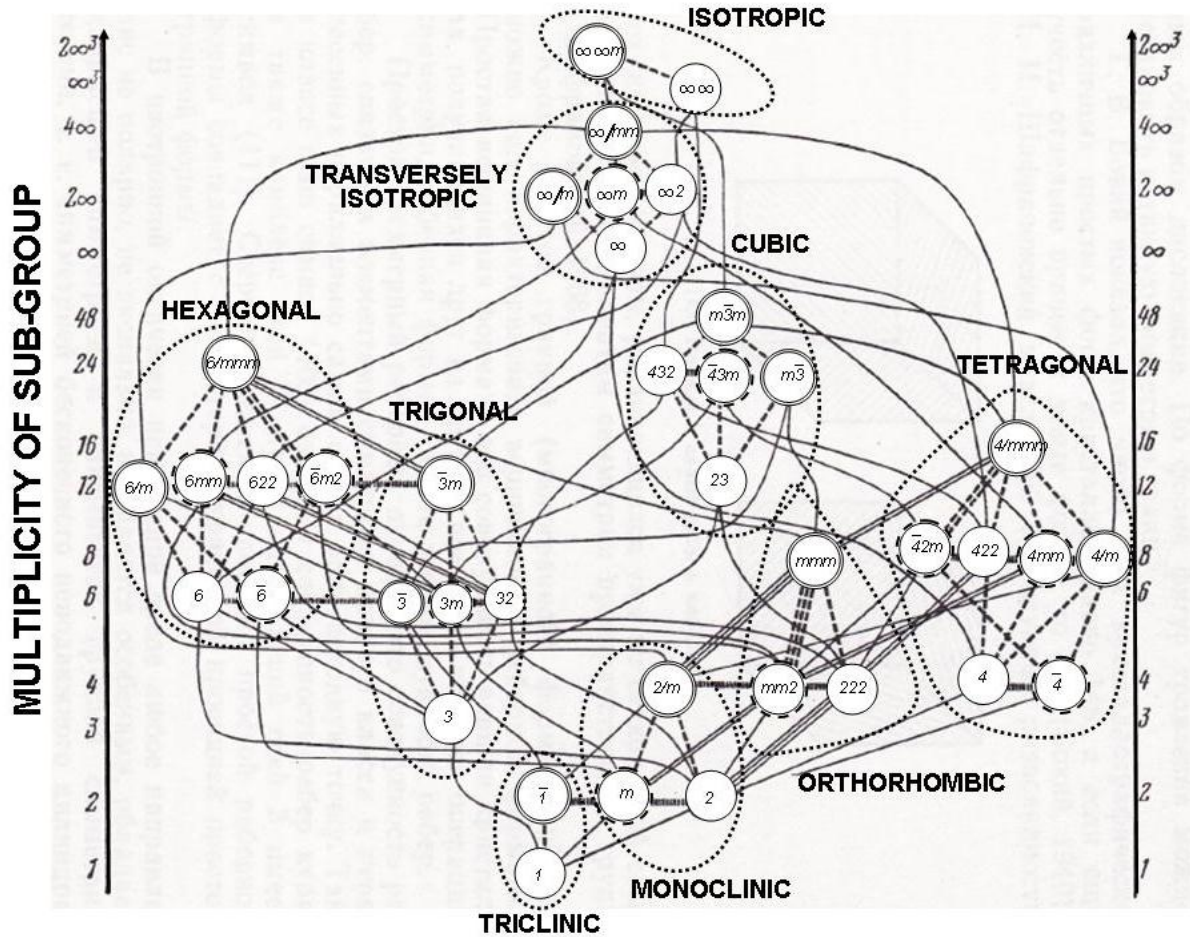


Figure 4.2.2-2: Hierarchical link between the seven non-crystallographic limit group of symmetry or Curie's symmetry groups and the crystallographic groups, from the least symmetric triclinic group 1 in the bottom of the figure to the most symmetric isotropic $\infty\infty m$ in the top of the figure (modified after Sirotnine and Chaskolskaya [1979]).

As for Curie's limit groups in the previous sub-section, all these symmetry groups can be gathered in nine systems, each system being bounded by a closed curve dashed line on the figure. The two systems gathering Curie's symmetry groups, namely the "cylindrical" or "transversely isotropic" system and the "spherical" or "isotropic" system have been studied in the previous sub-section, and are more symmetric than any of the seven remaining systems gathering the crystallographic groups. The seven crystallographic systems are the triclinic, the monoclinic, the orthorhombic, the trigonal, the tetragonal, the hexagonal and the cubic systems.

The cubic (or isometric) crystallographic system is a crystal system where the unit cell is a cube, the unit cell being the smallest divisible unit of a mineral that possesses the symmetry of the mineral. It gathers the 5 cubic groups, namely $m\bar{3}m$, 432 , $\bar{4}3m$, $m\bar{3}$ and 23 , each exhibiting at least four 3-fold axis of symmetry.

The hexagonal crystal system is a crystal system where the unit cell is hexagonal. Seven crystallographic groups, namely 6 , $\bar{6}$, $6/m$, 622 , $6mm$, $\bar{6}m2$ and $6/mmm$ compose this system, each exhibiting at least a 6-fold axis of symmetry.

The trigonal crystal system gathers the 5 symmetry groups, namely 3 , $\bar{3}$, 32 , $3m$ and $\bar{3}m$, each exhibiting at least a 3-fold axis of symmetry.

Seven crystallographic groups, namely 4 , $\bar{4}$, $4/m$, 422 , $4mm$, $\bar{4}2m$ and $4/mmm$ compose the tetragonal crystal system, each exhibiting at least a 4-fold axis of symmetry.

The orthorhombic crystal system gathers the 3 symmetry groups, namely 222 , $mm2$ and mmm , each exhibiting at least either three 2-fold axes of rotation or one 2-fold axis of rotation and two symmetry planes.

The monoclinic crystal system is composed of three symmetry groups, namely 2 , m and $2/m$, each exhibiting at least a 2-fold axis of symmetry or a symmetry plane.

Finally, the triclinic crystal system gathers two symmetry groups, namely 1 and $\bar{1}$, exhibiting no symmetry element and a center of symmetry respectively.

The description that follows is excerpt from Sirotine and Chaskolskaya [1975]. More details can be found in this reference. The links between the different groups are also represented diagrammatically on Figure 4.2.2-2. More precisely, the different symmetry groups of the same system are connected by heavy dashed lines, as the groups 1 and $\bar{1}$ of the triclinic system, or the groups $\infty\infty m$ and $\infty\infty$ of the isotropic system. A symmetry group of a given system is downward connected with its sub-groups belonging to another system by light solid lines. For instance the isotropic symmetry group $\infty\infty m$ (of which any axis is an axis of rotational invariance and any plane a symmetry plane) is connected with its transversely isotropic sub-group ∞/mm (characterized by an axis of rotational invariance and an infinite number of symmetry planes containing this axis) by a light solid line. In some cases three light solid lines connect a group and its sub-group. For instance the orthorhombic symmetry group 222 (characterized by three 2-fold axes mutually perpendicular) is connected by three light solid lines to its monoclinic sub-group 2 (characterized by a single 2-fold axis). The reason is that there are three possible orientations for the 2-fold axis, along one of the three coordinate axes.

4.2.2.2.2 Symmetry groups in Geological media

The overall symmetry of geological media is influenced by three main factors, namely:

- the rock fabric, that is to say the spatial and geometric configuration of all the elements that compose the rock (e.g., Sander [1930] and [1970]) and more generally the presence of heterogeneous rock components or structures (e.g., layering) spatially organized at scales smaller than the elastic wavelength,
- the presence of the mechanical defects, that is to say fractures, cracks, grain joints etc... (e.g., Jaeger et al. [2007]), due to paleo-stresses or created/ opened by present stress, and
- the present stress field (e.g., Zoback [2007])

Regarding rock fabric and more generally spatially aligned structures, according to Paterson and Weiss [1961], only some of the symmetry groups of Figure 4.2.2-2 may be encountered in sedimentary rock and igneous rock fabrics. The common types of symmetry to be expected are isotropic, transversely isotropic, orthotropic, monoclinic and triclinic, as illustrated by Figure 4.2.2-3. Note that without the presence of fractures/cracks, or more generally any mechanical defect, the orthotropic (orthorhombic) symmetry is seldom encountered.

Symmetry	Examples	
	Sedimentary rocks	Igneous rocks
ISOTROPIC $\infty\infty m$	Aggregates of equant grains, e.g., massive sandstones with spherical quartz grains lacking preferred orientation of crystallographic directions	Aggregates with randomly oriented grains, e.g., some granites and basalts (a hornfels is a metamorphic rock that can have this symmetry)
TRANSVERSELY ISOTROPIC ∞ / mm	Bedded sediments of equant and inequant grains, e.g., shales and limestones	Aggregates with bedding or nonlinear flow layering, or purely linear flow structures, e.g., some lava flows, minor and major intrusive rocks
ORTHOTROPIC (ORTHORHOMBIC) mmm	Rare	Rare
MONOCLINIC m	Bedded sediments containing linear structures, e.g., graywackes with groove and flute casts, imbrication, grain lineation	Aggregates containing laminar and linear flow structures, e.g., some plutonic and volcanic rocks
TRICLINIC 1	Bedded sediments containing nonparallel linear flow structures, convolute bedding, and so on	Aggregates containing irregular flow structures, e.g., convolutions

Figure 4.2.2-3: Symmetry types of rock fabric in sedimentary rocks and igneous rocks (modified after Paterson and Weiss [1961]). The symmetry types are introduced in the two previous sub-sections.

With respect to elasticity, the fractures/cracks, or mechanical defects in general, can be idealized either by elastic models with fractures with non-welded (linear slip) interfaces (e.g.,

Schoenberg and Douma [1988]; Schoenberg and Sayers [1995]), or by elastic models with aligned ellipsoidal cracks (e.g., Hudson [1980] and [1991]), as illustrated by Figure 4.2.2-4, and more generally by elastic models with multiple families of such fractures or cracks (for details see the last reference and section 4.6).

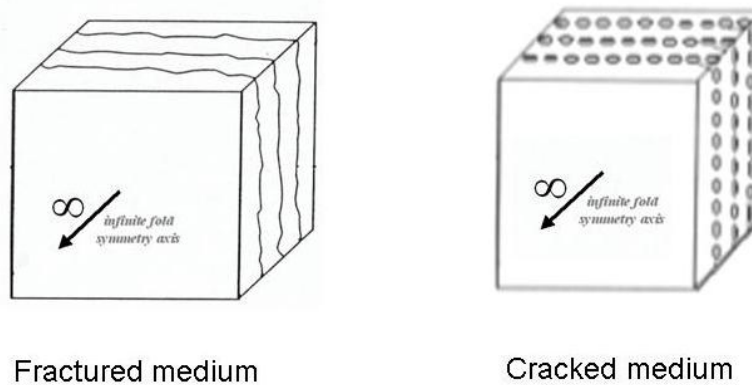


Figure 4.2.2-4: Two idealizations of an initially elastic isotropic model with a single family of aligned fractures (figure on the left) or with a single family of aligned cracks (figure on the right). Note that both models exhibit an axis of rotational invariance normal to the fracture plane or to the plane aligned with the cracks, which results in the overall transversely isotropic symmetry.

In the presence of a single family of aligned fractures/cracks the medium exhibits transverse isotropy with symmetry ∞/mm (after Figure 4.3.2-4 and the corresponding comments), characterized by an axis of rotational invariance (normal to the fracture/crack plane), an infinite number of symmetry planes (normal to the fracture/crack plane and containing the infinite-fold axis), and a symmetry plane parallel to the fracture/crack plane (see Figure 4.2.2-1 and the corresponding comments in sub-section 4.2.2.1).

In the presence of multiple families of aligned fracture/cracks, five symmetry cases are possible:

- Isotropic symmetry $\infty\infty m$ (any axis is an axis of rotational invariance and any plane is a symmetry plane) in the presence of a great number of crack/fracture families arbitrarily oriented,
- Transversely isotropic symmetry ∞/mm , characterized by an axis of rotational invariance, an infinite number of symmetry planes containing the infinite-fold axis), and a symmetry plane normal to this axis, in the case where the fracture/crack planes of all the families are parallel. Obviously the axis of rotational invariance is normal to the fracture/crack plane.
- Orthotropic (orthorhombic) symmetry mmm , characterized by 3 symmetry planes mutually perpendicular, in the case where the families of fractures/cracks are characterized by only two or three different directions of the normal to the fracture/crack plane, mutually orthogonal. The symmetry planes are parallel to the fracture planes.

- Monoclinic symmetry m , characterized by a single symmetry plane, in the case where the families of fractures/cracks are characterized by two different directions of the normal to the fracture/crack plane, not orthogonal. Thus the symmetry plane is the plane defined by the two normal directions.
- Triclinic symmetry $\bar{1}$, characterized by a center of symmetry, in the presence of more than two, but limited number of fracture/crack families.

Regarding the stress field itself, assumed overall uniform, the corresponding symmetry type cannot be lower than orthorhombic, more precisely mmm with three symmetry planes mutually perpendicular (see Figure 4.2.1-3 and the corresponding comments). Thus if σ_I , σ_{II} and σ_{III} designate the principal stresses (we impose no hierarchy on these stress values), three symmetry cases are possible:

- Isotropic symmetry $\infty\infty m$ in the case of an isotropic state of stress, that is to say if $\sigma_I = \sigma_{II} = \sigma_{III}$
- Transversely isotropic symmetry ∞/mm , in the case of a bi-axial state of stress, that is to say if $\sigma_I = \sigma_{II} \neq \sigma_{III}$, and
- Orthotropic (orthorhombic) symmetry mmm , in the case of a tri-axial state of stress, that is to say if $\sigma_I \neq \sigma_{II} \neq \sigma_{III}$.

The derivation of the overall symmetry due to three above causes is just a matter of applying Curie's symmetry principle, detailed in sub-section 4.2.1 and illustrated by 4.2.1-2. Note that the special case of a initially isotropic medium tri-axially stressed, illustrated by Figure 4.2.1-3, have been already considered in that sub-section.

For clarity we shall analyze another example of application of Curie's symmetry principle, illustrated by Figure 4.2.2-5. One considers an initially isotropic medium containing a single family of vertical fractures which is tri-axially stressed. Following the method described in the sub-section 4.2.1, the process is done in two steps, namely first enumerate all the causes of the physical phenomenon and the associated symmetry elements, in the sense defined in that sub-section, and then find the symmetry elements shared by all the causes.

There are three causes: namely the medium (G_1) itself, the single family of parallel fractures (G_2) and the stress (G_3).

The medium is initially isotropic with the symmetry $\infty\infty m$ (any axis is an axis of rotational invariance and any plane is a symmetry plane). The single family of parallel fractures exhibits the transversely isotropic symmetry ∞/mm , characterized by an axis of rotational invariance (of arbitrary azimuth), an infinite number of symmetry planes containing the infinite-fold axis), and a symmetry plane normal to this axis. The applied stress is "vertically" tri-axial of orthotropic symmetry mmm , characterized by 3 symmetry planes mutually perpendicular, one of the planes being horizontal.

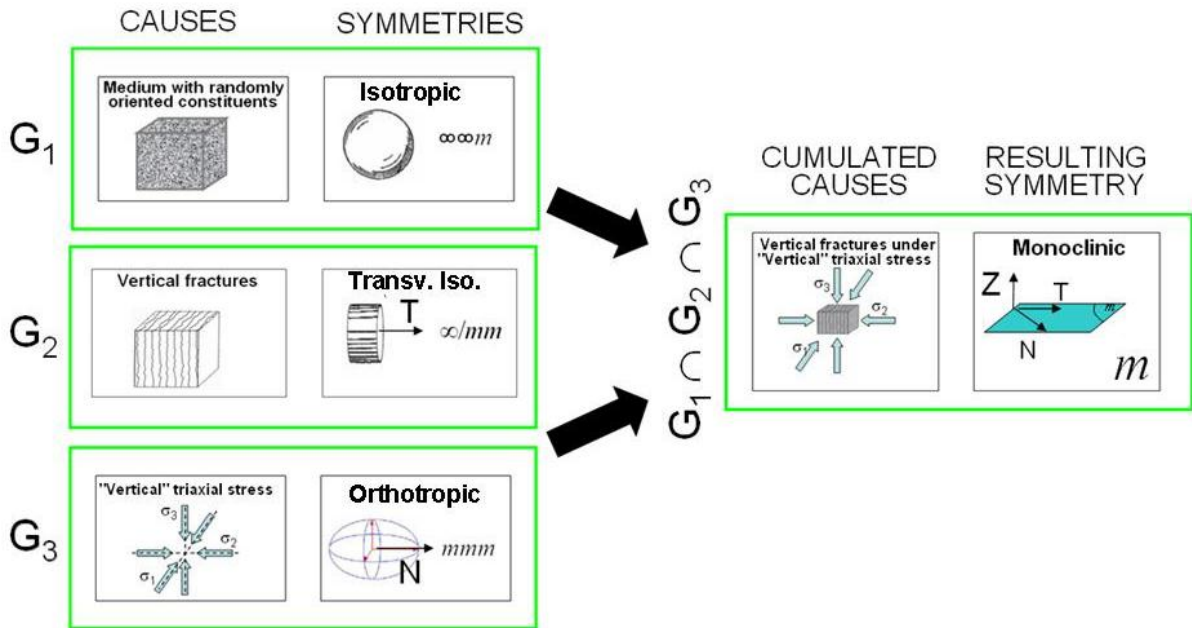


Figure 4.2.2-5: Curie's symmetry principle in action. A initially isotropic medium containing a single family of vertical fractures when tri-axially stressed cannot be less symmetric than monoclinic..

The only symmetry element shared by the three causes is the horizontal plane defined by the normal \mathbf{T} to the fracture planes and one of the principal stress direction \mathbf{N} . As a consequence the effects, for instance any physical property, in particular the elastic properties (not just linear elastic properties, but also nonlinear effects) are at least monoclinic with the symmetry m . As pointed out previously all these results are completely independent of the stress level and of the rock model. As a consequence the linear elastic property of the medium sketched by Figure 4.2.2-5 is defined by a maximum of 12 non-vanishing coefficients, as detailed on Figure 4.3.2-4 and the corresponding comments.

Curie's principle allows deducing the minimum symmetry level of a physical phenomenon due to multiple causes, given the symmetry of the causes. As a consequence, regarding elastic properties, it gives the maximum number of linear elastic constants characterizing a system such as the one illustrated by the left part of Figure 4.2.2-5, using Figure 4.3.2-4 and the corresponding comments.

Note that Curie's principle leads to a minimalistic direct formulation. The physical property can be characterized by less constants than that deduced from this principle. For instance, on Figure 4.2.1-3 and the corresponding comments, Curie's principle allows to deduce that an initially isotropic medium when tri-axially stressed cannot be less symmetric than orthorhombic. However Nikitin and Chesnokov [1981] and Rasolofosaon [1998b], using two different approaches, demonstrated that an initially isotropic medium when tri-axially stressed is not characterized by 9 independent elastic coefficients, as conventional orthorhombic media (see Figure 4.3.2-4 and the corresponding comments), but by only 6 independent coefficients.

All these examples illustrate the powerfulness of Curie's symmetry principle applied to the study of the symmetry of the physical phenomena in geological media. The application of this symmetry principle is strongly recommended in order to simplify the formulation and the quantitative analysis of the addressed problem. The detailed description given above should greatly help to put Curie's principle into practice.

4.3 Seismic anisotropy, the classical theory

4.3.1 Stress, strain and Voigt's notation

The detailed descriptions of the stress and of the strain can be found in sections 1.2.1.1 and 1.2.1.2 of Chapter 1 and do not need to be reported here.

The single index notation or contracted-index notation of Voigt for the strain tensor and for the stress tensor were defined respectively by equation (1.2.1-16) and by equation (1.2.1-25) and is illustrated by Figure 4.2.1-1. and are repeated here only for convenience:

$$(4.3.1-1) \left\{ \begin{array}{l} \sigma_{11} = \sigma_1 ; \sigma_{22} = \sigma_2 ; \sigma_{33} = \sigma_3 \\ \sigma_{23} = \sigma_4 ; \sigma_{13} = \sigma_5 ; \sigma_{12} = \sigma_6 \end{array} \right. \text{ and } \left\{ \begin{array}{l} \varepsilon_{11} = \varepsilon_1 ; \varepsilon_{22} = \varepsilon_2 ; \varepsilon_{33} = \varepsilon_3 \\ 2\varepsilon_{23} = \varepsilon_4 ; 2\varepsilon_{13} = \varepsilon_5 ; 2\varepsilon_{12} = \varepsilon_6 \end{array} \right.$$

Or in a more compact way [Helbig, 1994]:

$$(4.3.1-2) \left\{ \begin{array}{l} \sigma_I = \sigma_{ij} ; \varepsilon_J = (2 - \delta_{kl}) \varepsilon_{kl} \text{ with } I, J = 1, 2, \dots, 6 \text{ and } i, j, k, l = 1, 2, 3 \\ I = i\delta_{ij} + (1 - \delta_{ij})(9 - i - j) ; J = k\delta_{kl} + (1 - \delta_{kl})(9 - k - l) \end{array} \right.$$

The strain tensor and the stress tensor are mapped to two single-column matrices of dimension 6. Note the absence of the factors 2 for the components (23), (13) and (12) of the stress tensor, compared to the corresponding components of the strain tensor.

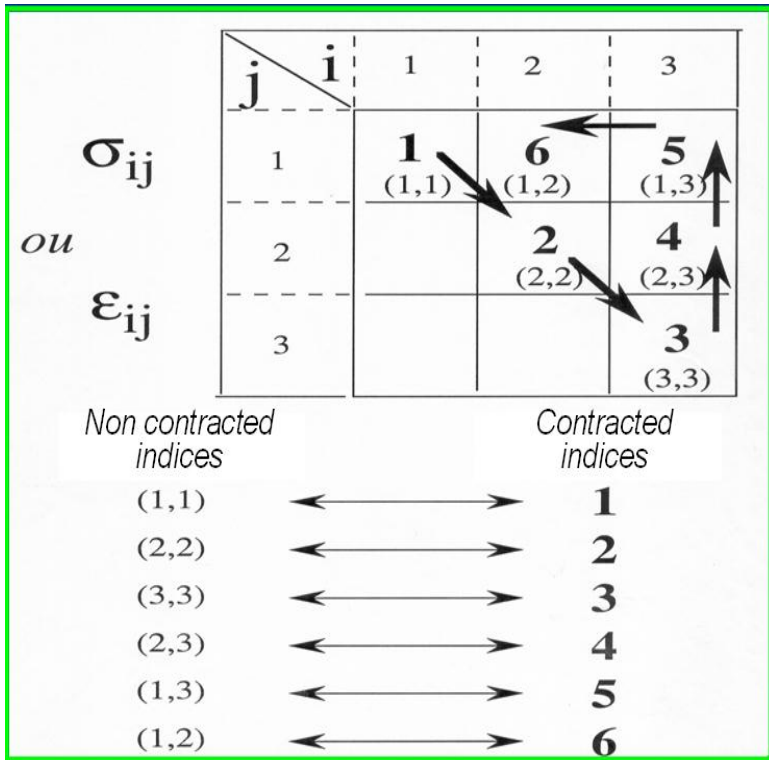


Figure 4.3.1-1: Voigt's convention for indice contraction

As pointed out in Chapter 1 the representation is not a true tensorial nor a vectorial mapping, in contrast to the so called Kelvin representation (Cowin [1987]; Helbig [1994]). However Voigt's mapping and notation have become standards and the corresponding elastic constants, described in the next sub-section, are those available in standard tables of constants (e.g., Aleksandrov [1961]; Bechmann [1966]) and found in any classical textbook on crystal acoustics (e.g., Auld [1973]; Dieulesaint and Royer [1974]). That is the reason why we adopt here this representation in the following, unless mentioned.

Regarding the strain matrix in Voigt representation, the three first components ϵ_I ($I=1,2,3$) correspond to elongations of the rock sample, that is to say a change of the dimension of the sample without any change of shape along the coordinate axes I ($I=1,2,3$), as illustrated by Figure 4.3.1-2. In other words a rectangular-parallelepiped sample (with six rectangular faces parallel to the coordinate planes) remains a rectangular parallelepiped with different dimensions. The relative length variation of the sample along a coordinate axis is equal to the corresponding component of the elongation in this direction as shown in Equation (1.2.1-11) and in the corresponding comments.

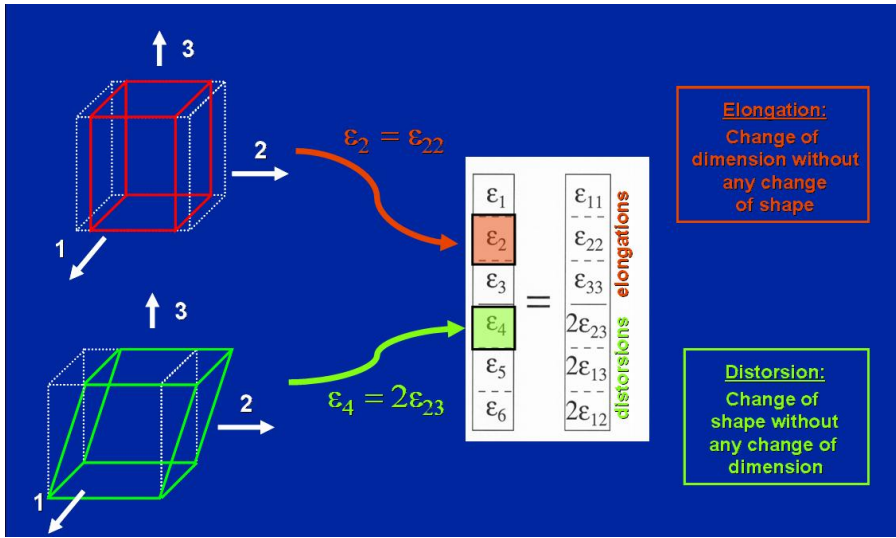


Figure 4.3.1-2: Voigt's convention for the strain

In contrast the three last components $\epsilon_4 (=2\epsilon_{23})$, $\epsilon_5 (=2\epsilon_{13})$ and $\epsilon_6 (=2\epsilon_{12})$ correspond to distorsions inducing changes of the shape of the sample in the coordinate planes 23 (yz), 13 (xz) and 12 (xy) respectively. The faces of the parallelepiped are no longer rectangles but parallelograms. As shown by Equation (1.2.1-15) and the corresponding comments, in the side of the parallelepiped parallel to the considered coordinate plane the induced angular deviation from a right angle is precisely equal to the distorsion strain in this plane.

Regarding the stress matrix in Voigt representation, the three first components σ_I ($I=1,2,3$) correspond to normal stress or uniaxial stress along the coordinate axes I ($I=1,2,3$), as illustrated by Figures 1.2.1-2 Chapter 1 and 4.3.1-3. The three last components $\sigma_4 (= \sigma_{23})$, $\sigma_5 (= \sigma_{13})$ and $\sigma_6 (= \sigma_{12})$ correspond to shear stresses in the coordinate planes 23 (yz), 13 (xz) and 12 (xy) respectively.

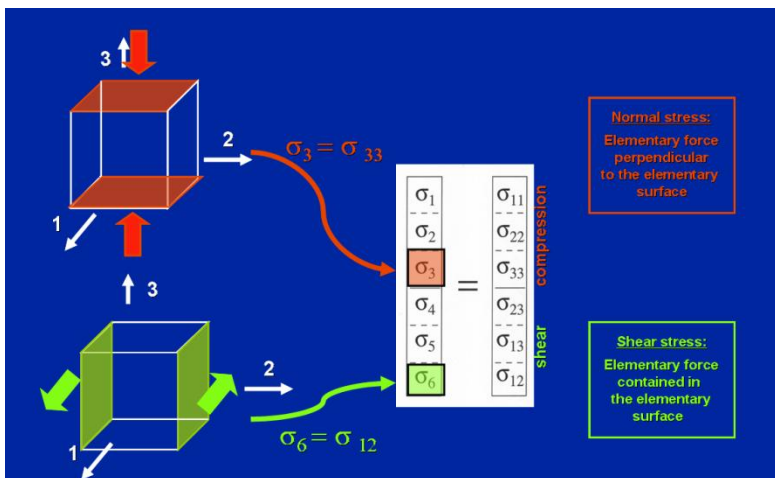


Figure 4.3.1-3: Voigt's convention for the stress

4.3.2 Anisotropic version of the generalized Hooke's law

4.3.2.1 Strain-stress and stress-strain relations, and elasticity matrix.

The most general linear relation between the components σ_{ij} of the stress tensor and the components ε_{kl} of the strain tensor is given by Equation (1.2.1-30) of Chapter 1, and can be written as a stress-strain relation or strain-stress relation in non-contracted notations, as follows:

$$(4.3.2-1) \quad \sigma_{ij} = C_{ijkl} \varepsilon_{kl} \quad \text{and} \quad \varepsilon_{ij} = S_{ijkl} \sigma_{kl} \quad \text{with} \quad i, j, k, l = 1, 2, 3$$

where C_{ijkl} and S_{ijkl} are the components of the stiffness tensor and of the compliance tensor. These tensors are inverse of each other, that is to say such that:

$$(4.3.2-2) \quad C_{ijmn} S_{mnkl} = I_{ijkl} = \frac{1}{2} (\delta_{il} \delta_{jk} + \delta_{ik} \delta_{jl})$$

where $I_{ijkl} = \frac{1}{2} (\delta_{il} \delta_{jk} + \delta_{ik} \delta_{jl})$ are the component of the identity tensor of rank 4, the δ s being the components of the unit tensor of rank 2 or Kronecker tensor (defined by $\delta_{ij} = 1$ if $i = j$, and $\delta_{ij} = 0$ if $i \neq j$).

The version of Equation (4.2.2-1) in contracted notation is:

$$(4.3.2-3) \quad \sigma_I = C_{IJ} \varepsilon_J \quad \text{and} \quad \varepsilon_I = S_{IJ} \sigma_J \quad \text{with} \quad I, J = 1, 2, \dots, 6$$

where C_{IJ} and S_{IJ} are the components of the stiffness matrix and the compliance matrix in Voigt notation. These matrices are inverse of each other, that is to say:

$$(4.3.2-4) \quad C_{IJ} S_{JK} = \delta_{IK}$$

The relations between the components of the stiffness/compliance tensor with contracted and with non-contracted indices are the followings (e.g., Helbig [1994]):

$$(4.3.2-5) \quad \begin{cases} C_{IJ} = C_{ijkl} ; & S_{IJ} = (2 - \delta_{ij})(2 - \delta_{kl}) S_{ijkl} \quad \text{with} \quad I, J = 1, 2, \dots, 6 \quad \text{and} \quad i, j, k, l = 1, 2, 3 \\ & I = i\delta_{ij} + (1 - \delta_{ij})(9 - i - j) \quad ; \quad J = k\delta_{kl} + (1 - \delta_{kl})(9 - k - l) \end{cases}$$

Because of the symmetry condition (Chapter 1 Eq.1.2.1-33) the stiffness matrix and the compliance matrix of dimension 6×6 are symmetric. As the consequence they are characterized by 21 ($=6+5+4+3+2+1$) independent coefficients in the most general case (triclinic).

We gave in Chapter 1 §1.2.1-3 the physical interpretation of all the elastic coefficients of isotropic linearly elastic media. Here we aim to do the same for arbitrarily anisotropic media. Although the physical interpretation of the elastic coefficients C_{ijkl} and S_{ijkl} , with non-contracted indices, is not straightforward, the elastic constants C_{IJ} and S_{IJ} , with contracted indices, are more easily interpretable. For this, let us consider two thought experiments sketched by the two next figures.

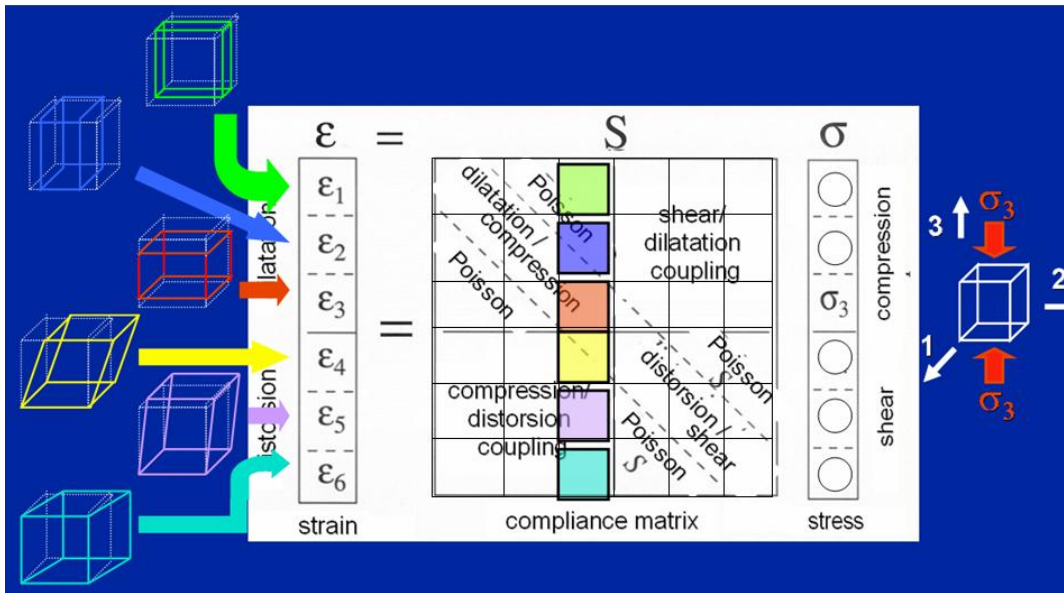


Figure 4.3.2-1: Physical interpretation of the third column of the compliance matrix of Hooke's law. Case of a uniaxial stress along the 3-axis or Z-axis.

First let us consider a rock sample submitted to an uniaxial stress along a coordinate axis, say along the 3-axis (i.e., $\sigma_3 \neq 0$ and $\sigma_I = 0$ for $I \neq 3$), as illustrated by Figure 4.3.2-1. After Equation (4.2.2-3) the induced deformations are given by:

$$(4.3.2-6) \quad \epsilon_I = S_{I3} \sigma_3 \quad \text{with} \quad I = 1, 2, \dots, 6$$

The third component $\epsilon_3 = S_{33} \sigma_3$ of the induced strain is the induced elongation along the 3-axis, and the coefficient S_{33} is simply uniaxial strain induced per unit axial stress in the direction 3. Thus S_{33} can be interpreted as the inverse of Young's modulus, or Young's compliance, in the direction 3.

As in the case of isotropic media, anisotropic media when uniaxially stressed in a given direction tends to change of dimension in the perpendicular direction. After Equation (4.3.2-3), and in a way similar to Equation (1.2.1-38), one has:

$$(4.3.2-7) \quad -\frac{\varepsilon_1}{\varepsilon_3} = -\frac{S_{13}}{S_{33}} = \nu_{31} \quad \text{and} \quad -\frac{\varepsilon_2}{\varepsilon_3} = -\frac{S_{23}}{S_{33}} = \nu_{32}$$

The opposite of the ratio between the radial strain ε_1 (respectively ε_2) in direction 1 (respectively in direction 2) and the axial strain ε_3 is a Poisson's ratio ν_{31} (respectively ν_{32}). Thus the ratio S_{13}/S_{33} (respectively S_{23}/S_{33}) can be interpreted as the opposite of Poisson's ratio ν_{31} (respectively ν_{32}), that corresponds to an elongation in direction 1 (respectively in direction 2) when uniaxial stress is applied in direction 3.

Additional counterintuitive effects, not observed in isotropic media, are the induced distorsion strains ε_4 , ε_5 and ε_6 in the three coordinate planes under uniaxial stress:

$$(4.3.2-8) \quad \varepsilon_4 = S_{43} \sigma_3 ; \quad \varepsilon_5 = S_{53} \sigma_3 \quad \text{and} \quad \varepsilon_6 = S_{63} \sigma_3$$

In other words a rectangular-parallelepiped sample (with six rectangular faces parallel to the coordinate planes) cannot remain a rectangular parallelepiped under uniaxial stress along a coordinate axis. The faces of the parallelepiped are no longer rectangles but parallelograms. As shown by Figure 4.3.1-2 and the corresponding comments, the induced angular deviations from a right angle are equal to $\varepsilon_4 (= 2\varepsilon_{23})$, $\varepsilon_5 (= 2\varepsilon_{13})$ and $\varepsilon_6 (= 2\varepsilon_{12})$ in the coordinate planes 23 (yz), 13 (xz) and 12 (xy) respectively. Thus, after Equation (4.3.2-7), S_{43} , S_{53} and S_{63} can be interpreted as the distorsion angles induced in planes 23 (yz), 13 (xz) and 12 (xy), respectively, per uniaxial stress in the direction 3 (z). We call this effect a coupling effect between compression and distorsion. If we define $\gamma_{IJ}^{(CD)}$ as the compression/distorsion (CD) coupling coefficient corresponding to a distorsion in the plane normal to the direction J when uniaxial stress is applied in the direction I, one has the relations:

$$(4.3.2-9) \quad S_{43} = \gamma_{31}^{(CD)} ; \quad S_{53} = \gamma_{32}^{(CD)} \quad \text{and} \quad S_{63} = \gamma_{33}^{(CD)}$$

By considering two similar uniaxial-stress experiments along the coordinate axes 1 (x) and 2 (y) it is possible to straightforwardly give the physical interpretations of all the compliance coefficients S_{IJ} (with $J \leq 3$) corresponding to the left part of the compliance matrix of Figure 4.3.2-1. For instance, S_{22} can be interpreted as the inverse of Young's modulus, or Young's compliance, in the direction 2, and S_{12}/S_{22} is the opposite of Poisson's ratio ν_{21} corresponding to an elongation in direction 1 when uniaxial stress is applied in direction 2. In the same way, S_{61} can be interpreted as the distorsion angle $\varepsilon_6 (= 2\varepsilon_{12})$ induced in planes the 12 (xy), per uniaxial stress in the direction 1 (x).

In order to interpret all the remaining compliance coefficients S_{IJ} (with $J \geq 4$) corresponding to the right part of the compliance matrix, let us consider a rock sample

submitted to a shear stress in the coordinate plane 12 (i.e., $\sigma_6 \neq 0$ and $\sigma_I = 0$ for $\sigma_I = 0$ for $I \neq 6$), as illustrated by Figure 4.3.2-2. After Equation (4.3.2-3) the induced deformations are given by:

$$(4.3.2-10) \quad \varepsilon_I = S_{I6} \sigma_6 \quad \text{with} \quad I = 1, 2, \dots, 6$$

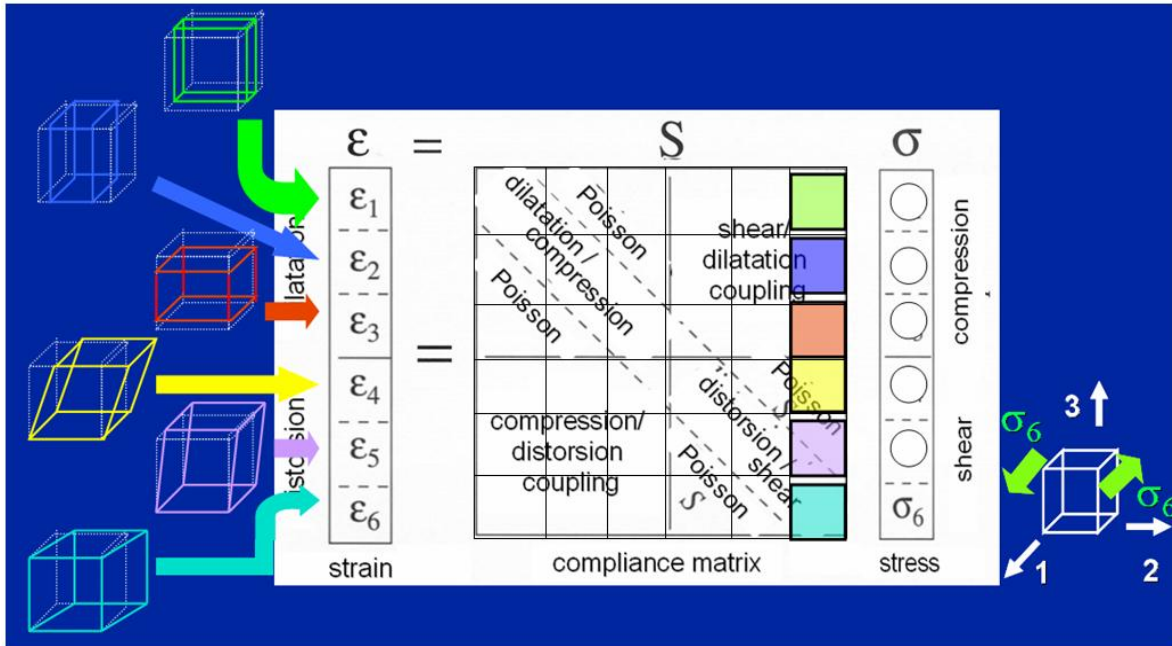


Figure 4.3.2-2: Physical interpretation of the sixth column of the compliance matrix of Hooke's law. Case of a shear stress in the 12-plane or xy-plane.

The sixth component $\varepsilon_6 = S_{66} \sigma_6$ of the induced strain is the induced distorsion in the 12-plane of stress, and the coefficient S_{66} is simply the distorsion angle induced per unit shear stress in the 12-plane. Thus S_{66} can be interpreted as the inverse of the shear modulus μ_3 , or in the normal to the direction 3, that is to say the 12-plane.

Additional counterintuitive effects, not observed in isotropic media, are the induced distorsion strains $\varepsilon_4 (= 2\varepsilon_{23})$ and $\varepsilon_5 (= 2\varepsilon_{13})$ in the two coordinate planes perpendicular to the 12-plane of the imposed shear stress. This effect is similar to the Poisson effect with the change of sample size in a direction perpendicular to the uniaxial stress direction. The main difference here is that we are dealing with distorsion strains and not elongation or uniaxial strains. That is why we call this effect a Poisson S effect, S standing for shear. In a way similar to Equation (4.3.2-7), we can define the Poisson S coefficients as follows:

$$(4.3.2-11) \quad \nu_{31}^{(S)} = \frac{\varepsilon_4}{\varepsilon_6} = \frac{S_{44}}{S_{66}} \quad \text{and} \quad \nu_{32}^{(S)} = \frac{\varepsilon_5}{\varepsilon_6} = \frac{S_{55}}{S_{66}}$$

where $\nu_{31}^{(S)}$ (respectively $\nu_{32}^{(S)}$) is a Poisson S ratio, that corresponds to distorsion in the plane normal to direction 1 (respectively to direction 2) when shear stress is applied in the plane normal to direction 3. Thus the ratio S_{44}/S_{66} (respectively S_{55}/S_{66}) can be interpreted as Poisson S ratio $\nu_{31}^{(S)}$ (respectively $\nu_{32}^{(S)}$).

Furthermore additional counterintuitive effects, not observed in isotropic media, are the induced elongation or uniaxial strains ε_1 , ε_2 and ε_3 in the three coordinate directions under shear stress:

$$(4.3.2-12) \quad \varepsilon_1 = S_{16} \sigma_6 ; \quad \varepsilon_2 = S_{26} \sigma_6 \quad \text{and} \quad \varepsilon_3 = S_{36} \sigma_6$$

In other words a rectangular-parallelepiped sample (with six rectangular faces parallel to the coordinate planes) necessarily exhibits change of dimension along the three coordinate axes under shear stress in a coordinate plane. Thus, S_{16} , S_{26} and S_{36} can be interpreted as the uniaxial strain induced in the direction 1 (x), in the direction 2 (y) and in the direction 3 (z), respectively, per shear stress in the 12-plane (xy-plane). We call this effect a coupling between shear and dilatation. If we define $\gamma_{IJ}^{(SD)}$ as the shear/dilatation (SD) coupling coefficient corresponding to a uniaxial strain in the direction J when shear stress is applied in the plane normal to the I, one has the relations:

$$(4.3.2-13) \quad S_{16} = \gamma_{31}^{(SD)} ; \quad S_{26} = \gamma_{32}^{(SD)} \quad \text{and} \quad S_{36} = \gamma_{33}^{(SD)}$$

Because of the symmetry of the compliance matrix ($S_{IJ} = S_{JI}$ with $I, J = 1, 2, \dots, 6$) the coefficients characterizing the coupling between shear and dilatation, introduced in Equation (4.3.2-13) and the corresponding comments, are equal to the corresponding coefficient characterizing the coupling between compression and distorsion, introduced in Equation (4.3.2-9) and the corresponding comments. For instance one has:

$$(4.3.2-14) \quad S_{16} = S_{61} \Rightarrow \gamma_{31}^{(SD)} = \gamma_{13}^{(CD)}$$

the general result being:

$$(4.3.2-15) \quad \gamma_{IJ}^{(SD)} = \gamma_{JI}^{(CD)} .$$

This simply means that the uniaxial strain measured in the direction J per unit shear stress applied in the plane normal to the direction I, namely $\gamma_{IJ}^{(SD)}$, is equal to the distortion in the plane normal to the direction I per unit uniaxial stress in the direction J, namely $\gamma_{JI}^{(CD)}$.

Finally, using the more explicit new coefficients, the compliance matrix simply writes:

$$(4.3.2-16) \quad \mathbf{S} = \begin{pmatrix} \frac{1}{E_1} & -\frac{\nu_{21}}{E_2} & -\frac{\nu_{31}}{E_3} & \gamma_{11}^{(SD)} & \gamma_{21}^{(SD)} & \gamma_{31}^{(SD)} \\ -\frac{\nu_{12}}{E_1} & \frac{1}{E_2} & -\frac{\nu_{32}}{E_3} & \gamma_{12}^{(SD)} & \gamma_{22}^{(SD)} & \gamma_{32}^{(SD)} \\ -\frac{\nu_{13}}{E_1} & -\frac{\nu_{23}}{E_2} & \frac{1}{E_3} & \gamma_{13}^{(SD)} & \gamma_{23}^{(SD)} & \gamma_{33}^{(SD)} \\ \gamma_{11}^{(CD)} & \gamma_{21}^{(CD)} & \gamma_{31}^{(CD)} & \frac{1}{\mu_1} & \frac{\nu_{21}^{(S)}}{\mu_2} & \frac{\nu_{31}^{(S)}}{\mu_3} \\ \gamma_{12}^{(CD)} & \gamma_{22}^{(CD)} & \gamma_{32}^{(CD)} & \frac{\nu_{12}^{(S)}}{\mu_1} & \frac{1}{\mu_2} & \frac{\nu_{32}^{(S)}}{\mu_3} \\ \gamma_{13}^{(CD)} & \gamma_{23}^{(CD)} & \gamma_{33}^{(CD)} & \frac{\nu_{13}^{(S)}}{\mu_1} & \frac{\nu_{23}^{(S)}}{\mu_2} & \frac{1}{\mu_3} \end{pmatrix}$$

Note that, in this form the compliance matrix does not seem to be symmetric. However the symmetry is straightforwardly re-established by noting the following relations:

$$(4.3.2-17) \quad \frac{\nu_{ij}}{\nu_{ji}} = \frac{E_i}{E_j} \quad ; \quad \gamma_{ij}^{(CD)} = \gamma_{ji}^{(SD)} \quad \text{and} \quad \frac{\nu_{ij}^{(S)}}{\nu_{ji}^{(S)}} = \frac{\mu_i}{\mu_j}$$

This completes the physical interpretation of all the compliance coefficients with contracted indices.

The physical interpretation of the compliance coefficients with non contracted indices, can be made in two steps. The first step is to contract the indices by using the relation (4.3.2-6) between the components of the stiffness/compliance tensor with contracted and non-contracted indices. Then we use the physical interpretation detailed above.

For instance and after Equation (4.3.2-5), S_{1213} is equal to $S_{65}/4$, which is equal to $\frac{\nu_{23}^{(S)}}{4\mu_2}$ after Equation (4.3.2-16). Thus S_{1213} can be interpreted as a quarter of the product of the Poisson S ratio $\nu_{23}^{(S)}$, corresponding to a distortion in the plane normal to direction 3 under

applied shear stress is in the plane normal to direction 2, and of the shear compliance $1/\mu_2$ in the plane normal to the direction 2.

Let us consider another example. For instance S_{1322} is equal to $S_{52}/2$ after Equation (4.3.2-5), and is equal to $\gamma_{22}^{(CD)}/2$ after Equation (4.3.2-16). Thus S_{1322} can be interpreted as a half of the distortion in the plane normal to the direction 2 per unit uniaxial stress applied in the direction 2.

This completes the physical interpretation of all the compliance coefficients.

The physical interpretation of the stiffness coefficients is quite similar. Let us consider two “dual” thought experiments corresponding to those considered on Figures 4.3.2-1 and 4.3.2-2. More precisely, instead of considering the strains induced by imposed uniaxial stress (Figure 4.3.2-1) or shear stress (Figure 4.3.2-2), we shall consider the stresses necessary to produce a uniaxial strain in a coordinate direction or a distortion strain in a given coordinate plane.

First let us impose a uniaxial strain along a coordinate axis, say along the 3-axis (i.e., $\varepsilon_3 \neq 0$ and $\varepsilon_I = 0$ for $I \neq 3$). After Equation (4.3.2-3) the stress necessary to produce such a strain is such that:

$$(4.3.2-18) \quad \sigma_I = C_{I3} \varepsilon_3 \quad \text{with} \quad I = 1, 2, \dots, 6$$

The stress necessary to produce uniaxial strain is not uniaxial but arbitrary, with both normal components (i.e., σ_1 , σ_2 and σ_3) and shear components (i.e., σ_4 , σ_5 and σ_6). In other words the stress matrix is not diagonal, that is to say the coordinate axes are not eigen axes of stress. The coefficients C_{13} , C_{23} and C_{33} are the normal stresses in the direction 1, 2 and 3, respectively, necessary to induce a unit uniaxial strain in the direction 3. In addition to the normal stresses, the shear stresses to be applied in the planes normal to the 1-axis, 2-axis and 3-axis per unit uniaxial strain in the direction 3 are equal to C_{43} , C_{53} and C_{63} respectively.

Similarly, let us consider a second thought experiment. We impose a distortion strain in the 12-plane (i.e., $\varepsilon_6 \neq 0$ and $\varepsilon_I = 0$ for $I \neq 6$). After Equation (4.3.2-3) the stress necessary to produce such a strain is such that:

$$(4.3.2-19) \quad \sigma_I = C_{I6} \varepsilon_6 \quad \text{with} \quad I = 1, 2, \dots, 6$$

Here again, the stress necessary to produce a distortion strain is not a pure shear stress but is arbitrary, with both normal components (i.e., σ_1 , σ_2 and σ_3) and shear components (i.e., σ_4 , σ_5 and σ_6). In other words the stress matrix is not diagonal, that is to say the coordinate axes are not eigen axes of stress. The coefficients C_{46} , C_{56} and C_{66} are the shear stresses in the

planes normal to the 1-axis , 2-axis and 3-axis, respectively, necessary to induce a unit distorsion strain in the 12-plane. At the same time, in addition to the shear stresses, the normal stresses to be applied along the 1-axis , 2-axis and 3-axis per unit distorsion strain in the 12-plane are equal to C_{16} , C_{26} and C_{36} respectively.

The physical interpretation of the remaining stiffness coefficients is straightforwardly obtained by considering other thought experiments, either imposing a uniaxial strain along another coordinate axis, or a distorsion strain in another coordinate plane. More precisely, the coefficients C_{IJ} with $J \leq 3$ refer to a uniaxial strain experiment along the direction J . And the physical interpretation of the coefficients C_{IJ} for fixed $J \leq 3$ and $I = 1, 2, \dots, 6$ is obtained by replacing 3 by J in the physical interpretation of the coefficients C_{I3} given above in the comments of equation (4.2.2-18). Similarly, the coefficients C_{IJ} with $J \geq 4$ refer to a distorsion strain experiment in the 23-plane for $J = 4$, in the 13-plane for $J = 5$, and in the 12-plane for $J = 6$. And the physical interpretation of the coefficients C_{IJ} for fixed $J \geq 4$ and $I = 1, 2, \dots, 6$ is obtained in the same way as for interpretation of the coefficients C_{I6} for $I = 1, 2, \dots, 6$ given above in the comments of equation (4.3.2-19).

This completes the physical interpretation of all the stiffness coefficients with contracted indices.

The physical interpretation of the stiffness coefficients with non-contracted indices, can be made in two steps. The first step is to contract the indices by using the relation (4.2.2-5) between the components of the compliance tensor with noncontracted and with non-contracted indices. Then we use the physical interpretation detailed above.

For instance and after Equation (4.3.2-5), C_{1213} is equal to C_{65} . C_{1213} refers to a distorsion strain experiment in the 13-plane. It is one of the components of the stress to be applied to the rock sample per unit distorsion strain in the 13-plane. These components are the normal stress components C_{1113} ($= C_{15}$), C_{2213} ($= C_{25}$) and C_{3313} ($= C_{35}$) along the direction 1, 2 and 3 respectively, and the shear stress components C_{23} ($= C_{32}$), C_{1313} ($= C_{55}$) and C_{1213} ($= C_{65}$) in the plane normal to the direction 1, 2 and 3 respectively, all of them being understood per unit distorsion strain in the 13-plane.

Let us consider another example. For instance C_{1322} is equal to C_{52} after Equation (4.3.2-5). C_{1213} refers to a uniaxial strain experiment in the direction 2. It is one of the components of the stress to be applied to the rock sample per unit uniaxial strain in the direction 2. These components are the normal stress components C_{1122} ($= C_{12}$), C_{2222} ($= C_{22}$) and C_{3322} ($= C_{32}$) along the direction 1, 2 and 3 respectively, and the shear stress components

$C_{2322} (=C_{42})$, $C_{1322} (=C_{52})$ and $C_{1222} (=C_{62})$ in the plane normal to the direction 1, 2 and 3 respectively, all of them being understood per unit uniaxial strain in the direction 2.

This completes the physical interpretation of all the stiffness coefficients.

4.3.2.2 Rotation of the elasticity tensor

Elementary 3D rotations $\mathbf{R}_\alpha^{(x)}$, $\mathbf{R}_\beta^{(y)}$ and $\mathbf{R}_\gamma^{(z)}$ respectively of angle α , β and γ about the coordinate axes x, y and z, respectively are defined by:

(4.3.2-20)

$$\mathbf{R}_\alpha^{(x)} = \begin{pmatrix} 1 & 0 & 0 \\ 0 & \cos \alpha & \sin \alpha \\ 0 & -\sin \alpha & \cos \alpha \end{pmatrix}, \quad \mathbf{R}_\beta^{(y)} = \begin{pmatrix} \cos \beta & 0 & -\sin \beta \\ 0 & 1 & 0 \\ \sin \beta & 0 & \cos \beta \end{pmatrix} \quad \text{and} \quad \mathbf{R}_\gamma^{(z)} = \begin{pmatrix} \cos \gamma & \sin \gamma & 0 \\ -\sin \gamma & \cos \gamma & 0 \\ 0 & 0 & 1 \end{pmatrix}$$

The most general rotation from an initial reference frame xyz to a final frame XYZ without any deformation can be defined by the so-called three Euler angles, namely the precession angle ψ , the nutation angle θ and the intrinsic rotation angle ϕ illustrated by Figure 4.3.2-3. It is the combination of three successive rotations.

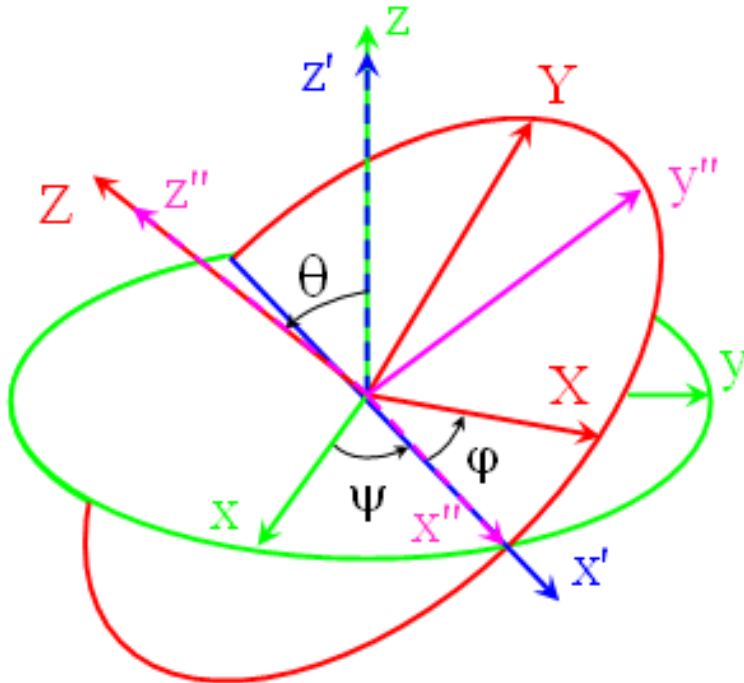


Figure 4.3.2-3: The three Euler angles ψ , θ , and φ characterizing the most general rotation in 3D from an initial reference frame xyz in green to a final reference frame XYZ in red (see detail in text).

More precisely, the starting reference frame is xyz (in green). The first rotation $\mathbf{R}_{\psi}^{(z)}$ of angle ψ about the z -axis brings the reference frame xyz to the position of the frame $x'y'z'$ (in blue). Then the second rotation $\mathbf{R}_{\theta}^{(x')}$ of angle θ about the x' -axis brings the reference frame $x'y'z'$ to the position of the frame $x''y''z''$ (in purple). Finally the last rotation $\mathbf{R}_{\varphi}^{(z'')}$ of angle φ about the z'' -axis brings the reference frame $x''y''z''$ to the position of the final frame XYZ (in red).

The overall rotation $\mathbf{R}_{xyz \rightarrow XYZ}$ is the combination of the three rotations in the order stated above:

$$(4.3.2-21) \quad \mathbf{R}_{xyz \rightarrow XYZ} = \mathbf{R}_{\varphi}^{(z'')} \mathbf{R}_{\theta}^{(x')} \mathbf{R}_{\psi}^{(z)} = \begin{pmatrix} C_{\varphi}C_{\psi} - C_{\theta}S_{\varphi}S_{\psi} & C_{\psi}C_{\theta}S_{\varphi} + C_{\varphi}S_{\psi} & S_{\varphi}S_{\theta} \\ -S_{\varphi}C_{\psi} - C_{\theta}C_{\varphi}S_{\psi} & C_{\psi}C_{\theta}C_{\varphi} - S_{\varphi}S_{\psi} & C_{\varphi}S_{\theta} \\ S_{\psi}S_{\theta} & -C_{\psi}S_{\theta} & C_{\theta} \end{pmatrix}$$

where, for conciseness, we let $C_{\psi} = \cos \psi$, $S_{\psi} = \sin \psi$, $C_{\theta} = \cos \theta$, $S_{\theta} = \sin \theta$, $C_{\varphi} = \cos \varphi$ and $S_{\varphi} = \sin \varphi$.

Any vector \mathbf{u} in the coordinate system xyz rotated to the final coordinate system XYZ is transform in the vector \mathbf{u}' such that:

$$(4.3.2-22) \quad \mathbf{u}' = \mathbf{R}_{xyz \rightarrow XYZ} \mathbf{u} \quad \text{or in terms of the components} \quad u'_i = \left(R_{xyz \rightarrow XYZ} \right)_{ij} u_j$$

The generalization to tensors of rank 4, can be illustrated with the stiffness tensor and with the compliance tensor (e.g., Auld [1973]; Dieulesaint and Royer [1974]; Nye [1985]; Helbig [1994]).

The components C_{ijkl} and S_{ijkl} in non-contracted notation of the stiffness tensor and of the compliance tensor, respectively, in the initial coordinate system xyz are linked to the corresponding components C'_{ijkl} and S'_{ijkl} in the final coordinate system XYZ by the relations :

$$(4.3.2-23) \quad \begin{cases} C'_{ijkl} = \left(R_{xyz \rightarrow XYZ} \right)_{im} \left(R_{xyz \rightarrow XYZ} \right)_{jn} \left(R_{xyz \rightarrow XYZ} \right)_{kp} \left(R_{xyz \rightarrow XYZ} \right)_{lq} C_{mnpq} \\ S'_{ijkl} = \left(R_{xyz \rightarrow XYZ} \right)_{im} \left(R_{xyz \rightarrow XYZ} \right)_{jn} \left(R_{xyz \rightarrow XYZ} \right)_{kp} \left(R_{xyz \rightarrow XYZ} \right)_{lq} S_{mnpq} \end{cases}$$

When dealing with the components of the stiffness tensor and of the compliance tensor in contracted notation the relations are more complicate although still easy to compute. The complication comes from the fact that in Voigt representation the compliance matrix and the stiffness matrix are not true tensors as previously pointed out. A specific technique, first developed by Bond [1943], must be used. The stiffness matrix \mathbf{C} and the compliance matrix

\mathbf{S} in the initial coordinate system xyz are linked to the stiffness matrix \mathbf{C}' and the compliance matrix \mathbf{S}' in the final coordinate system XYZ by the relations :

$$(4.3.2-24) \quad \mathbf{C}' = \mathbf{MCM}' \quad \text{and} \quad \mathbf{S}' = \mathbf{NSN}'$$

where:

$$(4.3.2-25) \quad \mathbf{M} = \begin{pmatrix} r_{11}^2 & r_{12}^2 & r_{13}^2 & 2r_{12}r_{13} & 2r_{11}r_{13} & 2r_{11}r_{12} \\ r_{21}^2 & r_{22}^2 & r_{23}^2 & 2r_{22}r_{23} & 2r_{21}r_{23} & 2r_{21}r_{22} \\ r_{31}^2 & r_{32}^2 & r_{33}^2 & 2r_{32}r_{33} & 2r_{31}r_{33} & 2r_{31}r_{32} \\ r_{21}r_{31} & r_{22}r_{32} & r_{23}r_{33} & r_{23}r_{32} + r_{22}r_{33} & r_{23}r_{31} + r_{21}r_{33} & r_{22}r_{31} + r_{21}r_{32} \\ r_{11}r_{31} & r_{12}r_{32} & r_{13}r_{33} & r_{13}r_{32} + r_{12}r_{33} & r_{13}r_{31} + r_{11}r_{33} & r_{12}r_{31} + r_{11}r_{32} \\ r_{11}r_{21} & r_{12}r_{22} & r_{13}r_{23} & r_{13}r_{22} + r_{12}r_{23} & r_{13}r_{21} + r_{11}r_{23} & r_{12}r_{21} + r_{11}r_{22} \end{pmatrix}.$$

and:

$$(4.3.2-26) \quad \mathbf{N} = \begin{pmatrix} r_{11}^2 & r_{12}^2 & r_{13}^2 & r_{12}r_{13} & r_{11}r_{13} & r_{11}r_{12} \\ r_{21}^2 & r_{22}^2 & r_{23}^2 & r_{22}r_{23} & r_{21}r_{23} & r_{21}r_{22} \\ r_{31}^2 & r_{32}^2 & r_{33}^2 & r_{32}r_{33} & r_{31}r_{33} & r_{31}r_{32} \\ 2r_{21}r_{31} & 2r_{22}r_{32} & 2r_{23}r_{33} & r_{23}r_{32} + r_{22}r_{33} & r_{23}r_{31} + r_{21}r_{33} & r_{22}r_{31} + r_{21}r_{32} \\ 2r_{11}r_{31} & 2r_{12}r_{32} & 2r_{13}r_{33} & r_{13}r_{32} + r_{12}r_{33} & r_{13}r_{31} + r_{11}r_{33} & r_{12}r_{31} + r_{11}r_{32} \\ 2r_{11}r_{21} & 2r_{12}r_{22} & 2r_{13}r_{23} & r_{13}r_{22} + r_{12}r_{23} & r_{13}r_{21} + r_{11}r_{23} & r_{12}r_{21} + r_{11}r_{22} \end{pmatrix}.$$

Note that for conciseness we let $r_{ij} = (R_{xyz \rightarrow XYZ})_{ij}$.

In the next subsection we shall see that in media exhibiting symmetry elements the corresponding stiffness/compliance matrix expressed in a coordinate system related to these symmetry elements have many vanishing coefficients. However when rotated to an arbitrary coordinate system the stiffness/compliance matrix may exhibit substantially more non-vanishing coefficients.

For instance, let us consider the strongly anisotropic Angers slate considered by Martin *et al* [1992] (Chapter 2 section 2.3.2.3) or Varade *et al.* [1996] (Chapter 2 section 2.3.3.3) of stiffness matrix in units of GPa:

$$(4.3.2-27) \quad \mathbf{C} = \begin{pmatrix} 139.49 & 32.51 & 18.91 & 0 & 0 & 0 \\ 32.51 & 139.49 & 18.91 & 0 & 0 & 0 \\ 18.91 & 18.91 & 71.65 & 0 & 0 & 0 \\ 0 & 0 & 0 & 15.88 & 0 & 0 \\ 0 & 0 & 0 & 0 & 15.88 & 0 \\ 0 & 0 & 0 & 0 & 0 & 53.49 \end{pmatrix}.$$

The rock symmetry is transversely isotropic with an axis of rotational invariance parallel to the z-axis, as detailed in the next sub-section. After the rotation defined by Euler angles $\psi = 0^\circ$, $\theta = 27^\circ$ and $\varphi = 15^\circ$, the rotated stiffness matrix \mathbf{C}' writes:

$$(4.3.2-28) \quad \mathbf{C}' = \begin{pmatrix} 137.05 & 29.99 & 22.72 & 4.72 & -9.14 & 4.49 \\ 29.99 & 109.39 & 35.86 & 26.45 & 0.78 & 3.48 \\ 22.72 & 35.86 & 67.66 & 0.64 & -0.17 & -3.79 \\ 4.72 & 26.45 & 0.64 & 33.16 & -2.55 & -1.72 \\ -9.14 & 0.78 & -0.17 & -2.55 & 24.31 & 14.10 \\ 4.49 & 3.48 & -3.79 & -1.72 & 14.10 & 46.02 \end{pmatrix}.$$

Note that the rotated matrix \mathbf{C}' apparently exhibits the most general symmetry with all its non-vanishing components, although the actual symmetry is much higher (transverse isotropy). This is a general result. The stiffness/compliance matrix have a simple reduced form only in the coordinate system with axes aligned with symmetry elements of the medium.

4.3.2.3 Hierarchical relation between the elastic symmetry systems

In section 4.2.2 we described the link between the 32 crystallographic groups and the 7 non-crystallographic limit group of symmetry or Curie's limit groups and pointed out their hierarchal structure illustrated by Figure 4.2.2-2. We also described in detail Curie's principle on the symmetry of physical phenomena, briefly summarized by the concise formulation: "the effects are more symmetric than the causes", as shown by Figure 4.2.1-1. As illustrated by Figure 4.2.1-2, in the case the only cause of the observed physical phenomenon is the medium itself, any physical phenomenon (elastic, electrical, hydraulic, thermal etc...), considered as an observed effect, is more symmetric than the medium itself. In other words and in mathematical language, this means that the symmetry group of the medium is a sub-group of the symmetry group of the physical property.

For instance, media of symmetry belonging to the hexagonal system (including all the different hexagonal symmetry groups) and transversely isotropic media (of symmetry belonging to one of the four Curie's limit groups characterized by an axis of rotational invariance as shown on Figure 4.3.2-4) are associated to the same elasticity symmetry system, namely the transversely isotropic system. Note that this is mainly due to the so called Hermann-German theorem (Hermann [1934]; German [1945]) as explained in Box 4.3.2-1.

The main consequence of Curie's symmetry principle is that the number of the symmetry groups associated with the elastic properties is less than the number of symmetry groups associated with the medium itself.

This is illustrated by Figure 4.3.2-4 which can be considered as a "projection" of Figure 4.2.2-2 on the space of the elastic tensors. More precisely, Figure 4.3.2-4 illustrates how different

symmetry systems from the “crystallographic” point of view of Figure 4.2.2-2 can be associated to the same elasticity symmetry class.

Based on the symmetry of the elasticity tensor the total number of symmetry classes for elasticity can be reduced to eight (e.g., Forte and Vianello [1996]; Chadwick et al. [2001]; Bona et al. [2004]; Helbig [2008]) as illustrated by Figure 4.3.2-4. This figure shows the hierarchical relation between the eight symmetry classes for elasticity.

Each class is represented by a box put in relation with other boxes with solid lines, each line starting from an elastic class of low symmetry and finishing at the next class of higher symmetry. The least symmetric triclinic class is in the bottom of the figure and the most symmetric isotropic in the top of the figure. In each box are displayed the conventional patterns of the stiffness or compliance matrix in Voigt notation as introduced in section 4.3.2.1. The notation conventions are given in the bottom right of Figure 4.3.2-4. All the symmetry groups, introduced in Figure 4.2.2-2 and belonging to a given symmetry class of elasticity are listed in the bottom of the corresponding box. The overall elasticity symmetry of the class is given next to the name of the class. For instance the transversely isotropic symmetry class for elasticity exhibits the overall symmetry ∞/mm , characterized by an axis of rotational invariance, an infinite number of symmetry planes containing the infinite-fold axis), and a symmetry plane normal to this axis (see Figure 4.2.2-1 and the corresponding comments in sub-section 4.2.2.1).

On the bottom right of the compliance/stiffness matrix are given two numbers. The number on the top is the number of coefficients characterizing the corresponding compliance/stiffness matrix according to classical textbooks on crystal acoustics (e.g., Auld [1973]; Dieulesaint and Royer [1974]). Using relevant rotations, the number of non-vanishing coefficient can be reduced to the number between parentheses below the previous number, as described below.

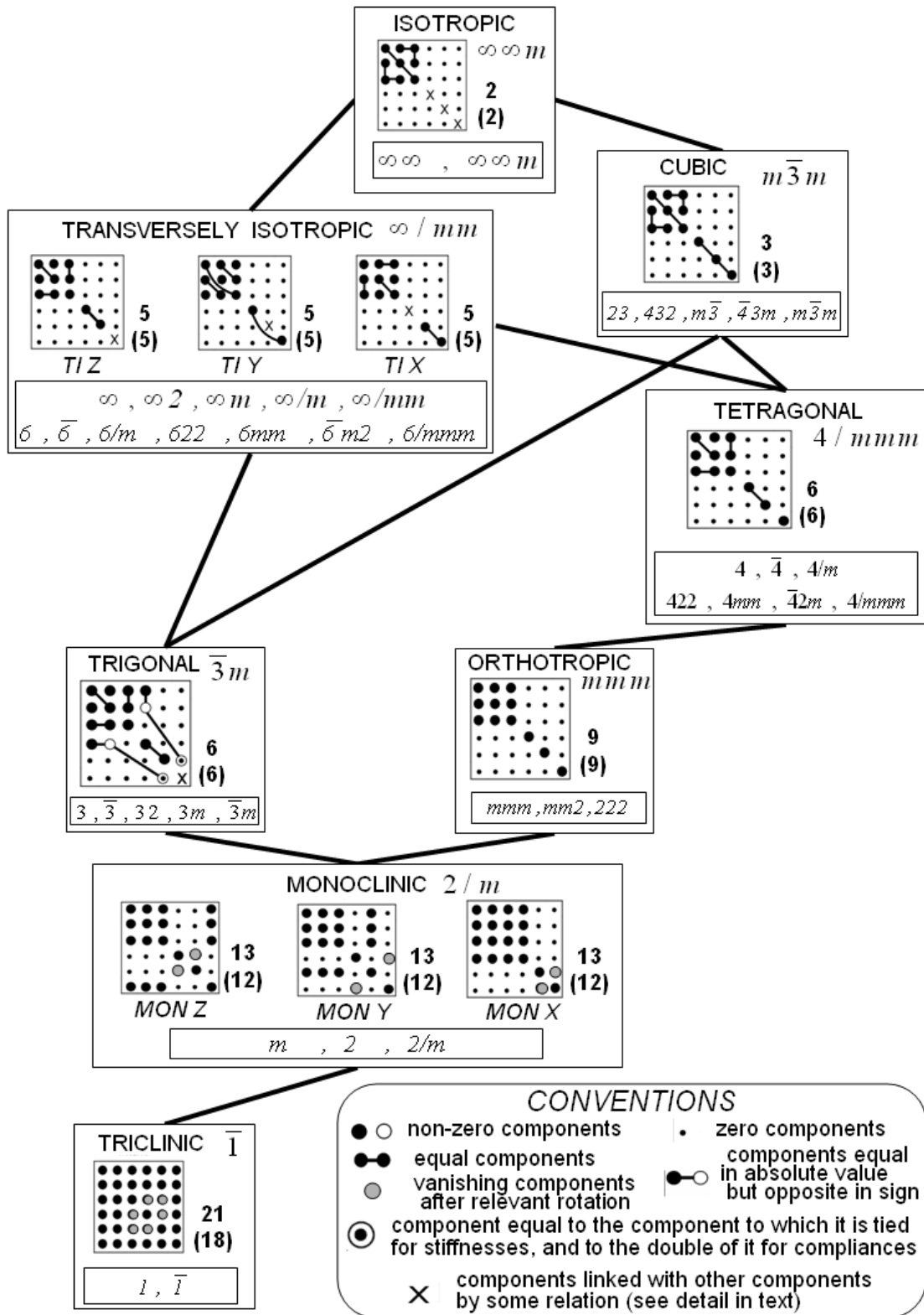


Figure 4.3.2-4: Hierarchical relation between the eight different symmetry classes in elasticity (from the least symmetric triclinic in the bottom of the figure to the most symmetric isotropic in the top of the figure) and the corresponding elasticity matrices.

BOX 4.3.2-1

Hermann-German theorem on symmetry axes and Hermann-Mauguin international notation for crystallographic groups

The Hermann-German theorem in crystal physics states that if a tensor of rank r possesses an axis of symmetry of order p with $p > r$, then this axis is also an axis of rotational invariance for the considered tensor (Hermann, 1934; German, 1945; Sirotine and Chalkoskaya, 1975; Helbig, 1994).

A direct consequence of this theorem is that hexagonal crystals, possessing a symmetry axis of order $p=6$, are rotationally invariant with respect to elastic properties, described by an elasticity tensor of rank $r=4$. Similarly cubic crystals, possessing for instance three axes of symmetry of order $p=4$ mutually perpendicular and each of them normal to a face of the cube, are also rotationally invariant about all these axes, and as a consequence are isotropic (i.e. rotationally invariant about any axis) with respect to any physical property characterized by a tensor of rank r smaller than 3. For instance any cubic crystal is isotropic with respect to optical/dielectric property, magnetic property, thermal or electrical conductivity, all described by tensors of rank $r=2$ (e.g., Nye, 1985).

The theorem, often called German's theorem (e.g., Helbig, 1994) or Herman's theorem (e.g., Andrushchak et al., 2004) and sometimes Hermann-German theorem (e.g., Dmitriev, 2000), was independently derived by the German professor of crystallography Carl Hermann (1898-1961) and the Russian scientist V.L. German (sometimes spelt "Herman", which contributes to the confusion). The former was a doctorate student of the famous German-British physicist and mathematician Max Born (1882-1970) at the university of Göttingen. He invented in 1928 the notation system of the crystallographic groups (used in Figure 4.1.2-2) later modified by the French professor of mineralogy Charles-Vainqueur Mauguin (1878-1958) in 1931. Considering the enormous contributions of these two scientists this notation, later adopted as the international standard notation, is called the Hermann-Mauguin notation (e.g., Haussühl, 1983; Hahn, 1996; Tilley, 2006).

The most general elastic symmetry class is the triclinic class, and characterized by no symmetry element, except possibly a center of symmetry. This elastic symmetry class includes the symmetry groups 1 and $\bar{1}$, and is characterized by 21 stiffness/compliance coefficients. It is always possible to vanish three of these coefficients by taking as one of the coordinate axes a longitudinal direction [Helbig, 1993].

A longitudinal direction is a direction along which three pure mode [that is to say modes polarized exactly parallel to the direction of propagation (longitudinal mode) or perpendicular to the direction of propagation (transverse modes)].

The existence of such directions have been discussed by many authors including Sakadi [1941], Borgnis [1955], Truesdell [1966], and Kolodner [1966], among others. Kolodner [1966] demonstrated that any anisotropic medium has at least three longitudinal directions.

Helbig [1993] proved that there are at the most thirteen longitudinal directions in an arbitrarily anisotropic medium. Furthermore he proposed a simple way to find such a longitudinal direction. It just consists in displaying in two dimensions (θ , λ) the length of the radius vector of the characteristic quartic surface $C_{ijkl}x_i x_j x_k x_l$ in contour plot, where $x_1 = \sin \theta \cos \lambda$; $x_2 = \sin \theta \sin \lambda$; $x_3 = \cos \theta$, the direction of the radius vector being referenced by the colatitude θ and the longitude λ . The longitudinal directions correspond to local extrema of this surface which can straightforwardly be computed and displayed using a modern mathematical software such as *Mathematica*, *Maple* or *Matlab*.

After Helbig [2008] if one of the longitudinal direction is chosen as the Z-axis (respectively as the Y-axis, or as the X-axis) the rotated stiffness coefficients (denoted with a prime accent) C'_{35} and C'_{34} (respectively C'_{24} and C'_{26} , or C'_{15} and C'_{16}) vanish. Furthermore rotating the coordinate system about the new Z-axis (respectively the new Y-axis, or the new X-axis) by $\frac{1}{2} \tan^{-1} \left(\frac{2C'_{45}}{C'_{55} - C'_{44}} \right)$ (respectively $\frac{1}{2} \tan^{-1} \left(\frac{2C'_{46}}{C'_{66} - C'_{44}} \right)$, or $\frac{1}{2} \tan^{-1} \left(\frac{2C'_{56}}{C'_{66} - C'_{55}} \right)$) allows to vanish the new rotated coefficient (denoted with a double prime accent) C''_{45} (respectively C''_{46} , or C''_{56}). It is in this new reference frame that the stiffness matrix of the triclinic class is tabulated in Figure 4.2.2-4 (here the Z-axis is chosen as the longitudinal direction).

Elastic media of the monoclinic class are particular triclinic elastic media exhibiting a symmetry plane. This elastic symmetry class includes the symmetry groups m , 2 and $2/m$. If the symmetry plane of elasticity is normal to the Z-axis (respectively to the Y-axis, or to the X-axis) the symmetry is denoted *MON Z* (respectively *MON Y*, or *MON X*), and any elastic stiffness/compliance coefficient containing an odd number of times the non-contracted index 3 (respectively 2, or 1) must vanish, such as C_{1312} ($=C_{56}$ in contracted indices) for *MON Z* elastic media [respectively C_{1222} ($=C_{26}$ with contracted indices) for *MON Y* elastic media, or

$C_{1311}(=C_{15}$ with contracted indices) for *MON X* elastic media. In total eight elastic coefficients have this property and must vanish, namely C_{14} , C_{15} , C_{24} , C_{25} , C_{34} , C_{35} , C_{46} and C_{56} in *MON Z* elastic media; C_{14} , C_{16} , C_{24} , C_{26} , C_{34} , C_{36} , C_{45} and C_{56} in *MON Y* elastic media; and C_{15} , C_{16} , C_{25} , C_{26} , C_{35} , C_{36} , C_{45} and C_{46} in *MON X* elastic media. In other words elastic media of the monoclinic class are characterized by 13 coefficients. Furthermore, a rotation about the Z-axis (respectively about the Y-axis, or about the X-axis)

in the *MON Z* case (respectively *MON Y* case, or *MON X* case) by $\frac{1}{2} \tan^{-1} \left(\frac{2C_{45}}{C_{55} - C_{44}} \right)$ (respectively $\frac{1}{2} \tan^{-1} \left(\frac{2C_{46}}{C_{66} - C_{44}} \right)$, or $\frac{1}{2} \tan^{-1} \left(\frac{2C_{56}}{C_{66} - C_{55}} \right)$) removes C_{45} (respectively C_{46} , or C_{56}).

In total monoclinic elastic media are characterized by twelve non-vanishing coefficients [Helbig, 2008], instead of thirteen as usually stated in classical textbooks on crystal acoustics (e.g., Auld [1973]; Dieulesaint and Royer [1974]). They can be illustrated for instance by a thinly layered medium containing a single family of parallel fractures neither perpendicular nor parallel to the bedding plane. In this last case the single symmetry plane is the plane perpendicular to the fractures plane and containing the axis of rotational invariance of the unfractured thinly layered medium.

A first special sub-class of the monoclinic symmetry class for elasticity is the orthotropic symmetry class for elasticity and includes all the orthorhombic symmetry groups, namely *mmm*, *mm2* and *222*. This sub-class is characterized by three symmetry planes mutually orthogonal. If the symmetry planes are parallel to the coordinate planes, the stiffness matrix is characterized by nine non-vanishing constants, namely the six diagonal elements C_{11} , C_{22} , ..., C_{66} and the three off-diagonal coefficients C_{12} , C_{13} and C_{23} . It can be illustrated for instance by a thinly layered medium containing a single family of parallel fractures perpendicular to the bedding plane.

A second special sub-class of the monoclinic symmetry class for elasticity (more precisely *MON X*) is the trigonal symmetry class for elasticity, including all the trigonal symmetry groups. This sub-class is characterized by a symmetry plane and a 3-fold symmetry axis. For this sub-class some of the coefficients of *MON X* have particular properties, namely $C_{11} = C_{22}$, $C_{13} = C_{23}$, $C_{44} = C_{55}$, $C_{34} = 0$, $C_{66} = (C_{11} - C_{12})/2$, and $C_{14} = -C_{24} = C_{56}$. In total this sub-class is characterized by 6 independent coefficients. Note that classical textbooks on crystal acoustics (e.g., Auld [1973]; Dieulesaint and Royer [1974]) consider two trigonal symmetry classes for elasticity. The sub-class named “trigonal II” for elasticity, including the symmetry groups 32 , $3m$ and $\bar{3}m$, has the same property as the trigonal symmetry class considered in this work. The sub-class named “trigonal I” for elasticity, including the remaining trigonal symmetry groups, namely 3 and $\bar{3}$, has three additional non-vanishing coefficients linked by the relation $C_{46} = C_{25} = -C_{15}$. However as pointed out

by Helbig [2008], a rotation about the 3-fold axis by $\frac{1}{3} \tan^{-1} \left(-\frac{C_{15}}{C_{14}} \right)$ removes C_{15} , and merges the sub-class “trigonal I” with the sub-class “trigonal II” forming the single sub-class of trigonal symmetry considered here.

A special sub-class of the orthotropic symmetry class for elasticity is the tetragonal symmetry class for elasticity, including all the tetragonal symmetry groups. This sub-class is characterized by five symmetry plane and a 4-fold symmetry axis. For this sub-class some of the coefficients of the orthotropic elasticity matrix have particular properties, namely $C_{11} = C_{22}$, $C_{13} = C_{23}$ and $C_{44} = C_{55}$. In total this sub-class is characterized by 6 independent coefficients. Here again, note that classical textbooks on crystal acoustics (e.g., Auld [1973]; Dieulesaint and Royer [1974]) consider two tetragonal symmetry classes for elasticity. The sub-class named “tetragonal II” for elasticity, including the symmetry groups $\bar{4}2m$, 422 , $4mm$ and $4/mmm$. has the same property as the tetragonal symmetry class for elasticity considered in this work. The sub-class named “tetragonal I” for elasticity, including the remaining tetragonal symmetry groups, namely 4 , $\bar{4}$, and $4/m$., has two additional non-vanishing coefficients linked by the relation $C_{16} = -C_{15}$. However as pointed out by Helbig [2008], a rotation about the 4-fold axis by $\frac{1}{4} \tan^{-1} \left(\frac{4C_{16}}{C_{11} - C_{12} - 2C_{66}} \right)$ removes C_{16} , and merges the sub-class “tetragonal I” with the sub-class “tetragonal II” forming the single sub-class of tetragonal symmetry considered here.

The transversely isotropic (TI) symmetry class for elasticity is characterized by an infinite-fold symmetry axis, that is to say an axis of rotational invariance, an infinite number of symmetry planes (each plane containing the symmetry axis) and the symmetry plane perpendicular to the symmetry axis. It can be illustrated for instance by a thinly layered elastic medium with randomly distributed constituents. This class includes all the seven hexagonal symmetry groups and the five rotationally-invariant limit groups of Curie, namely ∞ , $\infty 2$, ∞m , ∞/m and ∞/mmm . (see Figure 4.2.2-2 and the corresponding comments).

It can be considered as a sub-class of elastic symmetry either of the trigonal symmetry class, or of the tetragonal symmetry class (and, as a consequence, of the orthotropic symmetry class). It is characterized by five independent coefficients, namely $C_{11} = C_{22}$, C_{12} , $C_{13} = C_{23}$, C_{33} and $C_{44} = C_{55}$ if the symmetry axis is aligned with the Z-axis (the symmetry is called *TI Z*), $C_{11} = C_{33}$, C_{13} , $C_{12} = C_{23}$, C_{22} and $C_{44} = C_{66}$ if the symmetry axis is aligned with the Y-axis (the symmetry is called *TI Y*), and $C_{22} = C_{33}$, C_{23} , $C_{12} = C_{13}$, C_{11} and $C_{55} = C_{66}$ if the symmetry axis is aligned with the X-axis (the symmetry is called *TI X*). The last non-vanishing coefficient is linked to the previous coefficients by the relation $C_{66} = (C_{11} - C_{12})/2$ (respectively $C_{55} = (C_{22} - C_{13})/2$, or $C_{44} = (C_{33} - C_{23})/2$) in *TI Z* media (respectively in *TI Y* media, or in *TI X* media).

The cubic symmetry class for elasticity can be considered as a sub-class of the tetragonal symmetry class, or of the trigonal symmetry class for elasticity. It has all the symmetry elements of a cube, namely four 3-fold axes, three 4-fold axes and six 2-fold axes. It includes all the five cubic symmetry groups and is characterized by three independent coefficients, namely $C_{11} = C_{22} = C_{33}$, $C_{12} = C_{13} = C_{23}$, and $C_{44} = C_{55} = C_{66}$.

The isotropic symmetry class for elasticity can be considered as a sub-class either of the transversely isotropic or of the cubic symmetry classes for elasticity. For any medium of this sub-class any plane is a symmetry plane, and any axis is an axis of rotational invariance. It can be illustrated for instance by an elastic medium with randomly oriented and distributed constituents. It is characterized by two independent coefficients, namely $C_{11} = C_{22} = C_{33}$ and $C_{12} = C_{13} = C_{23}$. The three last non-vanishing coefficients are linked to the previous coefficients by the relations $C_{44} = C_{55} = C_{66} = (C_{11} - C_{12})/2$. Note that these stiffness coefficients are linked to the classical constants introduced in Chapter 1 (§ 1.2.1.3) by the relations $C_{11} = C_{22} = C_{33} = \lambda + 2\mu = K + 4\mu/3$, $C_{12} = C_{13} = C_{23} = \lambda = K - 2\mu/3$, and $C_{44} = C_{55} = C_{66} = \mu$, where λ is the first Lamé parameter, μ is the shear modulus or second Lamé parameter, and K the bulk modulus.

Finally, after subsection 4.2.2.2 the only symmetry classes relevant for geological media are isotropic, transversely isotropic, orthotropic, monoclinic and triclinic. Thus after Figure 4.3.2-4, with respect to elastic properties geological media can be either be considered as:

- an isotropic elastic medium exhibiting the symmetry $\infty\infty m$ (any axis is an axis of rotational invariance and any plane is a symmetry plane), or
- a transversely isotropic elastic medium exhibiting the overall symmetry $\infty/m m$, characterized by an axis of rotational invariance, an infinite number of symmetry planes containing the infinite-fold axis), and a symmetry plane normal to this axis (see Figure 4.2.2-1 and the corresponding comments in sub-section 4.2.2.1), or
- an orthotropic (orthorhombic) elastic medium exhibiting the overall symmetry $m m m$, characterized by 3 symmetry planes mutually perpendicular and, as a consequence, three 2-fold axes, each of them normal to one of the three symmetry planes, or
- a monoclinic elastic medium exhibiting the overall symmetry $2/m$, characterized by a symmetry plane and a 2-fold axis normal to this plane, or
- a triclinic elastic medium exhibiting the overall symmetry $\bar{1}$, characterized by a center of symmetry.

4.3.3 Anisotropic elastodynamics and Kelvin-Christoffel equations

Cauchy's equations of motion, in terms of the components of the displacement vector, for a continuum body with no body forces acting on it, can be written as:

$$(4.3.3-1) \quad \frac{\partial \sigma_{ij}}{\partial x_j} = \rho \frac{\partial^2 u_i}{\partial t^2}$$

where Einstein's summation convention on the repeated indices is assumed. The medium of propagation being assumed homogeneous, linearly elastic and anisotropic, the stress σ , the strain ε and the particle displacement \mathbf{U} induced by the wave are related by the anisotropic Hooke's law (e.g., Auld [1973]; Helbig [1994]):

$$(4.3.3-2) \quad \sigma_{ij} = C_{ijkl} \varepsilon_{kl} = C_{ijkl} \frac{\partial u_l}{\partial x_k}$$

where σ_{ij} , ε_{kl} , C_{ijkl} and u_l are the components of the stress, the strain, the stiffness tensor and the particle displacement, respectively. Due to the internal symmetry of the stress tensor and of the strain tensor and to the fact that the tensor C derives from a potential (in fact the elastic deformation potential) the components of C have the following index symmetry:

$$(4.3.3-3) \quad C_{ijkl} = C_{ijikl} = C_{ijlk} = C_{klij}$$

The behavior law (4.3.3-2) reported in the general equation of motion leads to the general elastodynamic equation:

$$(4.3.3-4) \quad \rho \frac{\partial^2 u_i}{\partial t^2} = \frac{\partial}{\partial x_j} \left(C_{ijkl} \frac{\partial u_l}{\partial x_k} \right)$$

Now, let us consider a harmonic plane wave propagating in a homogeneous linearly elastic medium of arbitrary anisotropy type (triclinic) and the associated particle displacement \mathbf{U} defined by:

$$(4.3.3-5) \quad \mathbf{U}(\omega, t) = \mathbf{U}_0 \exp[j(\omega t - \mathbf{K} \cdot \mathbf{r})]$$

where \mathbf{U}_0 designates the polarization vector, t the time, ω the angular frequency, \mathbf{r} the position vector, and \mathbf{K} the wave vector with:

$$(4.3.3-6) \quad \mathbf{K} = K \mathbf{n}$$

where \mathbf{n} is the unit real vector in the direction of propagation and K is the wavenumber.

The substitution of Eqs. (4.3.3-5) and (4.3.3-6) into the elastodynamic equation (4.3.3-4), and using Eq (4.3.3-2), leads to the Kelvin-Christoffel equation (Christoffel [1877]; Kelvin [1878]):

$$(4.3.3-7) \quad \left(\Gamma_{il} - \rho V^2 \delta_{il} \right) U_{0l} = 0$$

where $\Gamma_{il} = C_{ijkl} n_j n_k$ and U_{0l} are the components of the Kelvin-Christoffel tensor and of the polarization vector, δ_{il} the Kronecker tensor, and V the phase velocity. The quantities n_j are the

components the vector \mathbf{n} in the direction of propagation.

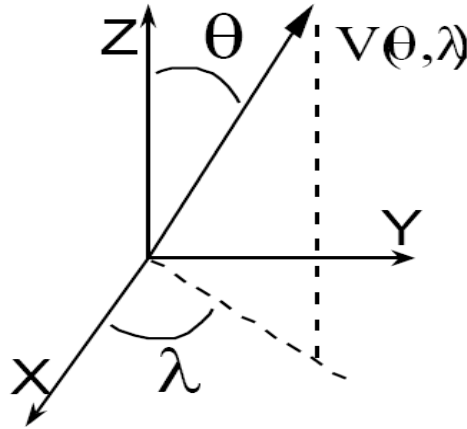


Figure 4.3.3-1: Coordinate system XYZ. The direction of the qP wave phase velocity $V(\theta, \lambda)$ is specified by the colatitude θ and the azimuth λ of the vector \mathbf{n} in the direction of propagation.

As illustrated by Fig. 4.3.3-1, this direction is defined by two angles, namely the colatitude θ and the longitude λ linked by the components of \mathbf{n} in the reference frame XYZ by the relations:

$$(4.3.3-8) \quad n_1 = S_\theta C_\lambda \quad ; \quad n_2 = S_\theta S_\lambda \quad ; \quad n_3 = C_\theta$$

where for reason of conciseness we use the notations $S_\theta = \sin \theta$, $C_\theta = \cos \theta$, $S_\lambda = \sin \lambda$, and $C_\lambda = \cos \lambda$.

The phase velocity V , the wave modulus M , the phase slowness S and the wavenumber K are linked by the classical relations (e.g., Bourbié et al. [1987]):

$$(4.3.3-9) \quad M = \rho(V)^2 = \rho(1/S)^2 = \rho \left(\frac{\omega}{K} \right)^2$$

The equation (4.3.3-7) is an eigenvalue/eigenvector equation, of which the eigenvalue solutions are the elastic wave moduli and the eigenvectors the corresponding wave polarizations. Due to symmetry of the C_{ijkl} with respect to the indice permutations $C_{ijkl} = C_{jikl} = C_{ijlk} = C_{klij}$ (see detail in Chapter 1§1.2.1-), Kelvin-Christoffel tensor Γ is symmetric (i.e., $\Gamma_{il} = \Gamma_{li}$). As a real-valued symmetric tensor of rank 2 in 3D, Γ has three real eigenvalues with three corresponding eigenspaces mutually orthogonal. In other words, three waves can propagate in a given propagation direction \mathbf{n} , with their polarization vector mutually perpendicular.

The resolution of Equation (4.3.3-7) imposes the cancellation of the determinant:

$$(4.3.3-10) \quad \det(\Gamma_{il} - M \delta_{il}) = 0$$

which simplifies in the following way (e.g., Cervený [2001]):

$$(4.3.3-11) \quad (M)^3 - Tr(\Gamma) \times (M)^2 + Tr[Com(\Gamma)] \times M - \det(\Gamma) = 0$$

where:

$$(4.3.3-12) \quad Tr(\Gamma) = \Gamma_{11} + \Gamma_{22} + \Gamma_{33}$$

designates the trace of the Christoffel matrix ,

$$(4.3.3-13) \quad Tr[Com(\Gamma)] = \Gamma_{11}\Gamma_{22} + \Gamma_{22}\Gamma_{33} + \Gamma_{33}\Gamma_{11} - \left[(\Gamma_{12})^2 + (\Gamma_{23})^2 + (\Gamma_{13})^2 \right]$$

the trace of the matrix $Com(\Gamma)$ of the cofactors of the matrix Γ , and

$$(4.3.3-14) \quad \det(\Gamma) = \Gamma_{11}\Gamma_{22}\Gamma_{33} - \Gamma_{11}(\Gamma_{23})^2 - \Gamma_{22}(\Gamma_{13})^2 - \Gamma_{33}(\Gamma_{12})^2 + 2\Gamma_{12}\Gamma_{23}\Gamma_{13}$$

the determinant of the matrix Γ . The explicit expressions of the components of the complex Christoffel matrix are the followings:

$$(4.3.3-15) \quad \left\{ \begin{array}{l} \Gamma_{11} = C_{11}n_1^2 + C_{66}n_2^2 + C_{55}n_3^2 + 2C_{56}n_2n_3 + 2C_{15}n_1n_3 + 2C_{16}n_1n_2 \\ \Gamma_{22} = C_{66}n_1^2 + C_{22}n_2^2 + C_{44}n_3^2 + 2C_{24}n_2n_3 + 2C_{46}n_1n_3 + 2C_{26}n_1n_2 \\ \Gamma_{33} = C_{55}n_1^2 + C_{44}n_2^2 + C_{33}n_3^2 + 2C_{34}n_2n_3 + 2C_{35}n_1n_3 + 2C_{45}n_1n_2 \\ \Gamma_{12} = C_{16}n_1^2 + C_{26}n_2^2 + C_{45}n_3^2 + (C_{25} + C_{46})n_2n_3 + (C_{14} + C_{56})n_1n_3 + (C_{12} + C_{66})n_1n_2 \\ \Gamma_{13} = C_{15}n_1^2 + C_{46}n_2^2 + C_{35}n_3^2 + (C_{36} + C_{45})n_2n_3 + (C_{13} + C_{55})n_1n_3 + (C_{14} + C_{56})n_1n_2 \\ \Gamma_{23} = C_{56}n_1^2 + C_{24}n_2^2 + C_{34}n_3^2 + (C_{23} + C_{44})n_2n_3 + (C_{36} + C_{45})n_1n_3 + (C_{25} + C_{46})n_1n_2 \end{array} \right.$$

Here, due to the indice symmetries summarized by Eqs. (4.3.3-3), we use in all the following the two indices contracted notations of Voigt for the components of stiffness tensor C and of the compliance tensor S of rank 4, instead of the classical 4 indices notation. The correspondence between the two notations is defined by [Helbig, 1994]:

$$(4.3.3-16) \quad C_{pq} = C_{ijkl} \quad \text{and}$$

$$(4.3.3-17) \quad S_{pq} = (2 - \delta_{ij})(2 - \delta_{kl}) S_{ijkl}$$

$$\text{with} \quad p = \delta_{ij} i + (1 - \delta_{ij})(9 - i - j) \quad \text{and} \quad q = \delta_{kl} k + (1 - \delta_{kl})(9 - k - l)$$

The indices i, j, k and l can take the values 1,2 or 3 and the contracted indices p and q the values 1, 2, 3,...,6. The stiffness tensor and the compliance tensor can be represented by the symmetric matrices C_{pq} and S_{pq} of rank 6, commonly called the stiffness matrix and the compliance matrix respectively.

Note that in the most general type of symmetry (triclinic) the complete set of stiffness coefficients is composed of 21 independent coefficients, whereas in the simplest case (isotropic) only 2 elastic constants are necessary (eg., Helbig [1994]).

The Christoffel matrix Γ , introduced in Eq. (4.3.3-7) being a real symmetric matrix, all its eigenvalues (i.e., the wave moduli) are real and its eigenvectors (i.e., the associated wave polarizations) are mutually orthogonal for a given propagation direction. Thus the cubic equation (4.3.3-11) has three real solutions, known after the great mathematicians of the Italian Renaissance, namely Scipione del Ferro, Niccolò Fontana Tartaglia and Gerolamo Cardano (e.g., Guilbaud [1930]). From the theory of the algebraic equations (e.g., Press et al. [1986]) the explicit expressions of the del Ferro-Tartaglia-Cardano solutions of Eq. (4.3.3-11) are:

$$(4.3.3-18) \quad M_I = \frac{1}{3} Tr(\Gamma) + 2\sqrt[3]{R} \cos\left(\frac{\Phi}{3} + (I-1)\frac{2\pi}{3}\right) \quad \text{with } I = 1, 2, 3$$

where:

$$(4.3.3-19) \quad R = \left\{ \frac{1}{3} \left[\frac{1}{3} (Tr(\Gamma))^2 - Tr[com(\Gamma)] \right] \right\}^{3/2} \quad \text{and}$$

$$(4.3.3-20) \quad \cos\Phi = \frac{\frac{2}{27} [Tr(\Gamma)]^3 - \frac{1}{3} [Tr(\Gamma)] \times Tr[com(\Gamma)] + \det(\Gamma)}{2R}$$

These solutions correspond to the explicit expressions of the phase moduli of the three plane bulk waves propagating in an homogeneous linearly elastic, and arbitrarily anisotropic medium.

Of these three solutions, in most cases one is always larger than the remaining solutions in any propagation direction. This largest solution corresponds to a wave nearly, but not exactly, polarized along the direction of propagation (e.g., Helbig [1994]). It is commonly called the quasi-longitudinal wave, or the quasi P-wave or even simply the qP-wave. The polarization vectors of the two remaining waves being perpendicular to the qP-wave polarization vector, are thus nearly, but not exactly, perpendicular to the propagation vector. The waves are commonly called the quasi-transversal waves, or the quasi S-waves or even simply the qS-waves. The slowest qS-wave is called the qS2-wave and the fastest qS-wave the qS1-wave.

Figure 4.2.3-2 illustrate the complete directional dependence of the phase velocities of the three bulk waves propagating in a sample of water-saturated Vosges sandstone ($\rho = 2310 \text{ kg/m}^3$), characterized by the stiffness matrix measured by Arts et al [1992] and Arts [1993]:

$$(4.3.3-21) \quad C = \begin{pmatrix} 27.6 & 13.0 & 12.5 & 0.9 & -0.1 & 0.4 \\ . & 25.2 & 13.3 & 0.8 & 0.2 & -0.5 \\ . & . & 29.7 & -0.4 & 0.3 & -0.4 \\ . & . & . & 7.4 & -0.1 & 0.2 \\ . & . & . & . & 8.2 & 0.1 \\ . & . & . & . & . & 7.0 \end{pmatrix} \text{GPa}$$

First of all one can clearly notice, as previously mentioned, the lack of symmetry element of the plots which confirms the triclinic symmetry of the sandstone sample. The qP-wave phase velocity varies from 3.38 km/s to 3.74 km/s, which roughly corresponds to 10% anisotropy. The qS1-wave phase velocity is always larger than 1.78 km/s and reaches a maximum of roughly to 2.00 km/s, representing a relative variation of more than 12%. And the qS2-wave phase velocity is comprised between 1.72 km/s and 1.92 km/s, corresponding to an anisotropy larger than 11%. In other words this rock sample exhibits moderate, but not weak, strength of velocity anisotropy.

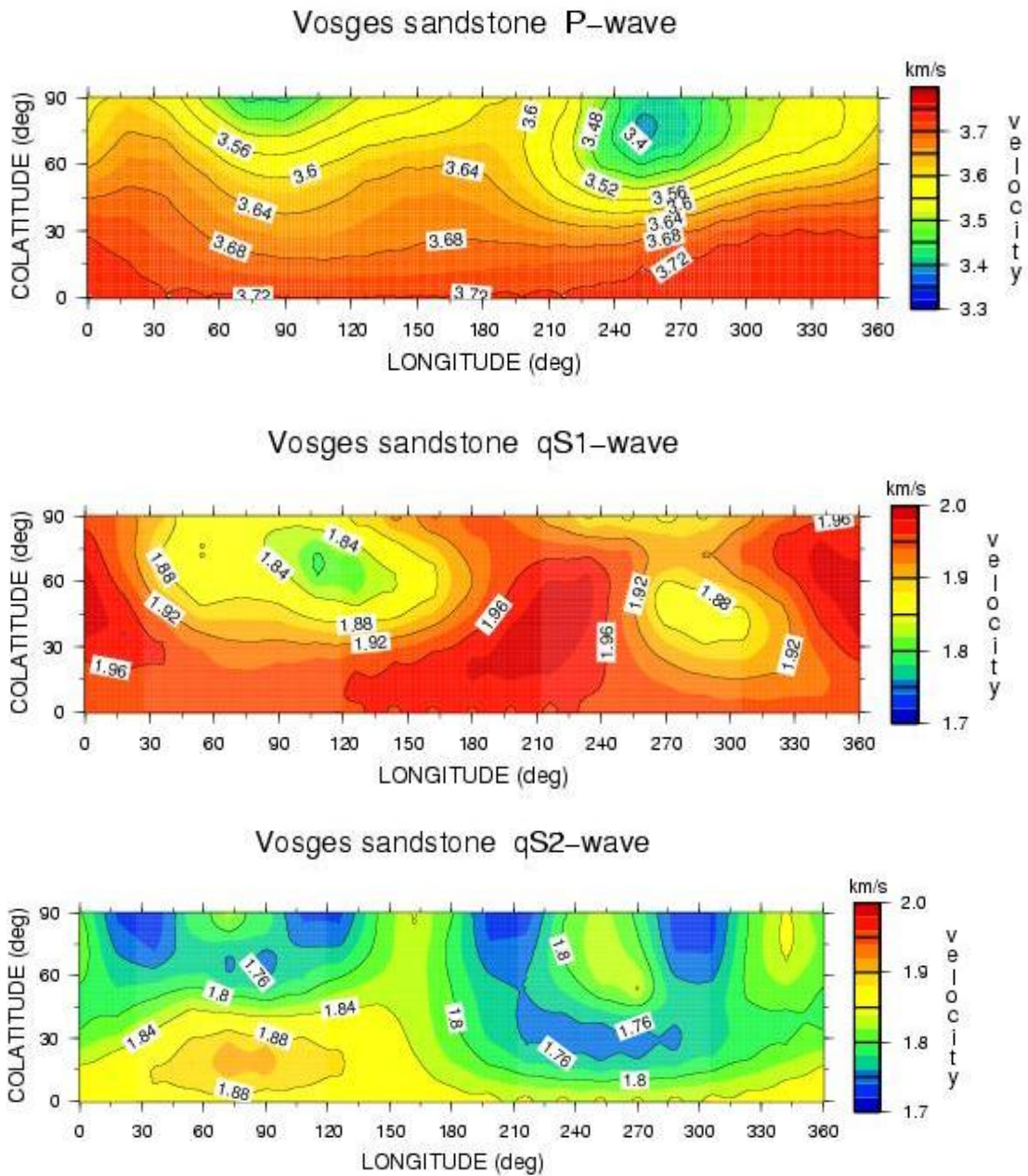


Fig.4.3.3-2: Complete directional dependence of the exact phase velocity in km/s of (top) the qP-wave, (middle) the qS1-wave and (bottom) the qS2-wave in Vosges Sandstone considered as an arbitrarily anisotropic elastic medium.

4.4 The main symptoms of seismic anisotropy

Seismic anisotropy has many expressions in the seismic data. Here we shall describe three of the main, but by no means the only, manifestations of the presence of elastic anisotropy, namely the directional dependence of the wave velocities, the shear wave birefringence (or shear-wave splitting), and the non-orthogonality of the energy velocity vector and the wavefront.

4.4.1 The directional dependence of the elastic velocities

In Chapter 1 §1.2.3.2 we defined *anisotropy*, with respect to a given physical property (e.g., elastic or electromagnetic wave velocity, electric or thermal conductivity, mechanical strength...), as the dependence of this property on the direction of observation. Thus the directional dependence of the elastic velocities can be considered, by definition, as the first manifestation of elastic anisotropy.

In the previous sub-section Figure 4.2.3-2 illustrates the complete directional dependence of phase velocity of the three bulk waves (i.e., the qP-wave, the qS1-wave and the qS2-wave) in Vosges Sandstone. Another example is illustrated by Figure 4.4.1-1, showing experimental results of Rasolofosaon and Zinszner [2002] on a sandstone reservoir rock from the North Sea. It allows to compare elastic anisotropy (here P-wave velocity) and hydraulic anisotropy (here diffusion surface from a point source). In this case elastic anisotropy and hydraulic anisotropy are closely correlated, for instance in terms of the symmetry directions, because they share the same cause, here the layering of the rock fractures). As pointed out in the last reference this is not a rule. In some other rocks, hydraulic properties and elastic properties are clearly uncorrelated.

Such directional dependence of the elastic velocities have been observed at various scales, from the global earth scale (e.g., Babuska and Cara [1991]), to the laboratory (e.g., Arts [1993]; Arts et al. [1991a] and [1991b]), passing through exploration seismic scale (e.g., Thomsen [2002]).

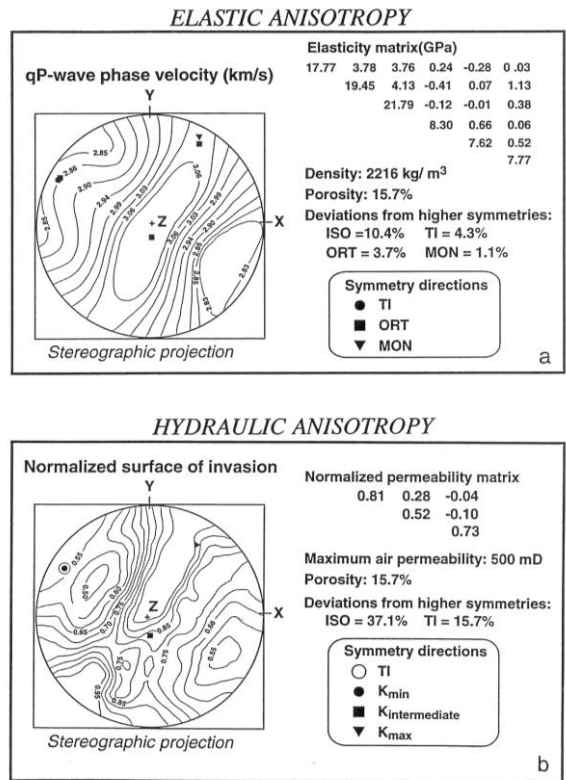


Fig.4.4.1-1: Comparison between elastic anisotropy and hydraulic anisotropy in a North Sea sandstone reservoir rock (modified after Rasolofosaon and Zinszner [2002]):

(a) elastic anisotropy: Left: stereographic projection of the qP-wave phase velocity surface (the unit of the isolines is km/s) Right (from top to bottom): matrix of elasticity (top half only); density; porosity; magnitude of the deviations from isotropy (ISO), transverse isotropy (TI), orthorhombic symmetry (ORT), and monoclinic symmetry (MON) as defined by Arts et al. [1991b], and

(b) hydraulic anisotropy: Left: stereographic projection of the normalized surface of hydraulic invasion (the isovalues are dimensionless). Right (from top to bottom): normalized matrix of permeability (top half only), maximum permeability, porosity, magnitude of the deviations from isotropy (ISO) and from transverse isotropy (TI), and captions for different particular directions plotted the direction of minimum permeability (solid circle), the direction of intermediate permeability (solid square), and the direction of the maximum permeability.

4.4.2 The shear wave birefringence or shear-wave splitting

Shear wave-birefringence or shear-wave splitting is the fact that a shear wave coming from an isotropic medium and entering an anisotropic elastic medium is splitted into two shear waves with different velocities and crossed polarizations, as illustrated by Figure 4.4.2-1 for the case of a fractured medium.

In the previous sub-section Figure 4.2.3-2 illustrates the complete directional dependence of of the two shear waves (i.e., the qS1-wave and the qS2-wave) in a sample of Vosges Sandstone.

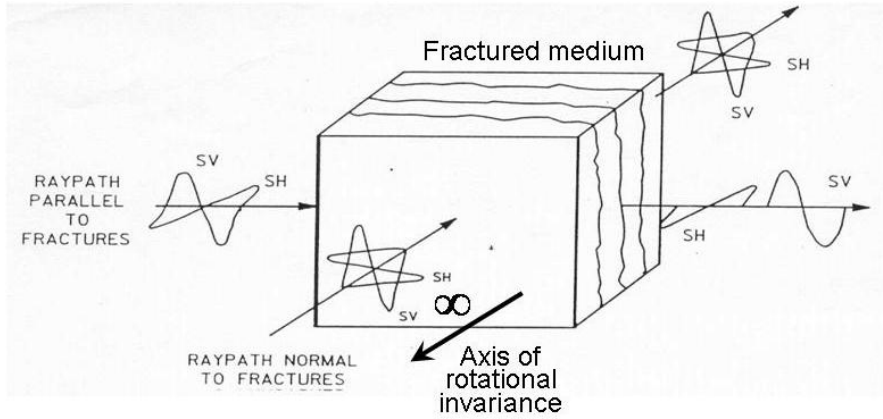


Fig.4.4.2-1: Shear wave birefringence or Shear wave splitting in an elastic medium with a single set of parallel vertical fractures, with an axis of rotational invariance normal to the fracture plane. A shear wave propagating along the fracture plane is splitted between two waves, namely the fastest shear wave (SV) which is polarized roughly in the plane perpendicular to the symmetry axis (eg., along the fracture strike), and the slowest shear wave (SH) which is roughly polarized along the symmetry direction (e.g., in the direction perpendicular to the fracture planes). Note that no shear-wave birefringence is observed for propagation along the symmetry axis (modified after Tatham McCormack [1991]).

The shear-wave birefringence is a phenomenon analogous to what is observed in crystal optics with the optical birefringence or double refraction (e.g., Born and Wolf [1999]). This is illustrated by Figure 4.4.2-2 in a monocrystalline sample of calcite.

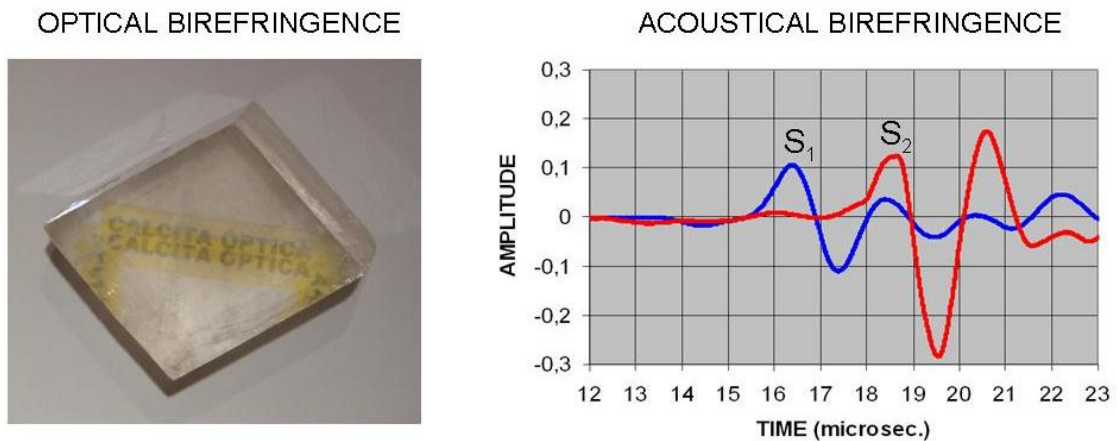


Fig.4.4.2-2: Optical birefringence (figure on the left side) and Acoustical birefringence (figure on the right side) observed in the same monocrystalline sample of calcite.

On the photograph on the left hand side, when you look through a calcite crystal sample, it splits the light rays in two, producing a double image of the message written (namely “calcita optica”, that is to say “optical calcite” in Spanish) on a piece of paper on which is laid the crystal sample.

On the figure on the right hand side shear-wave splitting has been measured using the technique, described in Chapter 2 §2.2.4 of, through the same monocrystalline sample of calcite with ultrasonic transducers of approximately 500kHz central frequency. The two splitted shear waves, namely the fast shear wave S1 in blue and the slow shear wave S2 in red are clearly visible.

Similar results in two rock samples are reported on Figure 4.2.2-3, in a strongly anisotropic marble sample and a moderately anisotropic sandstone sample. .

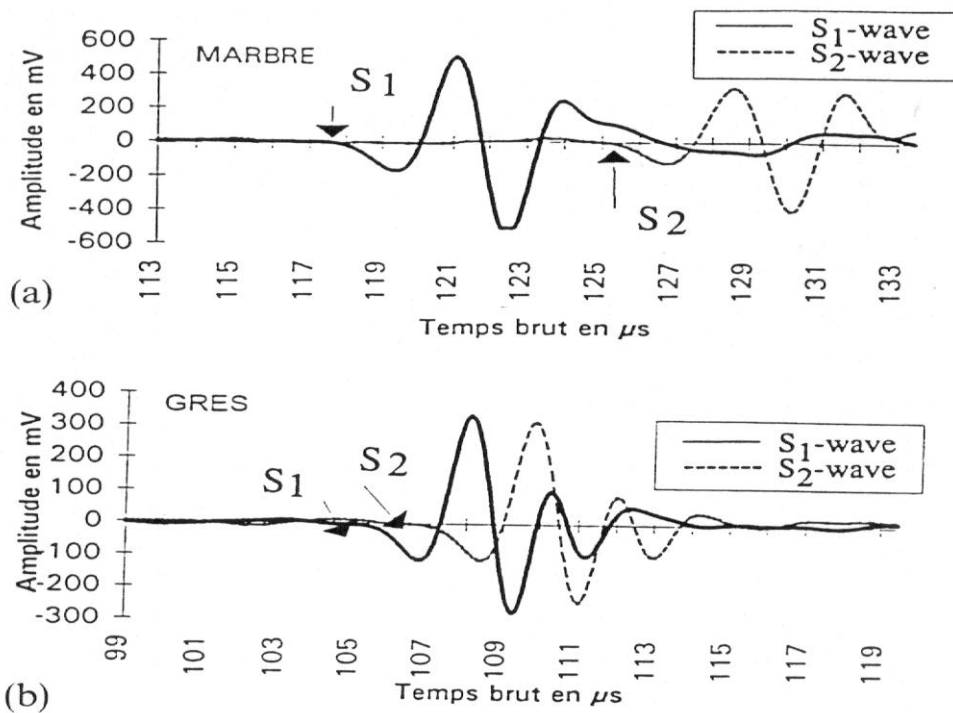


Fig.4.4.2-3: Shear birefringence measurements on two rock samples (a) a marble sample and (b) a sandstone sample.

Shear-wave birefringence has been observed at various scales, from the global earth scale (e.g., Savage [1999] and [2006]), to the laboratory (e.g., Nur and Simmons [1969]; Zamora and Poirier [1990]; Arts et al. [1991a]; Arts [1993]), passing through exploration seismic scale (e.g., Crampin [1987]; Crampin and Peacock [2005]; Thomsen [2002]), mainly in relation with the stress field and the presence of aligned fracture/cracks in the last case as detailed in sub-section 4.8.2 and in Chapter 8 on the Applications to seismic interpretation.

4.4.3 The ray velocity is not perpendicular to the wavefront

The last manifestation of elastic anisotropy that will be described here is probably the less obvious, but also one of the most important with respect to its practical implications in seismic data processing. The non-orthogonality of the energy velocity vector and the wavefront is illustrated by Figure 4.4.3-1

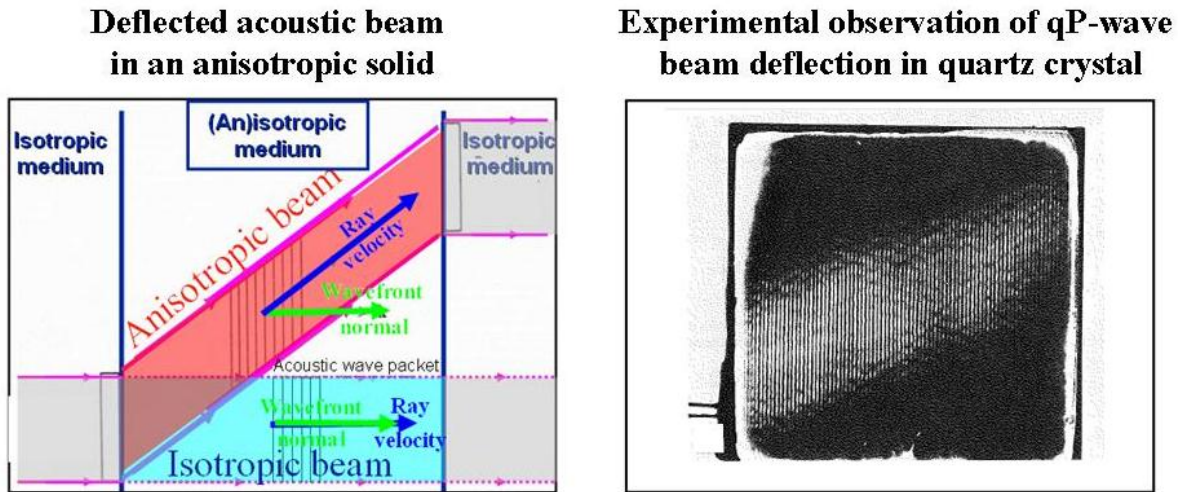


Fig.4.4.3-1: Deflection of an acoustic beam crossing an anisotropic medium: (left figure) sketch of experiment and of the physical phenomenon, and (right figure) experimental visualization of a qP-wave deflected beam using Schlieren imaging. Elastic wavefronts are normal to the Y-axis of quartz crystal (modified after Staudte and Cook [1967] and Auld [1973]).

The left part of the figure considers an acoustical beam (in grey) normally incident, crossing a plate of constant thickness made either of isotropic material or of anisotropic material, then normally outgoing (beams in grey on the right part) in an isotropic material. If the plate is made of an isotropic elastic material, the transmitted “isotropic beam” (in blue) is not deviated from the incident beam. The wavefront is parallel to the plate surface, and the ray velocity vector is equal to the phase velocity vector and is normal to the wavefront. In contrast, if the plate is anisotropic, the transmitted “anisotropic beam” (in red) is deviated and makes an angle with the incident beam. The wavefronts are still parallel to the plate surface (normal incidence in terms of the wave normal direction) but the ray velocity vector deviates from the normal to the wavefront. This is due to the fact that the energy velocity vector and the phase velocity vector are generally not collinear in anisotropic media. Using an experimental set-up similar to the one sketched on the left side, the right part of the figure shows an experimental observation of a deflected qP-wave beam in anisotropic quartz crystal using Schlieren imaging (e.g., Settles [2001]; Surhone et al. [2010]).

Assuming isotropy and not taking into account such anisotropic effects can lead to errors in different steps of seismic processing of field data such as velocity analysis, NMO, dip

moveout (DMO), time migration, time-to-depth conversion, and amplitude versus offset (AVO) analysis as discussed in many textbooks (e.g., Tsvankin [2001]; Thomsen [2002]; Grechka [2009]).

Regarding laboratory data, in sub-section 2.3.2.3 of Chapter 2 we report the physical modelling results of Martin et al. [1992] who analyzed the effect of anisotropy on wave propagation and on imaging using laser ultrasonic techniques. Using an “isotropic imaging” algorithm in a model made of strongly anisotropic slate with a tilted symmetry axis (transversely isotropic with non-vertical axis), strongly affects the reflector to be reconstructed (see Figure 2.3.2-15). In contrast, by using a simplified “anisotropic” migration algorithm, a nearly correct image of the structure is surprisingly recovered, and some cleavage planes in the slate can even be imaged as illustrated by Figure 2.3.2-17. Similar results have been reported with more conventional physical modelling techniques by Isaac and Lawton (1999) with a model made of transversely isotropic (TI) phenolic material.

4.5 Simplification of the formalism

The anisotropy type commonly encountered in the geological formation of the sedimentary basins is transverse isotropy (TI) often with a vertical infinite-fold axis of symmetry. However, this is not always the case. For instance, the bedding planes can sometimes substantially dip, in other cases the presence of one or a multiple set of fractures, or the possible causes of anisotropy do not necessarily share the same symmetry directions. All these causes imply that the medium can apparently exhibit a more complicate symmetry type, even the most complicate type (triclinic), in the coordinate system of acquisition of the seismic data. In such cases the development of the general equations for seismic wave propagation is quite complex (e.g., Helbig [1994]).

However if one assumes moderate anisotropy strength, as is practically always the case in most rocks, this greatly simplifies the theoretical derivations (e.g., Mensch and Rasolofosaon [1997]). Simple analytic expressions for the main kinematic and dynamic quantities of interest for seismic processing can be obtained. This is detailed in the two next sections.

4.5.1 Weak anisotropy approximation and Thomsen type parametrization in TI media

In the case of transverse isotropy (TI) with a vertical infinite-fold axis of symmetry, for a given direction of propagation the Christoffel matrix introduced in Eq. (4.3.3-7) simply writes:

$$(4.5.1-1) \quad \Gamma = \begin{pmatrix} C_{11} n_1^2 + C_{66} n_2^2 + C_{44} n_3^2 & C_{12} n_1 n_2 & C_{13} n_1 n_3 \\ C_{12} n_1 n_2 & C_{66} n_1^2 + C_{22} n_2^2 + C_{44} n_3^2 & C_{23} n_2 n_3 \\ C_{13} n_1 n_3 & C_{23} n_2 n_3 & C_{44} (n_1^2 + n_2^2) + C_{33} n_3^2 \end{pmatrix}$$

Using the relations (4.3.3-8) between the colatitude θ , the longitude λ and the components of propagation direction \mathbf{n} , the eigenvalues of G have the well-known expressions (e.g., Auld [1974], Helbig [1994]):

$$(4.5.1-2) \quad \begin{cases} 2M_{qP} = C_{44} + C_{11}S_{\theta}^2 + C_{44}C_{\theta}^2 + \sqrt{[(C_{11} - C_{44})S_{\theta}^2 - (C_{33} - C_{44})C_{\theta}^2]^2 + 4(C_{13} + C_{44})^2 S_{\theta}^2 C_{\theta}^2} \\ 2M_{qSV} = C_{44} + C_{11}S_{\theta}^2 + C_{44}C_{\theta}^2 - \sqrt{[(C_{11} - C_{44})S_{\theta}^2 - (C_{33} - C_{44})C_{\theta}^2]^2 + 4(C_{13} + C_{44})^2 S_{\theta}^2 C_{\theta}^2} \\ M_{SH} = C_{66}S_{\theta}^2 + C_{44}C_{\theta}^2 \end{cases}$$

where M_{qP} , M_{qSV} and M_{qSH} designate the wave moduli of the qP , the qSV and the SH - wave. The infinite-fold axis of symmetry Z being vertical, the qSV -wave is the qS -wave polarized in the vertical plane defined by the Z -axis and the propagation direction \mathbf{n} . The qSH -wave is the horizontally polarized qS -wave.

In the case of weakly anisotropic transversely isotropic (VTI) medium with a vertical symmetry axis, Thomsen [1986a)] derived the simplified form for Eq (4.5.1-2). The phase velocities of the three bulk waves are obviously independent of the azimuth λ , due to transverse isotropy, and have the same simplified form:

$$(4.5.1-3) \quad \left[\frac{V(\theta)}{V_{vertical}} \right]^2 \approx 1 + 2e S_{\theta}^2 + 2a S_{\theta}^4$$

In moderately anisotropic media, to the first order, this equation also holds for the group-, ray- or energy velocity provided that the colatitude θ and the azimuth λ refers no longer to the direction of the wave normal but to the ray direction [Backus, 1967].

Eq. (4.5.1-3) has a simple physical interpretation illustrated by Fig. (4.5.1-1). Let us assume a point source radiating in a VTI medium of infinite extension. If the constants e and a vanish the velocity have no directional dependence, the wavefront is spherical (blue curve on the figure), and the medium is isotropic. If the $e \neq 0$ but $a = 0$ the wavefront is elliptical (red curve on the figure), and the medium is said to be elliptical (e.g. Helbig [1994]). Lastly if both e and a differ from 0, the wavefront and the medium is anelliptical. If $a > 0$ (respectively $a < 0$) the wavefront, plotted in solid (resp. dashed) green line, gets ahead of (resp. is left behind by) the elliptical wavefront.

Here we detail the explicit expressions of the vertical velocity $V_{vertical}$, the elliptical constant e and of the anelliptical constant a for the three bulk waves.

- for the qP-wave:

$$(4.5.1-4) \quad V_{vertical} = V_{vertical}^P = \sqrt{C_{33} / \rho} \quad , \quad e = \varepsilon = \frac{C_{11} - C_{33}}{2C_{33}} \quad \text{and} \quad a = \varepsilon - \delta$$

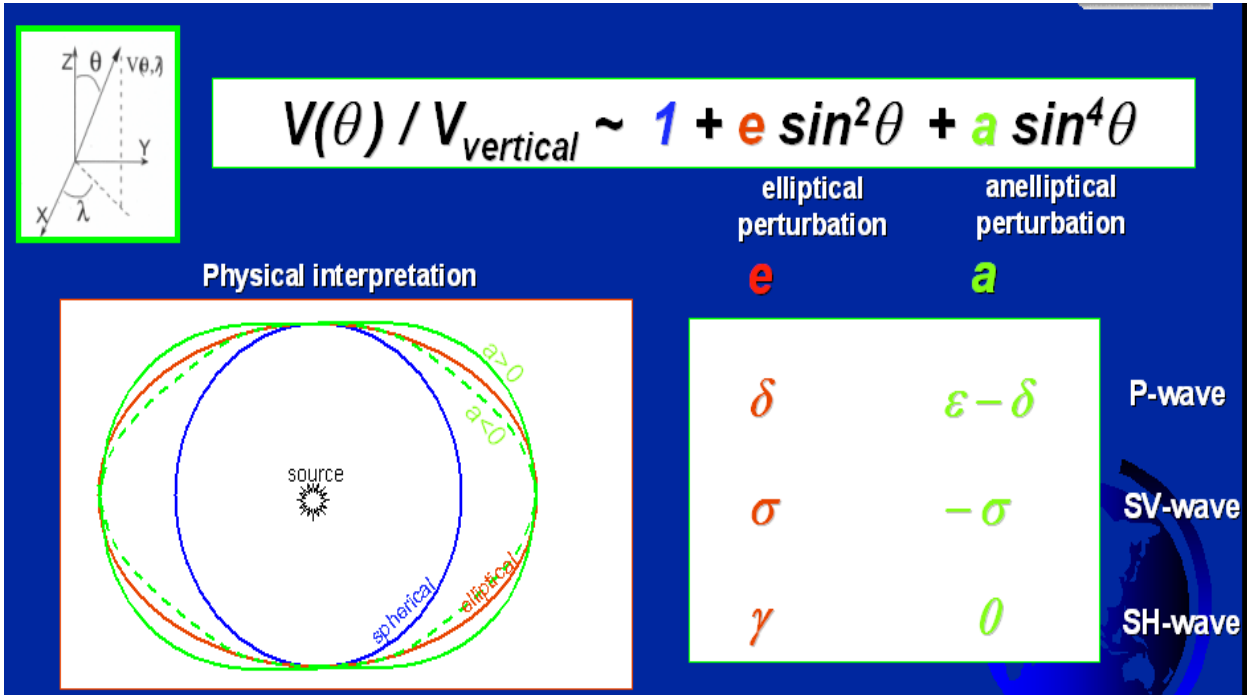


Fig.4.5.1-1: Physical interpretation of Eq. (4.5.1-1) describing the directional dependence of the three bulk waves in a weakly anisotropic transversely isotropic (VTI) medium. Bottom left: Cuts of the wave surfaces by a vertical plane, Bottom right: explicit expressions of the constants e and a for the three bulk waves.

V_{vertical}^P being the velocity of the qP-wave in the vertical direction, ρ the density, and

$$(4.5.1-5) \quad \delta = \frac{(C_{13} + C_{44})^2 - (C_{33} - C_{44})^2}{2C_{33}(C_{33} - C_{44})}$$

Since ε and δ can differ from 0, the P-wave directional dependence can be isotropic, elliptical or anelliptical. The physical interpretations of the P-wave anisotropy parameters ε and δ associated with Eq. (4.5.1-4) is simple and illustrated by Fig. 4.5.1-2.

The cases $\theta=90^\circ$ and $\theta=0^\circ$ in Eq. (4.5.1-3) correspond to vertical and horizontal directions of propagation. Thus ε can simply be interpreted as the relative deviation between the horizontal qP-wave velocity $\sqrt{C_{11}/\rho}$ and the vertical qP-wave velocity $\sqrt{C_{33}/\rho}$. The physical interpretation of the constant δ is less obvious [Thomsen, 1986a]. Let us consider a P-wave reflection survey over a VTI medium of constant thickness, and let us plot the squared offset X^2 versus the squared arrival time T^2 . The curve is nearly a straight line for small offset with a slope equal to the so-called squared Normal Moveout velocity $(V_{\text{nmo}})^2$, commonly computed in conventional seismic processing. In VTI media V_{nmo} often deviates from the vertical velocity V_p^{vertical} , and the relative deviation is quantified by the anisotropy constant δ .

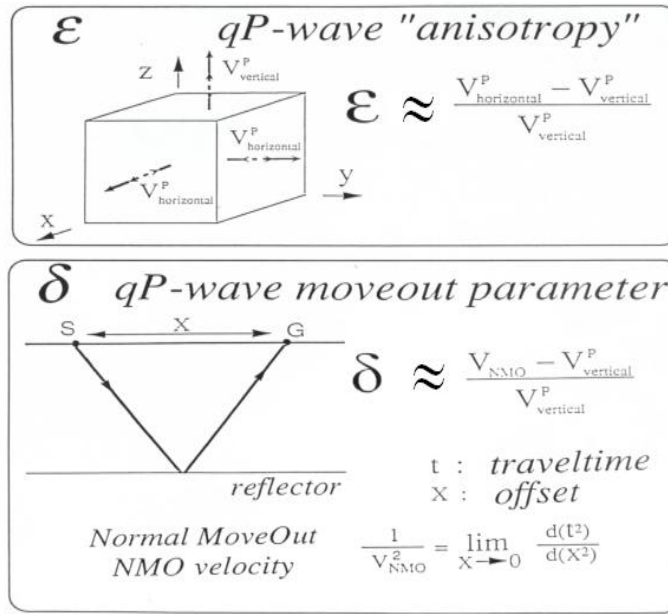


Fig.4.5.1-2: Physical interpretation of the two anisotropy parameters ϵ and δ of the qP-wave.

- for the qSV-wave:

$$(4.5.1-6) \quad V_{vertical} = V_{vertical}^S = \sqrt{C_{44} / \rho} \quad , \quad e = \sigma = \left(\frac{V_{vertical}^P}{V_{vertical}^P} \right)^2 (\epsilon - \delta) \quad \text{and} \quad a = -\sigma$$

where $V_{vertical}^S$ is the velocity of the qS-wave in the vertical direction.

Because the elliptical coefficient e and the anelliptical coefficient a are equal in absolute value and opposite in sign, the SV wave, that is to say the shear-wave polarized in a vertical plane is either isotropic (for $\sigma=0$) or anelliptical (for $\sigma \neq 0$), and cannot be elliptical.

- for the SH-wave:

$$(4.5.1-7) \quad V_{vertical} = V_{vertical}^S = \sqrt{C_{44} / \rho} \quad , \quad e = \gamma = \frac{C_{66} - C_{44}}{2C_{44}} \quad \text{and} \quad a = 0$$

The vanishing of the anelliptical coefficient a of the SH wave, that is to say the horizontally polarized shear-wave, implies that this wave can be either isotropic (for $\gamma=0$) or elliptical (for $\gamma \neq 0$), but not anelliptical.

The physical interpretations of the S-wave anisotropy parameters γ and σ associated with Eqs. (4.5.1-1), (4.5.1-4) and (4.5.1-5) is simple and illustrated by Fig. 4.5.1-4.

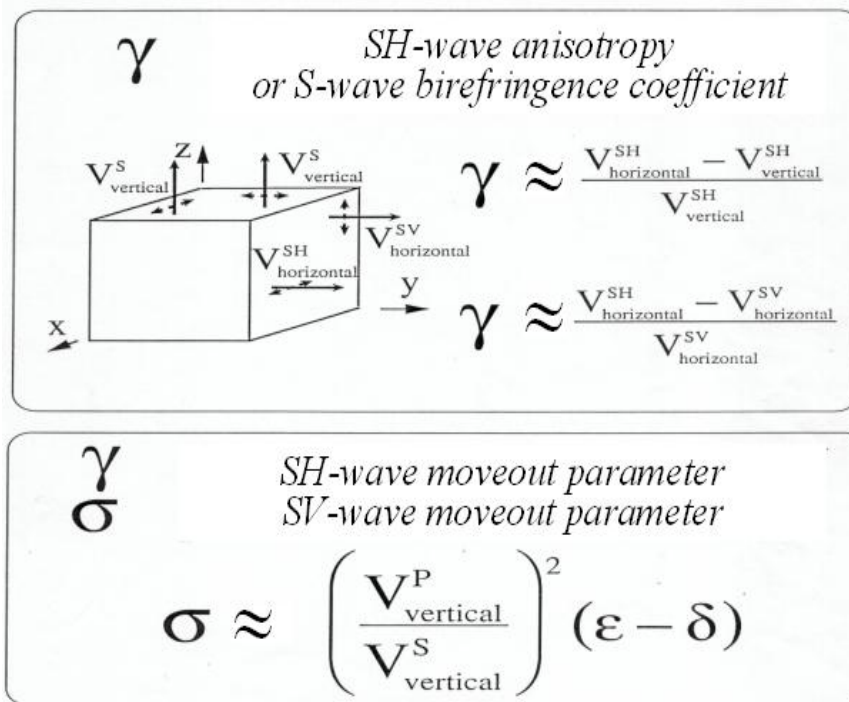


Fig.4.5.1-3: Physical interpretation of the two anisotropy parameters γ and σ of the qS-wave.

First of all the coefficient γ is the relative deviation between the horizontal and the vertical SH-wave velocity. It is for the SH-wave what the coefficient ϵ is for the P-wave. In VTI media γ is also equal to the relative deviation between the SH-wave velocity and the SV-wave velocity in the horizontal direction. Defined in that way the coefficient γ is commonly called the S-wave birefringence coefficient.

With reference to the previous reflection survey experiment, but now with the SH-wave and the SV-wave, the coefficients γ and σ can be interpreted as the moveout parameters respectively for the SH-wave and for the SV-wave. In other words γ and σ are for the SH-wave and for the SV-wave what the coefficient δ is for the P-wave.

Now we shall exploit the large data compilation of Thomsen [1986a] on elastic anisotropy in rocks to extract the major trends with respect to anisotropy, but not only. Note that the most represented lithology is shale, exhibiting a great diversity, either in terms of mineral composition, or in terms of burial depth and geologic age, and as a consequence in terms of level of compaction/diagenesis.

One of the most important effect of burial on sedimentary formations is the reduction of porosity and the velocity and stiffening increase (e.g., Nafe and Drake [1960] and Gardner et al. [1974]). In seismics, many empirical relationships between porosity, or velocity, and the depth of burial and geologic age are used (e.g., Bourbié et al. [1987] and Mavko et al. [1998]). The considered database is not an exception to the rule. A practical consequence is the trend observed and illustrated by Fig. 4.5.1-4, corroborating the simultaneous increase of both P-wave vertical velocity V_p , and S-wave vertical velocity V_s , with the density ρ . The

corresponding depth data being available for only some of the considered samples actually corroborate the effect of burial both on densities and on velocities.

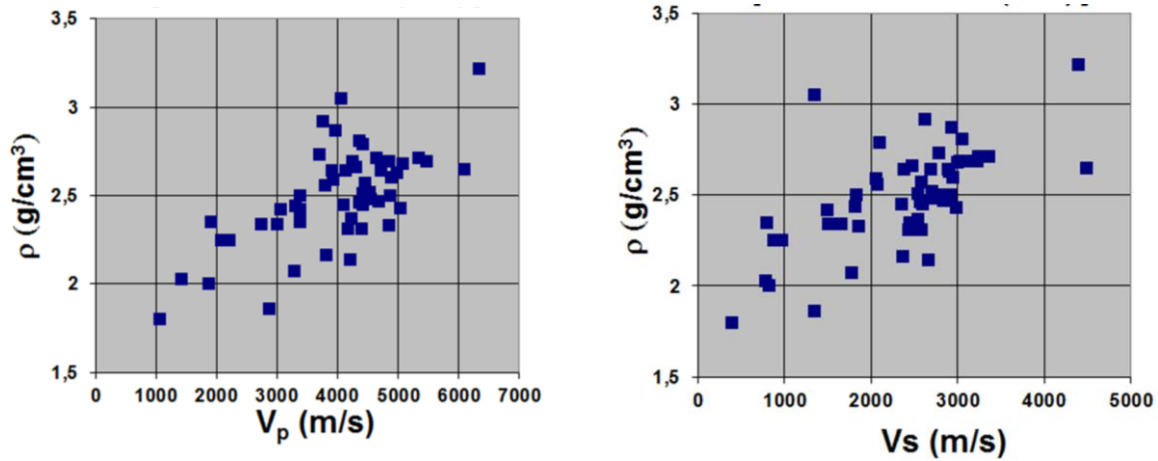


Fig.4.5.1-4: Density ρ as function of the P-wave vertical velocity V_p (Left), and of the S-wave vertical velocity V_s (Right) from the database of Thomsen [1986a].

In the next figure we check if the anisotropy parameters follow some similar general trend linked with compaction. For this, crossplots similar to those of the previous figure are shown on Fig. 4.5.1-5 between the anisotropy parameters ϵ (blue diamonds), δ (pink squares), γ (yellow triangles) and σ (green circles) and the qP-wave vertical velocity V_p (sub-figure on the left side), or the qS-wave vertical velocity (sub-figure on the right side). In contrast with the previous figures, no clear trend is observed for any of the anisotropy parameters. The systematic absence of anisotropy increase with velocity increase seems to imply that burial and/or compaction has no first order effect on seismic anisotropy increase. In other words, contrary to what has been conjectured by some authors (e.g., Hornby [1995]) there is no first order correlation between compaction and anisotropy strength.

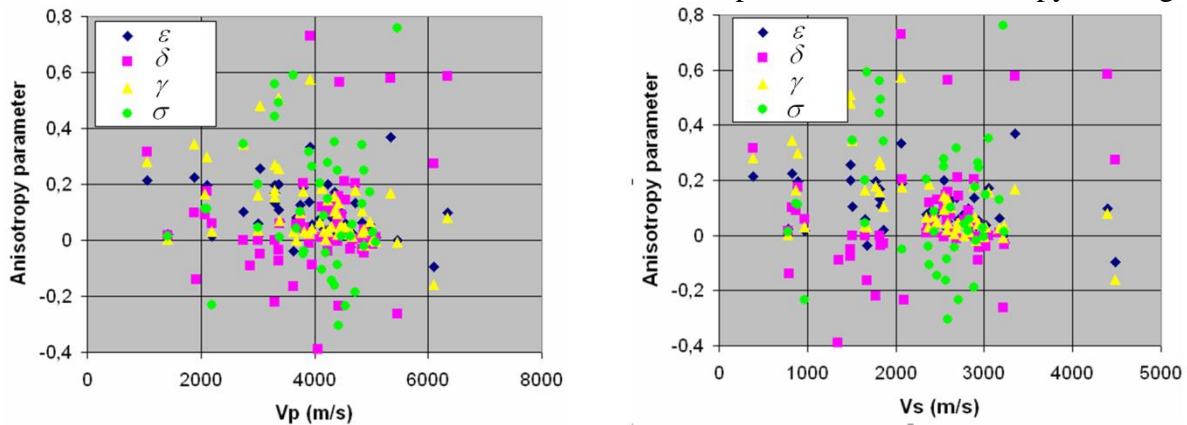


Fig.4.5.1-5: Crossplot between the anisotropy parameters ϵ , δ , γ and σ and (left) the qP-wave vertical velocity, or (right) the qS-wave vertical velocity (experimental data compilation from Thomsen [1986a]).

Furthermore there even seems to be a weak reversal trend between the anisotropy parameter γ (yellow triangles) and both velocities. This very rough decrease of γ with velocity increase can simply be explained by the increase of the vertical S-wave velocity V_s with compaction/diagenesis. Because V_s is present in the denominator of the mathematical expression of γ (see Figure 5.5.1-3 and the corresponding comments), an increase of the vertical velocity V_s tends to slightly decrease the anisotropy parameter γ .

Lastly, although Thomsen [1986a] mainly dealt with weak anisotropy, many rock samples of his database exhibit anisotropy that can be considered as moderate to strong (see the vertical scale of Fig.4.5.1-5). More precisely the absolute values of some anisotropy parameters can be much larger than 0.1-0.15, often considered as upper-bound values for the weak anisotropy approximation.

In contrast with the previous plots, the crossplot between the anisotropy parameters γ and ϵ exhibits clear positive correlation, as illustrated by Fig. 4.5.1-6. In other words one observes an increase of γ with ϵ .

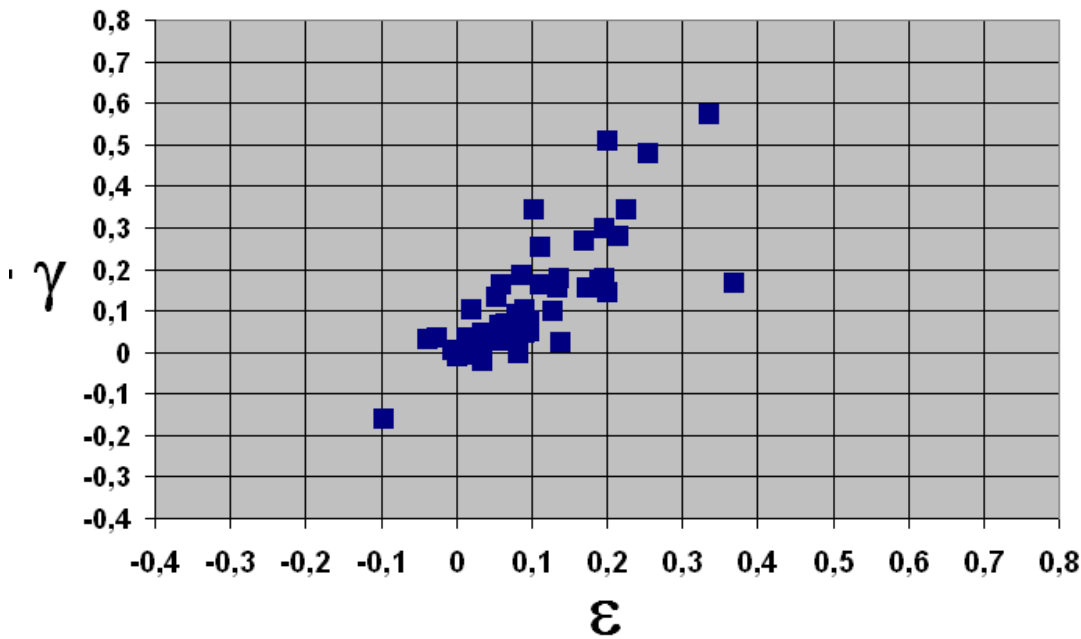


Fig.4.5.1-6: Crossplot of the anisotropy parameters ϵ and γ from the database of Thomsen [1986]

At least for shale, this is in agreement with the theoretical work of Sayers [2005] who described the elastic anisotropy of shales, assuming transverse isotropy for both the clay platelets and their Orientation Distribution Functions (see detail in sub-section 4.6.1.1). The main result was that the more aligned are the clay platelets, the larger the anisotropy parameters γ and ϵ , which is corroborated by many experimental results, including those of the present database. Thus the increase of γ with ϵ observed on Fig. 4.5.1-6 is not really surprising, and is linked with the orientation of the clay platelets. Furthermore, because neither γ nor ϵ increases with any of the velocities V_p and V_s , the increase of the clay

platelets alignment is definitely not linked to the level of compaction, at least to the first order.

Lastly, we see most of the rock samples, but not all of them, have positive anisotropy parameter γ and ε . According to Fig. 4.5.1-2, positive values of ε mean that the qP-wave generally propagates more slowly along the VTI symmetry axis than in the perpendicular direction. This is consistent with the wave propagation in media composed of stacks of thin layer isotropic constituents, a model often used to idealize sedimentary rocks. as will be detailed in section 4.6.1.2. Similarly, according to Fig. 4.5.1-3, positive values of ε mean that the SH-wave generally propagates more slowly along the VTI symmetry axis than in the perpendicular direction, which is also in agreement the theory of wave propagation in thinly layered media.

Note that the relation with the other anisotropy parameters is not as clear, as demonstrated by Sayers [2005] and as illustrated by the two next figures.

Fig. 4.5.1-7 shows a crossplot between the qP-wave anisotropy parameters ε and δ . No evident correlation is noted. In contrast with parameter ε , the parameter δ can take either positive or negative values. Note that rock samples verifying the elliptical property for the qP-wave (i.e., $\varepsilon=\delta$ in the comments on Fig 4.4.1-1) are more the exception than the rule.

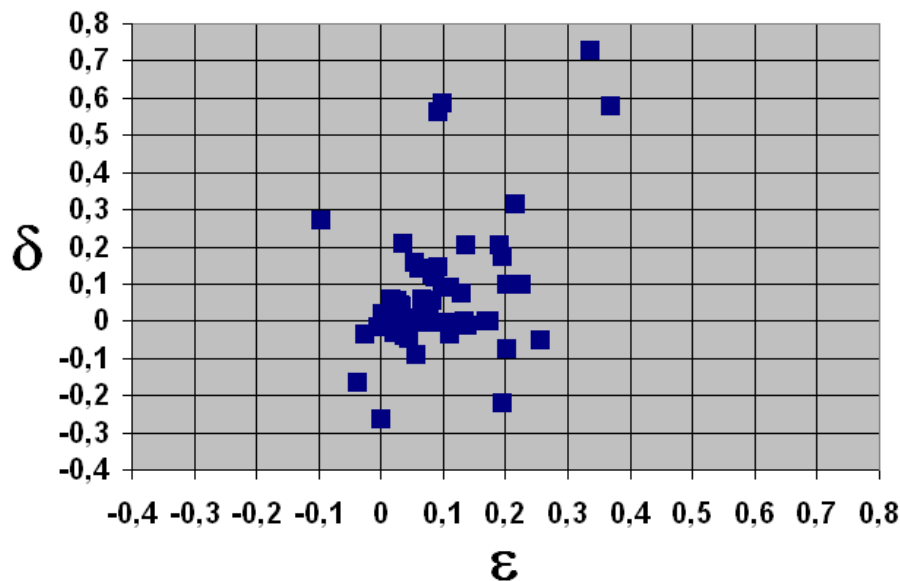


Fig.4.5.1-7: Crossplot between the qP-wave anisotropy parameters ε and δ (experimental data compilation from Thomsen [1986a]).

Also note that many rock samples exhibit values of ε smaller than δ [i.e negative anellipticity $a = \varepsilon - \delta$ in Eq. (4.5.1-4)], which in principle never occurs in thinly layered media, as will be detailed in section 4.6.1.2.

Fig. 4.5.1-8 shows a crossplot between the SV-wave anisotropy parameter σ and the SH-wave anisotropy parameter γ . In contrast with the other anisotropy parameters, the SV-wave anisotropy parameter σ have the largest range of variation (roughly from -0.3 to 0.8). This is due to the factor $(V_{vertical}^P / V_{vertical}^S)^2$ in its definition (4.5.1-6), which can be much larger than 2 in shales for instance. Like the anisotropy parameter δ , the parameter σ can take either positive or negative values, and have the opposite sign to the anellipticity parameter $a = -\sigma$ in Eq. (4.5.1-6).

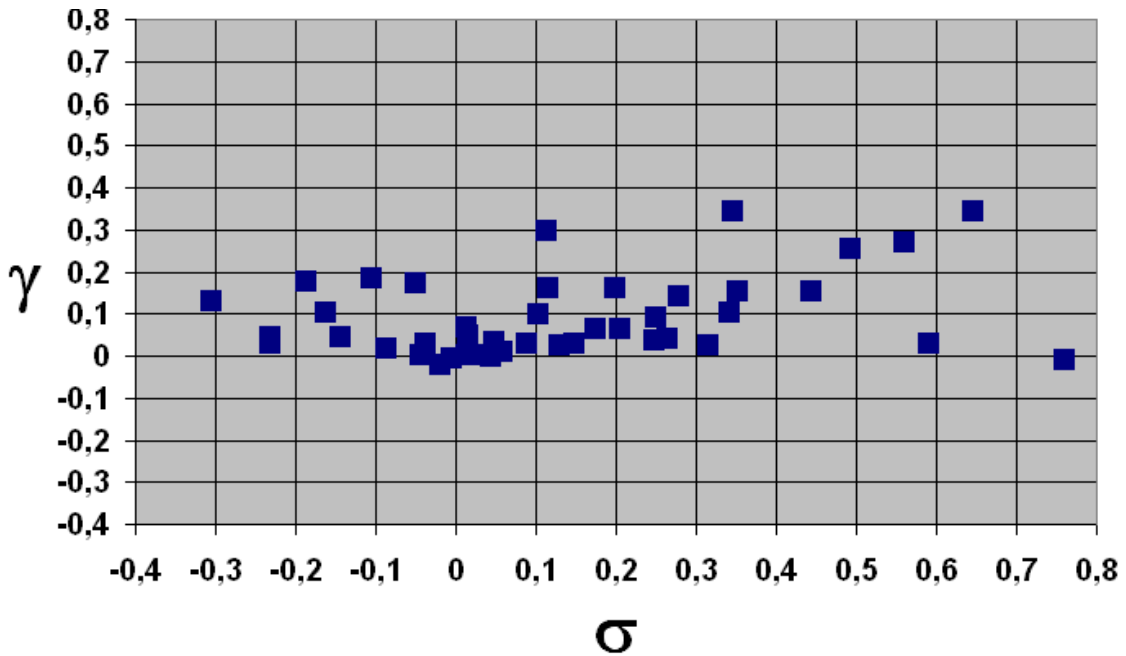


Fig.4.5.1-8: Crossplot between the qS-wave anisotropy parameters σ and γ (experimental data compilation from Thomsen [1986a]).

Regarding anisotropy in shale, we are aware that the intrinsic anisotropy of the clay platelets and their orientation distribution function are not the only causes of elastic anisotropy in shale. Some complicating factors, such as the the anisotropic distributions of discontinuities/porosity and the presence of aligned silt inclusions have drawn much less attention but have also been studied (e.g., Tiwary [2007] and Pervukhina et al. [2013]). Furthermore, note that the actual existence of such discontinuities in shale in natural condition is still controversial (see discussion at the end of §4.6.1.1.3).

However, because of the diversity of the shale samples of Thomsen [1986a] these complicating factors should not substantially change the above conclusions on the absence of

correlation between elastic anisotropy and compaction/diagenesis, at least to the first order. Furthermore, because compaction can be excluded as a major cause of seismic anisotropy in shale, shale platelet alignment, clearly concomitant with the presence of seismic anisotropy in shale, can simply be due, for instance, to the condition of deposition of the sediments. For instance in turbiditic environment one would expect a stochastic misalignment of the clay platelets, inducing quasi random Orientation Distribution Function of the clay platelets. As a consequence we could expect weak overall seismic anisotropy. In contrast, in a quiet deposition environment one would expect a good alignment of the clay platelets in the direction perpendicular to the gravity at the time of sediment deposition. As a consequence the resulting seismic anisotropy is expected to be stronger. This still needs to be confirmed by more detailed and careful studies on large databases.

4.5.2 General parametrization for other symmetry types

In this section we generalize the previous analysis, restricted to transversely isotropic media, in order to take into account arbitrary anisotropy type.

In the case of moderate strength of anisotropy, first order approximations of Eqs. (4.3.3-18) to (4.3.3-20) can be used (e.g., Mensch and Rasolofosaon [1997]). Using the slight changes of notations of Rasolofosaon [2000] the approximate qP-wave phase modulus M_P exhibits the following directional dependence:

$$(4.5.2-1) \quad \frac{M_P(\theta, \lambda)}{M_P^{REF}} = 1 + 2 \left[\delta(\lambda) C_\theta^2 S_\theta^2 + \varepsilon(\lambda) S_\theta^4 + \Delta E_{triclinic}(\theta, \lambda) \right]$$

where

$$(4.5.2-2) \quad \delta(\lambda) = \delta_x C_\lambda^2 + 2 \chi_z S_\lambda C_\lambda + \delta_y S_\lambda^2 \quad ,$$

$$(4.5.2-3) \quad \varepsilon(\lambda) = \varepsilon_x C_\lambda^4 + \delta_z S_\lambda^2 C_\lambda^2 + 2 S_\lambda C_\lambda (\varepsilon_{16} C_\lambda^2 + \varepsilon_{26} S_\lambda^2) + \varepsilon_y S_\lambda^4 \quad , \quad \text{and}$$

$$(4.5.2-4) \quad \Delta E_{triclinic}(\theta, \lambda) = 2 C_\theta S_\theta^3 (\varepsilon_{15} C_\lambda^3 + \varepsilon_{24} S_\lambda^3 + \chi_x S_\lambda C_\lambda^2 + \chi_y C_\lambda S_\lambda^2) + 2 S_\theta C_\theta^3 (\varepsilon_{34} S_\lambda + \varepsilon_{35} C_\lambda)$$

where M_P^{REF} is a P-wave reference modulus and $\delta(\lambda)$, $\varepsilon(\lambda)$ and $\Delta E_{triclinic}(\theta, \lambda)$ are directional functions which depend on the generalized anisotropy parameters δ_x , χ_z , δ_y , ε_x , ε_y etc... of Rasolofosaon [2000], introduced by Mensch and Rasolofosaon [1997], modified by Psencik and Gajewski [1998], and defined by:

(4.5.2-5)

$$\left\{ \begin{array}{l} \varepsilon_x = \frac{c_{11} - c_{33}}{2c_{33}}, \quad \varepsilon_y = \frac{c_{22} - c_{33}}{2c_{33}} \\ \delta_x = \frac{c_{13} - c_{33} + 2c_{55}}{c_{33}}, \quad \delta_y = \frac{c_{23} - c_{33} + 2c_{44}}{c_{33}}, \quad \delta_z = \frac{c_{12} - c_{33} + 2c_{66}}{c_{33}} \\ \chi_x = \frac{c_{14} + 2c_{56}}{c_{33}}, \quad \chi_y = \frac{c_{25} + 2c_{46}}{c_{33}}, \quad \chi_z = \frac{c_{36} + 2c_{45}}{c_{33}} \\ \gamma = \frac{c_{44} - c_{55}}{2c_{55}}, \quad \varepsilon_{16} = \frac{c_{16}}{c_{33}}, \quad \varepsilon_{26} = \frac{c_{26}}{c_{33}}, \quad \varepsilon_{15} = \frac{c_{15}}{c_{33}}, \quad \varepsilon_{24} = \frac{c_{24}}{c_{33}}, \quad \varepsilon_{34} = \frac{c_{34}}{c_{33}}, \quad \varepsilon_{35} = \frac{c_{35}}{c_{33}}, \quad \varepsilon_{45} = \frac{c_{45}}{c_{55}} \end{array} \right.$$

All the coefficients defined by this equation, are the dimensionless anisotropy parameters generalizing Thomsen's parameters ε , δ and γ of Eqs. (4.5.1-4), (4.5.1-5) and (4.5.1-7) .

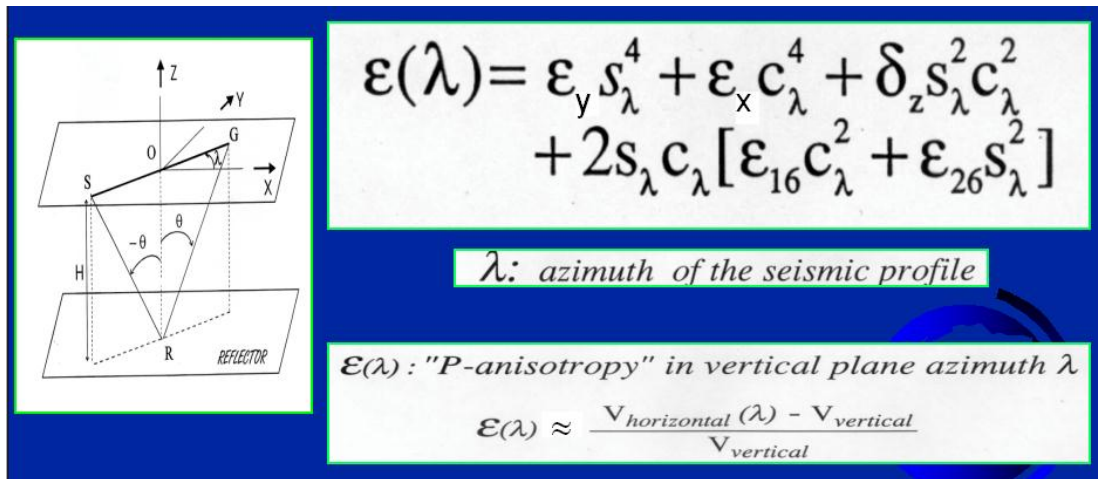


Fig.4.5.2-1: Physical interpretation of the anisotropy function $\varepsilon(\lambda)$ of Eq. (4.5.2-3) .

The physical interpretation of the function $\varepsilon(\lambda)$ defined by Eq. (4.5.2-3) is illustrated by Fig. (4.5.2-1). It is very similar to the interpretation of the parameter ε defined by Eq. (4.5.1-4). In effect, the cases $\theta=90^\circ$ and $\theta=0^\circ$ in Eq. (4.5.2-3) correspond to vertical and horizontal directions of propagation. In both cases the function $\Delta E_{\text{triclinic}}(\theta, \lambda)$ of Eq. (4.5.2-4) vanishes. As a consequence $\varepsilon(\lambda)$ quantifies the relative deviation between the horizontal qP-velocity and the vertical qP-velocity, but contrary to the VTI case, in general this quantity depends on the azimuth λ .

Fig.4.5.2-2 illustrates the physical interpretation of the function $\delta(\lambda)$ defined by Eq. (4.4.2-2).

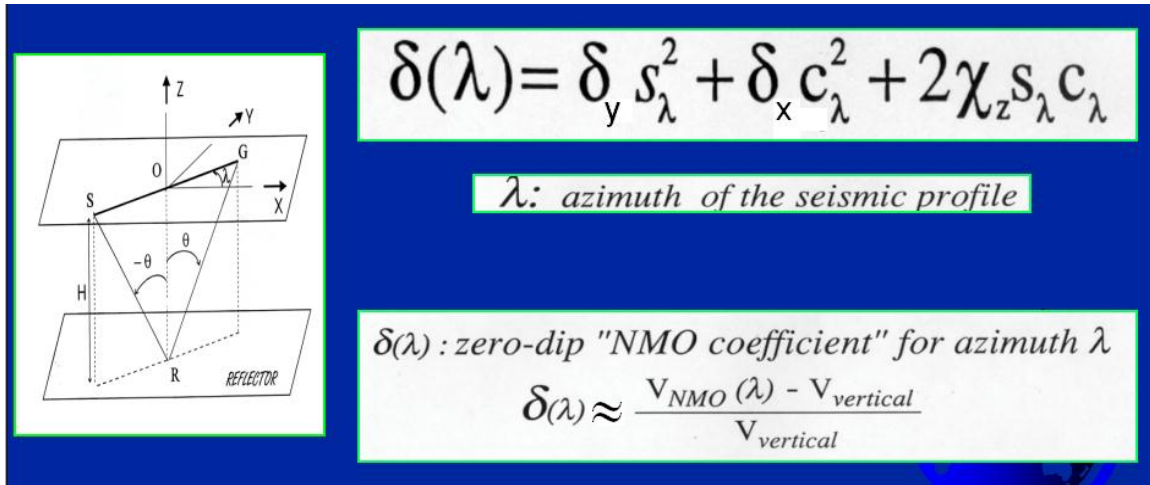


Fig.4.5.2-2: Physical interpretation of the anisotropy function $\delta(\lambda)$ of Eq. (4.5.2-2).

Because of the formal similarity between the qP-wave velocity equations Eqs. (4.5.1-3) and (4.5.1-4) in transversely isotropic (TI) media and the corresponding qP-velocity equation in media of monoclinic symmetry with a horizontal symmetry plane [for which $\Delta E_{triclinc}(\theta, \lambda) = 0$ in Eq.(4.5.2-1)] the function $\delta(\lambda)$ can simply be interpreted as the relative deviation between the Normal Moveout velocity, for a seismic profile along the azimuth λ , and the vertical velocity $V_p^{vertical}$. It can be shown that this is the case even for media of arbitrary anisotropy type [Rasolofosaon, 2001].

As discussed by Mensch and Rasolofosaon [1997] the reference medium can be arbitrarily chosen as long as the difference between the chosen reference elastic tensor and the considered elastic tensor is small enough to justify a perturbation approach. For the experimental check in the following we choose $M_P^{REF} = C_{33}$ but this is not limitative.

The expression of the moduli of the qS-waves are more complicate and write:

(4.5.2-6)

$$M^{S_1, S_2}(\theta, \lambda) = \frac{1}{2} \left[C_{44}^r(\theta, \lambda) + C_{55}^r(\theta, \lambda) \pm \sqrt{(C_{44}^r(\theta, \lambda) - C_{55}^r(\theta, \lambda))^2 + 4(C_{45}^r(\theta, \lambda))^2} \right]$$

where the directional-dependent functions $C_{44}^r(\theta, \lambda)$, $C_{55}^r(\theta, \lambda)$ and $C_{45}^r(\theta, \lambda)$ are defined by:

(4.5.2-7)

$$\frac{C_{44}^r(\theta, \lambda)}{M_{S1}^{REF}} = 1 + 2 \frac{M_P^{REF}}{M_{S1}^{REF}} \left[\sum_{i=1}^9 b_i^S Q_i^S(\theta, \lambda) \right]$$

(4.5.2-8)

$$\frac{C_{55}^r(\theta, \lambda)}{M_{S2}^{REF}} = 1 + 2 \frac{M_P^{REF}}{M_{S2}^{REF}} \left[\sum_{i=1}^{15} d_i^S R_i^S(\theta, \lambda) \right]$$

(4.5.2-9)

$$\frac{C_{45}^r(\theta, \lambda)}{M_P^{REF}} = \sum_{i=1}^{17} e_i^S W_i^S(\theta, \lambda)$$

The detailed definitions of the coefficients b_i^S , d_i^S and e_i^S , and of the directional functions $Q_i^S(\theta, \lambda)$, $R_i^S(\theta, \lambda)$, and $W_i^S(\theta, \lambda)$ are given here to correct some typos contained in Mensch and Rasolofosaon [1997].

The coefficients b_i^S , d_i^S and e_i^S are defined by:

$$(4.5.2-10) \quad \begin{cases} b_1^S = \gamma_y' & ; & b_2^S = \gamma_z' & ; & b_3^S = \varepsilon_x + \varepsilon_y - \delta_z \\ b_4^S = \varepsilon_{16} - \varepsilon_{26} & ; & b_5^S = \varepsilon_{45} & ; & b_6^S = \varepsilon_{24} - \chi_y \\ b_7^S = \varepsilon_{15} - \chi_x & ; & b_8^S = \varepsilon_{56} & ; & b_9^S = \varepsilon_{46} \end{cases}$$

$$(4.5.2-11) \quad \begin{cases} d_1^S = \varepsilon_z & ; & d_2^S = \varepsilon_y - \delta_y & ; & d_3^S = \varepsilon_x - \delta_x & ; & d_4^S = \delta_z - \varepsilon_y - \varepsilon_x \\ d_5^S = \gamma_x' & ; & d_6^S = -2\chi_z & ; & d_7^S = 2\varepsilon_{16} & ; & d_8^S = 2\varepsilon_{26} \\ d_9^S = \varepsilon_{45} & ; & d_{10}^S = \varepsilon_{35} & ; & d_{11}^S = \varepsilon_{34} & ; & d_{12}^S = \varepsilon_{15} \\ d_{13}^S = \varepsilon_{24} & ; & d_{14}^S = \chi_y & ; & d_{15}^S = \chi_x \end{cases}$$

$$(4.5.2-12) \quad \begin{cases} e_1^S = \delta_z - 2\varepsilon_x & ; & e_2^S = 2\varepsilon_y - \delta_z & ; & e_3^S = \delta_x - \delta_y & ; & e_4^S = -\gamma_z' & ; & e_5^S = 4(\varepsilon_{26} - \varepsilon_{16}) \\ e_6^S = \chi_z - \varepsilon_{26} & ; & e_7^S = \varepsilon_{16} - \chi_z & ; & e_8^S = \varepsilon_{45} & ; & e_9^S = \chi_y & ; & e_{10}^S = 2\chi_y - 3\varepsilon_{24} \\ e_{11}^S = 2\varepsilon_{24} - \chi_y & ; & e_{12}^S = -\chi_x & ; & e_{13}^S = 3\varepsilon_{13} - 2\chi_x & ; & e_{14}^S = \chi_x - 2\varepsilon_{15} & ; & e_{15}^S = -\varepsilon_{34} \\ e_{16}^S = \varepsilon_{35} & ; & e_{17}^S = -\varepsilon_{56} & ; & e_{18}^S = \varepsilon_{46} \end{cases}$$

The directional functions $Q_i^S(\theta, \lambda)$, $R_i^S(\theta, \lambda)$, and $W_i^S(\theta, \lambda)$ are given by:

$$(4.5.2-13) \quad \begin{cases} Q_1^S = S_\theta^2 & ; & Q_2^S = S_\lambda^2 C_\theta^2 & ; & Q_3^S = C_\lambda^2 S_\lambda^2 S_\theta^2 \\ Q_4^S = (C_\lambda S_\lambda^3 - C_\lambda^3 S_\lambda) S_\theta^2 & ; & Q_5^S = C_\lambda S_\lambda C_\theta^2 & ; & Q_6^S = C_\lambda^2 S_\lambda C_\theta S_\theta \\ Q_7^S = C_\lambda S_\lambda^2 C_\theta S_\theta & ; & Q_8^S = S_\lambda C_\theta S_\theta & ; & Q_9^S = C_\lambda C_\theta S_\theta \end{cases}$$

(4.5.2-14)

$$\begin{cases} R_1^S = C_\theta^2 S_\theta^2 & ; & R_2^S = S_\lambda^2 C_\theta^2 S_\theta^2 & ; & R_3^S = C_\lambda^2 C_\theta^2 S_\theta^2 & ; & R_4^S = C_\lambda^2 S_\lambda^2 C_\theta^2 S_\theta^2 & ; & R_5^S = S_\lambda^2 \\ R_6^S = C_\lambda S_\lambda C_\theta^2 S_\theta^2 & ; & R_7^S = C_\lambda^3 S_\lambda C_\theta^2 S_\theta^2 & ; & R_8^S = C_\lambda S_\lambda^3 C_\theta^2 S_\theta^2 & ; & R_9^S = C_\lambda S_\lambda \\ ; & R_{10}^S = C_\lambda (C_\theta S_\theta^3 - C_\theta^3 S_\theta) & ; & R_{11}^S = S_\lambda (C_\theta S_\theta^3 - C_\theta^3 S_\theta) & ; & R_{12}^S = C_\lambda^3 (C_\theta^3 S_\theta - C_\theta S_\theta^3) \\ R_{13}^S = S_\lambda^3 (C_\theta^3 S_\theta - C_\theta S_\theta^3) & ; & R_{14}^S = C_\lambda^2 S_\lambda (C_\theta^3 S_\theta - C_\theta S_\theta^3) & ; & R_{15}^S = C_\lambda S_\lambda^2 (C_\theta^3 S_\theta - C_\theta S_\theta^3) \end{cases}$$

(4.5.2-15)

$$\left\{ \begin{array}{l} W_1^S = C_\lambda^3 S_\lambda C_\theta S_\theta^2 ; W_2^S = C_\lambda S_\lambda^3 C_\theta S_\theta^2 ; W_3^S = C_\lambda S_\lambda C_\theta S_\theta^2 ; W_4^S = C_\lambda S_\lambda C_\theta \\ W_5^S = C_\lambda^2 S_\lambda^2 C_\theta S_\theta^2 ; W_6^S = S_\lambda^2 C_\theta S_\theta^2 ; W_7^S = C_\lambda^2 C_\theta S_\theta^2 ; W_8^S = (C_\lambda^2 - S_\lambda^2) C_\theta \\ W_9^S = C_\lambda^3 C_\theta^2 S_\theta ; W_{10}^S = C_\lambda S_\lambda^2 S_\theta^3 ; W_{11}^S = C_\lambda S_\lambda^2 S_\theta ; W_{12}^S = S_\lambda^3 C_\theta^2 S_\theta \\ W_{13}^S = C_\lambda^2 S_\lambda S_\theta^3 ; W_{14}^S = C_\lambda^2 S_\lambda S_\theta ; W_{15}^S = C_\lambda C_\theta^2 S_\theta ; W_{16}^S = S_\lambda C_\theta^2 S_\theta \\ W_{17}^S = C_\lambda S_\theta ; W_{18}^S = S_\lambda S_\theta \end{array} \right.$$

In order to illustrate these equations, Fig.4.5.2-3 show the complete directional dependences of the first-order approximation error on the phase velocity in the sample of water-saturated Vosges sandstone of Fig.4.3.3-2 of section 4.3.3, and characterized by the stiffness matrix of Eq. (4.3.3-21) and the corresponding dimensionless qP-wave anisotropy parameters:

$$(4.5.2-16) \left\{ \begin{array}{l} \varepsilon_x = -0.034 ; \varepsilon_y = -0.075 \\ \delta_x = -0.025 ; \delta_y = -0.054 ; \delta_z = -0.088 \\ \chi_y = 0.037 ; \chi_x = 0.020 ; \chi_z = -0.019 \\ \varepsilon_{16} = 0.014 ; \varepsilon_{26} = -0.015 ; \varepsilon_{45} = -0.003 \\ \varepsilon_{15} = -0.003 ; \varepsilon_{24} = 0.028 ; \varepsilon_{34} = -0.013 ; \varepsilon_{35} = 0.010 \end{array} \right.$$

The convention is the same as for this figure, Fig.4.5.2-3 is composed of three sub-figures, the top sub figure corresponding to the qP-wave, the middle figure to the qS1-wave and the bottom figure to the qS2-wave. The agreement between the exact theory and the first-order approximate theory is good for the qP-wave, with errors hardly exceeding 1%. The first-order approximations for the qS1- and qS2-wave are not as accurate as for the qP-wave, although being reasonable (typically smaller than 10%). The reasonable errors exhibited by the first-order approximations on the velocities were expected, considering the reasonable anisotropy strength of the velocities (typically smaller than 10%).

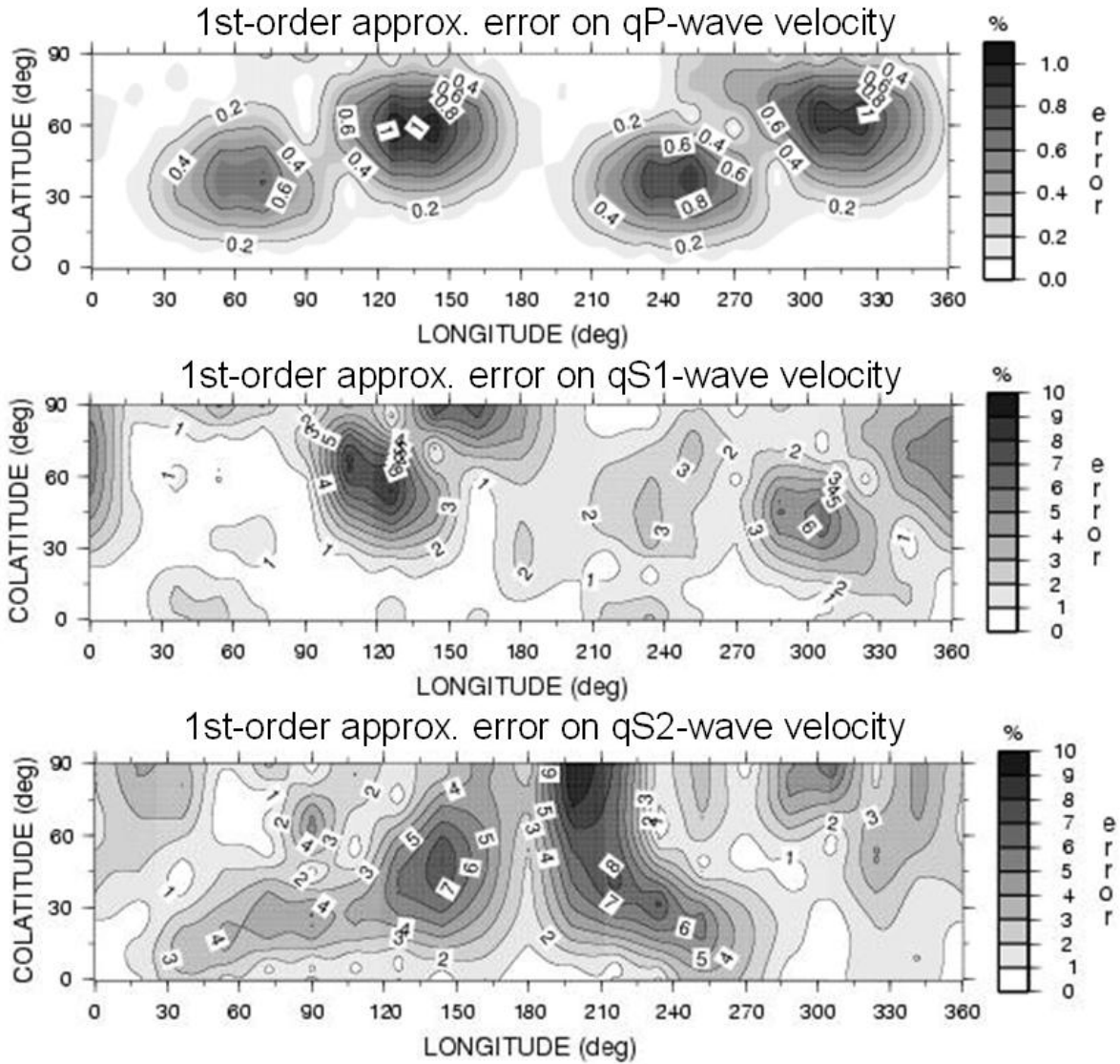


Fig.4.5.2-3: Complete directional dependence of the relative difference in % between the first-order-approximate velocity and the exact velocity (top) of the qP-wave, (middle) of the qS1-wave, and (bottom) of the qS2-wave in water-saturated Vosges Sandstone considered as an arbitrarily anisotropic elastic medium.

Furthermore, it is possible to improve the accuracy of the approximation by using higher order developments, as proposed by Farra [2001], Farra and Psencik [2003] and Farra [2004] for instance. For instance, the third-order approximations proposed by Farra [2001] are easy to implement and are not time-consuming because they need only computation of the first-order approximations. Most important and as a consequence, her third-order approximation do not need to introduce additional anisotropy parameters than those defined in section 4.5.2, and generalizing Thomsen's anisotropy parameters, which is quite convenient for practical applications. Figure 4.5.2-4 illustrates the high accuracy of the third-order approximation.

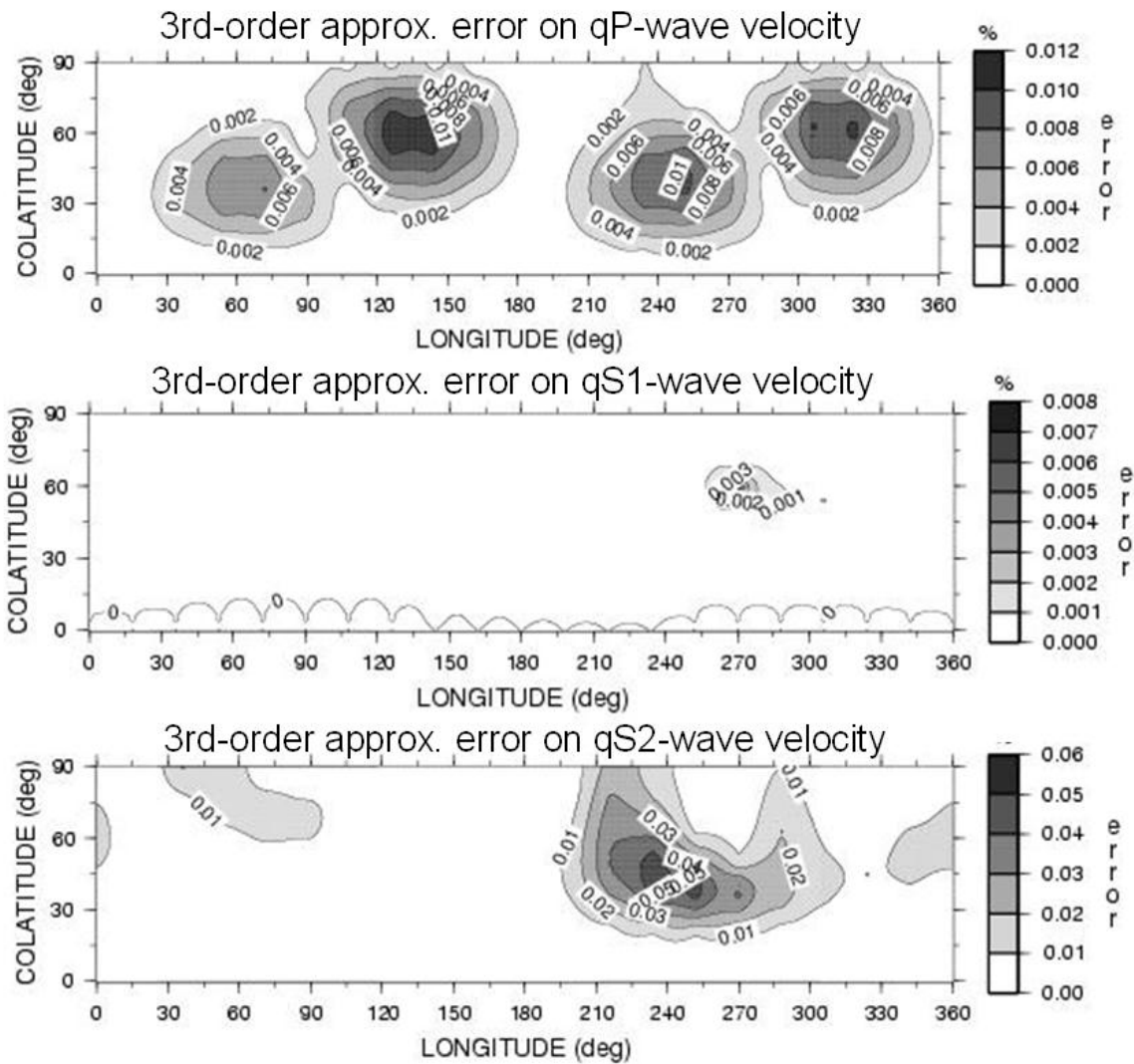


Fig. 4.5.2-4: Same plot as Fig. 4.5.2-3 but in the case of third-order-approximation.

The result is clear, third-order approximations are substantially more accurate than first-order approximations (compare the error scale on the right side of Figures 4.5.2-3 and 4.5.2-4). More precisely, the maximum value of third-order approximation error hardly exceeds 0.01% for the qP-wave, 0.008% for the qS1-wave, and 0.06% for the qS2-wave. This is quite comparable with the results obtained by Farra [2001] in an orthorhombic medium. The same technique has been adapted by Rasolofosaon [2010] to arbitrarily anisotropic viscoelastic media, and applied to data in strongly anisotropic water-saturated rocks. Results very similar to the one obtained here are reported. The maximum relative errors do not exceed 0.06% on all the velocities and 0.6% on all the quality factors Q , for third-order approximations.

4.6 *The main rock models incorporating elastic anisotropy*

Anisotropy, by definition, is the negative of isotropy as recalled in Chapter 1 § 1.2.3.2. Thus a medium exhibiting elastic anisotropy must lack the complete symmetry with respect to any plane and to any axis of rotational invariance. The identified causes of elastic anisotropy are the orientational distribution of the mineral constituents and of the compliant pores (cracks, microfractures, grain contacts...) at a scale much smaller than the elastic wavelength and the present state of stress (e.g., Helbig [1994]; Thomsen [2002]; Grechka [2009]). If one refers again to Curie's symmetry principle, detailed in section 4.2.1, at least one of those causes of anisotropy must lack this complete symmetry. In the next sub-sections we shall describe the anisotropy due to at least one of these three causes. We start with the anisotropy due to mineral and/or structure alignment. Then we describe the effect of the presence of aligned compliant pores on elastic anisotropy. Finally the stress-induced anisotropy will be examined.

4.6.1 Anisotropy due to mineral and/or structure alignment

4.6.1.1 Anisotropy due to mineral alignment or to the presence of shale

4.6.1.1.1 General formulation of the anisotropy due to mineral alignment.

We shall assimilate the rock as a microheterogeneous medium. Microheterogeneous media can be considered as heterogeneous on a microscale (e.g. scale of the grains and the pores in a rock) but homogeneous on a macroscale (typically a scale one order of magnitude larger than the microscale). Detailed developments of the theory of elasticity in such media can be found in Shermergor [1977], Gubernatis and Krumhansl [1975], or Nemat-Nasser and Hori [2005], and will be detailed in Chapter 5 on Frequency dependence and Heterogeneity effects.

Without entering details, let us consider an elastic medium characterized by a local stiffness field $C(M)$, M being an arbitrary point representative of the microscale of the microheterogeneous medium. Locally the generalized Hooke's law can be written as:

$$(4.6.1-1) \quad \sigma(M) = C(M) \varepsilon(M)$$

where $\sigma(M)$ and $\varepsilon(M)$ are the local stress and strain tensors. The local stiffness fields $C(M)$ are associated with statistical distribution functions of the material texture (e.g., for rocks: grain/pore types, shape, spatial orientation).

An additional hypothesis is that the medium is macrohomogeneous with respect to the elastic properties, which means that the average stress tensor $\langle \sigma \rangle$ and the average strain tensor $\langle \varepsilon \rangle$ are both spatially invariant. The bracket $\langle \rangle$ denotes averaging over the texture distribution and over a Representative Elementary Volume of the rock sample (see definition in Chapter 1 §1.3.3).

Given the statistical distribution of the stiffness field $C(M)$, M being any point in the rock sample, the problem is how to evaluate the effective stiffness tensor \bar{C} which relates $\langle \sigma \rangle$ and $\langle \varepsilon \rangle$ through the macroscopic generalized Hooke's law:

$$(4.6.1-2) \quad \langle \sigma \rangle = \bar{C} \langle \varepsilon \rangle$$

A classical way to solve this problem is to use scattering theory, a well-known technique in the fields of solid state physics and quantum mechanics (e.g., Gubernatis and Krumhansl [1975]). Since the medium is homogeneous at the macroscale the stiffness field $C(M)$ of Eq. (4.6.1-1) can be decomposed as follows:

$$(4.6.1-3) \quad C(M) = C^{(background)} + \delta C(M)$$

where $\delta C(M)$ describes the local variations of stiffness characterizing the local heterogeneities and $C^{(background)}$ the spatially invariant stiffness of the background medium, which can be chosen arbitrarily because of the non-unicity of the decomposition in Equation (4.6.1-3).

A simple approximation for the effective stiffness tensor \bar{C} can be found by assuming that the local strain field $\varepsilon(M)$ is equal to a constant ε_0 everywhere. Equation (4.6.1-2) takes the simplified form:

$$(4.6.1-4) \quad \bar{C} = \frac{\langle (C^{(background)} + \delta C) \varepsilon_0 \rangle}{\langle \varepsilon_0 \rangle} = \langle C \rangle = \bar{C}^{(Voigt)}$$

This iso-strain solution, called the Voigt model [Voigt, 1887], is simply the volume average of the local stiffness $C(M)$, it has been successfully used in the case where the contrast between the elastic components of the constituents of the medium is rather small, for instance to describe the elasticity of metamorphic rocks (for instance Siegesmund et al. [1989]; Mainprice [1990]) and shales (e.g., Sayers [1994] and [2005]) as will be detailed below.

Regarding the compliance tensors S , the strain/stress law writes:

$$(4.6.1-5) \quad \langle \varepsilon \rangle = \bar{S} \langle \sigma \rangle$$

and the compliance field $S(M)$, the equivalent of Equation (4.6.1-3), can be decomposed as follows:

$$(4.6.1-6) \quad S(M) = S^{(background)} + \delta S(M)$$

In analogy with Voigt model, a very simple approximation for the effective compliance tensor \bar{S} can be obtained by assuming that the local stress field $\sigma(M)$ is equal to a constant σ_0 everywhere:

$$(4.6.1-7) \quad \bar{S} = \frac{\langle (S^{(background)} + \delta S) \sigma_0 \rangle}{\langle \sigma_0 \rangle} = \langle S \rangle = \bar{S}^{(Reuss)}$$

This iso-stress model, or Reuss model [Reuss, 1929], simply consists of the volume average of the local compliances $S(M)$. Since azimuthal anisotropy measured in sedimentary basins, as the anisotropy commonly due to fractures, is very often moderate in the context of exploration seismics (e.g., Leary et al. [1990]; Crampin and Lovell [1991]; Thomsen [2002]) such simplified approaches is often justified and give comparable results with more sophisticated models such as the self-consistent method, as detailed in Chapter 5 on Frequency dependence and Heterogeneity effects. These are the most common theories used in the seismic exploration community, as will be detailed in the sub-section 4.6.2 in the study of the anisotropy due to aligned compliant pores (cracks, fractures, grain contacts...).

The elastic anisotropy of aggregates of crystals or “polycrystals”, such as natural materials (rocks) or engineering materials (ceramics, metals...) can be analyzed in the same way from the points of view of Voigt theory and of Reuss theory. In general these crystals are not randomly oriented but exhibit preferred orientations. These non-random orientation distribution or preferred orientations are called “textures” (e.g., Paterson and Weiss [1961]) and macroscopically induce in the aggregates a directional dependence of any physical property, including elastic properties.

In order to model the macroscopic anisotropy due to preferred orientation the crystal constituents, it is convenient to introduce the crystallographic frame XYZ attached to the individual crystal constituent, and the frame xyz attached to the sample to be analyzed. As illustrated by Figure 4.3.2-3, the most general rotation from the initial frame xyz to the final frame XYZ without any deformation is defined by the three Euler angles, ψ , the nutation θ and ϕ . The full 3D representation of the crystallographic texture is given by the Orientation Distribution Function (ODF) $W(\xi, \psi, \phi)$, where $\xi = \cos \theta$ and θ is angle between the axes z and Z. As detailed by Roe [1965], $W(\xi, \psi, \phi)d\xi d\psi d\phi$ is the volume fraction of crystals between ξ and $\xi+d\xi$, ψ and $\psi+d\psi$ and ϕ and $\phi+d\phi$. The ODF $W(\xi, \psi, \phi)$ integrated over all the interval of variation of the variables ξ (from -1 to 1), ψ (from 0 to 2π) and ϕ (from 0 to 2π) must give 100% of the volume fraction, which writes:

$$(4.6.1-8) \quad \int_0^{2\pi} \int_0^{2\pi} \int_{-1}^{+1} W(\xi, \psi, \phi) d\xi d\psi d\phi = 1$$

Designating by C' and S' rotated stiffness tensor of the crystal from the frame xyz to the crystallographic frame XYZ [the explicit expressions of the rotated stiffness and compliance matrices are given by Equation (4.3.2-24)], the effective stiffness tensor \bar{C} and compliance tensor \bar{S} are given by:

$$(4.6.1-9) \quad \begin{Bmatrix} \bar{C} \\ \bar{S} \end{Bmatrix} = \begin{Bmatrix} C^{(Voigt)} \\ S^{(Reuss)} \end{Bmatrix} = \int_0^{2\pi} \int_0^{2\pi} \int_{-1}^{+1} \begin{Bmatrix} C'(\xi, \psi, \phi) \\ S'(\xi, \psi, \phi) \end{Bmatrix} W(\xi, \psi, \phi) d\xi d\psi d\phi$$

As suggested by Roe (1965), and as extensively used by Sayers [1994] and [2005], the ODF $W(\xi, \psi, \phi)$ can be expanded in generalized Legendre functions $Z_{lmn}(\xi)$:

$$(4.6.1-10) \quad W(\xi, \psi, \varphi) = \sum_{l=0}^{\infty} \sum_{m=-l}^l \sum_{n=-l}^l W_{lmn} Z_{lmn}(\xi) e^{-im\psi} e^{-in\varphi}$$

and using the orthogonality relations between these functions [Morris, 1969]. The parameters W_{lmn} are the coefficients of this expansion. Fortunately, the elastic stiffness and compliance tensors being of rank 4 the above summations are restricted to $l \leq 4$. Furthermore if transverse isotropy is assumed for both the crystal symmetry and the ODF, as in the study of shales, the dependence in ψ and in φ must disappear in Equation (4.6.1-10), which implies $m = n = 0$. Thus, as pointed out by Sayers [1994] and [2005], only 2 coefficients are sufficient to compute the effective stiffness tensor \bar{C} and compliance tensor \bar{S} in Equation (4.6.1-9), namely W_{200} and W_{400} . The above approach will be used to describe the anisotropy of shales, as detailed below.

4.6.1.1.2 Case of isotropic orientation distribution of anisotropic crystals.

One of the simplest case is when the crystal constituents are totally randomly oriented. The compound medium is isotropic and characterized by an effective stiffness tensor $\bar{C}^{(ISO)}$. The tensor $\bar{C}^{(ISO)}$ is obtained by minimizing the “distance” $\|\bar{C} - \bar{C}^{(ISO)}\|$ between the stiffness tensor \bar{C} of the crystal constituent and the isotropic tensor $\bar{C}^{(ISO)}$, where the norm $\|\cdot\|$ of an arbitrary tensor A of rank 4 is the euclidian norm defined by $\|A\|^2 = A_{ijkl} A_{ijkl}$ (with implicit summation on the repeated indices) (e.g., Fedorov [1968]; Sayers [1994]; Arts [1993]; Mensch and Rasolofosaon [1997]). Two independent coefficients characterize the isotropic tensor $\bar{C}^{(ISO)}$, for instance the bulk modulus $\bar{K}^{(ISO)}$ and the shear modulus $\bar{\mu}^{(ISO)}$ given by:

$$(4.6.1-11) \quad \begin{cases} 9\bar{K}^{(ISO)} = C_{11} + C_{22} + C_{33} + 2C_{12} + 2C_{23} + 2C_{13} \\ 15\bar{\mu}^{(ISO)} = C_{11} + C_{22} + C_{33} - C_{12} - C_{23} - C_{13} + 3C_{44} + 3C_{55} + 3C_{66} \end{cases}$$

The complete stiffness matrix of the main crystal constituent of rocks can be found in the literature. For instance, the main crystal constituent of sedimentary rocks are quartz, calcite and dolomite. We find in Hearmon [1956],

for Quartz (trigonal symmetry) of density $\rho = 2650 \text{ kg} / \text{m}^3$

$$(4.6.1-12) \quad \mathbf{C} = \begin{pmatrix} 86.6 & 6.7 & 12.6 & -17.8 & 0 & 0 \\ 6.7 & 86.6 & 12.6 & 17.8 & 0 & 0 \\ 12.6 & 18.91 & 106.6 & 0 & 0 & 0 \\ -17.8 & 17.8 & 0 & 57.8 & 0 & 0 \\ 0 & 0 & 0 & 0 & 57.8 & -17.8 \\ 0 & 0 & 0 & 0 & -17.8 & 39.9 \end{pmatrix} \text{ GPa}$$

and for Calcite (trigonal symmetry) of density $\rho = 2712 \text{ kg/m}^3$

$$(4.6.1-13) \quad \mathbf{C} = \begin{pmatrix} 144 & 53.9 & 51.1 & -20.5 & 0 & 0 \\ 53.9 & 144 & 51.1 & 20.5 & 0 & 0 \\ 51.1 & 51.1 & 84.0 & 0 & 0 & 0 \\ -20.5 & 20.5 & 0 & 33.5 & 0 & 0 \\ 0 & 0 & 0 & 0 & 33.5 & -20.5 \\ 0 & 0 & 0 & 0 & -20.5 & 45.1 \end{pmatrix} \text{ GPa}$$

Bass [1995] gives for Dolomite (trigonal symmetry) of density $\rho = 2850 \text{ kg/m}^3$

$$(4.6.1-14) \quad \mathbf{C} = \begin{pmatrix} 205 & 71.0 & 57.4 & -19.5 & 13.7 & 0 \\ 71.0 & 205 & 57.4 & 19.5 & -13.7 & 0 \\ 57.4 & 57.4 & 113 & 0 & 0 & 0 \\ -19.5 & 19.5 & 0 & 39.8 & 0 & 0 \\ 13.7 & -13.7 & 0 & 0 & 39.8 & -13.7 \\ 0 & 0 & 0 & 0 & -13.7 & 67.0 \end{pmatrix} \text{ GPa}$$

Note that the complete set of the elastic coefficients of the main crystal constituents of rocks can also be found in Bass [1995].

Application of Equation (4.6.1-11) to the three stiffness matrix of Equations (4.6.1-12) to (4.6.1-13) gives

- for quartz $\bar{K}^{(ISO)} = 38,18 \text{ GPa}$ and $\bar{\mu}^{(ISO)} = 47,63 \text{ GPa}$, which are rather consistent with the values found in Bass (1995), namely $\bar{K}^{(ISO)} = 37,8 \text{ GPa}$ and $\bar{\mu}^{(ISO)} = 44,3 \text{ GPa}$, and in Mavko et al. (1998), namely $\bar{K}^{(ISO)} = 37 \text{ GPa}$ and $\bar{\mu}^{(ISO)} = 45 \text{ GPa}$

- for calcite $\bar{K}^{(ISO)} = 76,02GPa$ and $\bar{\mu}^{(ISO)} = 36,81GPa$, which are consistent with the values found in Bass (1995), namely $\bar{K}^{(ISO)} = 76,3GPa$ and $\bar{\mu}^{(ISO)} = 32GPa$, and in Mavko et al. (1998), namely $\bar{K}^{(ISO)} = 75GPa$ and $\bar{\mu}^{(ISO)} = 31GPa$

- for dolomite $\bar{K}^{(ISO)} = 99,4GPa$ and $\bar{\mu}^{(ISO)} = 51,8GPa$., which are rather consistent with the values found in Humbert and Plicque [1972], namely $\bar{K}^{(ISO)} = 94.9-90.2GPa$, and in Ross and Reeder [1992], namely $\bar{K}^{(ISO)} = 94.1 \pm 0.7GPa$.

4.6.1.1.3 Elastic anisotropy of shales

Although shales constitutes nearly three quarter of the clastic fill of sedimentary basins, they have not been much studied in the laboratory compared to other rocks [Jones and Wang, 1981]. This is also the case for elastic anisotropy studies, although shale, together with the sedimentary layer, play an important role in the seismic overall anisotropy of sedimentary formations.

Equation (4.6.1-9) has been applied by Sayers [1994] and [2005] to describe the elastic anisotropy of shales, assuming transverse isotropy for both the crystal symmetry and the ODF. The two inputs of the theory are the stiffness (or compliance) tensor of the shale “crystal” and the Orientation Distribution Function of the “crystals”, defined by the two expansion coefficients W_{200} and W_{400} . We put the word crystal between quotation marks because, instead of crystals, shale is arranged in groups of parallel clay platelets, called “domains” by Aylmore and Quirk [1959].

Different estimations of the stiffness coefficients of these Transversely Isotropic domains of clay platelets can be found in the literature.

Ortega et al. [2007] give $C_{11} = 44.9GPa$, $C_{33} = 24.2GPa$, $C_{44} = 3.7GPa$, $C_{66} = 11.6GPa$ and $C_{13} = 18.1GPa$, which correspond to the anisotropy coefficients $\varepsilon = 0.4277$, $\gamma = 1.0676$ and $\delta = 0.0554$. Note the huge anisotropy strength, especially for the shear wave birefringence coefficient $\gamma > 100\%$.

Sayers [2005] proposes $C_{11} = 40.0GPa$, $C_{33} = 16.8GPa$, $C_{44} = 2.7GPa$, $C_{66} = 13.1GPa$ and $C_{13} = 9.0GPa$, which correspond to the anisotropy coefficients $\varepsilon = 0.6905$, $\gamma = 1.9259$ and $\delta = -0.1307$. Note again the even larger anisotropy strength, especially for the shear wave birefringence coefficient $\gamma > 190\%$, and the negative value of δ .

The explicit expressions of the the effective stiffness coefficients \bar{C}_{IJ} are given by Sayers [1994]:

$$(4.6.1-15) \quad \left\{ \begin{array}{l} \bar{C}_{11} = \bar{K}_0 + \frac{4}{3}\bar{\mu}_0 + \frac{8\sqrt{10}}{105}\pi^2 a_3 W_{200} + \frac{4\sqrt{2}}{35}\pi^2 a_1 W_{400} \\ \bar{C}_{33} = \bar{K}_0 + \frac{4}{3}\bar{\mu}_0 - \frac{16\sqrt{10}}{105}\pi^2 a_3 W_{200} + \frac{32\sqrt{2}}{105}\pi^2 a_1 W_{400} \\ \bar{C}_{13} = \bar{K}_0 - \frac{2}{3}\bar{\mu}_0 + \frac{4\sqrt{10}}{315}\pi^2 (7a_2 - a_3)W_{200} - \frac{16\sqrt{2}}{105}\pi^2 a_1 W_{400} \\ \bar{C}_{44} = \bar{\mu}_0 - \frac{2\sqrt{10}}{315}\pi^2 (7a_2 + 2a_3)W_{200} - \frac{16\sqrt{2}}{105}\pi^2 a_1 W_{400} \\ \bar{C}_{66} = \bar{\mu}_0 + \frac{4\sqrt{10}}{315}\pi^2 (7a_2 + 2a_3)W_{200} + \frac{4\sqrt{2}}{105}\pi^2 a_1 W_{400} \end{array} \right.$$

where the three anisotropy parameters, depending on the elastic stiffness coefficients of the Transversely Isotropic domains of clay particles, are defined by:

$$(4.6.1-16) \quad \left\{ \begin{array}{l} a_1 = C_{11} + C_{33} - 2C_{13} - 4C_{44} \\ a_2 = -2C_{11} + 6C_{66} + 2C_{13} - 2C_{44} \\ a_3 = 4C_{11} - 3C_{33} - C_{13} - 2C_{44} \end{array} \right. ,$$

and \bar{K}_0 and $\bar{\mu}_0$ the effective bulk and shear moduli of a shale with randomly oriented TI domains (i.e. $W_{200} = W_{400} = 0$), classically given by [Fedorov, 1968] :

$$(4.6.1-17) \quad \left\{ \begin{array}{l} 9\bar{K}_0 = 4C_{11} + C_{33} - 4C_{66} + 4C_{13} \\ 15\bar{\mu}_0 = C_{11} + C_{33} + 6C_{44} + 5C_{66} - 2C_{13} \end{array} \right.$$

Applied to the data of Ortega *et al.* [2007] this equation gives $\bar{K}_0 \approx 25.5GPa$ and $\bar{\mu}_0 \approx 7.5GPa$, which does not substantially differ from the values $\bar{K}_0 \approx 21GPa$ and $\bar{\mu}_0 \approx 7GPa$ of Blangy *et al.* [1993]. Sayers [2005] gives smaller $\bar{K}_0 \approx 17.8GPa$ but comparable $\bar{\mu}_0 \approx 8GPa$. In spite of the variability of the shale sampling these results are surprisingly rather consistent.

In the case where the domains of clay particles are perfectly aligned, with their normal parallel to the axis of rotational invariance of the ODF, the expansion coefficients take their maximum values W_{200}^{\max} and W_{400}^{\max} given by [Sayers, 1994]:

$$(4.6.1-18) \quad W_{200}^{\max} = \frac{\sqrt{10}}{8\pi^2} \approx 0.04005 \quad \text{and} \quad W_{400}^{\max} = \frac{3\sqrt{2}}{8\pi^2} \approx 0.05373$$

The three next figures, excerpt from Sayers [2005], illustrate the link between the coefficients W_{200} and W_{400} of the ODF expansion and the effective anisotropy coefficients $\bar{\varepsilon}$, $\bar{\gamma}$ and $\bar{\delta}$ of the shale sample. With the choice of the stiffness coefficients of the Transversely Isotropic domains of clay platelets of the last reference, recalled above, Figures 4.6.1-1, 4.6.1-2 and 4.6.1-3 show the variations of $\bar{\gamma}$, $\bar{\varepsilon}$ and $\bar{\delta}$, respectively, with W_{200} and W_{400} . Each of these three figures are composed of two sub-figures, the sub-figure on the left corresponding to Voigt approximation and the sub-figure on the right to Reuss approximation.

The simplest variation is that of $\bar{\gamma}$ on Figures 4.6.1-1. More precisely, Voigt and Reuss approximations qualitatively give the same results. The effective S-wave birefringence coefficient $\bar{\gamma}$ is always positive, which means that for a vertical axis of symmetry of the ODF the SH-wave always propagates faster in the horizontal direction than in the vertical direction. Also, for propagation in the horizontal direction, the SV-wave is always slower than the SH-wave. The coefficient $\bar{\gamma}$ increases when any of the expansion coefficients W_{200} and W_{400} increases. This is not really surprising because the increase of the coefficients W_{200} and W_{400} corresponds to a better alignment of the clay platelets domains, thus to stronger anisotropy. The sensitivity of $\bar{\gamma}$ to the variations of W_{200} is roughly 1.5 times larger (Voigt approximation) to twice larger (Reuss approximation) than to the variations of W_{400} . The variations of $\bar{\epsilon}$ on Figures 4.6.1-2 are less simple. Voigt and Reuss approximations qualitatively give slightly different results. According to Voigt approximation, the effective P-wave anisotropy coefficient $\bar{\epsilon}$ increases when W_{200} increases, and when W_{400} decreases. Reuss approximation exhibits the same trend but only for W_{200} smaller than approximately 0.02. For $W_{200} > 0.02$ $\bar{\epsilon}$ increases when any of the expansion coefficients W_{200} and W_{400} increases, sensitivity to the variations of W_{200} being markedly larger. For instance, for

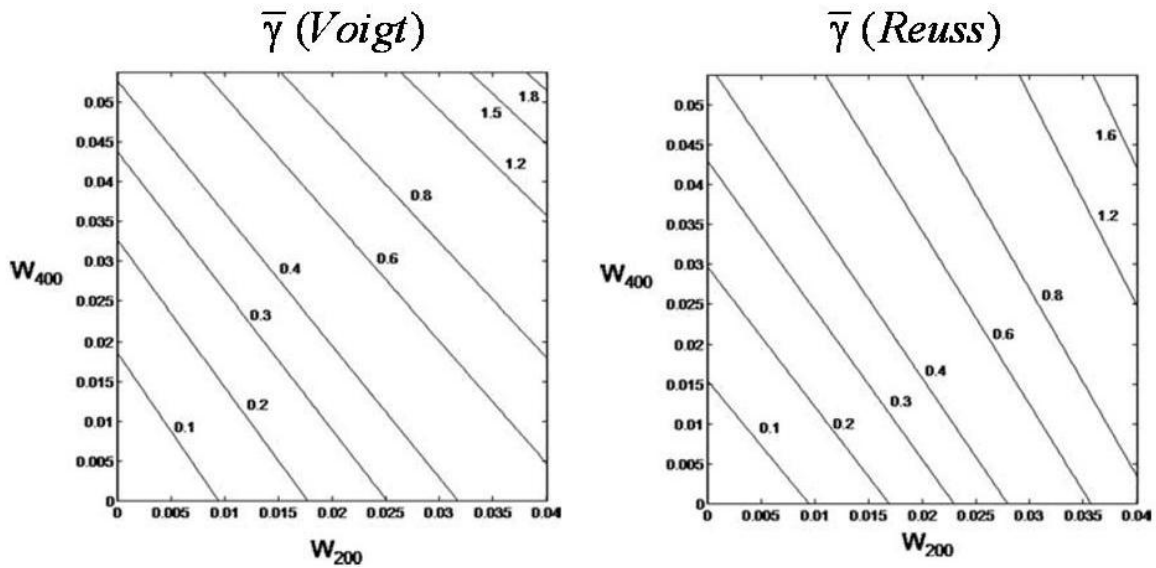


Figure 4.6.1-1: Variation of $\bar{\gamma}$ with W_{200} and W_{400} using (left) Voigt approximation and (right) Reuss approximation. See details in the text for the other parameters (modified after Sayers [2005])

$W_{200} \approx 0.02$ the values of $\bar{\epsilon}$ are virtually unchanged for any variation of the expansion coefficient W_{400} . Voigt and Reuss approximations both almost always predict positive values of the effective P-wave anisotropy coefficient $\bar{\epsilon}$, except for vanishing W_{200} and large values

of W_{400} . This means that for a vertical axis of symmetry of the ODF the P-wave almost always propagates faster in the horizontal direction than in the vertical direction.

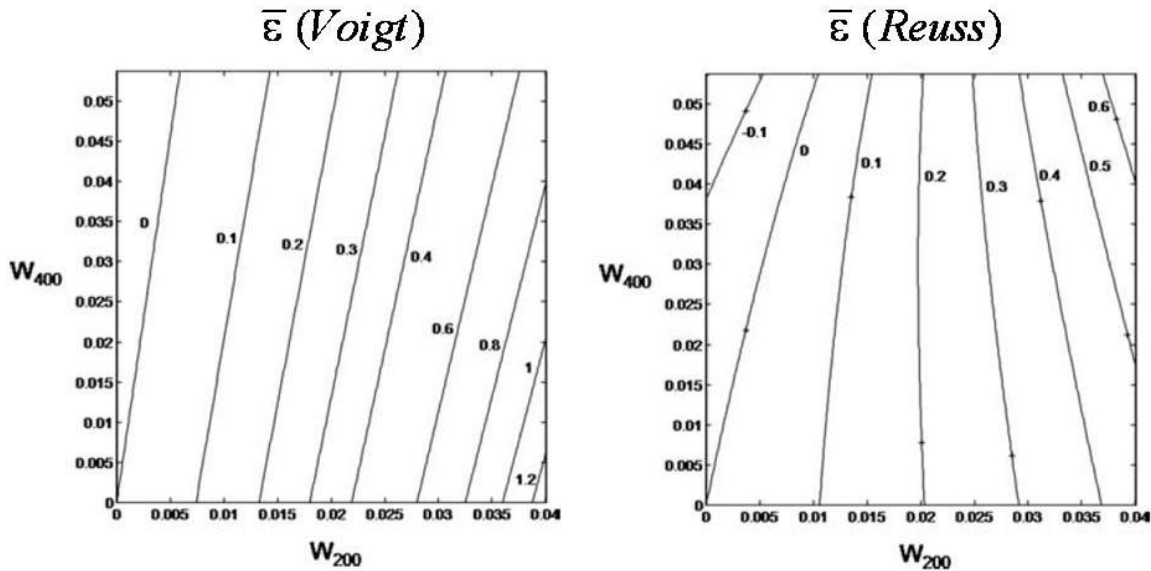


Figure 4.6.1-2: Variation of $\bar{\epsilon}$ with W_{200} and W_{400} using (left) Voigt approximation and (right) Reuss approximation. See details in the text for the other parameters (modified after Sayers [2005])

The variations of $\bar{\delta}$ with W_{200} and W_{400} on Figures 4.6.1-3 substantially differs from those of $\bar{\epsilon}$ and $\bar{\gamma}$. More precisely, simultaneous small or large increase of W_{200} and W_{400} , by roughly the same amount, surprisingly induces no substantial variation of $\bar{\delta}$. This all the more surprising since an increase of the coefficients W_{200} and W_{400} corresponds to better alignment of the clay platelets domains, should induce stronger anisotropy. This tends to mean that the relation between $\bar{\delta}$ and the texture of the rock is rather complex, and still misunderstood. Voigt and Reuss approximations qualitatively give the same results, and predict positive and negative values of $\bar{\delta}$. This is consistent with the large data base of Thomsen [1986a] exhibiting positive and negative values on shale samples determined from laboratory measurements.

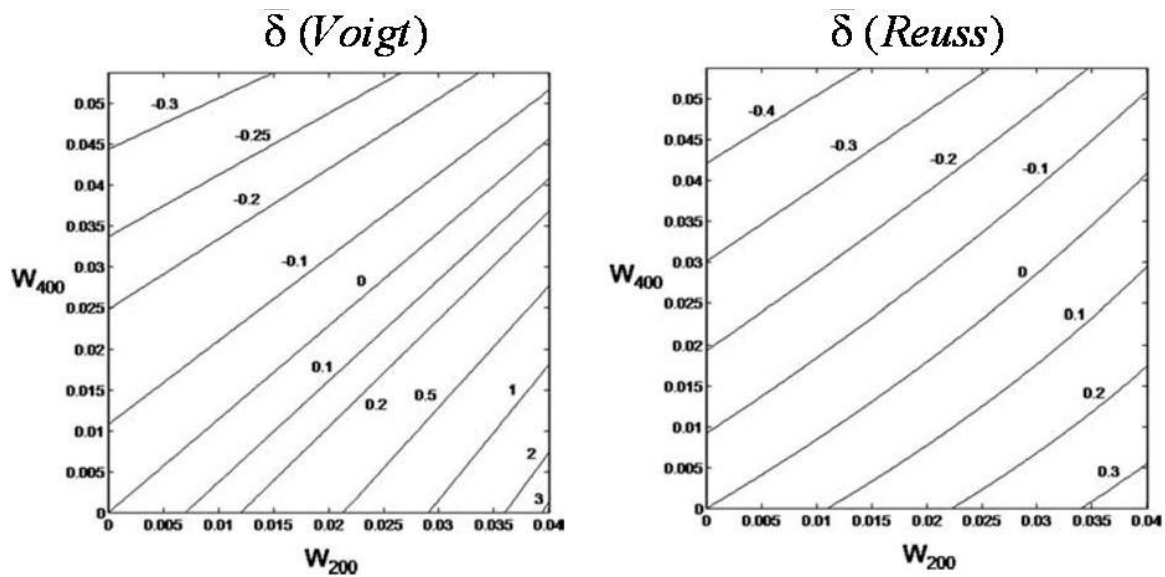


Figure 4.6.1-3: Variation of $\bar{\delta}$ with W_{200} and W_{400} using (left) Voigt approximation and (right) Reuss approximation. See details in the text for the other parameters (modified after Sayers [2005])

Regarding the inverse problem, after Equations (4.6.1-15) to (4.6.1-17), given the assumed stiffness coefficients of the clay platelets domains and the measured five elastic stiffness constants of the shale sample, it is possible to invert the equivalent isotropic effective bulk and shear moduli \bar{K}_0 and $\bar{\mu}_0$ of the shale and the two expansion coefficients W_{200} and W_{400} . In principle the input of the stiffness coefficients of the clay platelets domains imposes the values of \bar{K}_0 and $\bar{\mu}_0$, according to Equation (4.6.1-17). The comparison with the inverted coefficients \bar{K}_0 and $\bar{\mu}_0$ constitutes a first quality control of the inversion. A second quality control is the consistency of the values of the inverted coefficients W_{200} and W_{400} with their physical bounds W_{200}^{\max} and W_{400}^{\max} given by Equation (4.6.1-18).

This has been done with the data of Jones and Wang [1981] on a Cretaceous shale, and of Zinszner et al [2002] on a jurassic shale. The results are summarized in Figure 4.6.1-4. It is a table showing a comparison between the measured and the predicted elastic stiffnesses and anisotropy parameters of a cretaceous shale of the Williston basin, North Dakota [Jones and Wang, 1981] (in column 3) and of a jurassic shale of Tournemire, Aveyron in Southern France [Zinszner et al., 2002] (in column 4).

PETROACOUSTICS – CHAPTER 4

		Cretaceous Williston basin shale [Jones and Wang, 1981]	Jurassic Tournemire shale [Zinszner et al., 2002]
\bar{C}_{33}	measured	22.7	26.85
	inverted (1)	25.39	25.39
	inverted (2)	25.37	25.37
\bar{C}_{44}	measured	5.4	4.77
	inverted (1)	9.82	9.82
	inverted (2)	9.94	9.94
$\bar{\epsilon}$	measured	0.25	0.26
	inverted (1)	0.27	0.27
	inverted (2)	0.27	0.27
$\bar{\gamma}$	measured	0.48	0.45
	inverted (1)	0.25	0.25
	inverted (2)	0.24	0.24
$\bar{\delta}'$	measured	0.51	0.52
	inverted (1)	0.54	0.54
	inverted (2)	0.54	0.54
\bar{K}_0	assumed / inverted (1)	25.5 / 17.8	25.5 / 21.83
	assumed / inverted (2)	17.8 / 17.9	17.8 / 21.89
$\bar{\mu}_0$	assumed / inverted (1)	7.5 / 8.0	7.5 / 8.03
	assumed / inverted (2)	8.0 / 8.0	8.0 / 8.01
W_{200}	inverted (1)	0.02344	0.02806
	inverted (2)	0.01983	0.02382
W_{400}	inverted (1)	0.04153	0.0689 !...
	inverted (2)	0.02421	0.04036

Figure 4.6.1-4: Comparison between the measured and the predicted elastic stiffnesses and anisotropy parameters of the cretaceous shale of Jones and Wang [1981] and of the jurassic shale of Zinszner et al. [2002] . See details in text.

The measured/inverted parameters are listed in the first column, and include \bar{C}_{33} , \bar{C}_{44} , $\bar{\epsilon}$, $\bar{\gamma}$, $\bar{\delta}'$ (an alternate for $\bar{\delta}$ defined by $\bar{\delta}' = \frac{\bar{C}_{13} + 2\bar{C}_{44} - \bar{C}_{33}}{\bar{C}_{33}} = \bar{\delta} + \frac{\bar{\delta}^2}{2(1 - \bar{C}_{44}/\bar{C}_{33})}$ [Sayers, 1994]), \bar{K}_0 , $\bar{\mu}_0$, W_{200} and W_{400} .

For each of the parameters \bar{C}_{33} , \bar{C}_{44} , $\bar{\varepsilon}$, $\bar{\gamma}$, and $\bar{\delta}'$, the measured values, the inverted (1) values and the inverted (2) values. As detailed above, we used two different inputs for the stiffness coefficients of the shale platelets domains, the data of Ortega et al. [2007], here called number (1), and the data of Sayers [2005] here called number (2). The corresponding inversion results are called “inverted (1)” and “inverted (2)” respectively in 4.6.1-4.

For the parameters \bar{K}_0 and $\bar{\mu}_0$, we compared for data number (1) and number (2) the assumed values of \bar{K}_0 and $\bar{\mu}_0$, given by Equation (4.6.1-17), and the corresponding inverted values. Assumed values and inverted values are listed in columns 3 and 4 and are listed in the same cell and separated by a slash “/”. Finally the values of the inverted expansion coefficients W_{200} and W_{400} complete the list.

The results can be summarized in the following way.

Regarding the data of Jones and Wang [1981], the inverted \bar{K}_0 and $\bar{\mu}_0$ are more consistent with the inversion (2) of Sayers [2005] than with inversion (1) of Ortega et al [2007], which tends to underestimate \bar{K}_0 . The inverted values of the expansion coefficients W_{200} and W_{400} by inversion (1) are substantially larger than for inversion (2). This was expected because the shale platelets domain chosen in inversion (2) are substantially more anisotropic than those for inversion (1). More anisotropic shales are the result of more aligned shale platelets domains, thus larger expansion coefficients W_{200} and W_{400} . The comparison between the measured parameters and the inverted parameters \bar{C}_{33} , \bar{C}_{44} , $\bar{\varepsilon}$, $\bar{\gamma}$, $\bar{\delta}'$ is rather clear. The agreement between experiment and theory is reasonable for the P-wave parameters, that is to say the P-wave modulus \bar{C}_{33} for vertical propagation (measured: 22.7GPa to be compared with inverted: 25.39GPa and 25.37GPa) and the P-wave anisotropy coefficient $\bar{\varepsilon}$ (measured: 0.25 to be compared to inverted: 0.27 and 0.27). In contrast the S-wave parameters are systematically underestimated, that is to say the S-wave modulus \bar{C}_{44} for vertical propagation (measured: 5.4GPa to be compared with inverted: 9.82GPa and 9.94GPa) and the shear-wave birefringence coefficient $\bar{\gamma}$ (measured: 0.48 to be compared to inverted: 0.25 and 0.24).

Regarding the data of Zinszner et al. [2002], in contrast with the previous data, the inverted \bar{K}_0 and $\bar{\mu}_0$ are more consistent with the inversion (1) of Ortega et al [2007], than with inversion (2) of Sayers [2005]. \bar{K}_0 is overestimated by inversion (2). Once again the inverted values of the expansion coefficients W_{200} and W_{400} by inversion (1) are substantially larger than for inversion (2). The inverted coefficient $W_{400} \approx 0.0689$ by inversion (1) is even larger than the maximum admissible value in theory $W_{400}^{\max} \approx 0.05373$, after Equation (4.6.1-18).

The same conclusions as for the previous data set can be made regarding the comparison between the measured parameters and the inverted parameters \bar{C}_{33} , \bar{C}_{44} , $\bar{\varepsilon}$, $\bar{\gamma}$, $\bar{\delta}'$ and need not to be reiterated.

In conclusion, the theory can describe rather well the behaviour of the P-wave but tends to underestimate the anisotropy of the S-wave and the associated compliances. The different values obtained for the effective bulk and shear moduli \bar{K}_0 and $\bar{\mu}_0$ of the shale with randomly oriented TI clay platelets domains, seems to illustrate the variability of the elastic properties of the shale platelets. This contributes to complicate the inversion process. Anyway, in the absence of direct measurements of the elastic properties of the clay platelets domains, there is a clear need for a better estimation of the corresponding elastic stiffnesses in order to allow obtaining quantitative texture informations on shales from elastic anisotropy measurements.

Finally, up to now we have left apart the effect of the presence of compliant pores (cracks, microfractures...) in shales on elastic anisotropy, which has also been studied by Sayers [2005]. Beyond the various theory which have been developed, the main issue is the actual presence or not of the compliant pores in the shale sample due to the recovery process of the sample and the lack of perfect preservation process. The topic is quite controversial due to the contrasted experimental observations:

- some authors (e.g., Hornby [1998]; Sayers [2005]) measured substantial pressure dependence of shale velocities, even on preserved samples. Initially large anisotropy strengths on unstressed samples are substantially reduced under confining pressure. In both references the decrease in overall anisotropy of the shales with increasing confining pressure was found to be consistent with theoretical modelling of shale behaviour.
- some other authors reported the absence of stress dependence of the shale velocities on almost all the numerous and very freshly recovered shale samples of Amoco, before the merge with BP in December 1998 (L. Thomsen, personal communication on these unpublished data). Furthermore the stress-dependence appeared with time on the same samples, which seriously advocate for the presence of microcracks induced by the recovery process. Another example is the unaltered jurassic shale sample of Zinszner et al. (2002), which virtually exhibit no pressure dependence of the velocities and of the anisotropy coefficients. Furthermore, in the same study but unpublished, a collection of shale samples of the same geological period but substantially altered exhibited clear stress-dependence, which once again advocate for the major role of non-natural mechanical defects in the stress-dependence of shale velocities.

Note that effect of compliant pores (cracks, microfractures, grain conatcts...) on elastic anisotropy in general is discussed in sub-section 4.6.2.

4.6.1.2 Thinly layered media

A stack of thin isotropic layers randomly distributed in the vertical direction is the most common idealization of anisotropic geological media, especially sedimentary formations, as illustrated by Figure 4.6.1-5. By “Thin layers” we mean that the typical thickness of each individual layer is much smaller than the elastic wavelength. Although it is not the main cause of most of the observed anisotropy, even in sedimentary formations as will be

explained, this is the earliest and the most studied model, as pointed out by Helbig [1994]. From the point of view of the symmetry type, transverse isotropy with a vertical symmetry axis (VTI) is certainly the most likely type of symmetry in sedimentary formations. Due to symmetry of the sedimentation process in a passive basin driven by the gravity, characterized by a polar vector of symmetry ∞m (of a cone at rest) with an axis of rotational invariance and an infinite number of symmetry plane (i.e. any plane containing the infinite-fold axis) [see Figure 4.2.2-1 and the corresponding comments]. As a consequence, any physical property of such media, in particular elastic property, must have this symmetry level at least. Obviously, this is before any tectonic process operates, possibly inducing fracture/cracks and breaking the rotational invariance.

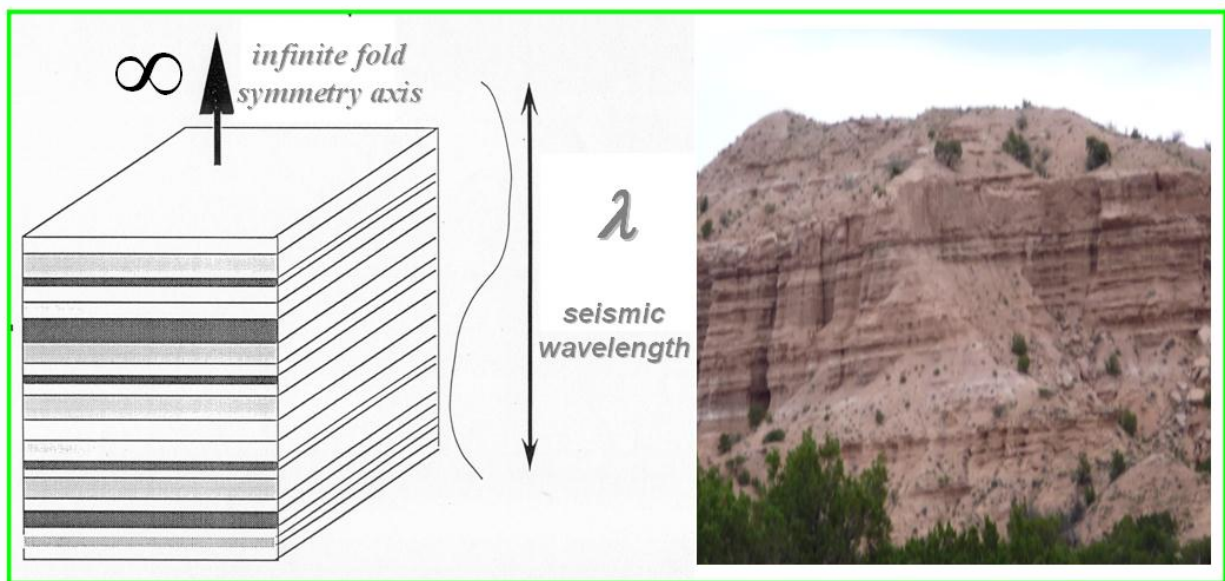


Figure 4.6.1-5: Layer-induced anisotropy the most common example of vertical transverse isotropy (VTI) in sedimentary formations:

(Left) Idealized model made of stack of thin horizontal layers made of isotropic material randomly distributed in the vertical direction, and

(Right) Photograph of an outcrop of Tesuque formation, close to Tesuque pueblo near Santa Fe (New Mexico), mainly composed of poorly consolidated buff-red arkosic sand, silts, clays and pebble beds, after Anderholm [1994].

Rudzki himself was the first to refer to a layer-induced anisotropic model [Rudzki, 1898].

Bruggman [1937] seems to be the first to have solved the direct problem, moreover in an elegant and concise way (e.g., Helbig [1994]), followed by many others (e.g., Riznichenko [1949]; Postma [1955]; Helbig [1956] and [1958]; Backus [1962]; Schoenberg & Muir [1989]). Nevertheless the solution described in the next equation is called Backus average solution in applied geophysics literature.

The direct problem is the following: Given the stiffness matrices $\mathbf{C}^{(i)}$ ($i=1,2,\dots,N$) of the constituents, N designating the number of constituents of the compound medium, and $\eta^{(i)}$ the volume fraction of the constituent number i , what is the stiffness matrix $\bar{\mathbf{C}}$ of the compound medium?

The generalized Hooke's law in each constituent writes:

$$(4.6.1-19) \quad \boldsymbol{\sigma}^{(i)} = \mathbf{C}^{(i)} \boldsymbol{\varepsilon}^{(i)}$$

where $\boldsymbol{\sigma}^{(i)}$ and $\boldsymbol{\varepsilon}^{(i)}$ designate respectively the stress and the strain in the constituent number i . Given the average stress $\langle \boldsymbol{\sigma} \rangle$ and the average strain $\langle \boldsymbol{\varepsilon} \rangle$ (the brackets $\langle \rangle$ meaning averaging over a Representative Elementary Volume (see definition in Chapter 1 §1.3.3) of the compound medium) defined by:

$$(4.6.1-20) \quad \langle \boldsymbol{\sigma} \rangle = \sum_{i=1}^N \eta^{(i)} \boldsymbol{\sigma}^{(i)} \quad \text{and} \quad \langle \boldsymbol{\varepsilon} \rangle = \sum_{i=1}^N \eta^{(i)} \boldsymbol{\varepsilon}^{(i)},$$

the direct problem consists in finding the stiffness matrix $\bar{\mathbf{C}}$ linking the average stress $\langle \boldsymbol{\sigma} \rangle$ and the average strain $\langle \boldsymbol{\varepsilon} \rangle$:

$$(4.6.1-21) \quad \langle \boldsymbol{\sigma} \rangle = \bar{\mathbf{C}} \langle \boldsymbol{\varepsilon} \rangle$$

Bruggeman [1937], Backus [1962] and Schoenberg & Muir [1989] approached the problem by considering the continuous quantities across each interface between the layers, assuming that the interfaces are perfectly welded. If the layers are normal to the 3-direction, all the displacements must be continuous, as well as their gradient in the 12-plane. Thus the strain components $\varepsilon_1 (= \varepsilon_{11})$, $\varepsilon_2 (= \varepsilon_{22})$ and $\varepsilon_6 (= 2\varepsilon_{12})$ are continuous across each interface, and as a consequence have a constant value throughout the compound medium. The same result stands for the three stress components on a surface normal to the 3-direction, due to the continuity of the stress across each interface. These continuous stress components are $\sigma_3 (= \sigma_{33})$, $\sigma_4 (= \sigma_{23})$ and $\sigma_5 (= \sigma_{13})$.

The next step is to express the continuous quantities as functions of the discontinuous remaining stresses $\sigma_1 (= \sigma_{11})$, $\sigma_2 (= \sigma_{22})$ and $\sigma_6 (= \sigma_{12})$, and strains $\varepsilon_3 (= \varepsilon_{33})$, $\varepsilon_4 (= 2\varepsilon_{23})$ and $\varepsilon_5 (= 2\varepsilon_{13})$. Schoenberg & Muir [1989] solved this problem for arbitrary anisotropic constituents. In the case of isotropic or transversely isotropic constituents, the most useful cases in practice, the results take the simple form [Helbig, 1998]:

$$(4.6.1-22) \quad \mathbf{v} = \mathbf{Q} \mathbf{f}$$

where:

$$(4.6.1-23) \quad \mathbf{v}^t = (\sigma_1 \quad \sigma_2 \quad \varepsilon_3 \quad \varepsilon_4 \quad \varepsilon_5 \quad \sigma_6)^t \quad \text{and} \quad \mathbf{f}^t = (\varepsilon_1 \quad \varepsilon_2 \quad \sigma_3 \quad \sigma_4 \quad \sigma_5 \quad \varepsilon_6)^t$$

designate the vector \mathbf{v} of the variable quantities layer by layer and \mathbf{f} of the continuous quantities. Note for both vectors the mix between the stress and the strain components, but the preserved order of the indices.

The square matrix \mathbf{Q} in Equation (4.6.1-22) is given by:

$$(4.6.1-24) \quad \mathbf{Q} = \begin{pmatrix} C_{11} - C_{13}^2 / C_{33} & C_{11} - 2C_{66} - C_{13}^2 / C_{33} & C_{13} / C_{33} & 0 & 0 & 0 \\ C_{11} - 2C_{66} - C_{13}^2 / C_{33} & C_{11} - C_{13}^2 / C_{33} & C_{13} / C_{33} & 0 & 0 & 0 \\ -C_{13} / C_{33} & -C_{13} / C_{33} & 1 / C_{33} & 0 & 0 & 0 \\ 0 & 0 & 0 & 1 / C_{44} & 0 & 0 \\ 0 & 0 & 0 & 0 & 1 / C_{44} & 0 \\ 0 & 0 & 0 & 0 & 0 & C_{66} \end{pmatrix}$$

Now let us take the average over the entire compound medium of each member of Equation (4.6.1-22) weighted by the respective volume fraction of each constituent:

$$(4.6.1-25) \quad \langle \mathbf{v} \rangle = \langle \mathbf{Q} \mathbf{f} \rangle$$

Because the vector \mathbf{f} is constant through the entire compound medium, Equation (4.6.1-22) takes the simplified form:

$$(4.6.1-26) \quad \langle \mathbf{v} \rangle = \langle \mathbf{Q} \rangle \mathbf{f} = \langle \mathbf{Q} \rangle \langle \mathbf{f} \rangle$$

The last equality is due to the fact that $\mathbf{f} = \langle \mathbf{f} \rangle$. The matrix linking the average quantities $\langle \mathbf{v} \rangle$ and $\langle \mathbf{f} \rangle$ can be called $\bar{\mathbf{Q}}$ and is defined by:

$$(4.6.1-27) \quad \langle \mathbf{v} \rangle = \bar{\mathbf{Q}} \langle \mathbf{f} \rangle$$

which by identification with Equation (4.6.1-26) leads to:

$$(4.6.1-28) \quad \bar{\mathbf{Q}} = \langle \mathbf{Q} \rangle \quad \text{or} \quad \bar{Q}_{IJ} = \langle Q_{IJ} \rangle \quad I, J = 1, 2, \dots, 6$$

Due to the expression of the matrix \mathbf{Q} given by Equation (4.6.1-24), the previous equation implies the following five relations:

$$(4.6.1-29) \quad \begin{cases} \bar{C}_{33} = \langle 1 / C_{33} \rangle^{-1} & ; & \bar{C}_{44} = \langle 1 / C_{44} \rangle^{-1} & ; & \bar{C}_{66} = \langle C_{66} \rangle \\ \bar{C}_{13} / \bar{C}_{33} = \langle C_{13} / C_{33} \rangle & ; & \bar{C}_{11} - \bar{C}_{13}^2 / \bar{C}_{33} = \langle C_{11} - C_{13}^2 / C_{33} \rangle \end{cases}$$

which allow to reconstruct the complete elasticity matrix $\bar{\mathbf{C}}$ of the compound transversely isotropic medium. We can see that for some elastic coefficients the effective elastic coefficient is a simple average, either of the stiffness, for instance \bar{C}_{66} , or of the compliances, for instance $1 / \bar{C}_{33}$ and $1 / \bar{C}_{44}$. For some others the effective elastic coefficient is more complicated, for instance \bar{C}_{11} and \bar{C}_{13} .

The density of the compound medium being obviously given by $\bar{\rho} = \langle \rho \rangle$, the complete directional dependence of the exact phase velocities of the three bulk waves can be computed using Equation (4.5.1-2).

The next figures summarize the main predictions of the model.

In Figures 4.6.1-6 and 4.6.1-8 we plotted the anisotropy coefficients $\bar{\epsilon}$ (curves in blue lines), $\bar{\delta}$ (in green lines), and $\bar{\gamma}$ (in red lines), all defined in sub-section 4.5.1, characterizing the compound medium as function of the volume fraction of shale. Both of these figures correspond to thinly layered models, namely a shale/sand model for Figures 4.6.1-6 and a shale/dolomite model for Figure 4.6.1-8.

Two sub-figures compose each of these figures, namely on the left side the case of strong contrast between the constituents of the model, and on the right side the case of weak contrast. On each subfigure two cases are considered, namely the case where all the constituents are isotropic (curves in dashed lines), and the case where all the constituents are transversely isotropic (curves in solid lines). The chosen parameters are given in Figure 4.6.1-7 for the shale/sand model of Figure 4.6.1-6, and in Figure 4.6.1-9 for the shale/dolomite model of Figure 4.6.1-8. They are all taken from the database of Mavko *et al.* [1998]. The input parameters of the models are the density $\rho^{(i)}$, the vertical P-wave velocity $V_{P0}^{(i)}$, the vertical S-wave velocity $V_{S0}^{(i)}$, and, for anisotropic constituent only, the anisotropic coefficients $\epsilon^{(i)}$, $\gamma^{(i)}$ and $\delta^{(i)}$ of each constituent ($i=2$ for shale and $i=1$ for the other constituent).

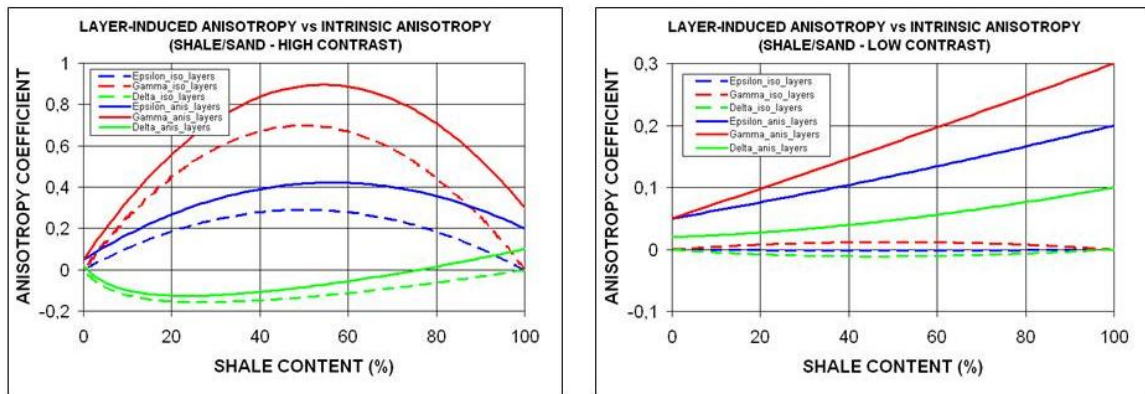


Figure 4.6.1-6: Anisotropy coefficients $\bar{\epsilon}$ (blue lines), $\bar{\delta}$ (green lines), and $\bar{\gamma}$ (red lines) as function of the shale content (in %) a shale/sand thinly layered model: (left) with high contrast between the elastic properties of the constituents, and (right) with low contrast between the elastic properties of the constituents.

For both figures the dashed lines correspond to the case of isotropic constituents, and the solid lines to anisotropic constituents. Note the different scales on the vertical axes of the two figures. See details in text.

PETROACOUSTICS – CHAPTER 4

	Strong contrast case		Weak contrast case	
	1st constituent (SAND)	2nd constituent (SHALE)	1st constituent (SAND)	2nd constituent (SHALE)
$\rho^{(i)}$ (kg/m^3)	2640	2340	2090	2340
$V_{P0}^{(i)}$ (m/s)	5520	2900	3130	2900
$V_{S0}^{(i)}$ (m/s)	3600	1400	1730	1400
$\varepsilon^{(i)}$	0,05	0,2	0,05	0,2
$\gamma^{(i)}$	0,05	0,3	0,05	0,3
$\delta^{(i)}$	0,02	0,1	0,02	0,1

Figure 4.6.1-7: Input parameters for the shale/sand models of Figure 4.6.1-6. See details in text.

For the cases of strong contrast, the chosen velocity contrasts are very large, typically of the order of a factor of 2, which is not representative of common situations in the field. More precisely such contrasts can be encountered very locally on acoustic well logs but not repeatedly at the scale of a seismic wavelength (typical a few 10^1m to 10^2m , see detail on Chapter 1 Figure 1.2.2-8 and the corresponding comments).

These strong contrast cases are considered only to illustrate numerically the phenomenon. The weak contrast cases, at least in average at the scale of the seismic wavelength, are more representative of the field situation.

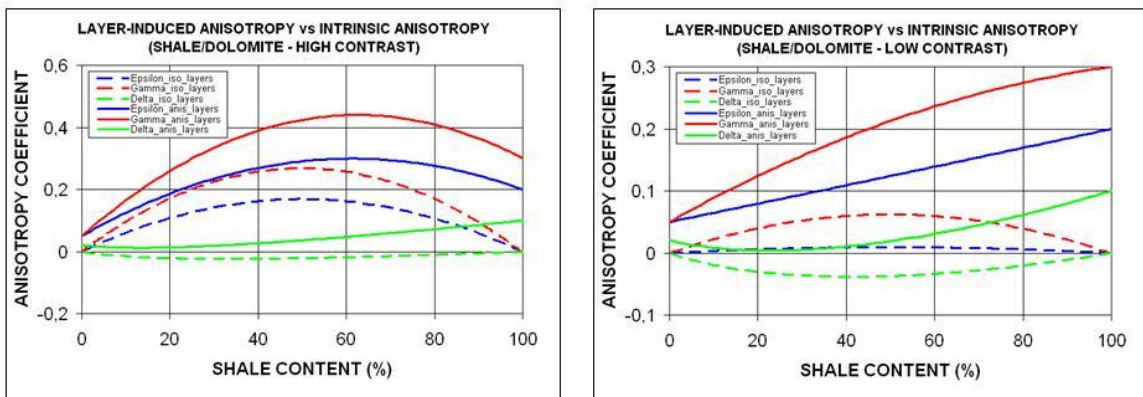


Figure 4.6.1-8: Same as Figure 4.6.1-6 in a shale/dolomite thinly layered model. Note the different scales on the vertical axes of the two figures. See details in text.

	Strong contrast case		Weak contrast case	
	1st constituent (DOLOMITE)	2nd constituent (SHALE)	1st constituent (DOLOMITE)	2nd constituent (SHALE)
$\rho^{(i)} (kg/m^3)$	2450	2340	2270	2340
$V_{P0}^{(i)} (m/s)$	5200	2900	3410	2900
$V_{S0}^{(i)} (m/s)$	2700	1400	2010	1400
$\varepsilon^{(i)}$	0,05	0,2	0,05	0,2
$\gamma^{(i)}$	0,05	0,3	0,05	0,3
$\delta^{(i)}$	0,02	0,1	0,02	0,1

Figure 4.6.1-9: Input parameters for the shale/dolomite models of Figure 4.6.1-8. See details in text.

Regarding anisotropy, in order to separate the layer-induced anisotropy from the anisotropy induced by the intrinsic anisotropy of the constituents on the overall anisotropy we considered two cases. In the first case (curves in dashed lines) all the constituents are isotropic, that is to say the anisotropic coefficients $\varepsilon^{(i)}$, $\gamma^{(i)}$ and $\delta^{(i)}$ are all equal to zero, the remaining parameters being unchanged. The overall anisotropy is only due to the layering. The non-vanishing anisotropy coefficients are used in the second case (curves in solid lines). We choose cases where the intrinsic anisotropy of the shale constituent ($\varepsilon^{(2)} = 0.2$, $\gamma^{(2)} = 0.3$ and $\delta^{(2)} = 0.2$) dominates the anisotropy of the other constituent ($\varepsilon^{(1)}$, $\gamma^{(1)}$, $\delta^{(1)} < 0.05$), which is often the case in the field. As a consequence an increasing volume fraction of shale induce an increasing intrinsic anisotropy at the scale of the compound medium. This intrinsic anisotropy is cumulated with the layer-induced anisotropy in the contribution to the overall anisotropy. The difference between the curve in solid line and the corresponding curve in dashed line is the part of the intrinsic anisotropy to the overall anisotropy. For a vanishing shale content this difference is equal to the intrinsic anisotropy of the non-shale constituent. In contrast for a 100% shale model this difference is equal to the intrinsic anisotropy of the shale constituent, These are consistent results.

The other results can be summarized in the following way:

- Only strong contrast of elastic properties (especially the shear moduli $\mu^{(i)}$), seldom encountered in reality, can induce substantial purely layer-induced anisotropy, that is to say anisotropy larger than 10%. This implies in practice that overall anisotropy larger than 10% cannot reasonably be purely layer-induced. Intrinsic anisotropy of at least one of the constituents (mainly shale in sedimentary basin) has to be involved.
- In the case of isotropic constituents, no contrast of the shear moduli $\mu^{(i)}$ imply isotropy of the compound medium, even in the presence of strong contrast of the bulk modulus or P-wave velocity [Helbig, 1998]. In the case of strong contrast, the purely

layer-induced anisotropy in the shale/sand model is substantially larger than that in the shale/dolomite model essentially because the S-wave velocity contrast, and as a consequence the shear modulus contrast, is substantially larger in the first model ($V_{S0}^{(1)} / V_{S0}^{(2)} > 2.50$) than in the second model ($V_{S0}^{(1)} / V_{S0}^{(2)} < 1.95$).

- in the presence of moderately to strongly anisotropic constituents (here shale), the intrinsic anisotropy of this constituent rapidly dominates the purely layer-induced anisotropy, as long as the volume fraction of this constituent becomes substantial. Roughly the overall anisotropy increases with the volume fraction of these anisotropic constituents.
- Purely layer-induced anisotropy always lead to positive values of the anisotropy coefficients $\bar{\epsilon}$ and $\bar{\gamma}$. This means that, for horizontal layers, the P-wave and the SH-wave always propagate faster along the layers than in the perpendicular direction. Also, for propagation in the horizontal direction, the SV-wave is always slower than the SH-wave.
- The effective anisotropy coefficient $\bar{\delta}$ can be positive or negative (e.g., see Figure 4.6.1-6: on the left side). Its absolute value is always smaller than the other anisotropy coefficients, and such that $\bar{\epsilon} - \bar{\delta} > 0$. In fact purely layer-induced anisotropy with stable isotropic constituent cannot exhibit $\bar{\epsilon} - \bar{\delta} < 0$ [Backus, 1962].

Replacing the complete set of the numerous parameters of the different constituents of a thinly layered geological formation by a considerably reduced number of equivalent VTI parameters of the compound medium at the seismic scale is important in seismic processing. This is illustrated by Figure 4.6.1-10 with the validation test made by Liner and Fei [2006] on data of a predominantly carbonate section, from a well of eastern Saudi Arabia. This figure is composed of three sub-figures. The sub-figure on the left-hand side shows a density log section and the corresponding P-wave and S-wave logs sections, roughly between the depths 3100m and 3600m. The sub-figure in the center part shows a snapshot of the waveform computed by 200 Hz finite difference method with depth sampling of roughly 30cm. From the top to the bottom of the section, this represents depth interval slightly larger than 500m sampled nearly feet by feet. This roughly represents 1670 depth points, each associated with 3 parameters (ρ , V_P and V_S), which makes a total of $1670 \times 3 = 5010$ parameters.

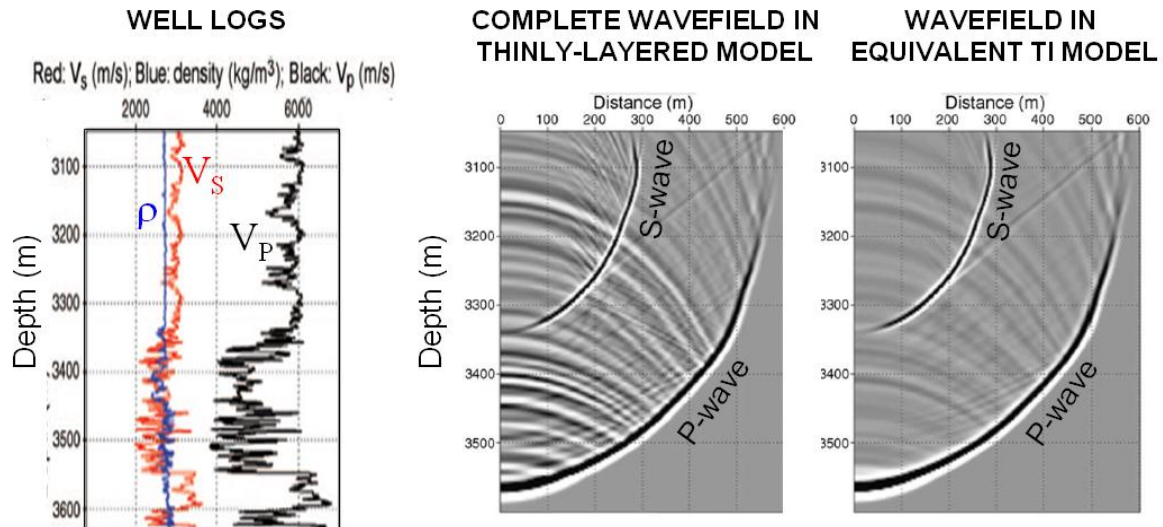


Figure 4.6.1-10: Numerical validation of the VTI averaging defined by Equation (4.6.1-2) illustrated by: a comparison between

(Center figure) the wavefield snapshot from 200 Hz finite difference simulation with depth sampling of roughly 30cm of the isotropic layered model of the figure on the left (obtained from measured density and acoustic logs in a predominantly carbonate section from a well of eastern Saudi Arabia), and

(Figure on the right side) the wavefield computed in the VTI equivalent medium with averaging length equal to 130% of the minimum dominant wavelength (roughly 8.5 m) (modified after Liner and Fei [2006]). See details in the text.

The stack of thin isotropic layers is replaced by a vertically smoother VTI elastic model using the averaging process summarized by Equation (4.6.1-11). The depth window for averaging is 130% of the minimum dominant wavelength (here 8.5 m), which is roughly 11m. The total depth interval of 500m sampled at 11m, roughly represents 45 depth points, each associated with 5 VTI parameters (ρ , V_P and V_S), which makes a total of $45 \times 5 = 225$ parameters, instead of more than 5000 in the stack of thin isotropic model. This constitutes a substantial reduction of the number of parameters of the model, roughly a division by a factor 20. Two-dimensional VTI elastic finite difference modeling was done on this model, and is illustrated by the subfigure on the right side. The first striking result is the absence of a loss of accuracy for the specular arrivals. The wavefront of the P-wave and of the SV-wave are perfectly reproduced, as well as the major reflections (corresponding to the the upgoing wavefronts). Unfortunately, the reduction of the number of parameters has a cost. One of them is the loss of integrity of the scattered field, for instance just after the specular wavefronts, which is due to the fact that the averaging length is over five times the limit for exact preservation of the wavefield, as detailed in the last reference.

4.6.2 Anisotropy due to aligned compliant pores (cracks, fractures, grain contacts...)

4.6.2.1 Fractures media with non-welded (linear slip) interfaces

4.6.2.1.1 The general formulation

In the framework of conventional seismic theories, the strain and the stress induced by an elastic wave are perfectly continuous when crossing the boundaries between different media (e.g., Aki and Richards [1980]). In theory it is possible to relax some of these conditions in considering less perfect reflectors. The most common model assumes the perfect continuity of the stresses induced by the seismic waves but introduces the discontinuity of the displacements at the reflectors (e.g., Tattersal [1973]; Schoenberg [1980]). Such a model has been adapted to deduce the effective seismic parameters of a fractured media (e.g., Schoenberg and Douma [1988]; Schoenberg and Sayers [1995]). Somehow or other all these models are more or less sophisticated versions of no-interaction Reuss model summarized by Eq. (4.6.1-7) in which the interactions between the microheterogeneities, here the cracks/fractures are neglected.

More precisely, after the last reference, if one considers an elementary representative volume V of the fractured medium, the average strain ϵ_{ij} over the volume V can always decomposed into the sum of two terms as follows:

$$(4.6.2-1) \quad \epsilon_{ij} = \epsilon_{ij}^{(m)} + \epsilon_{ij}^{(frac)}$$

where $\epsilon_{ij}^{(m)}$ and $\epsilon_{ij}^{(frac)}$ designate respectively the macroscopic strain associated with the intact rock matrix (rock without any fracture) and the additional macroscopic strain due to the presence of the fractures.

The macroscopic strain $\epsilon_{ij}^{(m)}$ is simply given by:

$$(4.6.2-2) \quad \epsilon_{ij}^{(m)} = S_{ijkl}^{(m)} \sigma_{kl}$$

where $S_{ijkl}^{(m)}$ designates the average compliance tensor of the intact rock, which may be of arbitrary symmetry, and σ_{kl} the macroscopic stress over the volume V . In the long wavelength limit one can assume that the wave-induced macroscopic stress is constant over the volume V . The interactions between the assumed roughly plane and parallel fractures being neglected, if S_p denotes the surface of the p^{th} fracture in the volume V the last reference introduces the "fracture compliance tensor" Z_{ij} , defined by:

$$(4.6.2-3) \quad Z_{ij} \sigma_{jk} n_k = \frac{1}{V} \sum_p \int_{S_p} [u_i] dS$$

where n_k designates the normal to the fracture planes, and $[u_i]$ the discontinuity of the displacement u_i across a fracture. The integral in the right-hand member of this equation is

computed on the surface S_p of the p^{th} fracture and summed over all the fractures. The tensor Z_{ij} is a symmetric tensor of rank 2, of which the components have the dimension of the inverse of a stress. The case $Z_{ij} = 0$ implies that the average displacement discontinuity in the right hand member of Eq. (5.3.3-20) also vanishes since the stress has finite value. This corresponds to perfectly rigid fractures, not visible by the seismic wave, for which $\varepsilon_{ij}^{(frac)} = 0$ in Eq. (5.3.3-18). In contrast, in the case where the norm of the tensor Z_{ij} is infinite (some of its components have infinite value) the average stress σ_{jk} must vanish in order to allow finite value of the average displacement discontinuity. This corresponds to infinitely compliant fractures unable to transmit the elastic wave.

Using Eq. (4.6.2-3) the additional strain due to the fractures is simply given by:

$$(4.6.2-4) \quad \varepsilon_{ij}^{(frac)} = \frac{1}{2} \left(Z_{iq} \sigma_{qs} n_s n_j + Z_{jt} \sigma_{tr} n_r n_i \right)$$

If more than a single family of parallel fractures are considered, the q^{th} family being characterized by its normal $n_i^{(q)}$ and by its compliance tensor $Z_{ij}^{(q)}$, the overall additional strain induced by all the non-interacting fractures is simply equal to:

$$(4.6.2-5) \quad \varepsilon_{ij}^{(frac)} = \sum_q \frac{1}{2} \left(Z_{ir}^{(q)} \sigma_{rs} n_s^{(q)} n_j^{(q)} + Z_{jt}^{(q)} \sigma_{tr} n_r^{(q)} n_i^{(q)} \right)$$

One can introduce the additional compliance tensor $S_{ijkl}^{(frac)}$ due to the fracture defined by:

$$(4.6.2-6) \quad S_{ijkl}^{(frac)} = S_{ijkl} - S_{ijkl}^{(m)}$$

where S_{ijkl} is the compliance tensor of the fractured rock. Because the stress is assumed constant over the volume V one has:

$$(4.6.2-7) \quad \varepsilon_{ij}^{(frac)} = S_{ijkl}^{(frac)} \sigma_{kl}$$

Using Eq. (A5) this gives:

(4.6.2-8)

$$S_{ijkl}^{(frac)} = \sum_q \frac{1}{4} \left(Z_{ik}^{(q)} n_j^{(q)} n_l^{(q)} + Z_{jk}^{(q)} n_i^{(q)} n_l^{(q)} + Z_{il}^{(q)} n_j^{(q)} n_k^{(q)} + Z_{jl}^{(q)} n_i^{(q)} n_k^{(q)} \right)$$

It is important to notice that the additional compliance due to the fractures is only function of the "fracture compliance tensor" Z_{ij} introduced in Eq. (4.6.2-3). According to Eq. (4.6.2-8)

and to the definition of Z_{ij} , in the case of one family of identical fractures the additional compliance tensor is proportional to the number of fractures per unit volume of the fractured medium. Furthermore since the tensor Z_{ij} is global tensor derived from a summation of displacement discontinuities due to fractures contained in the elementary representative volume V , there is a complete elastic equivalence between a medium containing a sparse family of compliant fractures and a medium containing a dense family of rather stiff fractures, at least in the context of this model.

4.6.2.1.2 *Special case of an isotropic medium with a single family of rotationally invariant parallel fractures*

A particular convenient case extensively used in the literature (e.g., Schoenberg et Douma [1988]; Arts [1993]) is the case of rotationally invariant fracture set of normal n_k , for which:

$$(4.6.2-9) \quad Z_{ij} = (Z_N - Z_T) n_i n_j + Z_T \delta_{ij}$$

where Z_N and Z_T designate the overall normal and tangential compliances of the fractures (see Fig.4.6.2-1), and δ_{ij} the Kronecker tensor (with $\delta_{ij} = 0$ for $i \neq j$ and $\delta_{ij} = 1$ for $i=j$). The fractured medium is Transversely Isotropic or rotationally invariant about an axis parallel to the direction normal to the fracture planes.

If the normal to the fractures is parallel to the Z axis the only non-zero components of the additional compliance tensor $S^{(frac)}$ due to the fracture are:

$$(4.6.2-10) \quad \begin{cases} S_{33}^{(frac)} = Z_N \\ S_{44}^{(frac)} = S_{55}^{(frac)} = Z_T \end{cases}$$

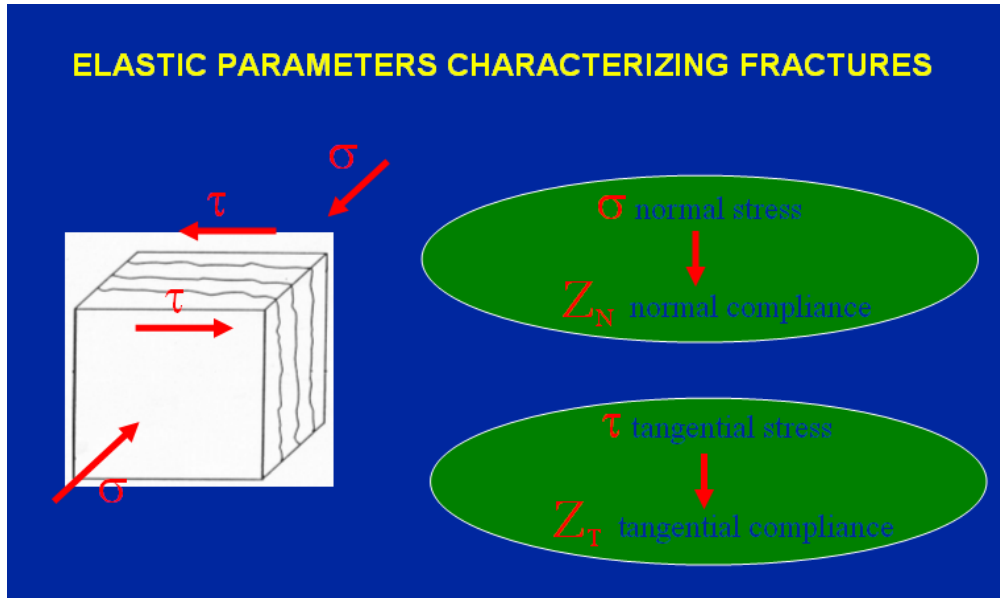


Figure 4.6.2-1: Fig.5.3.3-1: Parameters characterizing a medium containing a single family of rotationally invariant parallel fractures.

where the overall normal and tangential compliances Z_N and Z_T are linked to the individual compliance S_N and S_T of a single fracture and to the number of fractures per unit length n in the direction normal to the fracture planes by the relations:

$$(4.6.2-11) \quad Z_N = n S_N \quad \text{and} \quad Z_T = n S_T$$

As a consequence, if C and $C^{(m)}$ are the stiffness tensors of fractured rock and of the intact rock, the only non-zero components of the perturbation stiffness tensor $\Delta C^{(frac)} = C - C^{(m)}$ induced by the fractures are (Schoenberg and Douma [1988] ; Arts [1993]):

$$(4.6.2-12) \quad \left\{ \begin{array}{l} \Delta C_{11}^{(frac)} = \Delta C_{12}^{(frac)} = \Delta C_{22}^{(frac)} = -\zeta_1 \varepsilon_N \\ \Delta C_{13}^{(frac)} = \Delta C_{23}^{(frac)} = -\zeta_2 \varepsilon_N \\ \Delta C_{33}^{(frac)} = -\zeta_3 \varepsilon_N \\ \Delta C_{44}^{(frac)} = \Delta C_{55}^{(frac)} = -\zeta_4 \varepsilon_T \end{array} \right.$$

where:

$$(4.6.2-13)$$

$$\zeta_1 = \frac{(M_P^{(m)} - 2M_S^{(m)})^2}{M_P^{(m)}} ; \zeta_2 = M_P^{(m)} - 2M_S^{(m)} ; \zeta_3 = M_P^{(m)} ; \zeta_4 = M_S^{(m)}$$

with $M_S^{(m)} = \mu^{(m)}$ and $M_P^{(m)} = K^{(m)} + \frac{4}{3}\mu^{(m)}$ designating the S-wave and P-wave moduli in the intact rock of compliance $S_{ijkl}^{(m)}$ ($K^{(m)}$ and $\mu^{(m)}$ are the corresponding bulk and shear moduli).

The quantities ε_N and ε_T are dimensionless overall fracture compliances and defined by [Hsu and Schoenberg, 1993]:

$$(4.6.2-14) \quad \varepsilon_N = \frac{M_P^{(m)} Z_N}{1 + M_P^{(m)} Z_N} \quad \text{and} \quad \varepsilon_T = \frac{M_S^{(m)} Z_T}{1 + M_S^{(m)} Z_T}$$

Note that for moderately fractured media ($M_S^{(m)} Z_T, M_P^{(m)} Z_N \ll 1$) the quantities ε_N and ε_T are approximately equal to the dimensionless linearized overall fracture compliances:

$$(4.6.2-15) \quad \varepsilon_N \approx M_P^{(m)} Z_N \quad \text{and} \quad \varepsilon_T \approx M_S^{(m)} Z_T$$

Note that the P-wave anisotropy parameters ε and δ defined by Eq. (4.5.1-4) and (4.5.1-5) respectively, and of the S-wave birefringence parameter γ , defined by Eq. (4.5.1-7), are linked with the fracture compliances Z_N and Z_T by the relations:

$$(4.6.2-16) \quad \left\{ \begin{array}{l} \varepsilon \approx -2\zeta(1-\zeta)\varepsilon_N \\ \delta \approx -2\zeta[\varepsilon_T + (1-2\zeta)\varepsilon_N] \\ \gamma \approx \frac{1}{2}\varepsilon_T \end{array} \right.$$

where $\zeta = \frac{M_S^{(m)}}{M_P^{(m)}}$. Note that the S-wave birefringence parameter γ and the P-wave anisotropy parameter ε are proportional to the dimensionless compliances $M_S^{(m)}Z_T \approx \varepsilon_T$ and $M_P^{(m)}Z_N \approx \varepsilon_N$ respectively.

The three next figures illustrate the dependence of the anisotropy ε , δ and γ with the dimensionless overall fracture compliances ε_N and ε_T . On Fig.4.6.2-2 we plot the seismic anisotropy parameter ε , defined by Eq. (4.5.1-4) and Fig. 4.5.1-2, as function of the dimensionless overall normal compliance ε_N of the fractures, defined by Eq. (4.6.2-14). Since the anisotropy parameter ε is also function of the parameter ζ , as suggested by Eq. (4.6.2-16), we consider the three typical cases of sedimentary rocks, namely sandstone,

limestone and dolomite. For each case we choose the following values for the elastic constants of the grain constituent (e.g., Hearmon [1979]).

In sandstones the main grain constituent is quartz with $M_p^{(m)} \approx 96.9 \text{ GPa}$, $M_s^{(m)} \approx 44.3 \text{ GPa}$, and as a consequence $\zeta \approx 0.46$. Calcite is the main constituent of limestones, with $M_p^{(m)} \approx 115.9 \text{ GPa}$, $M_s^{(m)} \approx 32 \text{ GPa}$, and as a consequence $\zeta \approx 0.28$. For dolomites we took $M_p^{(m)} \approx 115.8 \text{ GPa}$, $M_s^{(m)} \approx 45.7 \text{ GPa}$, and as a consequence $\zeta \approx 0.29$.

As expected the seismic anisotropy parameter ε increases with the dimensionless overall fracture compliance ε_N . For moderately fractured media, typically for $\varepsilon_N < 0.15$, the linear dependence evidenced by Eq. (4.6.2-16) is verified. For more fractured media the anisotropy parameter ε increases more rapidly than ε_N . Lastly we also note that ε increases more rapidly with larger values of ζ , for instance compare sandstones ($\zeta \approx 0.46$) with limestones ($\zeta \approx 0.28$). This is true only for $0 < \zeta < 0.5$ and is due to the variations of the function $2\zeta(1-\zeta)$, in Eq. (4.6.2-16), with κ . Outside this interval, that is to say for $0.5 < \zeta < 0.75$ the opposite trend is observed. Here we remind that $0 < \zeta < 0.75$ in any isotropic elastic material (see Chapter 1 Equation (1.2.1-50))

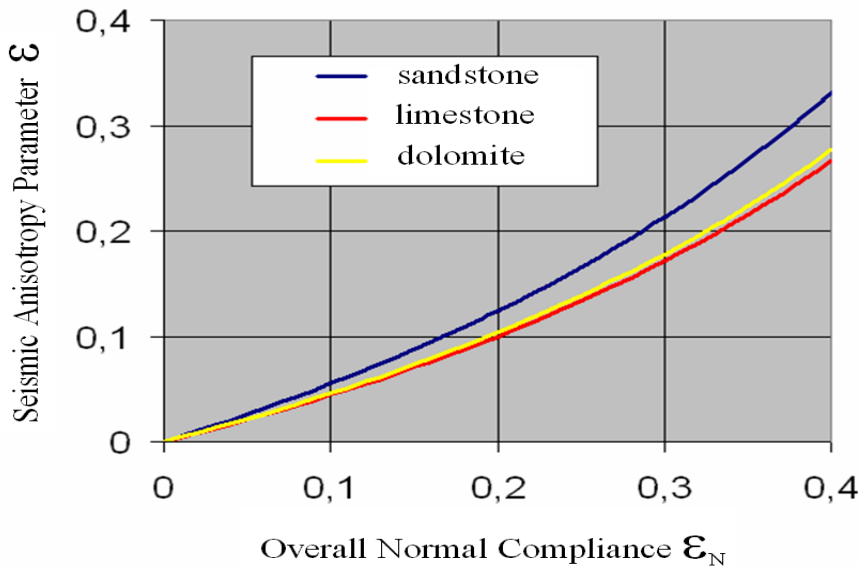


Figure 4.6.2-2: Seismic anisotropy parameter ε as function of the dimensionless overall normal compliance ε_N of the fractures in sandstone (blue line), limestone (red line) and dolomite (yellow line).

Fig.4.6.2-3 illustrates the variation of the seismic anisotropy parameter γ , defined by Eq. (4.5.1-7) and Fig. 4.5.1-3, as function of the dimensionless overall tangential compliance ε_T of the fractures, defined by Eq. (4.6.2-14). Since the parameter γ is only function of ε_T as shown by Eq. (4.6.2-16), and independent of the lithology, a single curve is plotted on this

figure. As expected the seismic anisotropy parameter γ increases with the dimensionless overall fracture compliance ε_T . Here again, for moderately fractured media (i.e., typically for $\varepsilon_T < 0.15$) the linear dependence evidenced by Eq. (4.6.2-16) is verified. For more fractured media the anisotropy parameter γ increases more rapidly than ε_T .

The behavior of the anisotropy parameter δ , defined by Eq. (4.5.1-5) and Fig. 4.5.1-2 is more complex, firstly because of its more complex definition containing quadratic expressions of the elastic constants, and secondly because of its dependence with both dimensionless overall compliances ε_N and ε_T , and on the lithology through the parameter ς . Fig. 4.6.2-4 shows a typical variation of the seismic anisotropy parameter δ with the dimensionless overall normal compliance ε_N , assumed equal to the dimensionless overall tangential compliance ε_T , for sandstone, limestone and dolomite, in the case of moderately fractured media. As for the other anisotropy parameters the seismic anisotropy parameter δ

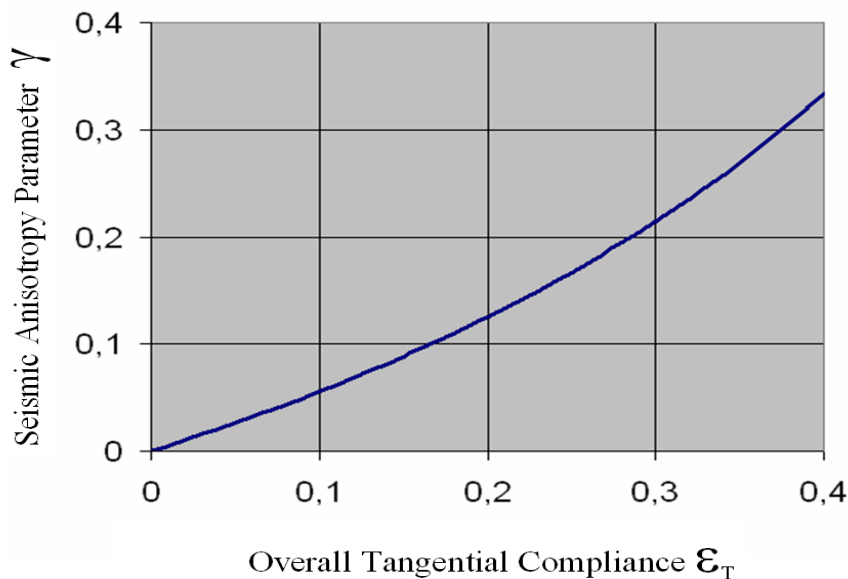


Fig.4.6.2-3: Seismic anisotropy parameter γ as function of the dimensionless overall tangential compliance ε_T of the fractures.

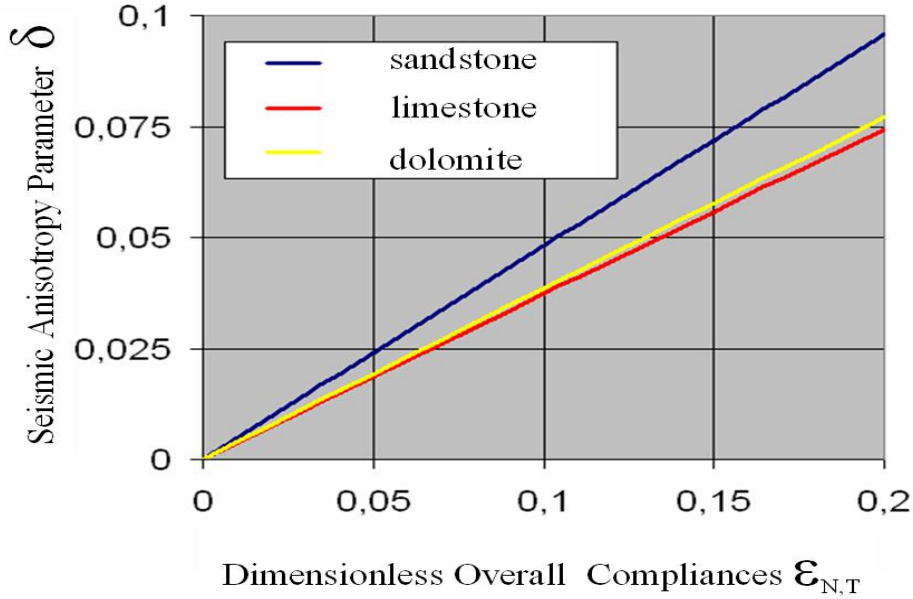


Fig. 4.6.2-4: Seismic anisotropy parameter δ as function of the dimensionless overall normal compliance ϵ_N , assumed to be equal to the dimensionless overall tangential compliance ϵ_T , for sandstone, limestone and dolomite, in the case of moderately fractured media.

increases with the dimensionless overall fracture compliances ϵ_N and ϵ_T , the linear dependence resulting from the moderately fractured character. Lastly, as for the anisotropy parameter ϵ , we also note that δ increases more rapidly with larger values of ζ , for instance compare the sandstones ($\zeta \approx 0.46$) with the limestones ($\zeta \approx 0.28$).

In the case of vertical fractures, for instance if the normal to the fractures is parallel to the X axis the only non-zero components of the additional compliance tensor $S^{(frac)}$ due to the fracture are:

$$(4.6.2-17) \quad \begin{cases} S_{11}^{(frac)} = Z_N \\ S_{55}^{(frac)} = S_{66}^{(frac)} = Z_T \end{cases}$$

The medium has an apparent orthorhombic symmetry or more precisely HTI, that is to say Transversely Isotropic with a horizontal symmetry axis parallel to the X-axis (e.g., Rügger [1997] and [1998]). Using the notations of Rügger [1997] and [1998] and of Eq.(4.5.2-5) one has in this special case:

$$(4.6.2-18) \quad \begin{cases} \epsilon_x = \epsilon^{(V)} = \epsilon \quad ; \quad \epsilon_y = 0 \quad ; \quad \gamma \approx -\gamma^{(V)} \\ \delta_x = \delta_z = \delta^{(V)} = \delta \quad ; \quad \delta_y = 0 \end{cases}$$

where ϵ , δ and γ are, in this case, given by Eq. (4.6.2-16), remembering that in this last equation the symmetry axis is vertical whereas in Eq. (4.6.2-18) this axis is horizontal and parallel to the X-axis. Lastly note that this model does not need any specification of the

geometry of the fractures, the fractures being characterized only by their phenomenologic behavior characterized by the compliances Z_N and Z_T of Eq. (4.6.2-17).

4.6.2.1.3 Multiple fractures/cracks families

Another generalization is the introduction of more than a single family of cracks /fractures in an initially isotropic medium. Hudson [1990] publish the results for the effective elastic moduli of a medium with an arbitrary distribution of penny-shaped cracks characterized by a crack density distribution function. Note that Eq. (4.6.2-8) deals with an arbitrary number of fractures with non-welded (linear slip) interfaces in a background medium, which may be arbitrarily anisotropic (triclinic). In cases where the background medium is isotropic and all the fracture families are vertical and rotationally invariant the effective media exhibit a horizontal symmetry plane, perpendicular to all the fractures, and the media exhibit a monoclinic symmetry (see section 4.3.2.1, or more detailed textbooks such as Helbig [1994]). Bakulin *et al* [2000] studied the special case of an isotropic host rock with two different non-orthogonal sets of rotationally invariant vertical fractures and discussed the inversion of the effective anisotropy parameters. The two next figures illustrate some typical predictions of this type of model. In Fig.4.6.2-5 we plot the azimuthal dependence of the relative difference between the horizontal velocity and the vertical velocity of the P-wave, quantified by the anisotropy function $\varepsilon(\lambda)$, defined by Eq. (4.5.2-3) and Fig.4.5.2-1. We consider an isotropic limestone background with two families of rotationally invariant vertical fractures of dimensionless overall normal compliances ε_{N1} and ε_{N2} , respectively, and of azimuth 90° and 120° , respectively. The sum of the dimensionless compliances $\varepsilon_{N1} + \varepsilon_{N2}$ is kept constant and equal to 30%, each individual dimensionless compliance varying by steps of 5%. As expected the minimum anisotropy, in absolute value, in terms of $\varepsilon(\lambda)$ is observed along an "average strike" of the fractures. In contrast the direction of maximum anisotropy, in absolute value, corresponds to an "average direction normal" to the fractures. The two limit positions corresponding to the cases where one of the fracture families vanishes. Obviously in these limit cases the exact symmetry directions are recovered .

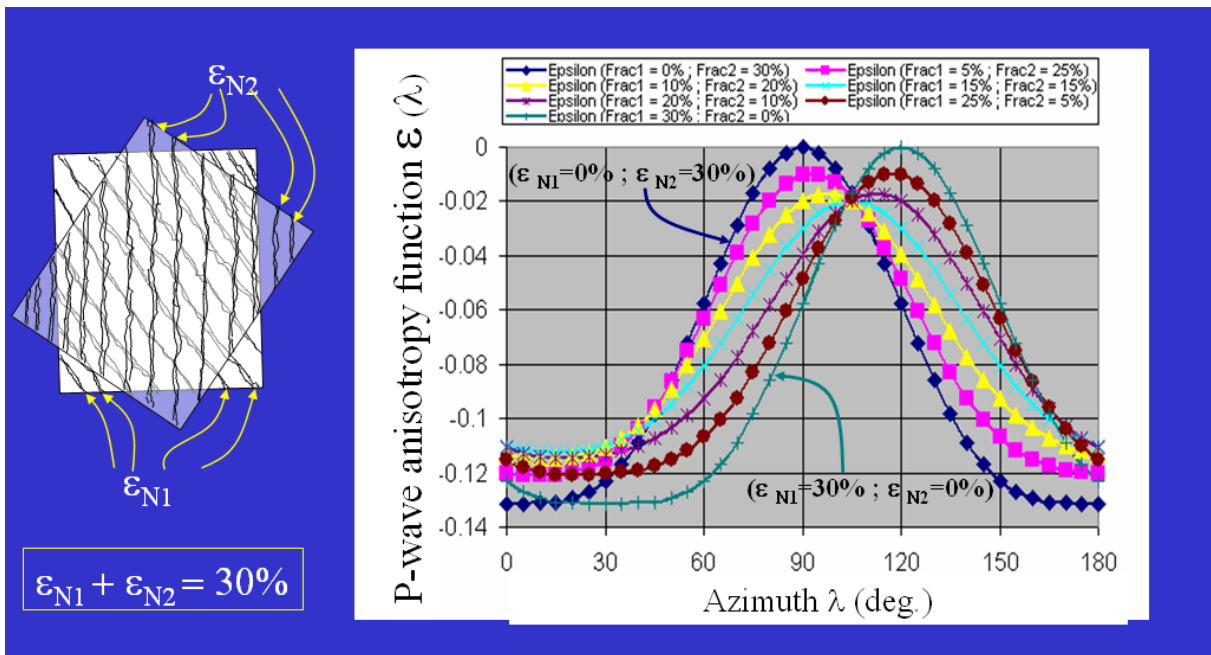


Fig.4.6.2-5: Seismic anisotropy function $\varepsilon(\lambda)$ as function of the azimuth of observation λ . Case of an isotropic limestone background with two families of rotationally invariant vertical fractures of dimensionless overall normal compliances ε_{N1} and ε_{N2} , respectively, and of azimuth 90° and 120° , respectively. The sum of the dimensionless compliances $\varepsilon_{N1} + \varepsilon_{N2}$ is kept constant and equal to 30%, each individual dimensionless compliance varying by steps of 5% (modified after Rasolofosaon [2002]).

Fig.4.6.2-5 is complementary to the previous figure and illustrates the variations of the direction of polarization of the vertically propagating fastest shear-wave, or S1-wave, with the relative magnitude of the two dimensionless overall tangential compliances ε_{T1} and ε_{T2} of a medium with two fracture families. An isotropic limestone background is still considered with two families of rotationally invariant vertical fractures of azimuth 90° and 120° . The sum of the dimensionless compliances $\varepsilon_{T1} + \varepsilon_{T2}$ is kept constant, each individual dimensionless compliance varying from 0 to 30%. The X-axis of Fig.4.6.2-6 corresponds to the dimensionless overall tangential compliances ε_{T1} of the first fracture family. Here again, as expected, the direction of polarization of the S1-wave is parallel to an "average strike" of the fractures. Obviously, the two limit positions corresponding to the cases where one of the fracture families vanishes. Obviously in these limit cases the exact polarization direction of the vertically propagating S1-wave exactly corresponds to the strike of the only remaining fracture family.

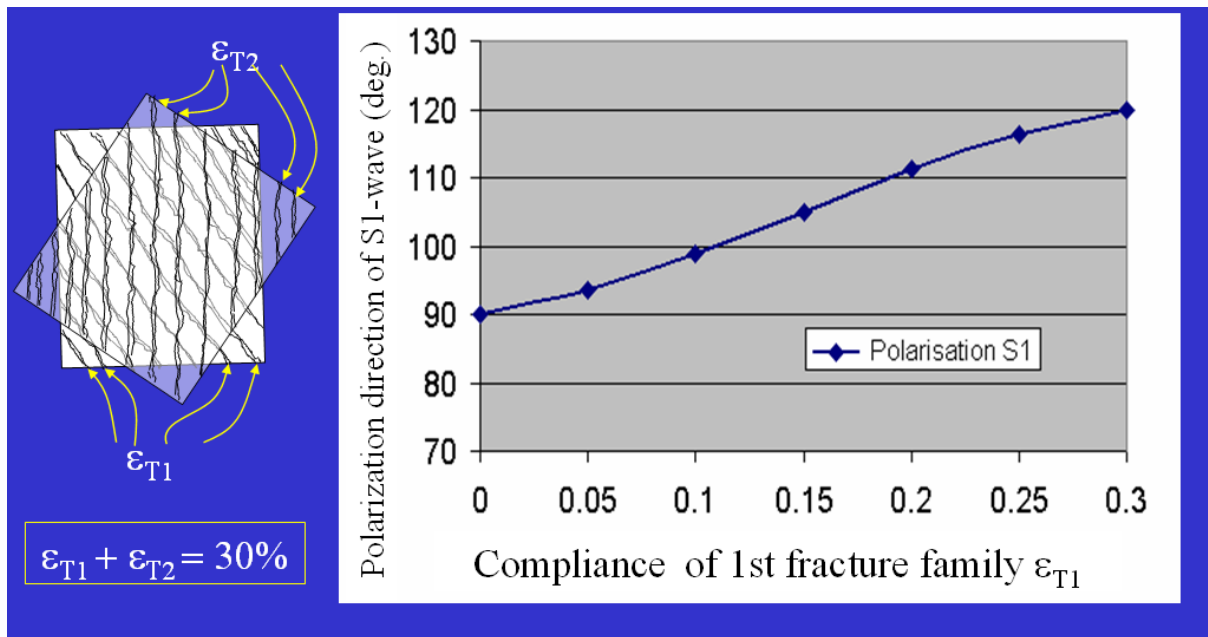


Fig.4.6.2-6: Direction of polarization of the vertically propagating fastest shear-wave as function of the dimensionless overall tangential compliances ϵ_{T1} of the first fracture family. Case of an isotropic limestone background with two families of rotationally invariant vertical fractures of dimensionless overall tangential compliances ϵ_{T1} and ϵ_{T2} , respectively, and of azimuth 90° and 120° , respectively. The sum of the dimensionless compliances $\epsilon_{T1} + \epsilon_{T2}$ is kept constant (modified after Rasolofosaon [2001]).

For practical applications, in contrast to what is observed in media with a single family of rotationally invariant vertical fractures, in the presence of multiple families of fractures the polarization direction of the vertically propagating S1-wave do not coincide with any of the symmetry directions of the P-wave anisotropy functions $\epsilon(\lambda)$ or $\delta(\lambda)$, rather easily recovered from subsurface measurements. This was confirmed on field data by Perez *et al.* [1999] and significantly complicate the inversion of the effective anisotropic parameters as discussed by Bakulin *et al.* [2000].

4.6.2.1.4 Fracture superimposed with other causes of anisotropy

Here, once again we note that Eq. (4.6.2-6) deals with a background medium, which may be arbitrarily anisotropic (triclinic), and an arbitrary number of fractures with non-welded (linear slip) interfaces. Any other causes of seismic anisotropy can be included in the anisotropy of the background medium. As discussed in sub-section 4.6.1-2, the most common anisotropy observed in sedimentary basins is Vertical Transverse Isotropy (VTI), with a vertical axis of rotational invariance, due to the presence of horizontal layerings at a scale much smaller than the seismic wavelength as illustrated by Fig.4.6.1-5. For instance, Bakulin *et al.* [2000] and Rasolofosaon [2002] considered VTI background media containing a single family of rotationally invariant parallel vertical fractures. Using Curie's symmetry principle, the effective medium exhibits 3 symmetry planes which are mutually perpendicular, namely the

fracture plane, the vertical plane normal to the fractures and the horizontal plane. As a consequence the medium exhibits orthorhombic symmetry (see sub-section 4.2.2.2, or more detailed textbooks such as Helbig [1994]). One of the most important result is that the presence of the layer-induced transverse isotropy, of the VTI type, obviously modifies the overall anisotropy of the fractured medium, but also preserves the azimuthal anisotropy, or more precisely the anisotropy difference between the two vertical symmetry planes. This is illustrated by the two next figures.

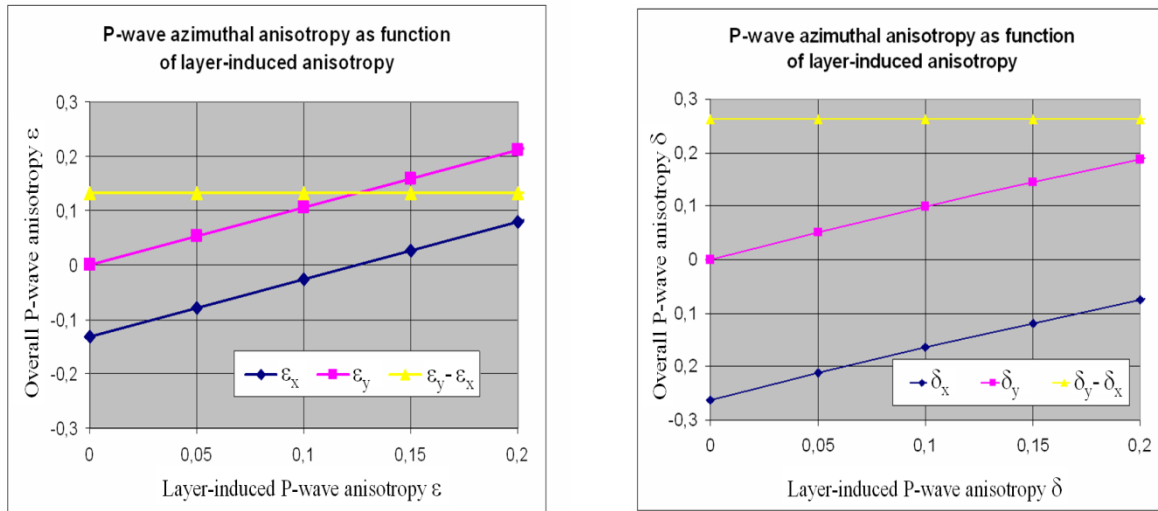


Fig.4.6.2-7: P-wave azimuthal anisotropy, in terms of coefficients ϵ (left) and δ (right), as function of the P-wave layer-induced anisotropy. See text for details. (modified after Rasolofosaon [2002]).

We consider a typical limestone reservoir. On Fig.4.6.2-7 the Y-axes are the overall P-wave anisotropy, in terms of coefficients ϵ (left) and δ (right), introduced in section 4.5.2. More precisely we consider the P-wave anisotropy coefficients ϵ_x (left) and δ_x (right) in the vertical plane normal to the fracture planes plotted in blue lines, the P-wave anisotropy coefficients ϵ_y (left) and δ_y (right) in the fracture planes plotted in pink lines, and the anisotropy differences $\epsilon_y - \epsilon_x$ (left) and $\delta_y - \delta_x$ (right) in yellow lines. The X-axes quantifies the P-wave layer-induced VTI anisotropy coefficient ϵ (left) and δ (right). Although the overall anisotropy increases with the anisotropy induced by the layering, the anisotropy difference (in yellow line) between the two vertical symmetry planes is constant. In conclusion, the practical consequence is that a differential measurement of P-wave anisotropy between the two vertical symmetry planes allows to eliminate the effect of the layer-induced anisotropy and to characterize the fractures only. This is clearly illustrated by Fig.4.6.2-8 showing the differential P-wave anisotropy, in terms of $\epsilon_y - \epsilon_x$ (blue line) and $\delta_y - \delta_x$ (pink line), and the S-wave birefringence coefficient γ (yellow line) for vertical propagation, as functions of the dimensionless overall fracture compliances $\epsilon_N = \epsilon_T$.

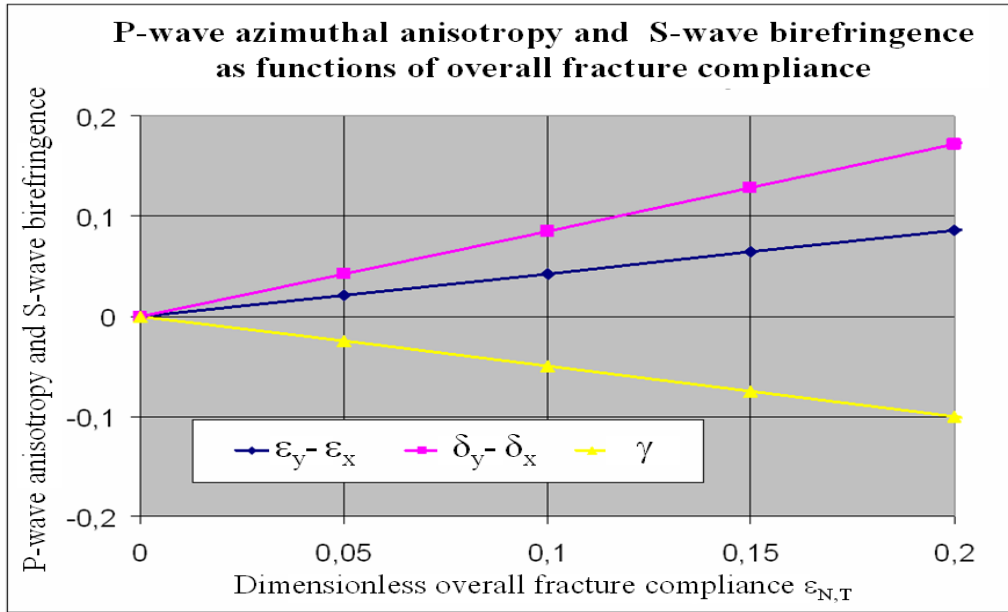


Fig.4.6.2-8: P-wave azimuthal anisotropy, in terms of $\varepsilon_y - \varepsilon_x$ (blue line) and $\delta_y - \delta_x$ (pink line) and S-wave birefringence coefficient γ (yellow line) for vertical propagation as functions of the dimensionless overall fracture compliances ε_N and ε_T , assumed equal. (modified after Rasolofosaon [2002]).

The effect of the VTI background medium is eliminated by considering differential anisotropy. And as expected the fracture-induced effects increases with the dimensionless overall fracture compliances, the linear dependence resulting from the moderately fractured character.

4.6.2.2 Aligned ellipsoidal cracks

4.6.2.2.1 The basic model with ellipsoidal cracks

Another well-known model is that of Hudson [1980 and 1981] with a set of parallel penny-shaped cracks (that is to say cracks of oblate ellipsoids of revolution of diameter $2a$ and thickness $2c$). The author used Born approximation of single scattering, as in section 5.2.2 in isotropic heterogeneous media, but adapted to anisotropic media and using the theoretical derivation of Eshelby [1957]. Schoenberg and Douma [1988] demonstrated that Hudson's model can be put in a one-to-one correspondence with the previous model through the relations:

$$(4.6.2-19) \quad \zeta = \frac{3}{4} \varepsilon_N \zeta (1 - \zeta) \left[1 + \frac{1}{\pi \alpha \zeta (1 - \zeta)} \frac{M_p^{(c)}}{M_s^{(m)}} \right] = \frac{3}{16} \varepsilon_T (3 - 2\zeta) \left[1 + \frac{4}{\pi \alpha (3 - 2\zeta)} \frac{M_s^{(c)}}{M_s^{(m)}} \right]$$

The dimensionless crack density parameter ζ is defined by $\zeta = N \langle a^3 \rangle$, where N is the number of cracks per unit volume and $\langle a^3 \rangle$ is the volume average of the crack radius cubed.

The other dimensionless parameter $\alpha = c/a$, called aspect ratio, is the ratio of the thickness to the diameter of a crack. The P-wave and S-wave moduli in the background uncracked medium are respectively designated by $M_P^{(m)}$ and $M_S^{(m)}$. And the quantities $M_P^{(c)}$ and $M_S^{(c)}$ designate the P-wave and S-wave moduli in the material contained in the cracks. In principle Hudson's theory is restricted to dilute concentrations of crack (typically for $\zeta < 0.1$) and for small aspect ratio α . For larger aspect ratio (typically for $\alpha > 0.3$) and/or larger crack density it is recommended to use alternative theories (e.g., Nishizawa [1982]; Cheng [1993]).

In the case of fluid-saturated cracks, the modulus $M_S^{(c)}$ vanishes and the previous equations are replaced by:

$$(4.6.2-20) \quad \zeta = \frac{3}{4} \varepsilon_N \zeta (1 - \zeta) \left[1 + \frac{1}{\pi \alpha \zeta (1 - \zeta)} \frac{M_P^{(c)}}{M_S^{(m)}} \right] = \frac{3}{16} \varepsilon_T (3 - 2\zeta)$$

which leads to the following expressions for Thomsen's anisotropy parameters in the case of moderate anisotropy, or more precisely of moderate value of fracture parameters ε_N and ε_T (e.g., Li [1997]), the axis of symmetry of the penny-shaped cracks being parallel to the Z-axis:

$$(4.6.2-21) \quad \left\{ \begin{array}{l} \varepsilon \approx \frac{8}{3} \pi \alpha \zeta (1 - \zeta) \left(\frac{V_S^{(m)}}{V_P^{(c)}} \right)^2 \\ \delta \approx \frac{8}{3} \zeta \left[\pi \alpha \left(\frac{V_S^{(m)}}{V_P^{(c)}} \right)^2 - \frac{4\zeta}{3 - 2\zeta} \right] \\ \gamma \approx \frac{8}{3} \frac{\zeta}{3 - 2\zeta} \end{array} \right.$$

where $V_P^{(c)}$ is the P-wave velocity in the saturating fluid and $V_S^{(m)}$ the S-wave velocity in the uncrack background solid. Eq. (4.6.2-21) is to be compared with Eq. (4.6.2-16) for the case of linear slip fractures.

In the case of dry cracks, Eq. (4.6.2-21) are replaced by:

$$(4.6.2-22) \quad \left\{ \begin{array}{l} \varepsilon \approx \frac{8}{3} \zeta \\ \delta \approx \frac{8}{3} \zeta \left[\frac{1}{1-\zeta} - \frac{4\zeta}{3-2\zeta} \right] \\ \gamma \approx \frac{8}{3} \frac{\zeta}{3-2\zeta} \end{array} \right.$$

After Eq. (4.6.2-20) we can see that the ratio $\varepsilon_N / \varepsilon_T$ of the dimensionless overall normal and tangential compliances is only function of the lithology, through the parameter $\zeta = \frac{M_S^{(m)}}{M_P^{(m)}}$, of the aspect ratio α of the cracks, and of the ratio $M_P^{(c)} / M_P^{(m)}$ of the P-wave moduli of the saturating fluid and of the grain constituent of the rock. Fig.4.6.2-9 illustrates this relationship.

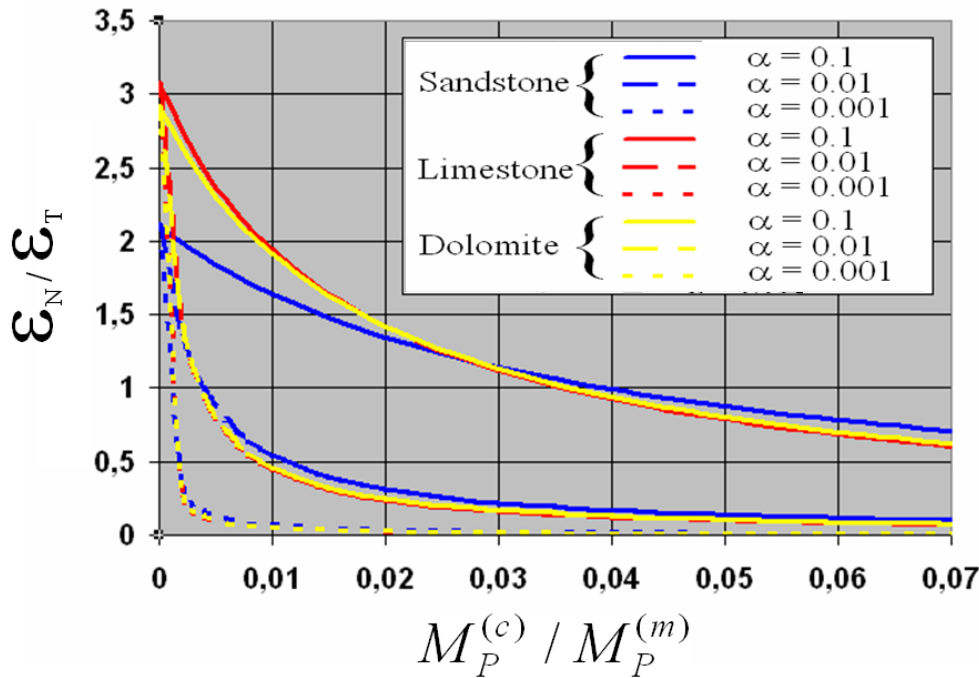


Fig.4.6.2-9: Ratio $\varepsilon_N / \varepsilon_T$ of the dimensionless overall normal and tangential compliances of the cracks/fractures as function of the ratio $M_P^{(c)} / M_P^{(m)}$ of the P-wave moduli of the saturating fluid and of the grain constituent of the rock. Three kinds of lithologies are considered, namely sandstones (in blue lines), limestones (in red lines) and dolomites (in yellow lines). For each lithology three aspect ratios are considered, namely $\alpha=0.1$ (solid lines), $\alpha=0.01$ (dashed lines), and $\alpha=0.001$ (dotted lines).

We plot the ratio $\varepsilon_N/\varepsilon_T$ as a function of the ratio $M_p^{(c)}/M_p^{(m)}$ for the three main lithologies of reservoir rocks, namely sandstones, limestones and dolomites, and for three aspect ratios, namely $\alpha=0.1$, $\alpha=0.01$ and $\alpha=0.001$. The bulk modulus $M_p^{(c)}$ of typical reservoirs fluids is smaller than 5GPa and the P-wave modulus of the grain constituent is of the order of 100GPa. As a consequence the ratio $M_p^{(c)}/M_p^{(m)}$ rarely exceeds 0.05, which explain the scale of the X-axis of Fig.5.3.3-5. First of all we note that all the curves are decreasing. In effect, as expected, for a given lithology (i.e., for fixed $M_p^{(m)}$ and κ), an increase of the stiffness $M_p^{(c)}$ of the fluid content tends stiffen the cracks/fracture, as a consequence to decrease ε_N with no effect on the dimensionless overall tangential compliance ε_T . Secondly, still as expected, for given rock and saturating fluid (i.e., for fixed $M_p^{(c)}/M_p^{(m)}$), the decreasing effect is stronger for smaller aspect ratio α , that is to say for more compliant cracks/fractures. Finally we notice that for fixed and sufficient small aspect ratio (i.e. α substantially smaller than 0.1) the phenomenon is practically independent of the type of lithology. It is also the case for rather large aspect ratio, for instance for $\alpha=0.1$ (which is at the limit of validity of the theory of Hudson [1980], as explained in the comments on Eq. (4.6.2-19) only for sufficiently stiff saturating fluid, typically for $M_p^{(c)}/M_p^{(m)}>0.02$.

Crack-induced elastic anisotropy has been observed in many rocks (e.g., see the many references contained in Thomsen [2002]). For instance, experimental data illustrating the link between microfractures/microcracks orientation distribution and ultrasonic anisotropy measured in rock samples in the laboratory is reported in the work of Rasolofosaon *et al.* [2000] and summerized in section 4.8.2.

4.6.2.2.2 Case of non-dilute fractures/crack densities

One of the first generalization is taking into account non-dilute crack/fracture concentration, that is to say typically $\zeta > 0.1$ in Eq. (4.6.2-19). The simplest solution is to use multiple-scattering summation or higher order expansion, beyond first-order Born approximation restricted to dilute concentrations of heterogeneities (as in section Chapter 5 §5.2.2 in isotropic heterogeneous media, but adapted to anisotropic media). For instance Hudson [1981] used the second order expansion. Unfortunately such an expansion is not a uniformly converging series and thus is not recommended.

A more popular generalization that avoids the complicate multiple-scattering summation, is the self-consistent method (SCM). This alternative approach consists in considering a single heterogeneity immersed in a background medium of which the elastic properties are precisely those of the effective medium (e.g., Hershey [1954]; Hill [1965]; Budiansky [1965]). The technique allows to roughly take into account the interactions between the microheterogeneities, and as a consequence to deal with slighter higher concentrations of heterogeneities than what is allowed for Born approximation. From a practical point of view the stiffness tensor of the background medium is taken equal to the unknown effective

stiffness tensor of the cracked medium, and a "single scattering" approximation of Eq. (4.6.2-19) (see the previous comments on this equation) is assumed. The thus derived implicit equation in the unknown effective stiffness tensor of the cracked medium can be solved numerically by iteration.

Finally note that for moderate crack/fracture induced seismic anisotropy as commonly encountered on the field, that is to say typically for $\zeta < 0.15$ in Eq. (4.6.2-19), the dilute concentration approximation and the self-consistent approximation lead to quite comparable results (e.g., Barthelemy [2006]).

4.6.3 Stress-induced anisotropy and anisotropic nonlinear elasticity

Stress-induced anisotropy, or the anisotropy only due to stress in a initially isotropic unstressed rock, and the anisotropy of the nonlinear elastic properties of rocks are detailed in the section 7.5.1 of Chapter 7 on Nonlinear Elasticity in rocks.

4.7 *Anisotropic viscoelasticity*

Many references deal with the complete description of wave propagation in anisotropic viscoelastic media (e.g., Carcione [2007]; Vavrycuk [2007]), especially with inhomogeneous waves. In inhomogeneous plane waves the planes of equal amplitude and the planes of equal phase are not parallel (e.g., Bourbié et al. [1987]). Here we only consider homogeneous plane waves, for which the equi-phase plane and equi-amplitude plane are parallel. In practice this is not really a problem because the velocity and the attenuation of the three bulk plane waves are practically insensitive to the homogeneity angle, that is to say the angle between the equi-phase plane and equi-amplitude plane, as long as the homogeneity angle is not too large. This is the case in most practical situations of seismic experiments in the field [Behura and Tsvankin, 2009]. In such situations the velocity and the attenuation of the three bulk plane waves do not substantially differ from their corresponding values in the case of homogeneous waves.

In the case of homogeneous plane waves, it is possible to apply the correspondence principle to derive the viscoelastic Kelvin-Christoffel equations from the corresponding equations in purely elastic media [see Equation (4.3.3-7)]. The correspondence principle (e.g., Biot [1955]; Rajagopal and Wineman [2008]) is the key-point here. In a few words, and quoting Biot [1955] verbatim: "Another principle which we call the principle of correspondence is a consequence of the formal analogy between the operational tensor and the elastic moduli... A complete correspondence exists between the two so that all static and dynamic solutions of elasticity may be immediately transposed into a corresponding viscoelasticity solution by simply replacing the elastic constants by operators". In other words, regarding homogenous plane waves in viscoelastic media, viscoelastic Kelvin-Christoffel equations, their solutions and their approximations in weakly anisotropic media are formally identical to the corresponding equations in purely elastic media, except that the quantities are complex, as

detailed in Rasolofosaon [2010]. These equations are equation (4.3.3-7) for Kelvin-Christoffel equations, equation (4.3.3-18) for the exact expression of the three bulk wave moduli, and equations (4.5.2-1) and (4.5.2-6) for the weak-anisotropy approximations of the qP-wave modulus and the qS-wave moduli respectively, as detailed in the previous reference.

Laboratory measurements of attenuation and velocity anisotropy in rocks are common (e.g., Bourbié et al. [1987]; Barton [2007]; and the references therein). In contrast Laboratory measurements of attenuation and velocity anisotropy in rocks of assumed idealized anisotropy type (e.g., transversely isotropic) are scarce (e.g., Yin and Nur [1992]; Best [1994]; Prasad and Nur [2003]; Best *et al.* [2007]).

Furthermore laboratory experimental data on rocks considered as arbitrarily anisotropic viscoelastic media are rare. To our knowledge Arts [1993] is the only reference providing a small database of such experimental results. We excerpt the following example from this reference. The considered rock is water-saturated Yugoslavian marble. The attenuation on the dry sample was too small to be measurable. The rock sample needed to be water-saturated in order to exhibit sufficient attenuation. The experimental set-up and procedure are those of Arts *et al.* [1992] and Arts [1993]. It is a conventional ultrasonic pulse-transmission experimental set-up (see chapter 2) but under controlled uniaxial stress. The chosen technique leads to the measurements of the attenuation and the velocity of the qP-, qS1 and qS2-waves in 9 different directions on cubes of rock with bevelled edges (see Figure 4.7.1-1).

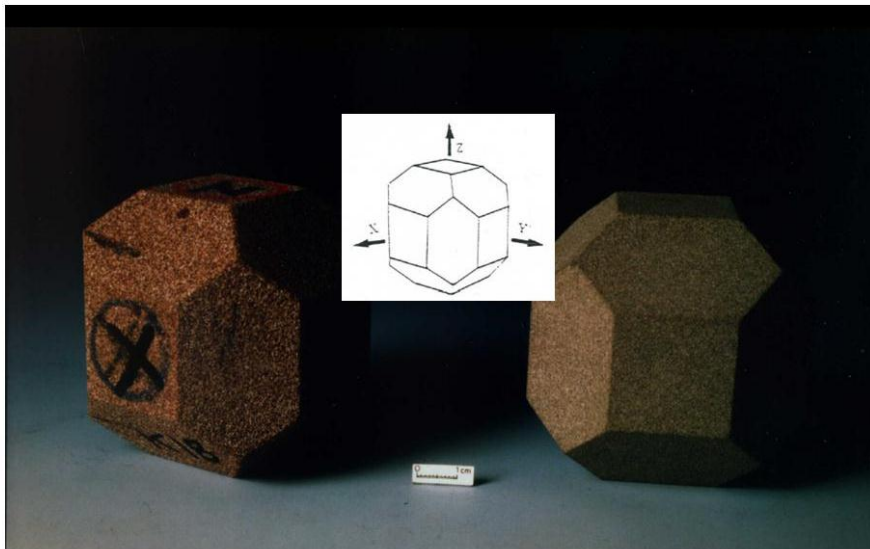


Fig.4.7.1-1: Rock samples with bevelled edges and 18 faces allowing velocity and attenuation measurements in 9 different directions.

The measured 27 complex wave moduli allow the inversion of the 21 non-vanishing complex coefficients of the complex stiffness matrix, as detailed in the two previous references. Measurement accuracy on the velocities are roughly 1% for the qP-wave, and 2% for the qS-waves. The attenuation measurements are one order of magnitude less accurate, with typical accuracy of 10% for the qP-wave, and 20% for the qS-waves.

Figure 4.7.1-2 illustrates a comparison between the experimental data and the theoretically calculated curves of the real and imaginary parts of the complex slownesses of the three bulk waves in the xz -plane of a sample of water-saturated white Yugoslavian marble. The inverted real part \mathbf{C}' and the imaginary part \mathbf{C}'' of the complex stiffness matrix \mathbf{C}^* are given in the next equations.

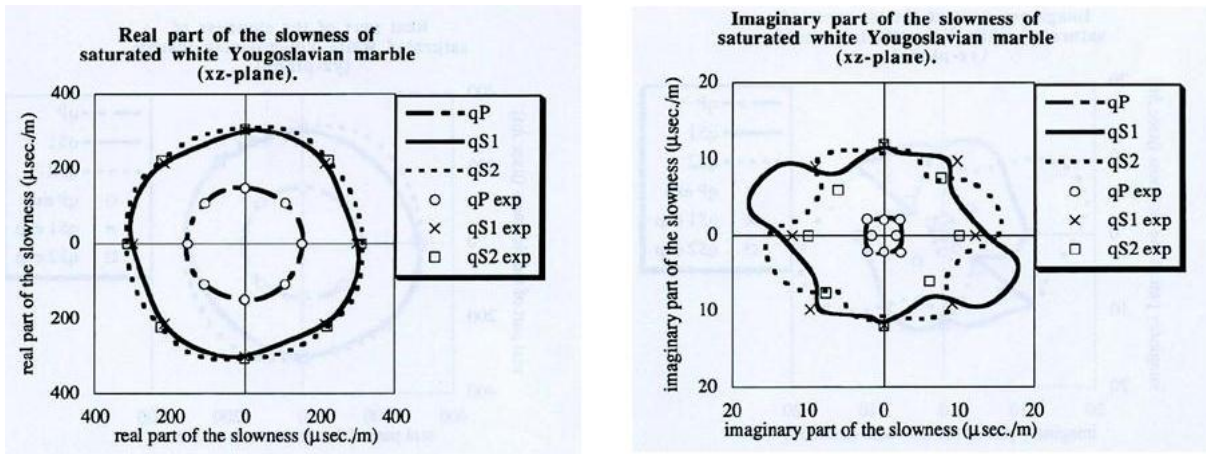


Fig.4.7.1-2: a) Section by the xz -plane of the surface (left) of the real part and (right) of the imaginary part of the complex phase slowness of the qP -wave in dashed lines, of the $qS1$ -wave in solid lines and of the $qS2$ -wave in dotted lines deduced from the inverted complete set of the viscoelastic complex moduli, compared to the corresponding measured slownesses (experimental points are circles for the qP -wave, crosses for $qS1$ -wave and squares for $qS2$ -wave. Case of water-saturated white Yugoslavian marble.

All the theoretical curves of the figure are deduced from the inverted complex stiffnesses as described further in this sub-section. The errors on the measured real part of the slowness curves are of the order of the size of the measurement points on the plots. The corresponding errors on the imaginary parts of the slowness are roughly three to four times larger. We clearly see that the theoretically calculated curves fall within the accuracy range of the measurements that illustrate the quality of the inversion. We also see the lack of symmetry of the theoretical curves illustrating the triclinic symmetry of the studied rock sample, which will be confirmed in the next lines.

The inverted real part \mathbf{C}' of the complex stiffness matrix in units of Gigapascals is:

PETROACOUSTICS – CHAPTER 4

$$(4.7.1-1) \quad \mathbf{C}' = \begin{pmatrix} 118.1 & 62.2 & 61.6 & -0.5 & 4.1 & 2.2 \\ 62.2 & 115.9 & 61.8 & 0.2 & 3.0 & -2.4 \\ 61.6 & 61.8 & 127.9 & -3.6 & -3.7 & 3.0 \\ -0.5 & 0.2 & -3.6 & 30.2 & -0.3 & -0.2 \\ 4.1 & 3.0 & -3.7 & -0.3 & 31.7 & -0.9 \\ 2.2 & -2.4 & 3.0 & -0.2 & -0.9 & 28.6 \end{pmatrix} \text{ GPa, and}$$

The inverted imaginary part \mathbf{C}'' of the complex stiffness matrix in units of Gigapascals is:

$$(4.7.1-2) \quad \mathbf{C}'' = \begin{pmatrix} 3.68 & 0.3 & -0.13 & 0.91 & 0.23 & -0.46 \\ 0.3 & 1.69 & -0.30 & 0.60 & 1.22 & 0.74 \\ -0.13 & -0.30 & 4.01 & -0.25 & -0.32 & -0.39 \\ 0.91 & 0.60 & -0.25 & 2.10 & -0.02 & 0.15 \\ 0.23 & 1.22 & -0.32 & -0.02 & 2.46 & -0.70 \\ -0.46 & 0.74 & -0.39 & 0.15 & -0.70 & 3.19 \end{pmatrix} \text{ GPa}$$

The corresponding relative errors, in percentage, on each coefficient of the inverted real part \mathbf{C}' of the complex stiffness matrix \mathbf{C}^* are:

$$(4.7.1-3) \quad \left[\frac{\Delta \mathbf{C}'}{\mathbf{C}'} \right] = \begin{pmatrix} 3 & 5 & 6 & 705 & 53 & 97 \\ 5 & 3 & 8 & 1778 & 76 & 115 \\ 6 & 8 & 3 & 101 & 70 & 73 \\ 705 & 1778 & 101 & 4 & 391 & 585 \\ 53 & 76 & 70 & 391 & 4 & 108 \\ 97 & 115 & 73 & 585 & 108 & 4 \end{pmatrix} \% , \text{ and}$$

The corresponding relative errors, in percentage, on each coefficient of the inverted imaginary part \mathbf{C}'' of the complex stiffness matrix \mathbf{C}^* are:

$$(4.7.1-4) \quad \left[\frac{\Delta \mathbf{C}''}{\mathbf{C}''} \right] = \begin{pmatrix} 34 & 214 & 306 & 96 & 279 & 124 \\ 214 & 67 & 148 & 118 & 71 & 97 \\ 306 & 148 & 31 & 250 & 236 & 279 \\ 96 & 118 & 250 & 32 & 4422 & 681 \\ 279 & 71 & 236 & 4422 & 26 & 100 \\ 124 & 97 & 279 & 681 & 100 & 19 \end{pmatrix} \% .$$

The values of the diagonal elements of the matrices of the errors in Equations (4.7.1-3) and (4.7.1-4) corresponding to the most meaningful stiffness coefficients located on the diagonal

of the matrices of the real part and of the imaginary part of the complex stiffness matrix in Equations (4.7.1-1) and (4.7.1-2), respectively. Note that they are roughly equal to the double of the relative error on the velocities and on the attenuation. This is simply due to the fact that, after Equation (4.7.1-5) which will be introduced below, the complex wave modulus is proportional to the complex squared velocity. As a consequence the relative errors of the moduli are equal to the double of the relative errors on the velocities.

We also note that the off-diagonal elements of the matrices of the errors in Equations (4.7.1-3) and (4.7.1-4) can be substantially larger than the diagonal elements. For instance the relative error on the coefficients C'_{24} and C''_{45} even exceed 1700% and 4000% respectively.

This is a classical result for experimentalists not to be worried about. More precisely, for instance, let us consider a second rank symmetric tensor (e.g., the stress tensor) with all the diagonal terms of the order of 100 (in units of MPa for instance), differing by less than $\pm 5\%$, and measured with a relative error of say $\pm 10\%$ (corresponding to an absolute error of ± 10). Furthermore let us assume that the absolute errors on the off-diagonal terms also roughly equal ± 10 . As long as the measured values of the off-diagonal terms are smaller than their corresponding error the most important result is that the considered second rank symmetric tensor can reasonably be approximated by an isotropic tensor. These off-diagonal terms may be of the order of 9 (case 1), 1 (case 2) or even 0.1 (case 3), the above conclusion is unchanged. But the conclusions regarding the relative errors are obviously more contrasted. In contrast to the case of the diagonal terms, the relative errors on the off-diagonal terms can obviously change of order of magnitude, namely $\pm 110\%$ in the first case, $\pm 1000\%$ in the second case, and even $\pm 10,000\%$ in the last case. In a similar way, this is what roughly happens in the case of the real part and the imaginary part of the complex stiffness matrix here. Such large relative errors on the least meaningful coefficients is a classical experimental result and need not be detailed further.

All the above data on Equations (4.7.1-1) and (4.7.1-2) allow to compute the complete directional dependence of the phase velocity and of the phase attenuation. More precisely, from the complex stiffness tensor $\mathbf{C}^* = \mathbf{C}' + i \mathbf{C}''$, it is possible to compute the complex Kelvin-Christoffel matrix using Equation (4.3.3-7) and the correspondence principle described above, for any direction of propagation. The complex wave moduli $M_{P,S1,S2}^*$ of the three bulk waves (qP, qS1 and qS2) are the eigenvalues of the complex Kelvin-Christoffel matrix for any direction of propagation. Due to the correspondence principle one has the classical relations:

$$(4.7.1-5) \quad M_{P,S1,S2}^* = \rho \left(V_{P,S1,S2}^* \right)^2 = \rho \left(1 / S_{P,S1,S2}^* \right)^2$$

where $V_{P,S1,S2}^*$ and $S_{P,S1,S2}^*$ designate the complex phase velocity and the complex phase slowness of the three bulk waves (qP, qS1 and qS2), and ρ the density (here the independently measured density is $\rho = 2750 \text{ kg} / \text{m}^3$).

The corresponding phase velocities $V_{P,S1,S2}$ and phase quality factors $Q_{P,S1,S2}$ are given by the relations (e.g., Bourbié et al. [1987]; Carcione [2007]):

$$(4.7.1-6) \quad \left\{ \begin{array}{l} V_{P,S1,S2} = \sqrt{\frac{2|M_{P,S1,S2}^*|^2}{\rho(|M_{P,S1,S2}^*| + |M'_{P,S1,S2}|)}} \\ Q_{P,S1,S2} = M'_{P,S1,S2} / M''_{P,S1,S2} \end{array} \right.$$

where $|M_{P,S1,S2}^*|$, $M'_{P,S1,S2}$ and $M''_{P,S1,S2}$ designate respectively the modulus, the real part and the imaginary part of the complex wave modulus.

Figures 4.7.1-3 and Fig.4.7.1-4 show the complete directional dependences of the phase velocity and of the phase quality factor, respectively, in the sample of water-saturated Yugoslavian marble of Figure 4.7.1-2. Both figures are composed of three sub-figures, the top sub-figure corresponding to the qP-wave, the middle sub-figure to the qS1-wave and the bottom sub-figure to the qS2-wave.

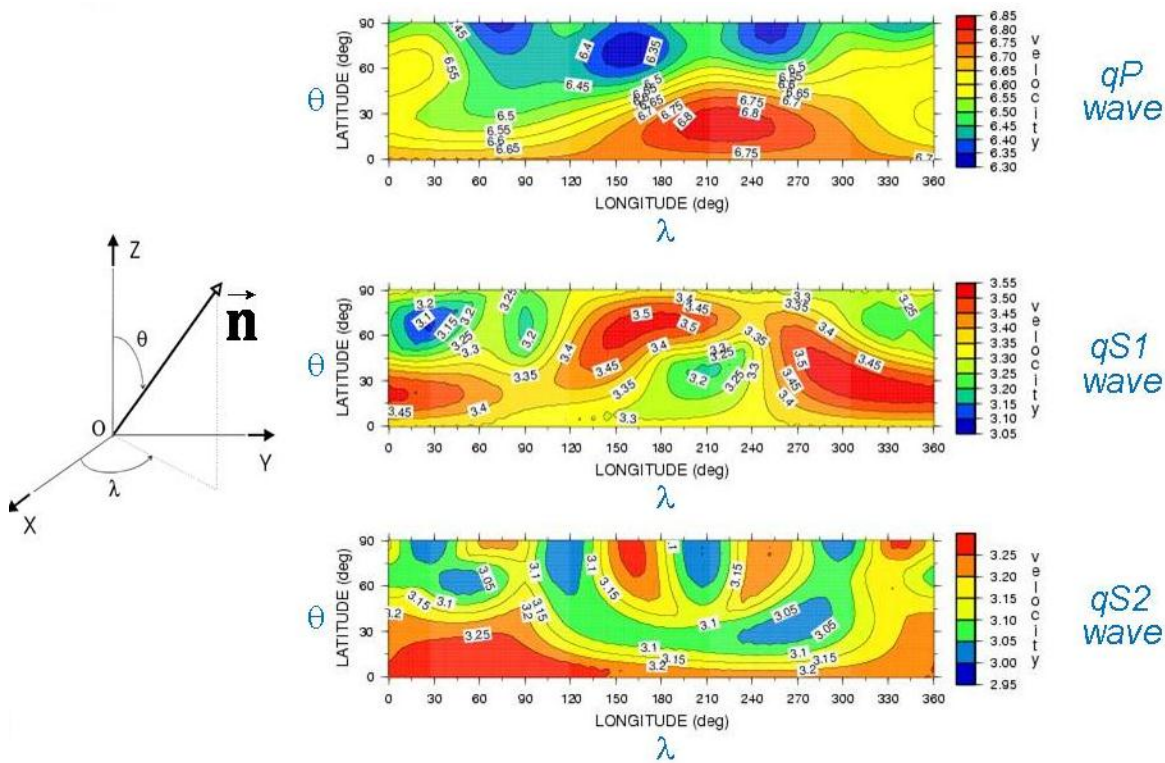


Fig.4.7.1-3: Complete directional dependence of the phase velocity (top of the qP-wave, (middle) of the qS1-wave, and (bottom) of the qS2-wave in water-saturated white Yugoslavian marble considered as an arbitrarily anisotropic viscoelastic medium.

First of all one can clearly notice the lack of symmetry element of the plots that confirms the triclinic symmetry of the marble sample. The qP-wave phase velocity varies from 6.30–6.85 km/s, which roughly corresponds to 8% anisotropy. The qS1-wave phase velocity is always

larger than 3.05 km/s and reaches a maximum of roughly 3.55 km/s, representing a relative variation of more than 16%. The qS2-wave phase velocity is comprised between 2.95–3.30 km/s, corresponding to an anisotropy of nearly 12%. This confirms the moderate but not weak, strength of velocity anisotropy.

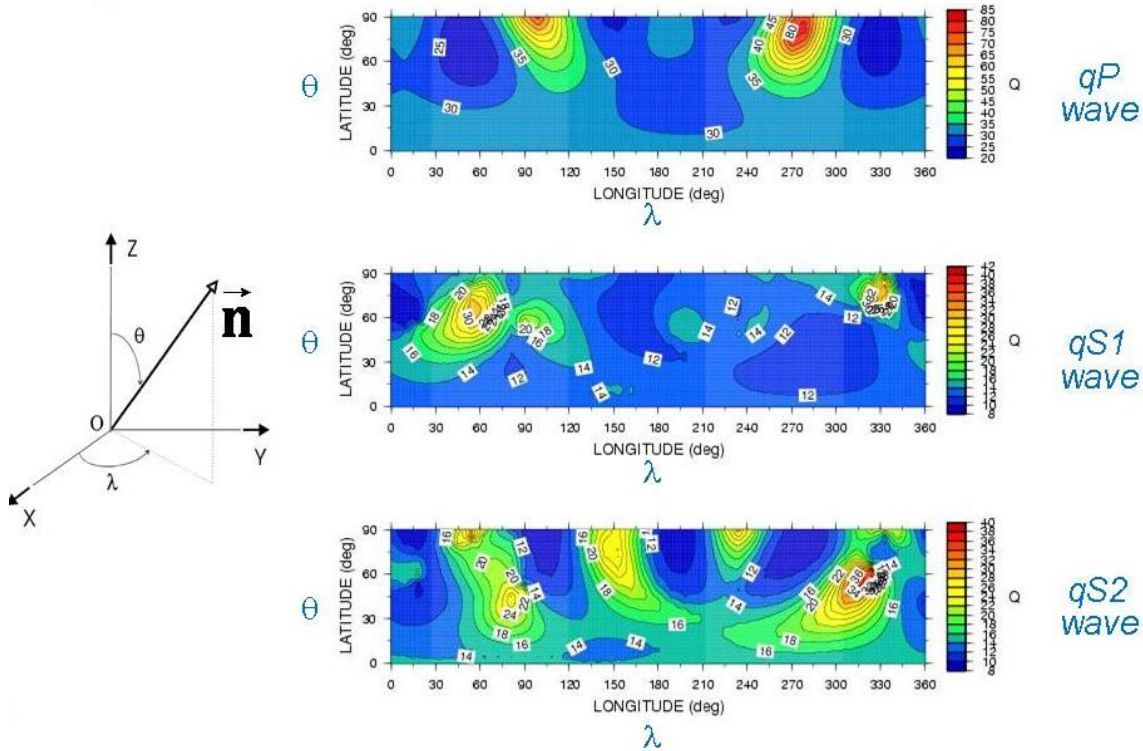


Fig.4.7.1-4: Complete directional dependence of the phase attenuation, in terms of $1000/Q$, (top) of the qP-wave, (middle) of the qS1-wave, and (bottom) of the qS2-wave in water-saturated white Yugoslavian marble considered as an arbitrarily anisotropic viscoelastic medium.

In contrast, the directional dependence of the three quality factors is very strong. More precisely, the qP-wave phase quality factor varies from 20 to 85, which roughly corresponds to more than 320% anisotropy. The quality factors of the qS1- and qS2-waves also exhibit a large directional dependence, slightly larger than that of the qP-wave. The qS1-wave (respectively qS2-wave) phase quality factor, with a minimum value of 8 (respectively 8.1) and a maximum value of 42 (respectively 40), exhibits more than 420% (respectively 390%) anisotropy. Furthermore, the small quality factors at least in some directions, typically smaller than 15 which denote strong attenuation, is typical of water saturated rock samples at atmospheric pressure (e.g., Bourbié et al. [1987]).

Lastly note that for each bulk wave the shape of the velocity surface is different from the shape of the attenuation surface. This has been pointed out by Jakobsen and Rasolofosaon [2009]. As a consequence it is not appropriate to assume that real and imaginary parts of the effective stiffness tensor generally share the same symmetry elements, as is often done for

convenience within the context of seismic modelling in real media (e.g., Carcione [2007]; Zhu and Tsvankin [2007]).

Laboratory experimental data, similar to those reported in this sub-section, can be found in Arts et al. [1992], Arts [1993] and Rasolofosaon [2010].

4.8 Seismic anisotropy for earth subsurface exploration and exploitation ... what is it for?

In the previous sections we have discussed in some detail theoretical aspects of elastic anisotropy always in close connection with experimental results, following the overall spirit of the book. The main topic of this section could be summarized by the following question: “what is the added value of taking into account seismic anisotropy for the exploration and/or exploitation of the earth subsurface? “.

In the historical section 4.1 of seismic anisotropy we pointed out that seismic anisotropy has quickly evolved from a sophisticated curiosity for specialists to a mainstream research topic leading to practical tools now routinely used in the earth subsurface exploration and exploitation (e.g., Thomsen [2002]; Grechka [2009]). This can be considered as a clear demonstration of the added value of taking into account seismic anisotropy. In this section we go further by describing the two main branches of research and development in seismic anisotropy, namely in seismic processing and in reservoir characterization

4.8.1 Anisotropy as noise to be eliminated or corrected ... for Seismic processing

In this first approach seismic anisotropy is considered as “noise” that contaminates or at least complicates seismic data. “Noise” in acoustics in general (e.g., Rossing [2007]) and in seismics in particular (e.g., Sheriff [1991]) is any “unwanted signal” that competes with the information that one wishes to extract from the data. Because of its ubiquitous presence in the earth’s subsurface, pointed out in the introduction of the present chapter, seismic anisotropy induces unwanted effects on the data that need to be corrected for.

Not taking into account for seismic anisotropy in seismic processing by using isotropic tools can lead to errors in all the different stages of seismic processing, namely velocity analysis , NMO, dip moveout (DMO), time migration, time-to-depth conversion, and amplitude versus offset (AVO) analysis as extensively discussed in the literature (for instance see Tsvankin [2001]; MacBeth [2002]; Thomsen [2002]; Grechka [2009] and all the references therein).

As steadily pointed out during the International Workshops on Seismic Anisotropy (IWSA) (see the historical section 4.1 of seismic anisotropy), the integration of seismic anisotropy has

played a substantial role in the recent progress of exploration geophysics (e.g., Thomsen, 2002), mainly because of the acquisition of seismic data of better quality (denser 3D to 4D acquisition, wider frequency spectra, new acquisition techniques: mainly Ocean Bottom Seismics and vertical cables), of the introduction of new concepts (new imaging algorithms, better way to use the amplitudes, more complete use of the vectorial nature of the waves), and of the set-up of new tools (more and more powerful computers, more and more user-friendly interfaces for seismic interpretation).

In each of these items seismic anisotropy play a substantial role, illustrated for instance:

- ◇ In the case of present seismic acquisitions with long source-receiver offsets involving large variations of the incidence angle and necessitating a good integration of the directional dependence of the velocities, one of the main manifestations of seismic anisotropy (see sub-section 4.4)
- ◇ For the quantitative analysis of the seismic amplitudes as functions of the source-receiver offset and the azimuth, as in the case of fractured reservoirs, necessitating a theory allowing to take into account the azimuth variation and the offset dependence of seismic reflectivity, which is quite well described by seismic anisotropy theory (e.g., Rüger [1996]; Grechka [2009]), and
- ◇ The complete integration of seismic anisotropy in all the stages of seismic processing, which would have been unthinkable less fifteen years ago, thanks to the spectacular improvements in computer technology .

We shall illustrate the above considerations by experimental data in the laboratory and in the field regarding seismic imaging.

Regarding seismic migration in the laboratory, in sub-section 2.3.2.3 of Chapter 2 we report the physical modelling results of Martin et al. [1992] who analyzed the effect of anisotropy on wave propagation and on imaging using laser ultrasonic techniques. The studied natural material is Angers slate, a strongly anisotropic rock approximated by a thinly layered medium exhibiting macro-fractures parallel to the layering. Both causes exhibiting rotational invariance about the normal to the layering and to the macrofracture planes, after Curie's symmetry principle, the rock can be approximated by an equivalent Transversely Isotropic (TI) medium of symmetry ∞/mm (see Figure 4.2.2-1 of section 4.2.1 and the corresponding comments). The data on a tilted slate model with the planes of schistosity rotated 22.5° from the vertical axis (see top of Figure 2.3.2-15 Chapter 2) were "isotropically" migrated, using an algorithm ignoring anitropy. The shape of the bottom reflector of the model is quite unrecognizable: the reflectors are mis-located, and the rounded ridge and the fault have completely disappeared as shown by Figure 2.3.2-15b. The effects of anisotropy amplified so that, without knowing the geometry of the model, it is very difficult to achieve even an approximate reconstruction of the geometry of the reflector. In contrast if anisotropy is taken into account in the migration algorithm the reconstructed image of the structure is surprisingly improved as illustrated by Figure 2.3.2-17, even unveiling the presence of strong dipping reflectors unambiguously corresponding to cleavage planes in the slate clearly shown on Figure 2.3.2.-10(b).

Similar results have been reported, with more conventional physical modelling techniques, by Isaac and Lawton [1999] with a model made of transversely isotropic (TI) phenolic material. The authors mainly emphasize the mispositioning of the reflectors due to dipping TI structure, pointed out in the previous reference and commented on the Figure 2.3.2-16 of Chapter 2, (excerpt from that reference).

Regarding seismic migration in the field we have selected offshore data from West Africa of Alkhalifah et al. [1996] reported on Figure 4.8.1-1. The figure compares the results of an isotropic migration and an anisotropic migration on the same data set.

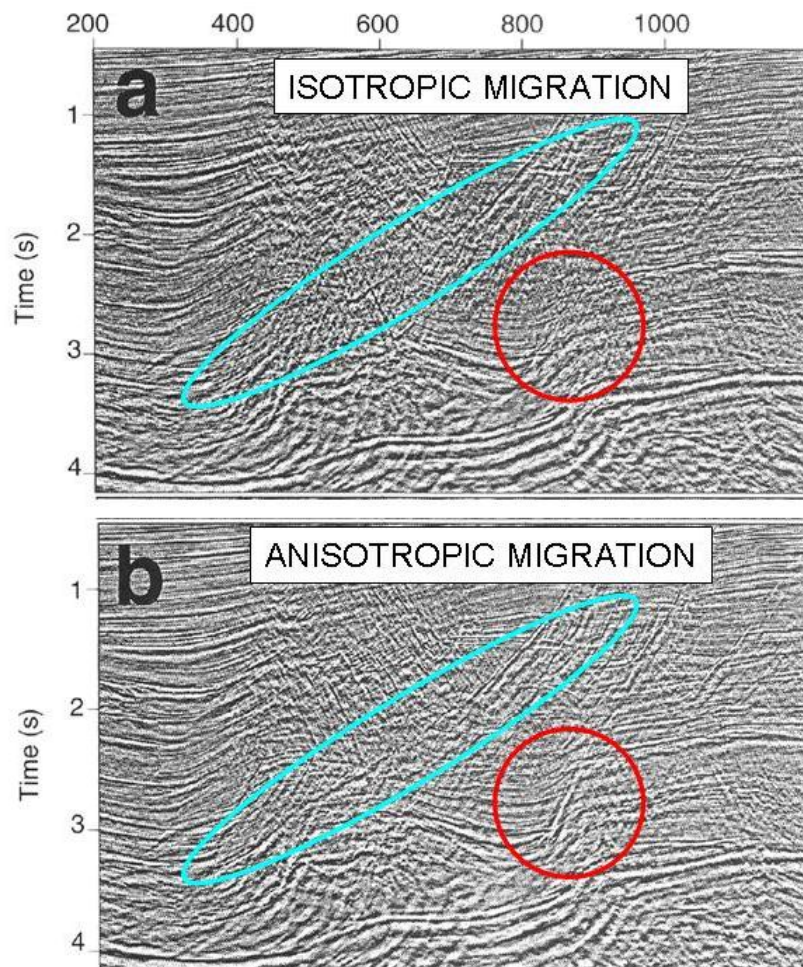


Figure 4.8.1-1: Comparison between (a) 2D isotropic migration and (b) 2D anisotropic migration on offshore data of West Africa (modified after Alkhalifah et al. [1996]).

The data have been migrated with a 2D phase shift time migration, using a methodology described in the last reference. In the anisotropic case, Transverse Isotropy with a Vertical axis (VTI) of rotational invariance is assumed. As for the physical modelling data in the laboratory, the benefits of taking into account seismic anisotropy is quite clear. As for the laboratory data, the most significant result is the un veiling of a fault (surrounded with a red circle) perfectly visible on the “anisotropically” migrated section and totally invisible, or at

least blurred, on the “isotropically” migrated section. Another substantial result is the improvement in the continuity of the dominant fault dipping to the left of the figure and highlighted by the blue ellipse. More details can be found in the last reference.

Many more examples of improvement of different stages of seismic processing by taking into account seismic anisotropy can be found for instance in Tsvankin [2001]; MacBeth [2002]; Thomsen [2002]; Grechka [2009] and all the references therein.

4.8.2 Anisotropy as an information to be used ... for Reservoir characterization

In contrast with the previous approach here seismic anisotropy is no longer considered as “noise” but a signature of the medium of propagation, that needs to be exploited in order to extract some properties of the medium. This is typically the field of seismic anisotropy for reservoir characterization, more specifically for fracture characterization. Here again the topic is extensively discussed in the literature (e.g., Thomsen [2002]; Crampin and Peacock [2005]; Grechka [2009]; and the references therein).

We shall illustrate the above considerations by experimental data in the laboratory and field data on a geothermal regarding seismic imaging.

Regarding the link between the presence of microfractures/microcracks and ultrasonic anisotropic in the laboratory we report the work of Rasolofosaon et al. [2000] on one of the crystalline rocks from a KTB, the German Continental Deep Drilling site, pilot well. The complete set of 21 elastic coefficients of the elasticity matrix were measured on a dry paragneiss sample at increasing levels of confining pressure P_c , up to $P_c=400\text{MPa}$, and fixed pore pressure equal to atmospheric pressure using the techniques described in Chapter 2 §2.2.4-1. Figure 4.8.2-1 show the complete directional dependence of the measured qP-wave phase velocity for $P_c=10\text{MPa}$ (figure on the left hand side) and for $P_c=400\text{MPa}$ (figure in the middle). Using the methodology developed by Arts et al. [1996] these data allow to separate the anisotropy due to the mechanical defects (i.e., microfractures, microcracks, grain joints etc...) and the anisotropy due to the intact rock (i.e. the rock without the defects).

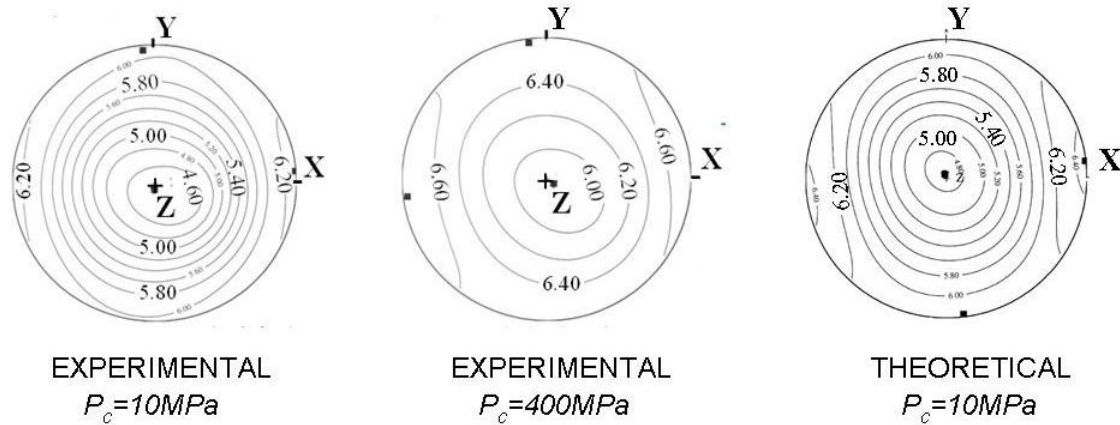


Figure 4.8.2-1: Complete directional dependence of the qP-wave phase velocity surface (Left) Experimental data for confining pressure $P_c=10\text{MPa}$, (Middle) Experimental data for confining pressure $P_c=400\text{MPa}$ (Right) Theoretical prediction for confining pressure $P_c=10\text{MPa}$. Equal area projection (lower hemisphere). Case of a Paragneiss sample (modified after Rasolofosaon et al. [2000]).

In summary, it is assumed that at the highest confining pressure (or terminal confining pressure) the rock practically behaves as an intact material (i.e. a material without mechanical defects). Thus its behaviour is governed by the grain constituents and the stiff pores (mainly roughly spherical pores which remain open under high confining pressure). Note that in sedimentary rocks (sandstones, limestones, dolomites...) the stiff pores can be abundant. In the case of the studied paragneiss sample the stiff porosity is practically nonexistent. Thus the anisotropic compliance tensor $S^{(terminal)}$ at terminal confining pressure is, by definition, equal to the anisotropic compliance tensor $S^{(intact\ rock)}$ of the background medium:

$$(4.8.2-1) \quad S^{(terminal)} = S^{(intact\ rock)}$$

In the theoretical model the intact rock is the background medium, in which cracks/fractures are added to build a fractured model following the relation (e.g., Schoenberg and Sayers [1995]):

$$(4.8.2-2) \quad S^{(fractured\ rock)} = S^{(intact\ rock)} + \Delta S^{(fractures)}$$

where $S^{(fractured\ rock)}$ is the compliance tensor of the fractured rock and $\Delta S^{(fractures)}$ the additional compliance due to the presence of the fractures/cracks. If one assumes that the compliance of the intact rock is practically independent of the confining pressure P_c one can deduce $\Delta S^{(fractures)}$ from the data:

$$(4.8.2-3) \quad \Delta S^{(fractures)}(P_c) = S^{(fractured\ rock)}(P_c) - S^{(intact\ rock)}(P_c) \approx S(P_c) - S^{(terminal)}$$

where $S(P_c)$ is the compliance tensor corresponding to the confining pressure P_c . The first equality is deduced from Equation (4.8.2-2) and the the second approximate equality is due to Equation (4.8.2-1) and to the assumption of pressure independence of the intact rock. The compliance tensors of the rock $S(P_c)$ at confining pressure and $S^{(terminal)}$ at terminal pressure being measured, the additional compliance $\Delta S^{(fractures)}$ due to the presence of the fractures/cracks can be deduced experimentally from Equation (4.8.2-3). If the interaction between each fracture/crack is neglected, each fracture/crack ignores the presence of the other fractures/cracks and is only influenced by the stress at infinity. After the last reference, under the noninteraction assumption the additional compliance due to the fractures/cracks is simply equal to the sum of the compliances of each fracture/crack without any interaction term. Furthermore, it is possible to approximate $\Delta S^{(fractures)}$ by the additional compliance due to three families of parallel fractures mutually orthogonal, using the method proposed by Rasolofosaon et al. [2000] and detailed in Arts et al [1996]. In the eigen-axes $X^{(I)}X^{(II)}X^{(III)}$ of the system of three fracture families, the orthotropic approximation of the rotated additional compliance matrix $\left[\mathbf{R}_{XYZ \rightarrow X^{(I)}X^{(II)}X^{(III)}} \left(\Delta S^{(fractures)} \right) \right]$ have the diagonal form (e.g., Schoenberg and Douma [1988]):

(4.8.2-4)

$$\left[\mathbf{R}_{XYZ \rightarrow X^{(c)}Y^{(c)}Z^{(c)}} \left(\Delta S^{(fractures)} \right) \right] \approx \text{Diagonal} \left\{ Z_N^{(I)}, Z_N^{(II)}, Z_N^{(III)}, Z_T^{(II)} + Z_T^{(III)}, Z_T^{(I)} + Z_T^{(III)}, Z_T^{(I)} + Z_T^{(II)} \right\}$$

where $\mathbf{R}_{XYZ \rightarrow X^{(c)}Y^{(c)}Z^{(c)}}$ is the rotation from the coordinates axes XYZ of the sample to the eigen-axes $X^{(c)}Y^{(c)}Z^{(c)}$ of the system of three fracture/crack families, and $Z_N^{(K)}$ and $Z_T^{(K)}$ the normal and tangential overall compliance of the fracture family number K ($K = I, II, III$). The recovered eigen axes of the cracks/ are given by $X^{(c)} = (0.096, -0.995, -0.035)$, $Y^{(c)} = (-0.028, -0.038, 0.999)$ and $Z^{(c)} = (0.995, 0.095, 0.032)$ in the coordinate axes of the sample. This means that the eigen-axes $X^{(c)}Y^{(c)}Z^{(c)}$ of the fracture/crack system are rather close to the coordinates axes XYZ of the sample, as can be seen on Figure 4.8.2-1. The recovered normalized compliances of each family of crack/fracture are:

$$(4.8.2-5) \quad \begin{cases} E_N^{(I)} = 9.2\% & ; & E_T^{(I)} = 6.2\% \\ E_N^{(II)} = 61.7\% & ; & E_T^{(II)} = 16.5\% \\ E_N^{(III)} = 2.0\% & ; & E_T^{(III)} = 1.9\% \end{cases}$$

where the normalized compliances are defined by $E_N^{(K)} = S_N^{(K)} C_{11}^{(intact\ rock)}$ and $E_T^{(K)} = S_T^{(K)} C_{44}^{(intact\ rock)}$ ($K = I, II, III$), with respect to the equivalent isotropic intact rock. The tensor $ISO C^{(intact\ rock)}$ is the best isotropic replacement tensor (e.g., Fedorov [1968];

Arts *et al.* [1991b]; Helbig [1994]; Sayers [1994] of the anisotropic stiffness tensor $C^{(intact\ rock)} = \left(S^{(intact\ rock)} \right)^{-1}$. Equation (4.8.2-4) shows that the crack/fracture family number II, nearly normal to the Z axis of the sample, is the dominant family. This is consistent with Figure 4.8.2-1. It is practically about the Z-axis that the qP-wave phase velocity variation with confining pressure is the largest. Furthermore the predictions of the simplified rock model with 3 families of cracks/fractures mutually perpendicular are in agreement with the experimental data (compare sub-figure on the right side and sub-figure on the left side of Figure 4.8.2-1).

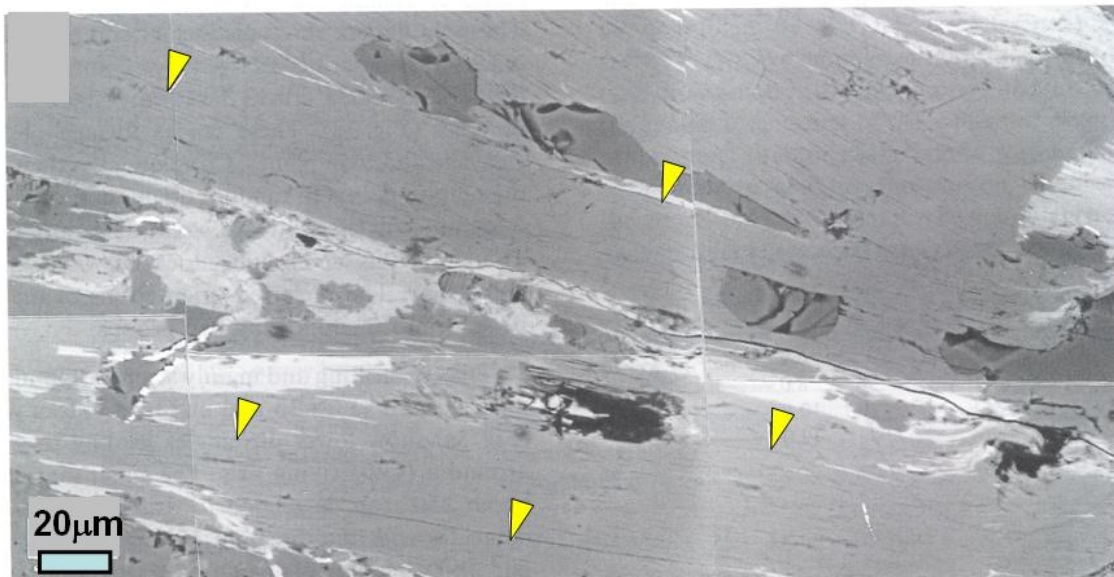


Figure 4.8.2-2: Scanning microscope image (back-scattered electrons) of a paragneiss sample from the German Continental Deep Drilling site (KTB pilot well), at a depth of 3145m, showing cleavage cracks in mica (yellow arrows), identified as the main cause of crack-induced ultrasonic anisotropy (modified after Rasolofosaon *et al.* [2000]).

Lastly, detailed analyses of mineral composition, textures and microcrack fabric showing that, on this rock sample, the main cause of the observed crack-induced anisotropy is the presence of cleavage cracks in mica (yellow arrows on Figure 4.8.2-2).

Regarding field experiments results, we have selected data on Coso geothermal field in California [Lou and Rial, 1997]. In this example, measurements of Shear-wave birefringence and polarization are used to characterize fracture orientation and density. This area is a very active seismic zone with an average of 20 microearthquakes per day, half of which are natural tremors and the rest are associated to geothermal field injection/production activity (Malin [1994]; Alvarez [1992]). Signals are recorded by a seismic network of 3-component borehole receivers located at depth of 100m or more, so that background noise is minimized and the interference of shear waves with the free surface is greatly reduced. More than 400 time

delays between the fast and slow shear-waves were measured in a target area of 21 (km)x 21 (km)x 6 (km).

As described in Section 4.6.2, and as illustrated by Figure 4.8.2-3 and the corresponding comments, the strikes of the assumed vertical cracks/fractures inferred from the polarization directions of the fastest shear-wave is clearly correlated with the independently observed lineaments on photographs and magnetically measured lineaments (modified after Lou and Rial [1997]).

More precisely, the rose diagrams of the polarization directions of the leading S-wave for nine stations exhibit three major directions, namely N40°-60°E (for stations S2, S7, N5), N0°-25°E (for stations S1, S4, S8, N1), and N25°-35°W (for station N4). These three fracture trends are in agreement with the photographically mapped lineaments (N60°E, N-S, and N35°W), in purple on the Figure [Bryan et al., 1990], and magnetically mapped lineaments (N40±E, N-S, and N55±W), in green on the Figure, all measured in the area [Moore and Erskine, 1990].

Regarding crack/fracture densities Lou and Rial use the shear-velocity equations of Hudson [1981], linked with the linear slip fracture model of Section 4.6.2:

$$(4.8.2-6) \quad \begin{cases} V_{S1}^2 = V_{S0}^2 \left\{ 1 - \frac{8\zeta V_{P0}^2 (1 + \cos 4\theta)}{3(3V_{P0}^2 - 2V_{S0}^2)} \right\} \\ V_{S2}^2 = V_{S0}^2 \left\{ 1 - \frac{8\zeta V_{P0}^2 (1 + \cos 2\theta)}{3(3V_{P0}^2 - 2V_{S0}^2)} \right\} \end{cases}$$

where V_{S1} and V_{S2} designate the velocities of the two shear waves polarized respectively parallel and at right angles to the local symmetry plane of the cracks/fractures, θ being the angle of propagation from the strike of the aligned cracks/fractures.

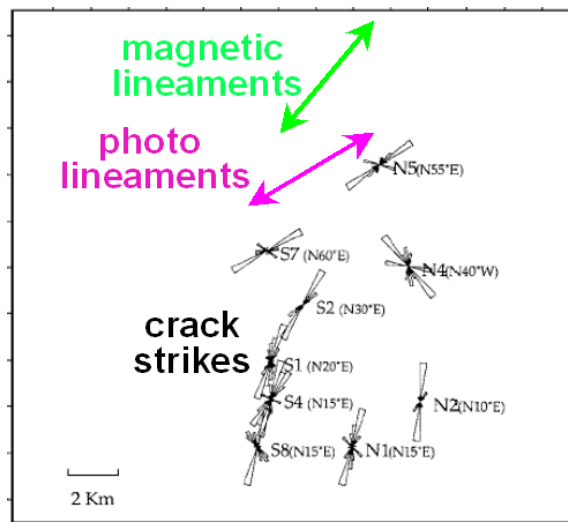


Figure 4.8.2-3: Map view of the crack/fracture strikes inferred from the polarization direction of the fastest shear wave, compared with the independently observed lineaments on photographs and magnetically measured lineaments (modified after Lou and Rial [1997])

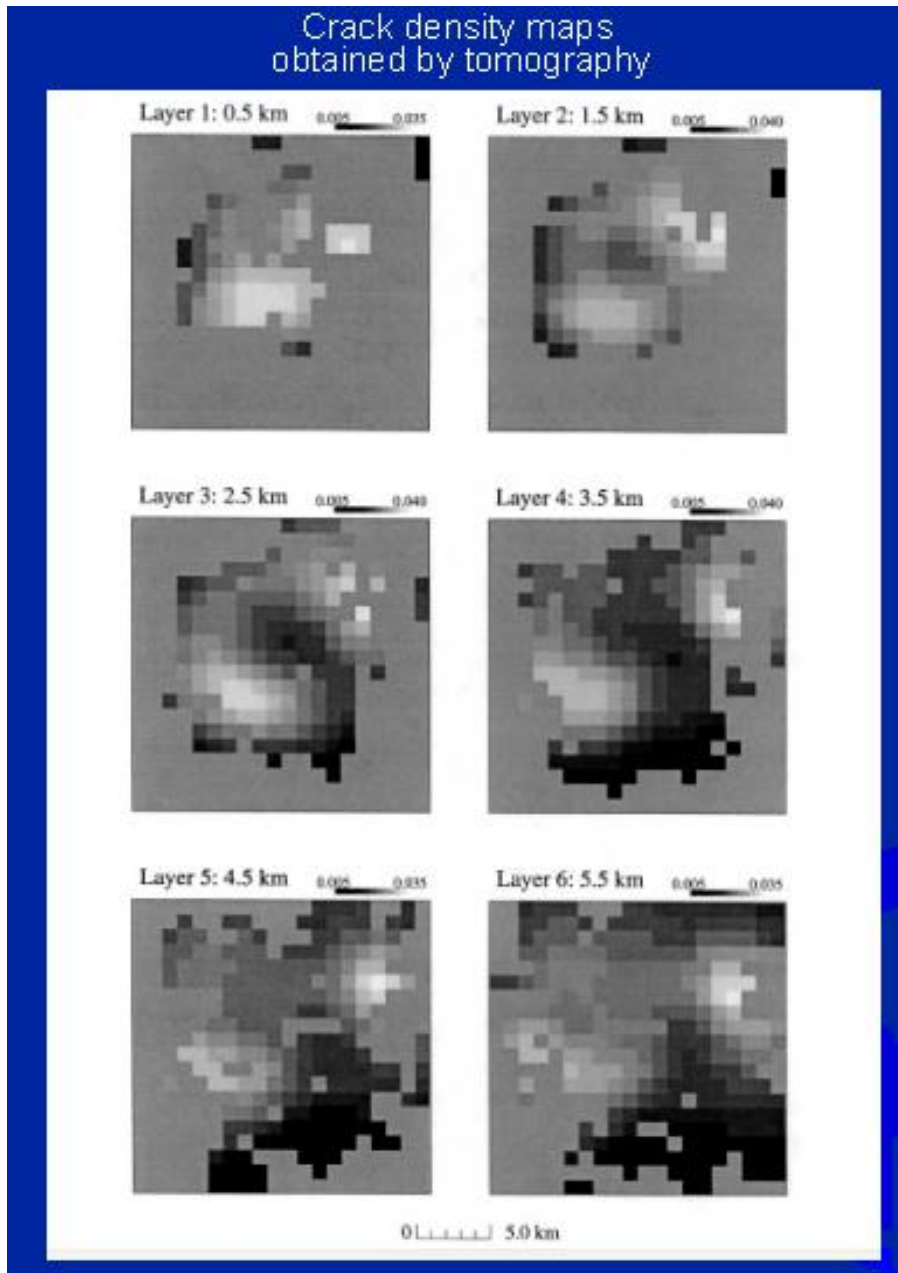


Figure 4.8.2-4: Tomographic maps of the crack/fracture density using shear wave birefringence. Dark shading indicates low crack density and light shading indicates high crack density (after Lou and Rial [1997]).

Seismic anisotropy is assumed to be due to aligned fluid-filled "penny-shaped" crack of density $\zeta = N \langle a^3 \rangle$, where N is the number of cracks per unit volume and $\langle a^3 \rangle$ is the volume average of the crack radius cubed.

The cracks are randomly distributed in an isotropic background medium (the host uncracked rock), characterized by P-wave and S-wave velocities V_{P0} and V_{S0} .

If L is the propagation distance between the source and the receiver the time delay τ between the fastest shear wave and the slowest shear wave is given by the expression:

$$(4.8.2-7) \quad \tau = L \left| \frac{1}{V_{S2}} - \frac{1}{V_{S1}} \right|$$

Assuming $V_{P0}/V_{S0} = \sqrt{3}$ (or equivalently Poisson's ratio ν equal to 0.25, after equation (1.2.2-19) of Chapter 1) for the background medium, Sato et al. [1991] derived from the two previous equations the following simple expression for the time delay:

$$(4.8.2-8) \quad \tau = 4\zeta (\cos 4\theta - \cos 2\theta) L / (7V_{S0})$$

In this equation the last authors used first order perturbation and assumed $60^\circ < \theta < 90^\circ$ [Sato et al., 1991].

With a total of 450 data points (time delays) in the target zone Lou and Rial, using the tomographic inversion scheme proposed by Shalev and Lou (1995), determined a 3-D crack density distribution at depths 0.5 km to 5.5 km (see Fig.5.4.2-2). Light shading indicates high crack density and dark shading indicates low crack density. The crack density typically ranges between 0.010 and 0.035 throughout the Coso volume. The relatively large crack density (around 0.035) areas concentrate on two northeast -trending blocks at depths between 1.5 - 3.5 km. These are in fact the most active geothermal production areas.

We clearly see that the method provide a rather simple tool for characterizing the 3D crack pattern in reservoirs. However there is a severe limitations mainly related to the uneven distribution of microearthquake locations and the low number of data points within the split shear-wave recording window. Rays included in the reliable shear-wave window are such that the corresponding incidence angle is smaller than a critical angle $i_C = \text{Arcsin}(V_{S0}/V_{P0})$. Outside this "window" S-waves along supercritical rays interact at any interface such that the time delay between the S-wave is irretrievably lost [Booth and Crampin, 1985]. For instance for $V_{P0}/V_{S0} = \sqrt{3}$ (or equivalently for Poisson's ratio equal to 0.25) the critical angle is roughly equal to 35° .

Many more examples of fracture characterization using seismic anisotropy in general, and not only shear-wave splitting, can be found in Thomsen [2002], MacBeth [2002], Crampin and Peacock [2001], and Grechka [2009] and all the references therein.

4.9 References

- Aki, K., Richards, P.G., 1980. *Quantitative Seismology*, Freeman and Co., New York
- Alford, R.M., 1986, Shear data in the presence of azimuthal anisotropy, *SEG Annual International Meeting, Expanded Abstracts*, 56, 476-479.
- Alkhalifah, T., Tsvankin, I., 1995, Velocity analysis for transversely isotropic media. *Geophysics*, 60, 1550-1566.
- Alvarez, M. G., 1992, The seismotectonics of the southern Coso range observed with a new borehole seismographic network: *M.Sc. thesis, Duke Univ.*
- Alkhalifah, T., Tsvankin, I., Larner, K., and Toldi, J., 1996, Velocity analysis and imaging in transversely isotropic media: Methodology and a case study: *The Leading Edge*, 15, 371–378.
- Anderholm, S. K. 1994. *Ground-water recharge near Santa Fe, north central New Mexico*. Water Resources Inventory Report 94-4078. U.S. Geological Survey, Albuquerque, New Mexico, USA.
- Anderson, D. L. (1989) *Theory of the Earth*. Blackwell Scientific Publications.
- Andronov, A.A. (1960) On natural rotation of polarization plane of sound. *Izv. Vuzov, Radiophys.*, III, 4, 645-649.
- Andrushchak, A.S., Bobitski, Y.V., Kaidan, M.V., Tybinka, B.V., Kityk, A.V., and W. Schranz, 2004, Spatial anisotropy of photoelastic and acoustooptic properties in β -BaB₂O₄ crystals, *Optical Materials*, 27, 619–624
- Aoki, T., Tan, C. P. & Bramford, W. E. 1993 Effects of deformation and strength anisotropy on boreholes failures in saturated rocks. *Int. J. Rock. Mech. Min. Sci. Geomech. Abstr.* 30, 1031–1034.
- Arago, D. F. , 1811, "Sur une modification remarquable qu'éprouvent les rayons lumineux dans leur passage a travers certains corps diaphanes, et sur quelques autres nouveaux phénomènes d'optique", *Memoires de l'Institut*, 12, 93-134.
- Arts, R. J., 1993, A study of general anisotropic elasticity in rocks by wave propagation - Theoretical and experimental aspects - . *Ph.D. thesis, Université Pierre et Marie Curie (Paris VI)*.
- Arts, R., O. Eiken, A. Chadwick, P. Zweigel, L. van der Meer and B. Zinsner, 2002, Monitoring of CO₂ Injection at Sleipner 4D Seismic Data. *Proceedings of the 6th International conference on Greenhouse Gas Control Technology*, Kyoto, Japan, 1-4 October 2002.
- Arts, R., Eiken, O., Chadwick, A., Zweigel, P., van der Meer, L., Zinsner, B., 2004, Monitoring of CO₂ injected at Sleipner using time-lapse seismic data, *Energy*, 29, Issue 9-10, 1383-1392.
- Arts, R.J., Rasolofosaon, P.N.J., Zinsner, B.E., 1991a, Complete inversion of the anisotropic elastic tensor in rocks (experiments vs. theory), *61st Annual International Meeting, SEG, Expanded Abstracts*, paper ST 2.5.
- Arts, R. J., Helbig, K., and Rasolofosaon, P. N. J., 1991b, General anisotropic elastic tensor in rocks - Approximation, invariants and particular directions: *61st Ann. Mtg., Soc. Expl. Geophys., Expanded Abstracts*, 1534-1537.
- Arts R.J., Rasolofosaon P.N.J. and Zinsner B.E. 1992. Experimental determination of the complete anisotropic viscoelastic tensor in rocks. *62nd SEG meeting, NewOrleans, Louisiana, USA, Expanded Abstracts*, 636–639.
- Arts, R. J., and P. N. J. Rasolofosaon, 1992, Complete elasticity tensor in dry and saturated rocks: Experiments versus theory: *62nd Annual International Meeting, SEG, Expanded Abstracts*, 648, doi: 10.1190/1.1822176.
- Arts, R. J., Rasolofosaon, P. N. J., and Zinsner, B. E. (1996). Experimental and theoretical tools for characterizing anisotropy due to mechanical defects in rocks under varying pore and confining pressures. In *Seismic Anisotropy* (S. E. Fjaer, Ed.), pp. 384–432. Society of Exploration Geophysicists, Tulsa, Oklahoma.
- Auld, B. A. , 1973, *Acoustic Waves and Fields in Solids*, Wiley Interscience.
- Aylmore, L. A. G. , and Quirk, J. P. , 1959, Swelling of clay-water system, *Nature*, 183, 1752-3.
- Babuska, V., and M. Cara, 1991, *Seismic Anisotropy in the Earth* (Kluwer Academic, Dordrecht, Netherlands).
- Backus, G. E., 1962, Long-wave elastic anisotropy produced by horizontal layering: *Journal of Geophysical Research*, 67, 4427–4440.
- Bakulin, A., Grechka, V., Tsvankin, I., 2000, Estimation of fracture parameters from to reflection seismic data—Part II: Fractured models with orthorhombic symmetry, *Geophysics*, 65, 1803–1817,
- Bakulin, A., Grechka, V., Tsvankin, I., 2000b, Estimation of fracture parameters from reflection seismic data—Part III: Fractured models with monoclinic symmetry, *Geophysics*, 65, no. 6 (november-december 2000); P. 1818–1830.
- Bakulin V.N. and Protosenya A.G. (1982) Nonlinear effects in travel of elastic waves through rocks (in Russian). *J. Dokl. Akad. Nauk SSSR*, 2, 314-316.

- Barthelemy, J.F., 2006, Etude multi-physique des milieux fissurés par changement d'échelle, IFP internal report.
- Barton, N. (2007). *Rock Quality, Seismic Velocity, Attenuation and Anisotropy*, Taylor & Francis, London.
- Behura, J., and I. Tsvankin, 2009, Role of the inhomogeneity angle in anisotropic attenuation analysis: *Geophysics*, 74, no.5, WB177–WB191.
- Best, A.I. 1994. Seismic attenuation anisotropy in reservoir sedimentary rocks, *64th SEG Meeting, Los Angeles, USA, Expanded Abstracts*, 822–825.
- Best, A. I., Sothcott, J. and C. McCann, 2007, Alaboratory study of seismic velocity and attenuation anisotropy in near-surface sedimentary rocks: *Geophysical Prospecting*, 55, 609–625, doi: 10.1111/j.1365-2478.2007.00642.x.
- Biot, M.A., 1955, Dynamics of viscoelastic anisotropic media: Proceedings Fourth Midwestren Conference on Solid Mechanics, Purdue University, Sept. 08-09, 1955, Publication #129, Eng. Experiment Station, Purdue University, Lafayette, Ind.
- Bona, A., and I. Bucataru, and M.A. Slawinski. Material symmetries of elasticity tensors. *Q. J. Mech. Appl. Math.*, 57:583–598, 2004.
- Bond, W.L., 1943. The mathematics of the physical properties of crystals, *Bell Sys. Tech. J.*, 22, 1–72.
- Booth, D. C., and Crampin, S., 1985, Shear-wave polarizations on a curved wavefront at an isotropic free-surface: *Geophys. J. Roy. Astr. Soc.*, 83, 31–45.
- Borgnis, F. E. , 1955, *Specific directions of longitudinal wave propagation in anisotropic media*, *Physical Review*, vol. 98, number 4, pages 1000-1005.
- Born M, Wolf E., 1999, *Principles of optics : electromagnetic theory of propagation, interference and diffraction of light*. Cambridge University Press; Cambridge ; New York.
- Bourbiaux, B., Basquet, R., Daniel, J.M., Hu, L.Y., Jenni, S., Lange, A., Rasolofosaon, P., 2004, Fractured reservoir management: recent progress and promising perspectives, 66th EAGE Conference & Exhibition, Paris, Extended abstracts, paper C033.
- Bourbié, T., Coussy, O. Zinszner, 1987, *Acoustics of Porous media*, IFP publications, Ed. Technip, Paris.
- Brown, R.J.S., Korringa, J. 1975. On the dependence of the elastic properties of a porous rock on the compressibility of the pore fluid. *Geophysics* 40: 608-616.
- Brown, R.J.S. , Lawton, D.C. (Eds.), 1993. Proceedings of the Fifth International Workshop on Seismic Anisotropy, Banff, Alberta, Canada, May 17– 22, 1992. *Can. J. Explor. Geophys.*, vol. 29.
- Bruggeman, D. A. G. (1937). Berechnung verschiedener physikalischer Konstanten von heterogenen Substanzen. III. Die elastische Konstanten der Quasiisotropen Mischkörper aus isotropen Substanzen. *Ann Physik Leipzig*, 29, 160–178.
- Brugger, K. , 1964, Thermodynamic definition of higher order elastic coefficients," *Physical Review B*, 133(6A), pp. 1611-1612.
- Brugger K. (1965) Pure mode for elastic waves in crystals. *J. Appl. Phys.*, 36, 759-768.
- Bryan, J.G., Baumgartner, E., and Austin, W., 1990, Remotely sensed controls on heat flow within the Coso geothermal area: implications for further exploration, Coso Field Trip, edited by Moore, J., and Erskine, M.: *Am. Assn. Petr. Geol. EMD* 1, 41–60.
- Budiansky, B., 1965, On the elastic moduli of some heterogeneous materials, *J. Mech. Phys. Solids*, 13, 223-227.
- Cady, W.G., 1946, *Piezoelectricity*; McGraw-Hill, New York, 1946.
- Calvert, R., 2005, Insights and Methods for 4D Reservoir Monitoring and Characterization, Distinguished Instructor series n°8, SEG, Tulsa.
- Carcione, J.M., 2007, *Wave Fields in Real Media: Theory and Numerical Simulation of Wave Propagation in Anisotropic, Anelastic, Porous and Electromagnetic Media*, Elsevier, Amsterdam.
- Cardona, R., 2002. Two theories for fluid substitution in porous rocks with aligned cracks. 72nd Ann. Internat. Mtg., Soc. Expl.Geophys., Expanded Abstracts. Paper ANI, vol. 3.5.
- Chadwick, P., M. Vianello, and S. C. Cowin, 2001, A new proof that the number of linear elastic symmetries is eight. *J. Mech. Phys. Solids*, 49:2471–2492, 2001.
- Chapman, M., 2003. Frequency-dependent anisotropy due to mesoscale fractures in the presence of equant porosity. *Geophys. Prospect.* 51, 369– 379.
- Cheng, A.H.D. 1997. Material coefficients of anisotropic poroelasticity, *Int. J. Rock Mech. Min. Sc. Geomech. Abstr.* 34: 199-205.
- Cheng, C.H., 1993, Crack models for a transversely isotropic medium, *J. Geophys. Res.*, 98, 675-684.
- Chesnokov, E. M., Kukharenko, Y. A. , Kukharenko, P. Y., 1998, Frequency dependence of physical parameters of microinhomogeneous media. Space statistics, *Proceedings of the 8th International Workshop on Seismic Anisotropy*, Boussens, France, April 20– 24, 1998, *Revue de l'Institut Français du Pétrole*, vol. 5., pp. 729-735.

- Chesnokov, E. M., Queen, J.H., Vichorev, A.A., Lynn, H.B., Hooper, J.M., Bayuk, I.O., Castagna, J.A., Roy, B., 2001, Frequency dependent anisotropy, SEG Technical Program Expanded Abstracts, pp. 2120-2123.
- Chesnokov, E. M., Zatsepin, S.V., 1991, Effects of applied stress on effective elastic anisotropy in cracked solids, *Geophys. J. Int.*, 107, 563-569.
- Chichinina, T.I., Obolentseva I.R (1998) Gyrotropy and anisotropy of rocks: similarities and differences. *Revue de l'Institut Français du Pétrole*, **53**, 655–667.
- Coussy O. 2004, *Poromechanics*. Wiley: New York.
- Christoffel, E. B., 1877, Über die Fortpflanzung von Stößen durch elastische feste Körper: *Annali di Matematica*, **8**, 293–243.
- Crampin , S., 1978, Seismic wave propagation through a cracked solid: Polarization as a possible dilatancy diagnostic, *Geophys. J. Roy. Astr. Soc.*, 53, 467-496.
- Crampin , S., 1981, A review of wave motion in anisotropic and cracked elastic media, *Wave Motion*, 3, 343-391.
- Crampin , S., 1985, Evaluation of anisotropy by shear-wave splitting, *Geophysics*, 50, 343-391.
- Crampin , S., 1987, Shear-wave polarizations: A plea for three-component recording, in S
- Crampin , S., Lovell, J.H., 1991, A decade of S-wave splitting in the earth's crust: what does it mean? what use can we make of it? and what shall we do next?, *Geophys. J. Int.*, 107, 387-407.
- Crampin , S., and Y. Gao, 2009, A review of a quarter century of International Workshops on Seismic Anisotropy in the crust (OIWSA–12IWSA), *J Seismol* (2009) 13:181–208.
- Crampin, S., and S. Peacock, 2005, A review of shear-wave splitting in the compliant crack-critical anisotropic earth: *Wave Motion*, 41, 59–77.
- Curie, P., 1894, Sur la symétrie dans les phénomènes physiques, symétrie d'un champ électrique et d'un champ magnétique, *J. Phys., Ser.3, III*, 393-415.
- Curie P, and J. Curie, 1880, Développement, par pression, de l'électricité polaire dans les cristaux hémihédres à faces inclinées. *Comptes Rendus (France)* 91:294–295.
- Curie P, and J. Curie, 1881, Contractions et dilatations produites par des tensions électriques dans les cristaux hémihédres à faces inclinées. *Comptes Rendus (France)* 93:1137–1140
- Danbom, S.H., and S.N. Domenico, eds., *Shear-wave exploration: SEG, Geophysical Developments* 1, 227–251.
- Desbrandes, R., 1985, *Encyclopedia of well logging*, IFP publications, Ed. Technip, Paris.
- Detournay, E., Cheng, A.H.D., 1993. Fundamentals of poroelasticity. In: Hudson, J.A. (Ed.), *Comprehensive Rock Engineering: Principles, Practice & Projects*. Pergamon, Oxford, pp. 113–171.
- Dewangan, P., and V. Grechka, 2003, Inversion of multicomponent, multi-azimuth, walkaway VSP data for the stiffness tensor.: *Geophysics*, **68** , no.3, 1022-1031.
- Dieulesaint, E and Royer D., 1974, *Ondes élastiques dans les solides* 2014 Application au traitement du signal (Masson, Paris) .
- Dmitriev, V., 2000, "Tables of the second rank constitutive tensors for linear homogeneous media described by the point magnetic group of symmetry," *Progress in Electromagnetics Research*, J. A. Kong (ed.), Vol. 28, 47–99, EMW Publishing, Cambridge, MA, 2000.
- Domany, E., Gubernatis, J.E., Krumhansl, J.A., 1975. The elasticity of polycrystals and rocks. *J. Geophys. Res.* 80, 4851–4856.
- Dziewonski, A.M. & Anderson, D.L., 1981. Preliminary reference earth model, *Phys. Earth planet. Inter.*, **25**, 297–356.
- Einstein, A., 1916, *Grundlage der allgemeinen Relativitätstheorie* (the foundation of the general theory of relativity), *Annalen der Physik* IV, 49, 284–339, available in Balibar, Françoise, 1993 *Albert Einstein, Oeuvres choisies* 2, *Relativités I, Relativité générale, cosmologie et théories unitaires*, Paris : Seuil CNRS, 179.
- Farra, V., 1989. Ray perturbation theory heterogeneous hexagonal anisotropic media. *Geophys J. Int.*, 99, 723-738.
- Farra, V., 1999. Computation of second order travelttime perturbation by Hamiltonian ray theory. *Geophys J. Int.*, 136, 205-217.
- Farra, V., 2001, High-order perturbations of the phase velocity and polarization of qP and qS waves in anisotropic media: *Geophysical Journal International*, **147**, 93-104.
- Farra, V., 2004, Improved First-Order Approximation of Group Velocities in Weakly Anisotropic Media: *Studia Geophysica et Geodaetica*, **48**, 199-213.
- Farra, V., Psencik, I., 2003, Properties of the zeroth-, first-, and higher-order approximations of attributes of elastic waves in weakly anisotropic media, *The Journal of the Acous. Soc. of Am.*, 114, 3, pp. 1366-1378.

- Fedorov, F.I., 1968. *Theory of Elastic Waves in Crystals*, Plenum Press, New York, NY.
- Fjaer, E., Holt, R.M., Rathore, J.S. (Eds.), 1996. Seismic Anisotropy. Proceedings of the 6th International Workshop on Seismic Anisotropy, Trondheim, Norway, July 03– 08, 1994. Society of Exploration Geophysicists, Tulsa.
- Forte, S. and Vianello, M. (1996). Symmetry classes for elasticity tensors, *J. of Elasticity*, 43 : 81–101.
- Fortunato, G., Rasolofosaon, P.N.J., 2002, Modélisation de la propagation des ondes sismiques dans les milieux poreux fracturés avec prise en compte des substitutions fluides, IFP report N°57175.
- Fung, Y. C., 1994, A First Course in Continuum Mechanics: For Physical and Biological Engineers and Scientists (Prentice Hall, Englewood Cliffs, NJ, ed. 3)
- Gajewski, D., Vanelle, C. , Psencik, I., 2003, Proceedings of the Tenth International Workshop on Seismic Anisotropy (10IWSA), Tutzing (Germany), April 14–19, 2002, *Journal of Applied Geophysics* 54 (2003) 453–454.
- Gardner, G.H.F., Gardner, L. W. and Gregory, A. R., 1974, Formation velocity and density—The diagnostic basics for stratigraphic traps: *Geophysics*, v. 39, p. 770-780.
- Gassmann, F. 1951. Über die elastizität poröser medien, *Vierteljahrsschrift der Naturforschenden Gesellschaft in Zürich* 96: 1-23.
- German, V. L., 1945, “Some theorem about anisotropic media,” *The Academy of Sciences Reports, USSR*, Vol. 48, 95–98, 1945.
- Grechka, V., 2009, Application of Seismic Anisotropy in the Oil and Gas Industry.: EAGE.
- Green, G., 1838, On the laws of reflexion and refraction of light at the common surface of two noncrystallized media: *Transactions of the Cambridge Philosophical Society*, CollectedWorks, 245–268.
- Gubernatis, J.E., Krumhansel, J.A., 1975, Macroscopic engineering properties of polycrystalline materials: Elastic properties, *J. Appl. Phys.*, 46(5), 1875-1883.
- Gupta, I.N., 1973a, Dilatancy an premonitory variation of P, S traveltimes, *Bull. Seis. Soc. Am.*, 63, 1157-1161.
- Gupta, I.N., 1973b, Premonitory variations in S-wave velocity anisotropy before earthquakes in Nevada, *Science*, 182, 1129-1132.
- Gurevich, B., 2003, Elastic properties of saturated porous rocks with aligned fractures, *Journal of Applied Geophysics*, 54, 203– 218.
- Hahn, T., Ed., 1996, *International Tables for Crystallography*, 4th ed.; Kluwer Academic Publishers: Boston, MA, 1996.
- Hall, S., J. -M. Kendall, O. Barkved, and M. Mueller, 2000, Fracture characterization using P-wave AVOA in 3-D OBS data: 70th Annual International Meeting, SEG, Expanded Abstracts , 1409-1412.
- Hamermesh, M., 1962, *Group Theory and its Applications to Physical Problems* (Addison-Wesley, Reading)
- Haussühl, S. (1983). *Physical Properties of Crystals*. Weinheim:Wiley- VCH.
- Hearmon, R.F.S, 1979, The elastic constants of crystals and other anisotropic materials, in *Landolt-Börnstein Tables, III/11, 1-244*, eds K.H. Hellwege and A.M. Hellwege, Springer-Verlag, Berlin.
- Helbig, K., 1956, Die Ausbreitung elastischer Wellen in anisotropen Medien: *Geophysical Prospecting*, **4**, 70–104.
- Helbig, K., 1958, Elastische Wellen in anisotropen Medien: *GerlandsBeiträge zur Geophysik*, **67**, 177–211, 256–288.
- Helbig, K., 1993, Longitudinal directions in media with arbitrary anisotropy: *Geophysics*, **58**, 680–691.
- Helbig, K., 1994. *Foundations of Anisotropy for Exploration Seismics*. Pergamon, New-York.
- Helbig, K., 1998, Layer-induced elastic anisotropy - part 1: forward relations between constituent parameters and compound medium parameters, *Rev. Bras. Geof.* vol.16 n.2-3 São Paulo July/Nov. 1998.
- Helbig, K., 2003, The first 100 years of elastic anisotropy, *J. Appl. Geophys.* **54**, 163.
- Helbig, K., 2008, The structure of the elasticity tensor, Internal report for Prague Center of MATHematical Geophysics, Meteorology and their Applications (MAGMA), Prague, Czech Republic
- Helbig, K. and P. Rasolofosaon, 2004, Anisotropic elasticity is Green, 11th International Workshop on Seismic Anisotropy, St John's, Canada.
- Helbig, K. and Thomsen, L. (2005). 75-plus years of anisotropy in exploration and reservoir seismics: A historical review of concepts and methods. *Geophysics*, 70(6):9ND–23ND.

PETROACOUSTICS – CHAPTER 4

- Hermann, C., 1934, Tensoren und Kristallsymmetrie, *Zeitschrift für Kristallographie*, A., 89, 32–48, 1934.
- Hershey, A. V., 1954, The elasticity of an isotropic aggregate of anisotropic cubic crystals, *J. Appl. Mech.*, 21, 236–240.
- Hill, R., 1965, A self-consistent mechanics of composite materials, *J. Mech. Phys. Solids*, 13, 213–222.
- Hood, J., Schoenberg, M., 1989, Estimating of vertical fracturing from measured elastic moduli, *J. Geophys. Res.*, 94, 611–618.
- Hornby, B. E., 1995, The elastic properties of shales, PhD dissertation, Univ. of Cambridge, Cambridge, England.
- Hudson, J. A., 1980, Overall properties of a cracked solid: *Math. Proc. Camb. Phil. Soc.*, **88**, 371–384.
- Hudson, J. A., 1981, Wave speeds and attenuation of elastic waves in material containing cracks: *Geophys. J. Roy. Astr. Soc.*, **64**, 133–150.
- Hudson, J. A., 1990, Overall elastic properties of isotropic materials with arbitrary distribution of circular cracks, *Geophys. J. Int.*, 102, 465–469.
- Hughes D.S. and Kelly J.L., 1953, Second-order elastic deformation of solids. *Phys. Rev.*, 92, 1145–1149.
- Hurwic, A., 1995, *Pierre Curie*, Flammarion, Paris..
- Ikeda, T., 1996, *Fundamentals of Piezoelectricity*, Oxford Science Publications.
- Ikelle, L., Gangi, T. (Eds.), 2000. Anisotropy 2000: Fractures, Converted Waves and Case Studies. Transactions of the 9th International Workshop on Seismic Anisotropy Society of Exploration Geophysicists, Tulsa, OK.
- Isaac, J. H., and Lawton, D. C., 1999, Image mispositioning due to dipping TI media: A physical seismic modeling study: *Geophysics*, 64, 1230–1238.
- Jaeger, J.C., Cook, N.G.W. and R. Zimmerman, 2007, *Fundamentals of Rock Mechanics*, 4th Edition. 2007: Wiley-Blackwell.
- Jakobsen, M. and P.N.J. Rasolofosaon, 2009, Do the Velocity and Attenuation Surfaces in Anisotropic Viscoelastic Media always share the same symmetries?, EAGE meeting, Amsterdam, paper S042.
- Jech, J., 1991, Computation of elastic parameters of anisotropic medium from traveltimes of quasi-compressional waves, *Phys. of the Earth and Plan. Int.*, 66, 153–159.
- Johnson, P.A. and P. N. J. Rasolofosaon, 1996, “Nonlinear elasticity and stressinduced anisotropy in rock,” *J. Geophys. Res.* 101, 3113–3124.
- Joshi, A.W., 1982, *Elements Of Group Theory For Physicists*, John Wiley and Sons
- Kelvin, Lord (William Thomson), 1856, On stresses and strains (XXI. Elements of a mathematical theory of elasticity, Part 1): *Philosophical Transactions of The Royal Society*, 166, 481–489.
- Kelvin, Lord (William Thomson), 1878, Elasticity: Mathematical theory of elasticity: *Encyclopedia Britannica*, 7, 796–825.
- Kolodner, I. , 1966, *Existence of longitudinal waves in anisotropic media*, *J. Acoust. Soc. Am.*, vol. 40, pages 729–730.
- Lavergne, M., 2001, *Seismic methods*, IFP publications, Ed. Technip, Paris.
- Lay, T., and T. C. Wallace (1995). *Modern Global Seismology*, Academic Press, San Diego, 521 pp.
- Leary, P. C., Crampin, S., McEvilly, T.V., 1990, Seismic fracture anisotropy in the earth's crust: an overview, *J. Geophys. Res.*, 95, 11105–11114.
- Lefevre, F., 1990, *Détection et mesure de la biréfringence des ondes S à partir de profil sismiques de puits verticaux*, Thèse de Docteur de l'Université de Grenoble.
- Lefevre, F., 1994, And if the P-waves were enough?: *SEG Annual International Meeting*, Expanded Abstracts, 64, 942–945.
- Li, X.Y. (1997) Viability of azimuthal variation in P-wave moveout for fracture detection. *67th Internat. Mtg. Soc. Explor. Geophys.*, Expanded Abstracts, 1555–1558.
- Lou, M. and J.A. Rial, 1997, Characterization of geothermal reservoir crack patterns using shear-wave splitting, *Geophysics*, VOL. 62, NO. 2 (March-April 1997); P. 487–494.
- Love, A. E. H., 1892, *A treatise on the mathematical theory of elasticity*: Cambridge University Press.
- Lubbe, R., 2005, A field and laboratory investigation of the compliance of fractured rock, D. Phil. Thesis, Oxford University, UK.

- Lubbe, R., Worthington, M.H., 2006, A field investigation of fracture compliance, *Geophys. Prosp.*, 54, 319-331.
- Lynn, H., Thomsen, L.A., 1986, Shear-wave exploration along the principal axes, *SEG Annual International Meeting, Expanded Abstracts*, 56, 473-476.
- MacBeth, C., 2002. Multi-Component VSP Analysis for Applied Seismic Anisotropy. *Handbook of Geophysical Exploration – Seismic Exploration*. Elsevier Science, Volume 26.
- Mainprice, D., 1990, A Fortran program to calculate seismic anisotropy from lattice preferred orientation minerals, *Computers and Geosciences*, 16(3), 385-393.
- Malin, P., 1994, The seismology of extensional hydrothermal system: Geothermal Resources Council, *TRANSACTIONS*, 18, 17–22.
- Martin, D., A. Ehinger, and P. N. J. Rasolofosaon, 1992, Some aspects of seismic modeling and imaging in anisotropic media using laser ultrasonics: 62nd Annual International Meeting, SEG, Expanded Abstracts, 1373–1376.
- Maultzsch, S., Chapman, M., Liu, E., Li, X.Y., 2003, Modelling frequency dependent seismic anisotropy in fluid saturated rock with aligned fractures: implication of fracture size estimation from anisotropic measurements, *Geophys. Prosp.*, 51, 381-392.
- Mavko, G., Mukerji, T., and Dvorkin, J., 1998, *The rock physics handbook*: Cambridge Univ. Press.
- Mensch, T., Rasolofosaon, P.N.J., 1997. Elastic wave velocities in anisotropic media of arbitrary symmetry - Generalization of Thomsen's parameters ϵ , δ and γ . *Geophys J. Int.*, 128, pp 43-64.
- Moore, J., and Erskine, M., Eds., 1990, *Coso Field Trip: Am. Assn. Petr. Geol. EMD* 1, 41–61.
- Myer, L.R., Hopkins, D., Peterson J.E., Cook, N.G.W., 1995, Seismic wave propagation across multiple fractures, in *Fractures and Jointed Rock Masses*, Eds. L.R. Myer, C.F. Tsang, N.G.W. Cook and R.E. Goodman, p. 105-109, Balkema.
- Nafe, J. E., and C. L. Drake, 1960, Physical properties of marine sediments, in *The Sea*, M. N. Hill, (Editor) Vol. 3. Interscience, New-York, 794–815.
- Naville, C., 1986, Detection of anisotropy using shear-wave splitting in VSP surveys: requirement and applications, *SEG annual Meeting, Houston*, S5.2, 391.
- Nicoletis, L., Cllet, C., Lefeuvre, F., 1987, Shear-wave splitting measurements from multishot VSP data, *SEG annual Meeting, Anaheim*, POS 6.1, 527.
- Nishizawa, O., 1982, Seismic velocity anisotropy in a medium containing oriented cracks – transversely isotropic case, *J. Phys. Earth*, 30, 331-347.
- Nemat-Nasser, S., Hori, M., 1993, *Micromechanics: Overall properties of heterogeneous materials*: North-Holland, Amsterdam.
- Nikitin L.V. and Chesnokov E.M. (1981) Influence of a stressed condition on the anisotropy of elastic properties in a medium. *Izvestiya Earth Physics*, 17, 174-183.
- Nikitin L.V. and Chesnokov E.M. (1984) Wave propagation in elastic media with stress-induced anisotropy, *Geophys. J. R. Astr. Soc.*, 76, 129-133.
- Nowick, A.S., 1995, *Crystal Properties via Group Theory*, Cambridge University Press, Cambridge.
- Nur, A., and G. Simmons, 1969, Stress-induced velocity anisotropy: An experimental study, *J. Geophys. Res.*, 74, 6667-6674.
- Nye, J.F., 1985 *Physical Properties of Crystals: Their Representation by Tensors and Matrices*. 1985, Oxford: Oxford University Press.
- Obolentseva I.R. (1992) Seismic gyrotropy. In: *Investigations of Seismic Waves Propagation in Anisotropic Media*. I.S. Chichinin (Ed.) 6-45, Nauka, Novosibirsk.
- Paterson, M. S. & Weiss, L. E. 1961. Symmetry concepts in the structural analysis of deformed rocks. *Bull. geol. Soc. Am.* 72, 841-882.
- Perez, M. A., Grechka, V., and Michelena, R. J., 1999, Fracture detection in a carbonate reservoir using a variety of seismic methods, *Geophysics*, 64, 1266–1276.
- Pervukhina, M., Golodoniuc, P. and D.N. Dewhurst, 2013, Phenomenologic study of seismic anisotropy in shales: 75th EAGE Conference & Exhibition incorporating SPE EUROPEC 2013 London, UK, paper We-P15-05.

- Podio-Lucioni, A., 1968, *Experimental Determination of the Dynamic Elastic Properties of Anisotropic Rocks, Ultrasonic Pulse Method*: PhD University of Texas at Austin.
- Ponte Castaneda, P., Willis, J.R., 1995. The effect of spatial distribution on the effective behaviour of composite materials and cracked media. *J. Mech. Phys. Solids* 43, 1919– 1951.
- Portigal D.L. and Burstein E. (1968) Acoustical activity and other first-order spatial dispersion effects in crystals. *Phys. Rev.* 170, 3, 673-678.
- Postma, G. W., 1955, Wave propagation in a stratified medium: *Geophysics*, **20**, 780–806.
- Prasad M. and Nur A. 2003. Velocity and attenuation anisotropy in reservoir rocks. 73rd SEG Meeting, Dallas, USA, Expanded Abstracts, 1652–1655.
- Pšenčík, I. and D. Gajewski, 1998. Polarization, phase velocity and NMO velocity of qP-waves in arbitrary weakly anisotropic media: *Geophysics* **63**, 1754-1766.
- Pyrak-Nolte, L. J., Myer, L.R., Cook, N.G.W., 1990, Transmission of seismic waves across natural fractures, *J. Geophys. Res.*, 95, 8617-8638.
- Rajagopal, K.R. and A.S. Wineman, 2008, A quasi-correspondence principle for quasi-linear viscoelastic solids: *Mech Time-Depend Mater* (2008) 12: 1–14, DOI 10.1007/s11043-008-9050-0
- Rasolofosaon, P.N.J. (Ed.), 1998a. Proceedings of the 8th International Workshop on Seismic Anisotropy, Boussens, France, April 20– 24, 1998. *Revue de l’Institut Français du Pétrole*, vol. 5. Technip, Paris.
- Rasolofosaon, P.N.J., 1998b. Stress-induced seismic anisotropy revisited, Proceedings of the 8th International Workshop on Seismic Anisotropy, Boussens, France, April 20– 24, 1998. *Revue de l’Institut Français du Pétrole*, vol. 5. 679-692.
- Rasolofosaon, P.N.J., 2000a. Normal move-out from horizontal and dipping reflectors in weakly anisotropic media of arbitrary symmetry. *Geophysics*, 65(4), 1294-1304.
- Rasolofosaon, P. N. J., 2000b. From transverse isotropy to arbitrary anisotropy for qP-waves in weakly anisotropic media. In: *Anisotropy 2000: Fractures, converted waves and case studies* (L. Ikelle , T. Gangi., Eds), *Transactions of the 9th International Workshop on Seismic Anisotropy*, Society of Exploration Geophysicists, Tulsa.
- Rasolofosaon, P.N.J., 2002, Étude de la sensibilité de la réponse sismique aux paramètres de fracturation, IFP report N°56689.
- Rasolofosaon, P.N.J., 2003. Any P-wave kinematic algorithm for vertical transversely isotropic media can be ADAPTEd to moderately anisotropic media of arbitrary symmetry type. *Journal of Applied Geophysics* 54 (2003) 335– 346
- Rasolofosaon, P.N.J., 2005, Fracture characterization in an Algerian gas reservoir using seismic azimuthal anisotropy, *Transactions of the 2nd EAGE North African Mediterranean Petroleum and Geosciences conference and exhibition*, Algiers, 10-30 april 2005, paper A-31.
- Rasolofosaon, P. N. J., 2009, Unified phenomenological model for the mechanical behavior of rocks: *Geophysics*, 74, WB107–WB116.
- Rasolofosaon, P. N. J., 2010, Generalized anisotropy parameters and approximations of attenuations and velocities in viscoelastic media of arbitrary anisotropy type – theoretical and experimental aspects, *Geophysical Prospecting*, **58**, 637-655.
- Rasolofosaon, P. N. J., 2011, Toward phenomenological universality of the mechanical behaviour of arbitrarily anisotropic porous rocks: *Geophysics*, 76, WA167–WA183.
- Rasolofosaon, P.N.J, Rabbel, W., Siegesmund, S., Vollbrecht, A., 2000, Characterization of crack distribution: fabric analysis versus ultrasonic inversion, *Geophys. J. Int.*, **141**, 413-424.
- Rasolofosaon P. and Yin H. (1996) Simultaneous characterization of anisotropy and nonlinearity in arbitrary elastic media, in: *Seismic Anisotropy*. E. Fjaer, R.N. Holt and J.S. Rathore (Eds), *Transactions of the 6th Int. Workshop on Seismic Anisotropy, SEG*, Tulsa OK.
- Rasolofosaon, P.N.J, Zinszner, B.E., 2002, Comparison between permeability anisotropy and elasticity anisotropy of reservoir rocks, *Geophysics*, 67(1), 230-240.
- Rasolofosaon P.N.J and Zinszner, B.E. (2007) The unreasonable success of Gassmann’s Theory—revisited. *Journal of Seismic Exploration*, 16, 281-301.

- Reuss, A. (1929). "Berechnung der Fließgrenze von Mischkristallen auf Grund der Plastizitätsbedingung für Einkristalle". *Journal of Applied Mathematics and Mechanics* **9**: 49–58.
- Riznichenko, J. W., 1948, The propagation of seismic waves in discrete and heterogeneous media: *Izvestiya AN SSSR, ser. geogr. i geoph.*, 13, 115–128.
- Rosmorduc, J., 1988, Arago et la naissance de la polarimétrie, *Revue d'histoire des sciences*, Tome 41 n°1, 25-38.
- Rossing, T. D., 2007, *Springer Handbook of Acoustics* _Springer Science_Business Media, LLC, New York.
- Rudzki, M. P., 1898, Über die Gestalt elastischer Wellen in Gesteinen, IV Studie aus der Theorie der Erdbebenwellen: *Bulletin of the Academy of Sciences Cracow*, 373–384.
- Rüger, A., 1996, Reflection coefficients and azimuthal AVO analysis in anisotropic media: Ph.D. thesis, Colorado School of Mines.
- Sakadi, Z., 1941, *Elastic waves in crystals*, Proc. Physico-Mathematical Soc. of Japan, vol. 23, pages 539-547.
- Sander, B., 1930, *Gefügekunde der Gesteine*. Springer, Berlin.
- Sander, B., 1970, An introduction to the study of fabrics of geological bodies, 641 p. Pergamon Press, Oxford.
- Sato, M., Matsumoto, N., and Niitsuma, H., 1991, Evaluation of geothermal reservoir cracks by shear-wave splitting of acoustic emission: *Geothermics*, **20**, 197–206.
- Savage, M.K. 1999. Seismic anisotropy and mantle deformation: What have we learned from shear wave splitting? *Rev. Geophys.* 37:65–106.
- Savage, M., 2006, An overview of seismic anisotropy determined from earthquakes, 12th International Workshop on Seismic Anisotropy, Beijing, China.
- Sayers, C.M., 2005, Seismic anisotropy of shales: *Geophysical Prospecting*, **53**, 667–676.
- Schoenberg, M., (1980). Elastic behavior across linear slip interfaces. *Journal of Acoustic Society of America*, Vol. 68, pp. 1516-1521.
- Schoenberg, M., Douma, J., 1988, "Elastic wave propagation with parallel fractures and aligned cracks", *Geophysical Prospecting*, 36, 571-590.
- Schoenberg, M., and Sayers, C. M., 1995, Seismic anisotropy of fractured rock: *Geophysics*, 60, 204–211.
- Settles, G. S., 2001, *Schlieren and Shadowgraph Techniques* (Springer, New York, 2001).
- Shalev, E., and Lou, M., 1995, A preliminary tomographic inversion of crack density in the Coso geothermal field: *EOS (Transactions)*, **76**, no. 46, 351.
- Shearer, P. M., 1999. *Introduction to seismology*, Cambridge University Press, Cambridge, UK.
- Sheriff, R.E., 1991. *Encyclopedic dictionary of exploration geophysics*, 3rd ed. Society of Exploration Geophysicists, Tulsa, OK.
- Shermergor, T. D., 1977, *Theory of Elasticity of Microheterogeneous media*: Nauka, Moscow.
- Shubnikov, A. V. (1956) On the works of Pierre Curie on symmetry, *Uspekhi Fizicheskikh Nauk*, 59, 591–602 (in Russian); English translated in Shubnikov, A. V. (1988) *Comp. Math. Appl.*, 16, 357–364.
- Siegesmund, S., Takeshita, T., Kern, H., 1989, Anisotropy of V_p and V_s in an amphibolite of the deeper crust and its relationship to the mineralogical, microstructural and textural characteristics of rocks, *Tectonophysics*, 157, 25-38.
- Sirotnina, Y. I., and M. P. Chaskolskaya, 1975, *Fundamentals of crystal physics* (in Russian): Nauka, Moscow.
- Staudte J.H., Cook B.D., 1967, Visualization of quasilongitudinal and quasitransverse elastic waves, *J. Acoust. Soc. Amer.* 1967. V. 41. N. 6. P. 1547-1548.
- Stoneley, R., 1949, The seismological implications of anisotropy in continental structure, *Mon. Not. R. Astron. Soc., Geophys. Suppl.*, 5, 222–232, 1949.
- Surhone, L.M., Timpledon, M.T. and S.F. Marseken, 2010, *Schlieren Imaging: Phased Array Ultrasonics, Radiography, Schlieren Photography*, Betaschrift publishing.
- Tabti, H., Rasolofosaon, P.N.J., 1998. Velocity analysis using nonhyperbolic moveout in anisotropic media of arbitrary symmetry – Synthetic and field data studies. in *Proceedings of the Eighth International Workshop on Seismic Anisotropy*, *Revue de l'Institut Français du Pétrole*, 53, 5, pp 555-570.

- Tatham R.B. and McCormack M.D. 1991. Multicomponent seismology in petroleum exploration. In: *Investigations in Geophysics*, No. 6. (eds). E.B. Neitzel and D.F. Winterstein SEG.
- Tattersall, H.G., 1973. The Ultrasonic Pulse -Echo Technique as Applied to Adhesion Testing. *J. Phys. D : Appl. Phys.*, Vol.6, 1973.
- Thomsen, L.A., 1986a. Weak elastic anisotropy. *Geophysics*, 51, pp 1954-1966.
- Thomsen, L.A., 1986b, Reflection seismology in azimuthally anisotropic media, SEG Annual International Meeting, Expanded Abstracts, 56, 468-470.
- Thomsen, L., 1995. Elastic anisotropy due to aligned cracks in porous rock. *Geophys. Prospect.* 43, 805– 829.
- Thomsen, L.A., 2002, Understanding seismic anisotropy in exploration and exploitation, SEG/EAGE Distinguished Instructor short course, N°5, SEG, Tulsa.
- Tilley, R. J. D. , 2006, Crystals and crystal structures, (John Wiley, New York).
- Tiwary, D. K., 2007, Mathematical Modeling and Ultrasonic Measurement of Shale Anisotropy and a Comparison of Upscaling Methods from Sonic to Seismic, PhD dissertation, University of Oklahoma.
- Truesdell, C. , 1966, *Existence of longitudinal waves*, *J. Acoust. Soc. Am.* , vol. 40, pages 730-730.
- Tsvankin, I., 1996. P-wave signatures and notation for transversely isotropic media – An overview. *Geophysics*, 61, pp 467-483.
- Tsvankin, I., 2001, Seismic signatures and analysis of reflection data in anisotropic media: Elsevier Science Publ. Co., Inc.
- Varadan, V.K, Varadan, V.V., 1982, Elastic wave scattering and propagation, Ann Arbor Science.
- Varadé, A., Bayon, A., Rasolofosaon, P. N. J., and Gascon, F., 1996, Experimental results on bulk waves and Rayleigh waves in slate: *J. Acoust. Soc. Am.*, **99**, 292–298.
- Vavrycuk, V., 2007. Ray velocity and ray attenuation in homogeneous anisotropic viscoelastic media, *Geophysics*, **72**, No. 6, D119-D127, doi:10.1190/1.2768402.
- Vestrum, R. W., 1994, Group- and Phase-velocity inversions for the general anisotropic stiffness tensor , PhD University of Calgary, Canada.
- Voigt, W. (1887). "Theoretische Studien über die Elasticitätsverhältnisse der Krystalle". *Abh.Kgl.Ges.Wiss.Göttingen, Math.Kl.* **34**: 3–51.
- Wang, H. F. , 2000, Theory of Linear Poroelasticity: Princeton University Press, Princeton, NJ.
- Widess, M.B., 1973, How thin is a thin bed, *Geophysics*, 38(6), 1176-1180.
- Willis, J.R., 1977, Bound and self-consistent estimates for the overall properties of anisotropic composites: *J. Mech. Phys. Solids*, 25, 185-202.
- Willis, J.R., 1981. Variational and related methods for the overall properties of composites. *Adv. Appl. Mech.* 21, 1 – 78.
- Willis, H., Rethford, G., Bielanski, E., 1986, Azimuthal anisotropy: Occurrence and effect on shear wave data quality, SEG Annual International Meeting, Expanded Abstracts, 56, 476-479.
- Worthington, M.H., Hudson, J.A., 2000, Fault properties from seismic Q, *Geophys. J. Int.*, 143, 937-944.
- Wooster, W. A., 1973, Tensors and Group Theory for the Physical Properties of Crystals (Oxford: Clarendon).
- Yin H. and Nur A. 1992. Stress-induced ultrasonic velocity and attenuation anisotropy of rocks, 62nd SEG Meeting, New Orleans, USA, Expanded Abstracts, 1073–1076.
- Zamora, M., 1990, Experimental study of the effect of the geometry of rock porosity on the velocities of elastic waves (in French), Docteur ès Sciences thesis, Univ. of Paris VII, Paris.
- Zamora, M. and Poirier, J.P., 1990. Experimental study of acoustic anisotropy and birefringence in dry and saturated Fontainebleau sandstone, *Geophysics*, **55**, 1455–1465.
- Zarembo, L., K., and V . A. Krasil'nikov, 1971, Nonlinear phenomena in the propagation of elastic waves in solids, *Sov. Phys. Usp.*, Engl. Transl., 13, 778-797, 1971
- Zeller, R., Dederich, P.H., 1973. Elastic constants of polycrystals. *Phys. Status Solidi, B Basic Res.* 55, 831–843.
- Zhu, Y., and I. Tsvankin, 2006, Plane-wave propagation in attenuative transversely isotropic media: *Geophysics*, 71, T17–T30.
- Zhu, Y. and Tsvankin, I., 2007, Plane wave attenuation anisotropy in orthorhombic media.

PETROACOUSTICS – CHAPTER 4

Geophysics, 72, pp. D9-D19.

Zinov'eva, G.P., Nesterov, I.I., Zhdakhin, E., Artma, E.E., and Y.U. Gorbunov, 1989, Investigation of rock deformation properties in terms of the nonlinear acoustic parameter (in Russian), Dokl. Akad. Nauk SSSR, 307, 337-341.

Zinsner, B., Meynier, P., Cabrera, J. and P. Volant, 2002, Vitesse des ondes ultrasonores, soniques et sismiques dans les argilites du tunnel de Tournemire. Effet de l'anisotropie et de la fracturation naturelle, *Oil & Gas Science and Technology – Rev. IFP*, Vol. 57 (2002), No. 4, pp. 341-353.

Zoback M., 2007 *Reservoir Geomechanics*: Cambridge University Press., 2007.

4.10 Subject index

additional compliance (fractures)	90, 91, 96, 116, 117	crack-induced anisotropy	104, 118
anisotropy parameters (for TI media)	53-61	crystallographic groups	14-15
anisotropy parameters (for arbitrarily anisotropic media)	61-67	Curie's limit groups	5, 8, 10-20, 33, 34, 39
anisotropy parameters (of P-wave)	53-55, 61-63	Curie's symmetry principle	1, 7-10, 14, 16-20, 34, 65, 95, 109
anisotropy parameters (of S-waves)	55-56, 63-65	dilute concentration	102, 105
axial vector	11	DipMove Out (DMO)	<i>see</i> Seismic processing
axial symmetry	5	double refraction (optical)	<i>see</i> birefringence (optical)
azimuthal anisotropy	70, 97, 100, 101	Einstein's summation convention	40
birefringence (shear-wave)	1, 46, 47-49, 55, 57, 70, 71, 76, 89, 96, 97, 114, 116, 126	elasticity symmetry classes	35
birefringence (optical)	48	elliptical coefficient	55
Born approximation	97, 100	Euler angles	31
Cauchy's equations of motion	<i>see</i> Kelvin-Christoffel tensor	fracture compliance	93-94, 96, 100, 101
Christoffel equations	<i>see</i> Kelvin- Christoffel equations	fracture density	120
Christoffel tensor	42-43	German theorem	<i>see</i> Hermann- German theorem
complex moduli	107	Hermann theorem	<i>see</i> Hermann- German theorem
complex stiffness coefficients	106-109	Hermann-German theorem	34, 36
complex stiffness matrix	106-109	Hooke's law (generalized)	23
complex stiffness tensor	109	index symmetry of elasticity tensor	42
compliance (additional)	<i>see</i> additional compliance	International Workshop on Seismic Anisotropy (IWSA)	5
compliance coefficients (interpretation of)	23-28	intrinsic rotation angle	<i>see</i> Euler angles
compliance matrix	23-28, 32-35, 44, 117, 32	isotropic replacement tensor	117
compliance tensor	23, 28, 30, 32, 44, 69, 70, 71, 89, 90, 91, 96, 116, 117	Kelvin representation	21
contracted indices	<i>see</i> Voigt notation	Kelvin-Christoffel equations	40-43, 101
cracks (ellipsoidal)	17, 101	Kelvin-Christoffel tensor	41
		layer-induced anisotropy	81, 86, 87, 100

PETROACOUSTICS – CHAPTER 4

<p>linear slip (fractures, interfaces...) 16, 89-91, 99, 102, 119</p> <p>longitudinal direction 38</p> <p>microcracks 80, 115</p> <p>mineral alignment (anisotropy due to) 68</p> <p>monoclinic 10, 15, 16, 18, 19, 38, 39, 41, 48, 63, 97</p> <p>Neumann's principle 160</p> <p>nonlinear elasticity 105</p> <p>normal compliance (fracture) 93-96</p> <p>Normal Move Out (NMO) <i>see</i> Seismic processing</p> <p>nututation angle <i>see</i> Euler angles</p> <p>optical birefringence <i>see</i> birefringence (optical)</p> <p>orthorhombic 8, 9, 10, 15, 16, 17, 18, 19, 39, 41, 48, 67, 96, 100</p> <p>orthotropic 17</p> <p>piezoelectric(ity) 9, 10</p> <p>Poisson's ratio (anisotropic) 25</p> <p>Poisson S effect 26</p> <p>Poisson S ratio (or coefficient) 26, 27, 28</p> <p>polar vector 11</p> <p>polarization vector 42, 43, 45</p> <p>precession angle <i>see</i> Euler angles</p> <p>Preliminary Reference Model (PREM) 4</p> <p>pressure (confining) 80, 115, 116, 117, 118</p> <p>pressure (terminal) 117</p> <p>propagation direction 43, 45</p> <p>Q or quality factor (anisotropic) 67, 109, 110, 111</p> <p>qP-wave <i>see</i> quasi P-wave</p> <p>qS-waves <i>see</i> quasi S-waves</p> <p>qS1-wave <i>see</i> quasi S-waves</p> <p>qS2-wave <i>see</i> quasi S-waves</p>	<p>quasi-longitudinal wave <i>see</i> quasi P- wave</p> <p>quasi P-wave 44, 45</p> <p>quasi S-waves 45</p> <p>quasi-transversal waves <i>see</i> quasi S- waves</p> <p>Representative Elementary Volume (REM) 3, 68, 82</p> <p>rotation of the elasticity tensor 30-33</p> <p>seismic anisotropy (history of) 11</p> <p>rotational invariance 5, 9, 11, 13, 14, 17, 18, 33, 34, 35, 39, 41, 68, 81, 99, 113, 114</p> <p>self-consistent (method, approximation) 70, 104, 105</p> <p>shale (anisotropy due to) 56, 68</p> <p>shear-wave birefringence <i>see</i> birefringence (shear-wave)</p> <p>shear-wave splitting <i>see</i> splitting (shear-wave)</p> <p>splitting (shear-wave) 1, 46, 47-49, 117, 120, 122, 123, 124</p> <p>stiffness coefficients (interpretation of) 29-30</p> <p>stiffness matrix 23, 32, 33, 35, 38, 39, 44, 45, 65, 71, 82, 106</p> <p>stiffness matrix (complex) <i>see</i> complex stiffness matrix</p> <p>stiffness tensor 23, 32, 42, 44, 69, 70, 71, 92, 104</p> <p>stiffness tensor (complex) <i>see</i> complex stiffness tensor</p> <p>strain tensor 20</p> <p>stress tensor 20</p> <p>stress-induced anisotropy 68, 105</p> <p>symmetry breaking 10</p> <p>symmetry group 7, 8, 9, 11, 12, 14, 15, 16, 34, 35, 38-41</p> <p>symmetry classes 13, 35, 36, 39-41</p> <p>symmetry classes for elasticity 33-40</p>
--	---

PETROACOUSTICS – CHAPTER 4

symmetry of geological media		15-20	
tangential compliance (fracture)	91-92,		
		94-96, 98, 99, 103, 104	
thinly layered media	13,		
		39, 40, 59, 60, 80-88	
Thomsen's parameters			
	<i>see</i>	anisotropy parameters	
transversely isotropic	13,		
		15, 16, 17, 18, 33, 34, 35, 40, 41,	
		52, 53, 54, 61, 63, 73, 74, 82, 83,	
		84, 91, 96, 106, 113, 114	
transverse isotropy	13, 17, 34,		
		48, 52, 53, 58, 71, 73, 81, 99, 100,	
		114	
			triclinic
			14, 15, 16,
			18, 23, 35, 36, 38, 41, 42, 44, 45,
			52, 97, 99, 107, 110
			viscoelasticity (anisotropic)
			1, 67, 105-
			112
			Voigt notation
			20-23, 32, 34,
			43
			Voigt representation
			21, 22, 32
			Young's modulus (anisotropic)
			24-25
			weak anisotropy
			1, 52-
			61, 61-67
			weakly anisotropic
			53,
			54, 105

4.11 Authors index

Aki, K.	85, 118	Bourbiaux, B.	119
Alford, R.M.	118	Bourbié, T.	42, 101, 102, 105, 107, 119
Alkhalifah, T.	118	Bramford, W. E.	118
Alvarez, M.G.	114, 118	Brown, R.J.S.	119
Anderholm, S.K.	78, 114	Bruggeman, D.A.G.	79, 119
Anderson, D.L.	4, 118, 120	Brugger, K.	119, 125
Andronov, A.A.	13, 118	Bryan, J.G.	114, 119
Andrushchak, A.S.	36, 118	Bucataru, I.	119
Aoki, T.	118	Budiansky, B.	100, 119
Arago, D. F.	13, 118, 124	Burstein, E.	13, 123
Arts, R.	1, 44, 46, 47, 49, 68, 87, 88, 102, 107, 111, 112, 113, 118	Cabrera, J.	126
Auld, B. A.	21, 32, 34, 38, 39, 40, 50, 52, 118	Cady, W.G.	9, 119
Austin, W.	119	Calvert, R.	119
Babuska, V.	1, 46, 118	Cara, M.	1, 46, 118
Bakulin, A.	93, 95, 118	Carcione, J.M.	4, 101, 105, 107, 119
Bakulin V.N.	118	Chadwick, A.	118
Backus, G. E.	52, 78, 79, 83, 118	Chadwick, P.	34, 119
Barkved, O.	121	Chapman, M.	119, 123
Barthelemy, J.F.	101, 118	Chaskolskaya, M.P.	9, 11, 13, 14, 15, 36, 125
Barton, N.	102, 118	Cheng, A.H.D	119, 120
Basquet, R.	119	Cheng, C.H.	98, 119
Baumgartner, E.	119	Chesnokov, E.M.	5, 19, 119, 123
Bayon, A.	125	Chichinina, T.I.	13, 119
Bayuk, I.O.	119	Christoffel, E. B.	4, 40-43, 51, 101, 105, 119
Behura, J.	101, 118	Cliet, C.	123
Best, A.I.	102, 118	Cook, N.G.W.	122, 123
Bielanski, E.	126	Cook, B.D.	50, 125
Biot, M.A.	101, 119	Coussy, O.	119
Bobitski, Y.V.	118	Cowin, S.C.	4, 21, 119
Bona, A.	34, 119	Crampin, S.	5, 49, 67, 111, 117, 119, 120, 122
Bond, W.L.	32, 119	Curie, J.	9, 120
Booth, D.C.	117, 119	Curie, M.	6
Borgnis, F.E.	37, 119		
Born, M.	36, 48, 97, 100, 119		

PETROACOUSTICS – CHAPTER 4

Curie, Pierre	1, 5, 7-10, 11-14, 16, 18-20, 33, 34, 39, 65, 95, 109, 120	Hahn, T.	8, 12, 36, 121
Danbom, S.H.	120	Hall, S.	121
Daniel, J.M.	119	Hamermesh, M.	14, 121
Dederich, P.H.	126	Haussühl, S.	13, 14, 36, 121
Desbrandes, R.	120	Hearmon, R.F.S	68, 89, 121
Detournay, E.	120	Helbig, K.	1-5, 13, 20, 21, 23, 32, 34, 37-40, 43, 44, 51, 52, 65, 77-79, 83, 93, 96, 113, 118, 121
Dewangan, P.	120	Hermann, C.	34, 36, 121
Dieulesaint, E	9, 21, 32, 34, 38, 39, 120	Hershey, A. V	100, 121
Dmitriev, V	36, 120	Hill, R.	100, 121
Domany, E.	120	Holt, R.M.	120, 124
Domenico, S.N.	120	Hood, J.	121
Douma, J.	16, 85, 87, 88, 97, 112, 125	Hooper, J.M.	119
Drake, C.L.	56	Hopkins, D.	123
Dziewonski, A.M.	4, 120	Hori, M.	65, 123
Ehinger, A.	122	Hornby, B.	57, 80
Eiken, O.	118	Hu, L.Y.	119
Einstein, A.	40, 120	Hudson, J. A.	16, 93, 97, 98, 100, 115, 120, 121, 122, 126
Erskine, M.	115, 119, 123	Hughes, D.S.	122
Farra, V.	63, 64, 120	Ikeda, T.	9, 122
Fedorov, F.I.	68, 71, 113, 120	Ikelle, L	122, 124
Fjaer, E.	118, 120, 124	Isaac, J. H.	51, 109, 122
Forte, S.	34, 120	Jaeger, J.C.	16, 122
Fortunato, G.	120	Jakobsen, M.	107, 122
Fung, Y. C.	9, 120	Jech, J.	122
Gajewski, D.	59, 121, 123	Jenni, S.	119
Gangi, T.	122, 124	Jones, E. A.	70, 74, 75, 76, 122
Gassmann, F.	121, 124	Johnson, P.A.	9, 122
Gao, Y.	5, 120	Joshi, A.W.	14, 122
Gardner, G.H.F.	56	Kaidan, M.V.	119
German, V. L.	34, 36, 121	Kelly, J.L.	122
Grechka, V.	5, 51, 65, 108, 109, 111, 117, 118, 120, 121, 123	Kelvin	2, 4, 21, 40-43, 101, 105, 122
Green, G.,	2, 4, 121	Kendall, J.M.	121
Gubernatis, J.E.	120	Kern, H.	125
Gupta, I.N.	121	Kolodner, I.	37, 122
Gurevich, B.	121	Korringa, J.	119

PETROACOUSTICS – CHAPTER 4

Krumhansl, J.A.	120	Neumann's principle	16
Kukharenko, Y.A.	119	Nicoletis, L.	123
Kukharenko, P.Y.	119	Niitsuma, H.	117, 124
Kityk, A.V.	119	Nikitin, L.V.	19, 123
Lange, A.	119	Nishizawa, O.	98, 123
Larner, K.	118	Nowick, A.S.	11, 123
Lavergne, M.	122	Nur, A.	8, 49, 102, 123, 126
Lawton, D.C	51, 109, 119, 122	Nye, J.F.	9, 32, 36, 123
Lay, T.	13, 122	Obolentseva, I.R.	13, 119, 123
Leary, P. C.	67, 122	Paterson, M.S.	1, 16, 67, 123
Lefeuvre, F.	122, 123	Peacock, S.	49, 111, 117, 120
Li, X.Y.	98, 122	Perez, M.A.	95, 123
Love, A. E. H.	1, 13, 122	Peterson, J.E.	123
Lou, M.	114, 115, 116, 117, 122, 125	Pervukhina, M.	60
Lovell, J.H.	67, 120	Podio-Lucioni, A.	123
Lubbe, R.	122	Ponte-Castaneda, P.	123
Lynn, H.B.	119, 122	Portigal, D.L.	13, 123
Mauguin, C.V.	36	Postma, G. W.	78, 123
MacBeth, C.	108, 110, 117, 122	Prasad, M.	102, 123
Mainprice, D.	66, 122	Protosenya A.G.	118
Malin, P.	114, 122	Psencik, I.	59, 63, 120, 121
Martin, D.	51, 109, 122	Pyrak-Nolte, L. J.	123
Marseken, S.F.	125	Queen, J.H.	119
Matsumoto, N.,	117, 124	Rajagopal, K.R.	101, 123
Maultzsch, S.	122	Rasolofosaon, P.	3, 4, 9, 19, 46, 47, 51, 59, 61, 64, 68, 94, 95, 96, 97, 100, 101, 107, 111, 112, 114, 118, 119, 120, 121, 122, 123, 124, 125, 126
Mavko, G.	69, 80, 123	Rathore, J.S.	120, 124
McCann, C.	118	Rethford, G.	126
McCormack, M.D.	48, 125	Reuss, A.	67, 71, 72, 73, 74, 85, 124
McEvelly, T.V.	122	Rial, J.A.	114, 115, 116, 117, 122
Mensch, T.	1, 51, 59, 61, 68, 123	Richards, P.	85, 118
Meynier, P.	126	Riznichenko, J. W.	78, 124
Michelena, R. J.	123	Rosmorduc, J.	13, 124
Moore, J.	115, 119, 123	Rossing, T. D.	108, 124
Mueller, M.	121		
Myer, L.R.	123		
Nafe, J.E.	56		
Naville, C.	123		
Nemat-Nasser, S.	65, 123		

PETROACOUSTICS – CHAPTER 4

Royer, D.	9, 21, 32, 34, 38, 39, 120	Timpledon, M.T.	125
Rudzki, M. P.	4, 78, 124	Tiwary, D.K.	60
Rüger, A.	109, 124	Truesdell, C.	37, 125
Sakadi, Z.	37, 124	Tsvankin, I.	13, 51, 101, 107, 108, 110, 118, 125, 126
Sander, B.	15, 124	Toldi, J.	118
Sato, M.	117, 124	Tybinka, B.V.	119
Savage, M.K.	4, 49, 124	van der Meer, L.	119
Sayers, C.M.	16, 66, 67, 68, 70-77, 85, 112, 113, 124, 125	Vanelle, C.	121
Schoenberg, M.	16, 78, 79, 85, 87, 88, 89, 97, 112, 121, 125	Varadé, A.	33, 125
Schranz, W.	119	Vavrycuk, V.	101, 125
Settles, G. S.	50, 125	Vestrum, R.	125
Shalev, E.	117, 125	Vianello, M.	34, 119, 120
Shearer, P. M.	13, 125	Vichorev, A.A.	119
Sheriff, R.E.	108, 125	Voigt, W.	7, 20-23, 32, 34, 43, 66, 67, 71-74, 126
Shermergor, T. D.	65, 125	Voigt notation	20-23, 32, 34
Shubnikov, A. V.	5, 6, 125	Volant, P.	126
Siegesmund, S.	66, 125	Wallace, T. C.	13, 122, 23
Sirotime, Y. I.	9, 11, 13, 14, 15, 36, 125	Wang, H.F.	70, 74, 75, 76, 122
Slawinski, M.A.	119	Weiss, L.E.	1, 16, 67, 123
Sothcott, J.	118	Willis, J.R.	123, 126
Staudte, J.H.	50, 125	Willis, H.	126
Stoneley, R.	125	Wineman, A.S.	101, 123
Surhone, L.M.	50, 125	Wooster, W.A.	14, 126
Tabti, H.	125	Worthington, M.H.	122, 126
Takeshita, T.	125	Yin, H.	102, 124, 126
Tan, C. P.	118	Zamora, M.	49, 126
Tatham, R.B.	48, 125	Zatsepin, S.V.	119
Tattersall, H.G.	85, 125	Zeller, R.	126
Thomsen, L.A.	4, 5, 13, 46, 49, 51-60, 64-67, 73, 77, 98, 100, 108, 110, 111, 117, 121-125	Zhu, Y.	107, 126
Thomson, W.	<i>see</i> Kelvin	Zimmerman, R.	122
Tilley, R..J.D.	14, 36, 125	Zinszner, B.	46, 47, 74, 75-77, 118, 119, 124, 126
		Zoback, M.	16, 126
		Zweigel, P.	119